Determination of Charge Transfer and Recombination Dynamics in Perovskite Solar Cells

Doctoral Thesis

Katarzyna Pydzińska-Białek

UaM

Adam Mickiewicz University, Poznań
Faculty of Physics
Department of Quantum Electronics

Determination of Charge Transfer and Recombination Dynamics in Perovskite Solar Cells
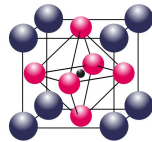
PhD thesis based on original publications

Katarzyna Pydzińska-Białek

Supervised by:

Prof. dr hab. Marcin Ziółek

Poznań, 2022

ACKNOWLEDGEMENTS

TABLE OF CONTENTS

ABSTRACT

The perovskite solar cells (PSCs) are the most promising and low-cost novel solar cells permitting in 2021 reach over 25 % efficiency, which makes them a very good alternative to silicon solar cells, commonly used on house roofs.

The presented thesis is based on a series of seven original papers, focused on charge transport dynamics in the PSCs, published in the following journals: ACS Chemistry of Materials, ACS Applied Materials and Interfaces, Chemistry-A European Journal, The Journal of Physical Chemistry C, RSC Advances, Physical Chemistry Chemical Physics and Synthetic Metals.

Over the period of realization of the presented research work, at the Faculty of Physics, Adam Mickiewicz University, Poznań a perovskite fabrication facility has been developed that allowed reaching 18 % efficiency of PSCs in 2021.

The presented doctoral dissertation concerns investigation of perovskite materials of different degree of complexity, from simple $MAPbI_3$, through $(FAPbI_3)_{0.85}(MAPbBr_3)_{0.15}$, up to $FA_{0.76}MA_{0.16}Cs_{0.05}Pb(I_{0.81}Br_{0.19})_3$ composition (where MA – methylammonium, FA – formamidinium). Apart from the perovskite compositions, various synthesis conditions were also studied. Precursor solutions were modified by using a variety of $MAI:PbI_2$ molar ratios and different *N,N*-dimethylformamide:dimethylsulfoxide (DMF:DMSO) ratios. The synthesis conditions considered were: open air (with the presence of humidity and oxygen) and dry box. PSCs of different structures were used, that is normal mesoporous ones and planar inverted ones. Different hole and electron transporting materials were characterized and their performances in PSCs were compared, i.e., 2,2',7,7'-tetrakis-(*N,N*-di-4methoxyphenylamino)-9,9'-spirobifluorene (spiro-OMeTAD), 2,2',7,7'-tetrakis(*N,N*-di(4-methoxyphenyl)amino)-spiro-(fluorine-9,9'-xanthene) (X60), poly(3,4-ethylenedioxythiophene:polystyrene sulfonate) (PEDOT:PSS), different quality TiO_2, phenyl-C61-buteric acid methyl ester (PCBM), 2,7-bis(diphenylphosphoryl)-9,9'-spirobifluorene (SPPO16) and *N,N'*-dipentyl-3,4,9,10-perylene dicarboximide (PenPTC). The above variations allow investigation of charge transport in perovskite materials with different modifications and containing selective transporting materials of different quality or chemical compositions. The changes in the PSCs induced by physical, instead of chemical, interactions were also examined, e.g., the effects of application of potential bias or additional 1Sun illumination in the experiments. The experiments were conducted in complete PSCs (in the last paper even including gold electrodes) by time-resolved laser spectroscopy, sometimes in incomplete cells (without particular layer or layers) as reference samples.

The methods applied in the studies included femtosecond transient absorption, picosecond to nanosecond time-resolved emission and electrochemical impedance spectroscopy. The processes were monitored in the time scale from femtosecond to second. The methodologies of using the above techniques to get information relevant for understanding PSCs operation were proposed. Moreover, correct assignment of transient absorption signal in perovskite material and its proper interpretation is also presented in the thesis.

The undertaken research work was aimed at characterization of the electron and hole dynamics in different composition perovskite material, determination of the effects of preparation conditions on solar cells operation, evaluation of the influence of different hole or electron transporting materials (including those in normal and inverted configuration) on the charge transfer in PSCs, and the correlation of the macroscopic parameters of the PSCs with ultrafast processes dynamics.

Study of perovskite material layers showed that the best quality layer exhibits the best photovoltaic performance and the fastest photoexcited charge carriers decay due to the fastest interfacial charge transfer. For example the cell made with a mesoporous TiO_2 layer of ~200 nm in thickness (30-nm-size nanoparticles) exhibiting the highest efficiency of ~18 % and relative photocurrent ~100 % (all absorbed photons converted into electrons in the short circuit conditions) showed faster electron injection than the PSCs with a thicker layer made of smaller nanoparticles, efficiency about 11 % (relative photocurrent ~70 %) and with poorer homogeneity (thickness ~350 nm, 18 – 20 nm nanoparticles size). Electrons in the cell with selective transporting material most often used in inverted cells, PCBM, are extracted faster (first order rate constant of the charge decay k_1=0.61 ns^{-1}) than in those with alternative materials such as PenPTC (k_1=0.44 ns^{-1}) or SPPO13 (k_1=0.33 ns^{-1}). However, sometimes a desired fast charge injection can be accompanied by unwanted charge recombination. Investigation of the selective charge carrier transporting materials has revealed that in X60 cells both, holes extraction and interfacial recombination, are faster than in the commonly used in normal PSCs spiro-OMeTAD.

The asymmetry in the charge transfer between electron and hole transporting materials in the PSCs was revealed owing to the selective probing of different interfaces. Photoinduced spectral and kinetic changes were observed for perovskite close to TiO_2/perovskite interface. The applied voltage close to open circuit potential causes retardation of charge injection.

The presented work contributed to understanding of charge transport in perovskite solar cells and might help to understand and further develop non-carbon-emissive electric current sources.

STRESZCZENIE

Perowskitowe ogniwa słoneczne (*perovskite solar cells* – PSC) są najbardziej obiecującymi, nowymi układami fotowoltaicznymi o niskich kosztach produkcji, które osiągajęły w 2021 roku certyfikowaną wydajność przekraczającą 25 %. Co czyni je bardzo dobrą alternatywą do powszechnie stosowanych na dachach ogniw krzemowych.

Niniejsza rozprawa doktorska jest oparta na serii siedmiu oryginalnych publikacji naukowych skupionych na dynamice transportu ładunków w ogniwach PSC, które opublikowane zostały w następujących czasopismach: ACS Chemistry of Materials, ACS Applied Materials and Interfaces, Chemistry-A European Journal, The Journal of Physical Chemistry C, RSC Advances, Physical Chemistry Chemical Physics i Synthetic Metals.

W ramach prowadzonych badań, stworzone zostało zaplecze chemiczne do wytwarzania ogniw perowskitowych na Wydziale Fizyki Uniwersytetu im. Adama Mickiewicza, co przyczyniło się do zsyntetyzowania w 2021 roku ogniw o wydajności sięgającej 18 %.

Tematyka przedkładanej rozprawy doktorskiej łączą badania materiału perowskitowego o różnej złożoności, od najprostszej formy $MAPbI_3$, poprzez $(FAPbI_3)_{0.85}(MAPbBr_3)_{0.15}$, aż do mieszanki $FA_{0.76}MA_{0.16}Cs_{0.05}Pb(I_{0.81}Br_{0.19})_3$ (gdzie, MA – metyloamina, FA – formamidyna). Oprócz składu perowskitu, przeanalizowane zostały rożne warunki syntezy. Roztwór prekursorów był modyfikowany poprzez użycie różnego stosunku molowego $MAI:PbI_2$, a także różnego stosunku *N,N*-dimetyloformamidu (DMF) do dimetylosulfotlenku (DMSO). Co więcej, zmieniane były warunki, w których odbywa się synteza, np. ogniwa były wytwarzane w warunkach panujących w laboratorium (w obecności wilgoci i tlenu) oraz wewnątrz suchej komory rękawicowej. Ponadto, analizowane były ogniwa o różnych konfiguracjach, tj. normalne z warstwą mezoporowatą oraz o odwróconej konfiguracji planarne. Scharakteryzowane oraz porównane ze sobą zostały różne materiały transportujące dziury i elektrony, np. 2,2',7,7'-tetrakis-(*N,N'*-di(4-metoksyfenylo) amino)-9,9'-spirobifluoren (spiro-OMeTAD), 2,2',7,7'-tetrakis-(*N,N'*-di(4-metoksyfenylo)amino)-spiro-(fluoreno-9,9'-ksanten) (X60), poli(3,4-etylenodioksy-tiofen:siarczan(VI) polistyrenu) (PEDOT:PSS), TiO_2 o różnej jakości, ester metylowy kwasu [6, 6]-fenylo-C61-masłowego (PCBM), 2,7-bis(difenylofosforylo)-9,9'-spirobifluoren (SPPO16) oraz imid kwasu *N,N'*-dipentylo-3,4,9,10-perylenowego (PenPTC). Powyższe modyfikacje pozwoliły na badania transportu ładunków w materiałach perowskitowych z różnymi zmianami oraz w obecności materiałów selektywnie transportujących ładunki o różnej jakości lub strukturze chemicznej. Niezależnie od zmian chemicznych, wprowadzone zostały również zmiany fizyczne w PSC poprzez przyłożenie napięcia lub oświetlanie dodatkowym światłem (1Sun) w trakcie eksperymentów. Doświadczenia czasowo-rozdzielczej spektroskopii laserowej były przeprowadzane w pełnych ogniwach PSC (w ostatniej publikacji także ze złotymi elektrodami)

lub niekiedy dla pomiarów kontrolnych, w niepełnych ogniwach (z pominięciem jednej warstwy lub kilku warstw).

Badania były oparte głównie na technikach czasowo-rozdzielczych, tj. femtosekundowej absorpcji przejściowej, czasowo-rozdzielczej emisji w zakresie od pikosekund do nanosekund oraz elektrochemicznej spektroskopii impedancyjnej, umożliwiających obserwowanie procesów w skali czasów od femtosekund od sekund. W celu uzyskania poprawnych informacji dotyczących działania ogniw perowskitowych, została zaproponowana metodologia badań przy użyciu wyżej wymienionych technik. Co więcej, w niniejszej rozprawie doktorskiej został zaprezentowany szczegółowy opis sygnałów absorpcji przejściowej w materiale perowskitowym oraz ich dogłębna analiza.

Głównymi celami prezentowanej rozprawy było: zbadanie dynamiki transportu elektronów oraz dziur w różnych mieszankach perowskitowych; zbadanie wpływu warunków, w których są przygotowane warstwy, na działanie ogniw słonecznych; zbadanie wpływu różnych materiałów selektywnie transportujących dziury lub elektrony na transport ładunku w ogniwie (włączając te w normalnej jak i odwróconej konfiguracji) oraz korelacja parametrów makroskopowych ogniwa PSC z dynamiką ultraszybkich procesów.

Badania materiału perowskitowego pokazały, że warstwy o najlepszej jakości dają najlepsze parametry fotowoltaiczne oraz najszybszy zanik wzbudzonych ładunków poprzez najszybszy transport ładunków na złączach. Dla przykładu, ogniwo z mezoporowatą warstwą TiO_2 o grubości ~200 nm (i nanocząstkach 30 nm) wykazujące najlepszą wydajność ~18 % oraz względny fotoprąd ~100 % (wszystkie zaabsorbowane fotony konwertowane są na elektrony w warunkach zwarcia ogniwa) wykazywały szybsze wstrzykiwanie elektronów od ogniw z grubszą warstwą, zbudowaną z mniejszych nanocząstek o wydajności około 11 % (względny prąd ~70 %) oraz o gorszej jednorodności (grubość ~350 nm, 18 – 20 nm nanocząstki). Elektrony w najbardziej powszechnym materiale w odwróconych ogniwach PSC – PCBM są ekstrahowane szybciej (stała czasowa pierwszego rzędu zaniku ładunków k_1=0.61 ns^{-1}) niż w ogniwach z jego alternatywami: PenPTC (k_1=0.44 ns^{-1}) lub SPPO13 (k_1=0.33 ns^{-1}). Jednakże, niekiedy pożądanemu szybszemu wstrzykiwaniu ładunków może towarzyszyć niechciana rekombinacja ładunków. Badania nad materiałami selektywnie transportującymi ładunki ujawniły, że w ogniwach z X60 ekstrakcja dziur jak i rekombinacja na złączu są szybsze niż w najbardziej powszechnym materiale w normalnej konfiguracji PSC – spiro-OMeTAD.

Asymetria w transporcie ładunków na złączach z materiałami transportującymi elektrony i dziury została zaobserwowana poprzez selektywne sondowane odpowiedniego złącza. Fotoindukowane spektralne i kinetyczne zmiany zostały zaobserwowane dla perowskitu blisko złącza TiO_2/perowskit. Przyłożenie napięcia bliskiego napięciu obwodu otwartego powoduje spowolnienie wstrzykiwania ładunków w ogniwie.

Zaprezentowane w niniejszej rozprawie doktorskiej badania przyczyniły się do zrozumienia transportu ładunków w perowskitowych ogniwach słonecznych oraz mogą pomóc w zrozumieniu i dalszym rozwoju nieemisyjnych źródeł energii elektrycznej.

List of Published Articles Constituting the Thesis

KPB-1   Effects of different small molecule hole transporters on the performance and charge transfer dynamics of perovskite solar cells

K.Pydzińska, P. Florczak, G.Nowaczyk, M.Ziółek

Synthetic Metals, 232 (2017), 181 – 187

IF = 3.266, MEiN points = 70

KPB-2   Differences in photoinduced optical transients in perovskite absorbers for solar cells

K.Pydzińska, J.Karolczak, M.Szafrański, M.Ziółek

RSC Advances, 8 (2018), 6479 – 6487

IF = 3.361, MEiN points = 100

KPB-3   Insights into the femtosecond to nanosecond charge carrier kinetics in perovskite materials for solar cells

K.Pydzińska-Białek, J.Szeremeta, K.Wojciechowski, M.Ziółek

The Journal of Physical Chemistry C, 123 (2019), 110 – 119

IF = 4.126, MEiN points = 140

KPB-4   Understanding the effect of different synthesis conditions on the physicochemical properties of mixed-ion perovskite solar cells

B.Quere, **K.Pydzińska-Białek**, J.Karolczak, G.Nowaczyk, E.Coy, M.Ziółek

Chemistry-A European Journal, 25 (2019), 5978 – 5986

IF = 5.236, MEiN points = 140

KPB-5 Understanding the interfaces between triple-cation perovskite and electron or hole transporting material

K.Pydzinska-Białek, V.Drushliak, E.Coy, K.Załęski, J.Flach, J.Idigoras, L.Contreras-Bernal, A.Hagfeldt, J.A.Anta, M.Ziółek

ACS Applied Materials and Interfaces, 12 (2020), 30399 – 30410

IF = 9.229, MEiN points = 200

KPB-6 Impact of improvements in mesoporous titania layers on ultrafast electron transfer dynamics in perovskite and dye-sensitized solar cells

K.Pydzińska-Białek[†], A.Glinka[†], V.Drushliak, G.Nowaczyk, P.Florczak, M.Ziółek

Physical Chemistry Chemical Physics, 22 (2020), 21947 – 21960

[†] authors contributed equally

IF = 3.676, MEiN points = 100

KPB-7 Complete perovskite solar cells with gold electrodes studied in the visible and near-infrared range

K.Pydzińska-Białek, G.Nowaczyk, M.Ziółek

ACS Chemistry of Materials, (2022), DOI: 10.1021/acs.chemmater.2c00845

IF = 9.811 , MEiN points = 200

OTHER PUBLICATIONS

Solar cells sensitized with near-infrared absorbing dye: problems with sunlight conversion efficiency revealed in ultrafast laser spectroscopy studies

K.Pydzińska, M. Ziółek

Dyes and Pigments, 122(2015), 272 – 279

IF = 4.889, MEiN points = 100

Determination of interfacial charge-transfer rate constants in perovskite solar cells

K.Pydzińska, J.Karolczak, I.Kosta, R.Tena-Zaera, A.Todinova, J.Idigoras, J.A.Anta, M.Ziółek

ChemSusChem, 9 (2016), 1 – 14

IF = 8.928, MEiN points = 140

Improving the spatial resolution in direct laser writing lithography by using a reversible cation photoinitiator

M.Duocastella, G.Vicidomini, K.Korabchevskaya, **K.Pydzińska**, M.Ziółek, A.Diaspro, G.Miguel

The Journal of Physical Chemistry C, 121(2017), 16970 – 16977

IF = 4.126, MEiN points = 140

AIMS OF THE THESIS

The overriding aim of the thesis was explanation of the charge carriers dynamics in perovskite solar cells (PSCs) with different modifications in the perovskite material, different selective transporting materials or different architectures of the cell. Realization of this aim requires the following:

1. Characterization of the electron and hole dynamics in perovskite materials of different compositions.
2. Determination of the preparation conditions' effects on solar cell operation.
3. Evaluation of the effects of different hole or electron transporting materials (including those in normal and inverted configurations) on the charge transfer in PSCs.
4. Investigation of the complete PSCs in the conditions the closest possible to the standard Sun illumination (with applied voltage under Sun illumination).
5. Correlation of the macroscopic parameters of PSCs with the ultrafast processes dynamics.
6. Correct assignment of transient absorption signals of perovskite materials and their proper interpretation.

1 INTRODUCTION

1.1 ENERGY CONSUMPTION

In the 21st century we are facing probably the one of the most difficult challenge of the whole history of humankind – the global warming. We have to change the way we used to live over centuries or find new technological solutions to apply in everyday life. The report by The Intergovernmental Panel on Climate Change (IPCC) in 2021 clearly indicates that immediate and profound decrease in greenhouse gases emission and also removal of excess CO_2 from the air is necessary to pull back global warming [1]. The most greenhouse gases emitting sector, responsible for about 73 % of total emission is the energy use (including energy use in buildings – 17.5 %, transport – 16.2 % and industry – 24.2 %) [2]. The non-renewable sources (gas, oil, coal) have been dominating electric energy generation up to now [3]. However, scientists predict that in 2050 another energy source will be prevailing – the Sun.

1.2 PHOTOVOLTAICS

Although the first patents of devices called "solar cells" were published at the end of 19th century [4]–[6], true bloom of photovoltaic (PV) technology took place in 1950s after the Bell Labs demonstrated the first practical silicon solar cell [7]. Over the years, new PV technologies have been developed that can be grouped in three generations, shown in Figure 1, with indicated record efficiency values collected by National Renewable Energy Laboratory (NREL) [8]. The 1st generation group contains single-crystal cells, the above-mentioned silicon (c-Si) and gallium arsenide (GaAs) based ones, reaching the highest efficiency in the PV. Due to very high price of fabrication of highly pure crystals, the 2nd generation was developed, with the absorbing materials much thinner than in the 1st generation cells, however, showing lower efficiencies. This group contains copper indium gallium diselenide (CIGS), cadmium telluride (CdTe) and amorphous silicon (a-Si). Recently, the greatest fuss in the PV world has been caused by the youngest generation of solar cells, the 3rd generation, which includes the so-called Emerging PV group. It comprises the dye-sensitized (DSSC), perovskite (PSC), organic (OPV), inorganic (CZTSSe) and quantum dot (QD) solar cells. The use of very cheap and easily available materials, when compared to those used in previous generations make this group very promising in PV world, especially the perovskite solar cells, which demonstrate outstanding 25.7 % record efficiency [8].
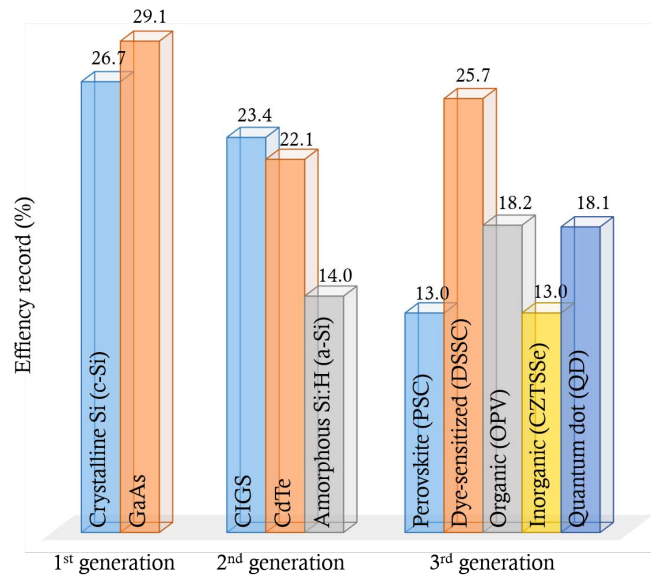
Figure 1 Photovoltaic cells generations and its efficiency records [8].

1.3 PEROVSKITE SOLAR CELLS

1.3.1 Perovskite Material

Perovskite solar cells took their name from the crystallographic structure of their absorbing material with the generic formula ABX_3 and the unit cell presented in Figure 2. In the most common PSCs, positions A (corners of the unit) are occupied by large organic cations like methylammonium (MA^+), formamindinium (FA^+) or small metal cation like cesium (Cs^+) while positions B (making an octahedral shape surrounded by 4 A ions) are taken by inorganic cations like lead (Pb^{2+}), tin (Sn^{2+}) or rubidium (Rb^{2+}). Position X (at the center of the octahedron) hosts halogen anions like iodide (I^-), chloride (Cl^-) or bromide (Br^-) [9].
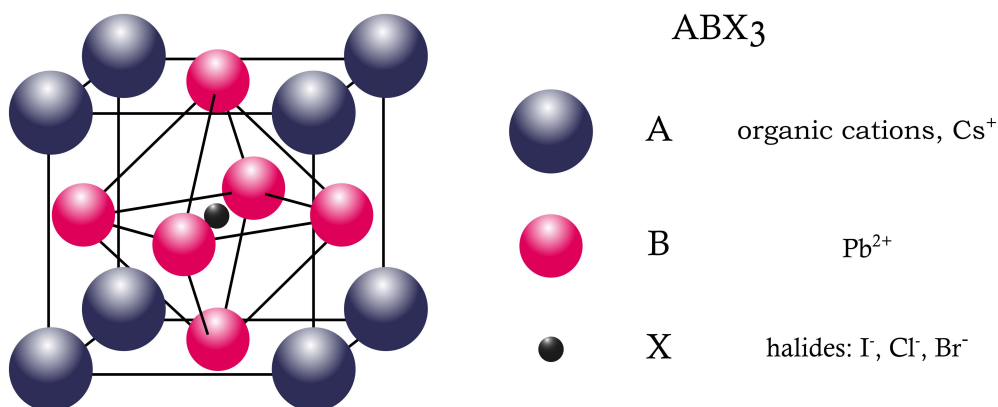
Figure 2 Perovskite crystal unit cell structure with indicated exemplary ion positions.

At the beginning of PSC development, the most common perovskite was methylammonium lead iodide (MAPbI$_3$). Later on, different mixtures of the above ions were introduced to change

optoelectronic properties of this material [9]. As presented in Figure 3, incorporation of bromide anion in MAPbI$_3$ structure causes an increase in the perovskite bandgap, which leads to a blue-shift of the absorption edge and the fluorescence band [10]. Analogous findings have been reported for FAPbI$_3$ [11]. Incorporation of small amounts of MA and Br ions into FAPbI$_3$ stabilizes the proper for perovskite α-phase at ambient temperature and provides higher tolerance of humidity [12]. The perovskite of the ratio (FAPbI$_3$)$_{0.85}$(MAPbBr$_3$)$_{0.15}$ was shown to have the optimal composition leading to a new record of PSC efficiency of 17.9 % in 2014 [13]. Further incorporation of small cesium cation to the optimized formula, to get the co-called triple-cation: FA$_{0.76}$MA$_{0.16}$Cs$_{0.05}$Pb(I$_{0.81}$Br$_{0.19}$)$_3$ makes the perovskite humidity resistant and less susceptible to structural impurities [14], [15]. Tin or bismuth have also been used in order to reduce toxicity and rubidium to enhance charge mobility [15]–[17]. It shows that perovskite material is very versatile and can be modified to meet different needs. However, perovskites without lead show low photovoltaic efficiency when applied in solar cells [18].
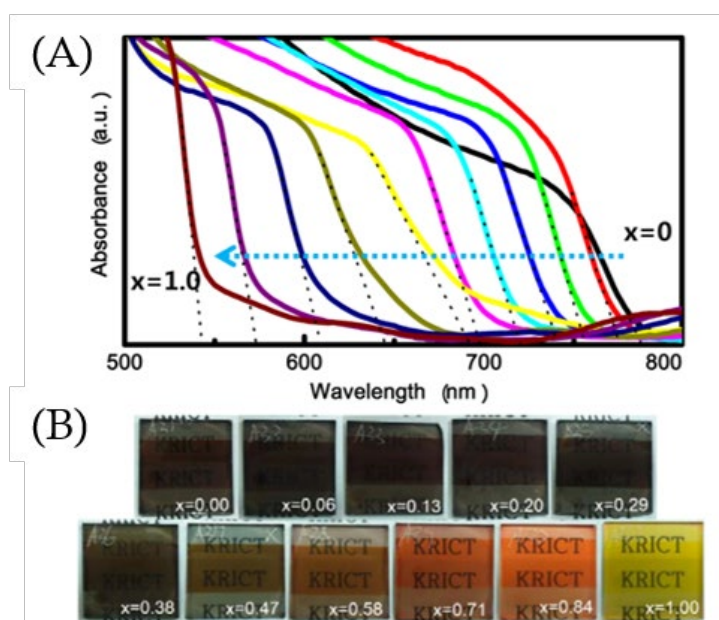
Figure 3 Absorption spectra (A) and images of obtained layers (B) of MAPb(I$_{1-x}$Br$_x$)$_3$ with different iodide to bromide ratio. Adapted with permission from [10]. Copyright 2013 American Chemical Society.

Perovskite material properties are very intriguing as they combine soft mater with solid state physics not only for application but also for basic research. In particular, the optoelectrical properties of perovskite materials are unique. These materials show a strong optical absorption and their bandgap is highly prone to adjustment. Moreover, perovskite material is characterized by long charge carrier diffusion lengths, high carrier mobility, ambipolar charge transport properties, low exciton binding energy and high tolerance of defects [19], [20]. It is also worth mentioning that perovskite material is not only used in solar cells but also in light emitting diodes (LEDs) and lasers [21].

1.3.2 Solar Cell Structure

The first report about the solid-state perovskite solar cells appeared in 2012 and the cell efficiency obtained by the authors was 10 % [22], [23]. Since the appearance of this report, PSCs have been attracting tremendous attention of scientists around the world, resulting in an increase in the efficiency of up to 25.7 % in 2021 [8].

The most common PSCs configurations are shown in Figure 4. In all of them perovskite is sandwiched between selective transporting materials: hole (p-type, HTM) and electron (n-type, ETM) layers. Additionally, electrons and holes are collected from the HTM or the ETM by transparent conductive oxide (TCO) or a metal layer (electrode) [24]. Two main configurations can be distinguished: normal (formal, n-i-p type, Figure 4 top) in which electrons are transported to the TCO and holes to metal electrode and inverted configurations (p-i-n type, Figure 4 bottom) where electrons go towards metal electrode and holes in the opposite direction, respectively. Besides, materials of two different transporting structures are used: planar (Figure 4 left) and mesoporous (Figure 4 right) [24].
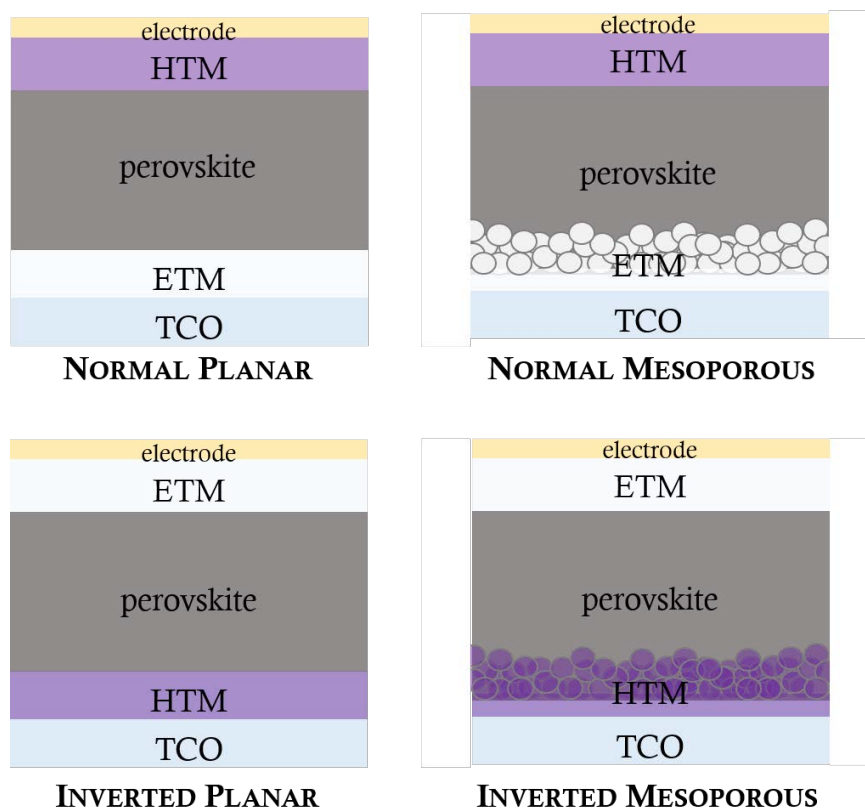
Figure 4 The most common perovskite device configurations: normal planar and mesoporous (top) and inverted planar and mesoporous (bottom). TCO – transparent conductive oxide, ETM/HTM – electron/hole transporting material.

Figure 5 presents the energy levels of the conduction (CB) and valence (VB) bands (in solids) or the lowest unoccupied (LUMO) and highest occupied (HOMO) molecular orbitals (in molecules)

of several different materials commonly used in the PSCs. The levels are shown for the TCO materials in first section from the left, followed by the ETMs, MAPbI₃, the HTMs and metal electrodes that are plotted at the very right.
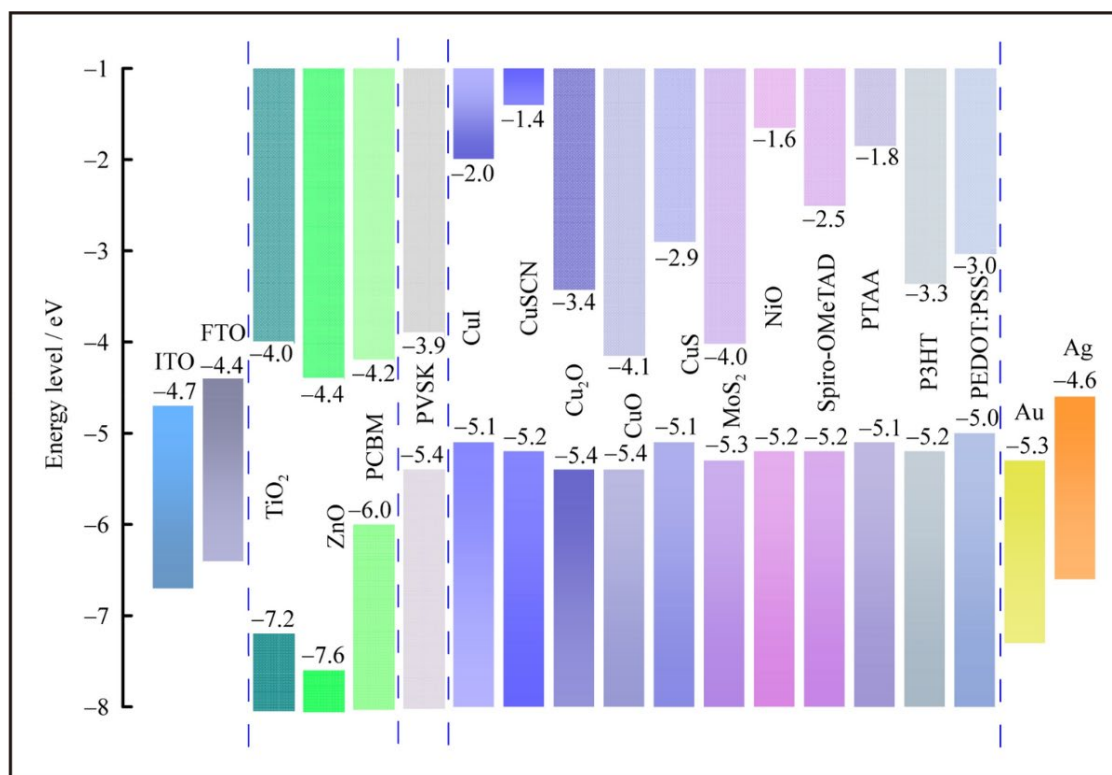
Figure 5 Energy levels of conduction (CB) and valence (VB) band (in solids) or lowest unoccupied (LUMO) and highest occupied (HOMO) molecular orbital (in molecules) of several different materials used in the PSCs. First section from left – TCOs, – ETMs, MAPbI₃, HTMs and the metal electrodes. Taken from [25]. Copyright © 2021, Youke Publishing Co., Ltd.

The TCO layer

The role of the TCO layer is to transport electrons or holes from ETM or HTM to the circuit.

The most common TCO layer in the normal configuration is fluorine doped tin oxide (FTO), deposited on glass substrate called the FTO glass. In the inverted structure, indium tin oxide (ITO) on top of glass or even poly(ethylene terephthalate) (PET) foil is also used [26]. However, the FTO has several advantages over ITO such as higher conductivity, better thermal stability and lower costs of production [27].

The ETM layer

The purpose of the presence of the ETM layer in PSC is to extract electrons from the perovskite, separate active material from the electrode, create potential barrier and thus, block the hole transport to the electrode. In the inverted structure, it encapsulates the cell and protects from moisture and air. Also it is a substrate for perovskite formation in the normal cell architecture [28].

The most popular ETM in the normal planar structure is a dense, uniform titanium (IV) oxide (TiO_2) layer. However, there are many other ETMs used in PSC such as ZnO, SnO_2 [28]. In the inverted structure, the most popular ETM is fullerene derivative phenyl-C61-buteric acid methyl ester (PCBM). Simpler, pristine fullerene C_{60} is also known as a very good ETM material [26]. Usually, on top of these two materials a very thin blocking layer of bathocuproine (BCP) is deposited [29].

In the normal cell architecture a mesoporous layer is deposited on top of the planar, metal oxide layer and it contains nanoparticles of the same metal oxide – usually TiO_2 [28].

The HTM layer

The HTM layer is mainly responsible for hole extraction and transport from the perovskite to the electrode. Additionally, it creates an energy barrier and prevents the electron transfer throughout HTM to the electrode as well as isolates the perovskite from the electrode. It helps to increase the open circuit voltage (V_{oc}) when the energy level of the highest occupied molecular orbitals (HOMO, in molecules) or the valence band (VB, in solids) is well matched to the perovskite valence band. In the normal structure it also encapsulates a cell [25].

Usually, in the PSCs of normal architecture (planar and mesoporous) organic 2,2',7,7'-tetrakis-(*N,N*-di-4methoxyphenylamino)-9,9'-spirobifluorene (spiro-OMeTAD) is used as the HTM. Due to a low hole mobility (only 2 x 10^{-4} $cm^2 V^{-1} s^{-1}$) [25] in this structure, two common additives are used. Bis(trifluoromethane)sulfonamide lithium salt (Li-TFSI) in the accompaniment of 4-tert-buthylpyridine (tBP), which increase Li-TFSI solubility, is added to increase the hole mobility by the presence of Li^+ ions [25]. There are several more organic HTMs used (mostly in inverted architecture) like poly(bis(4-phenyl)(2,4,6-trimethylphenyl)amine) (PTAA), poly(3,4-ethylenedioxythiophene) : poly(styrenesulfonate) (PEDOT:PSS) and poly(3-hexylthiophene-2,5-diyl) (P3HT). Inorganic HTMs such as Cu_2O, CuSCN, CuI, NiO, MoS_2 are also used [25],[29]. Many other HTMs are synthesized every year in order to find better replacement for spiro-OMeTAD (without additives, cheaper and/or increasing efficiency of a cell).

The metal electrode layer

The electrode laying on top of a cell is in most cases made of gold due to its low work function (-5.1 eV). Additionally, gold as a noble metal does not create oxide layer or reacts with other layers in PSCs [21]. In the inverted structure an aluminum electrode is sometimes chosen [26], [29].

1.4 PSCs OPERATION

1.4.1 General description

As mentioned in the previous section, the PSC operation, from the general point of view, can be simply presented as in Figure 6. Upon illumination, electrons are generated in the optically active perovskite material, and then are transported towards the photoanode (ETM, TCO) and leave holes behind [30]. The latter are transported in the opposite direction, towards the cathode (HTM, gold). In this way, electric current is generated in the circuit. In an ideal cell, without energy dissipation, efficiency of each process would be equal to 100 %. However, from time-resolved point of view, charge dynamics is very complex and its description and then minimization of energy loses are ones of the most important parts in the PSCs development.
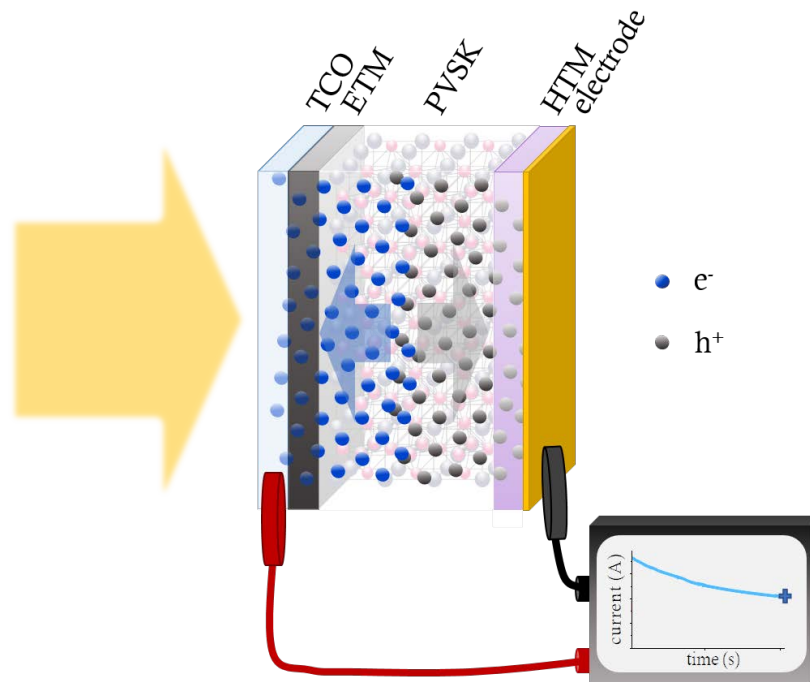
Figure 6 Schematic picture of the PSC operation.

Absorption of a photon, in a perovskite material occurs in a volume dependent on the penetration depth ($d_{penetration}$) at which the light intensity decreases to $1/e$ (about 37 %) of its initial incident value [31]:

$$d_{penetration}(\lambda) = \frac{1}{\alpha(\lambda)} \tag{1}$$

Where α – absorption coefficient of perovskite material for a particular wavelength.

In literature, the penetration depth of $FA_{0.76}MA_{0.16}Cs_{0.05}Pb(I_{0.81}Br_{0.19})_3$ material, for the wavelength equal to 450 nm is almost 7 times shorter than that for the wavelength of 700 nm [32]. However, for the wavelength of 450 nm it is only 50 nm, so photon absorption in the whole spectrum occurs mostly close to the front perovskite interface. Transport of electrons and holes is governed by diffusion and also partially, by the driving force created on the perovskite interfaces by the ETM and HTM work functions. In this process (charge transport) electrons and holes can meet impurities, ion vacancies, dislocations or grain boundaries in the perovskite layer that increases the probability of charge recombination competitive to injection of a charge carrier to ETM or HTM [33]. Illumination or applied potential can lead to ion migration which causes different perovskite composition segregations (e.g., in double halide perovskite) or ion rearrangement (in triple-cation perovskite) in perovskite mixes [34]. Also, ion movement as well as trap states on titania surface is taken as one of the reasons why the so called current voltage hysteresis is observed in the PSCs. Such a hysteresis is manifested as the higher maximum power for the reverse than forward voltage scan (described in Section 3.1.1).

1.4.2 Time domain description

In the research presented in this thesis pulse laser techniques were used to study charge carrier dynamics. The laser perturbation conditions are different than those related to constant (1Sun) radiation, e.g., local charge density can be several orders of magnitude higher than under normal solar cell operation.

The charge carrier transport dynamics studied upon pulse excitation can be divided into two stages. The first is the dynamics of the charges in the perovskite material and the second is the dynamics after charge injection into ETM or HTM.

Figure 7 shows schematically what happens after light absorption in the perovskite material. After excitation (femtosecond time scale), an electron from the valence band (VB) is promoted to the conduction band (CB). When the energy of the quantum of light is bigger than the bandgap of the perovskite material, hot electrons and holes relax to the conduction and valence band minima (Figure 7A) via electron-phonon interactions [35]. After this process is finished (in about 1 ps), electrons and holes occupy minima of the respective bands. At that point several processes can occur. Electrons can repopulate the valence band by recombination with holes by trap-states in the perovskite crystal structure (Figure 7B, first order process), by band-to-band radiative transition (Figure 7D, second order process) or by Auger three-molecular process (Figure 7E, third order process). In a perovskite sandwiched between ETM and HTM, the electrons and holes can also be injected into them (Figure 7C, first order process), which is essential for proper operation of solar cell and is highly desirable to be as efficient as possible [35], [36].
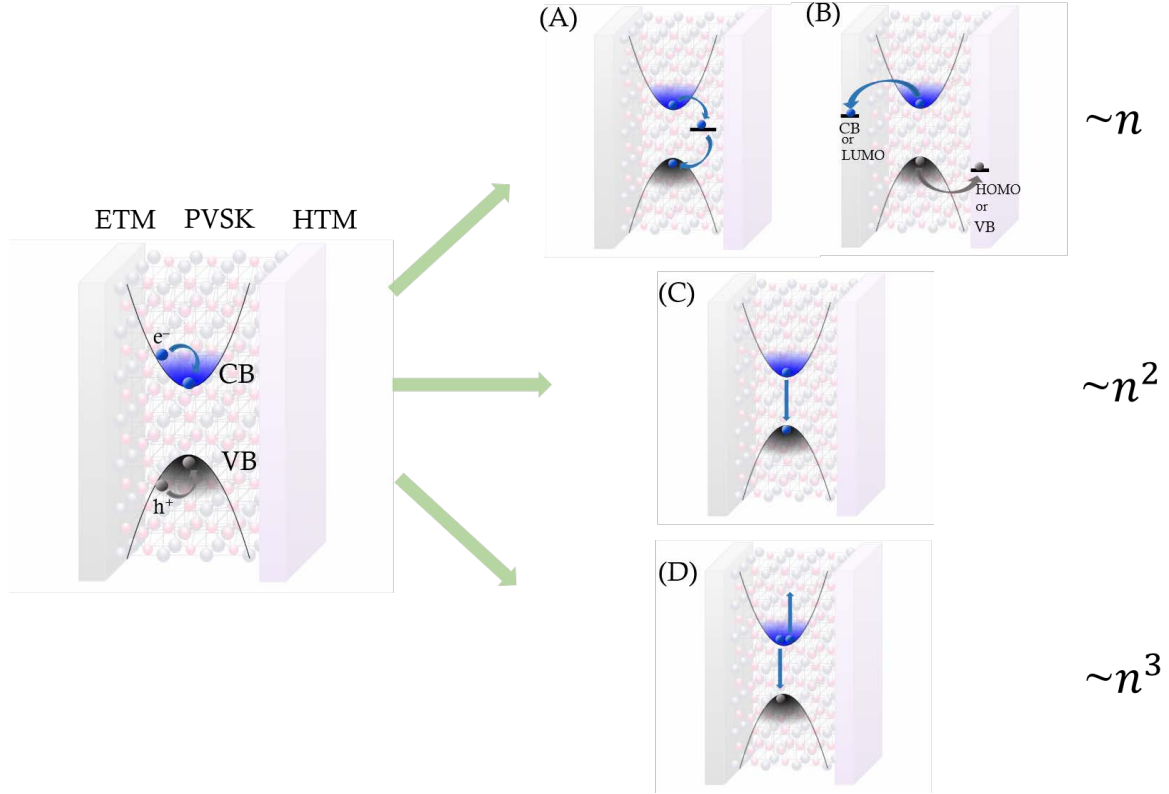
Figure 7 Schematic illustration of the processes taking place after absorption in the PSCs. A – Absorption and charge cooling, B – recombination by trap states, C – charge injection into ETM/HTM, D – radiative band-to-band recombination, E – Auger recombination. CB – conduction band, VB – valence band, LUMO – lowest unoccupied molecular orbital, HOMO – highest occupied molecular orbital.

All of above processes have impact on the number of excited carriers (n) at the particular time point (t), which is described by the formula [37]:

$$\frac{dn}{dt} = -k_1 n - k_2 n^2 - k_3 n^3 \tag{2}$$

$$k_1 = k_{1\,rec} + k_{1\,inj} \tag{3}$$

Where: k_1, k_2, k_3 – first, second, third order processes rate constants, $k_{1\,rec}$ – first order recombination rate, $k_{1\,inj}$ – first order injection rate

It shows that at low light intensity, recombination by trap states and injection (if ETM or/and HTM is/are present) mainly govern the time changes of the excited charge carrier density. With increasing excitation light intensity, higher order recombination processes occur, dominating the carrier dynamics. However, under the cell working condition (1Sun illumination), the second order processes are negligible [38]. The above equation is simplified and does not describe fully what is happening in PSCs because it does not take into account the diffusion process as well as reabsorption effect, occurring in the perovskite [39], [40].

After injection of an electron into ETM and a hole into HTM, the charge carriers can recombine at the perovskite interface with excited electron (hole) or excited hole (electron), as shown in Figure 8, making charge collection less efficient.
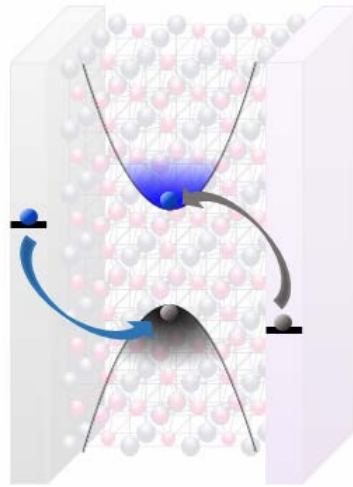
Figure 8 Recombination of injected electron (blue ball) and hole (gray ball) with excited hole and electron, respectively.

As described above, charge-involving processes in PSCs take place in different time scales (over 15 orders of magnitude). Figure 9 collects the most important processes occurring in PSCs in the time domain, described above.
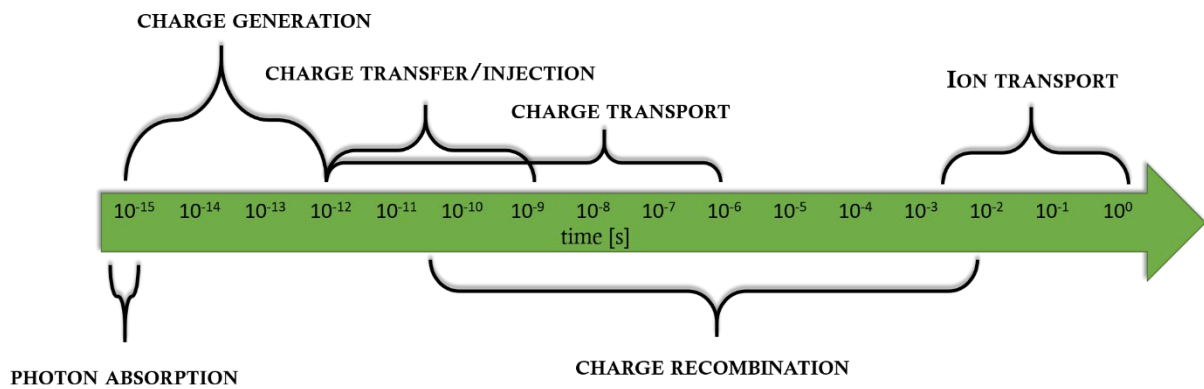
Figure 9 The most important processes occurring in PSCs. Reconstructed from [35], [36]

2 SAMPLES

2.1 SOLAR CELL CONFIGURATIONS USED IN THE RESEARCH

In the studies described in this thesis, two cell configurations were used, shown schematically in Figure 10. Normal mesoporous PSCs were used in the studies reported in all papers except the samples described in the article KPB-3, provided by our collaborators (J. Szeremeta and K. Wojciechowski from Saule Technologies) whose used the inverted planar structures.
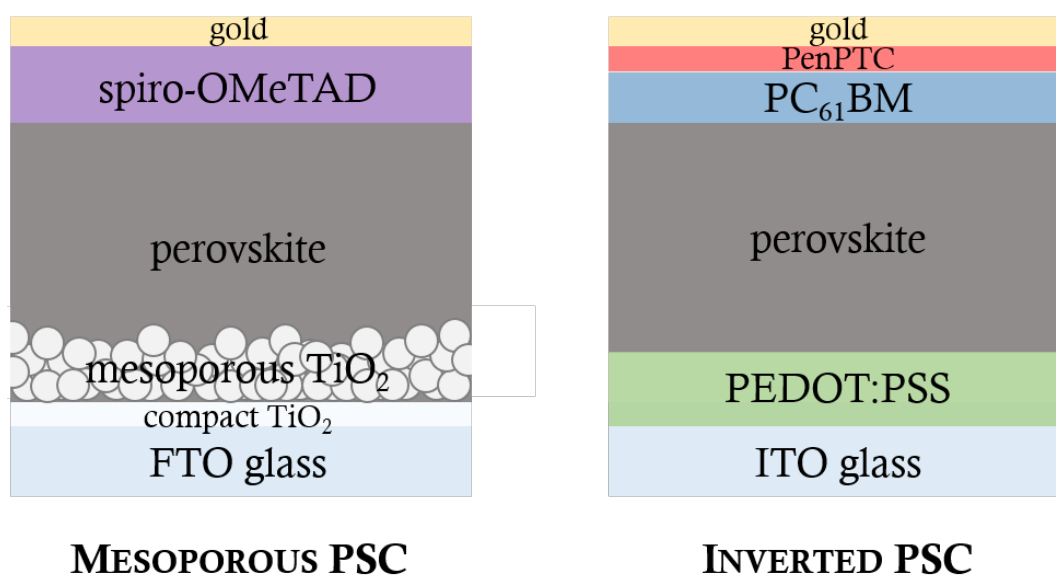
Figure 10 Solar cell configurations used in the research.

Table 1 collects the most important information about the fabricated layers of PSCs and their modifications used in the studies reported in each publication.

Table 1 The most important information about fabricated layers in PSCs and their modifications used in each publication.

Publication	TCO	ETM	Perovskite	HTM	Electrode
KPB-1	FTO	mesoporous TiO_2	$MAPbI_3$, (one-step, two-step method 1:1, 1:3 PbI_2: MAI ratio)	spiro-OMeTAD / X60 / spiro-OMeTAD:X60	gold
KPB-2	FTO	mesoporous TiO_2	$MAPbI_3$, (one-step, two-step method 1:1, 1:3 PbI_2: MAI ratio)	spiro-OMeTAD	gold
KPB-3	ITO	PCBM / PenPTC / SPPO13	$MAPbI_3$ (one-step)	PEDOT:PSS	gold
KPB-4	FTO	mesoporous TiO_2 (different nanoparticle sizes and layer quality)	$FA_{0.85}MA_{0.15}Pb(I_{0.85}Br_{0.15})_3$ (different synthesis atmosphere conditions)	spiro-OMeTAD	gold
KPB-5	FTO	mesoporous TiO_2	$FA_{0.76}MA_{0.16}Cs_{0.05}Pb(I_{0.81}Br_{0.19})_3$ (different synthesis atmosphere conditions)	spiro-OMeTAD	gold
KPB-6	FTO	mesoporous TiO_2 (different nanoparticle sizes)	$FA_{0.76}MA_{0.16}Cs_{0.05}Pb(I_{0.81}Br_{0.19})_3$	spiro-OMeTAD	gold (different size and thickness)
KPB-7	FTO	mesoporous TiO_2	$FA_{0.76}MA_{0.16}Cs_{0.05}Pb(I_{0.81}Br_{0.19})_3$	spiro-OMeTAD	gold (different thickness)

2.2 Detailed Fabrication Method of the Samples

A detailed fabrication method of PSC will be presented below in order to enrich usually short, synthetic description in the articles and to make the synthesis easier for other researchers. Only the synthesis protocol of the layers used in the most efficient cells are described. This protocol is mostly based on the recipe reported by Saliba et al. [41]. However, since 2016 many other synthesis methods have been used in the thesis, but their protocols are easy to reconstruct from the information provided in the methods section in particular articles and the data presented below.

Prior to PSCs fabrication, it is important to provide chemicals, which should be of the highest available purity, new or very recently open and kept in glove box in inert gas atmosphere with the lowest possible H_2O content. Working space must be clean and free from dust. Weighing should also be performed in glovebox as well as whole synthesis of perovskite and HTM layer.

2.2.1 FTO etching

At the beginning, 2.4 x 2.4 cm FTO glass substrates (FTO glass, ≈13 Ω/sq, Sigma-Aldrich) were partially etched in order to prevent recombination electrons in FTO layer with holes in gold electrodes. The etching process is schematically shown in Figure 11. Firstly, the whole substrate area, except the part (0.4 cm) to be etched was covered with simple nail polish to protect the FTO layer (Figure 11A). Then, zinc powder (Sigma-Aldrich) was applied on the substrate and hydrochloric acid (2 M, Sigma-Aldrich) was applied drop-by-drop on top using plastic Pasteur pipette (Figure 11B). After 15 min it was rinsed with distilled water (Figure 12C) and nail polish was removed by acetone in ultrasonic bath (Figure 11D).
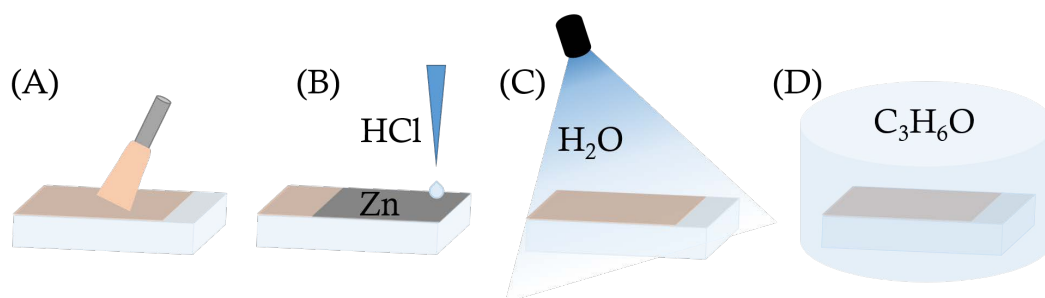
Figure 11 Stages of the FTO etching: A – nail polish application, B – Zn and HCl deposition, C – rinsing with water, D – acetone dripping.

2.2.2 Substrates cleaning

The etched substrates were cleaned with toothbrush and diluted detergent (Hellmanex III or Trilux, 20 %). Then, they were rinsed with water and cleaned in ultrasound cleaner with distilled water and detergent (2 %), pure distilled water, acetone and 2-propanol subsequently, for 15 min each. After that, the substrates were picked one by one using tweezers and, immediately after

taking out of the solution, dried using compressed air gun. Finally, the samples were cleaned by an UV ozone cleaner for 15 min.

2.2.3 Compact TiO₂ deposition

Two methods were used for deposition of a compact TiO_2 layer, i.e., spin-coating and spray pyrolysis, both shown schematically in Figure 12. Both provide very firm, dense layer, but spray-pyrolysis provides thinner coating more easily.

(A)   (B)

spin-cating   spray pyrolysis
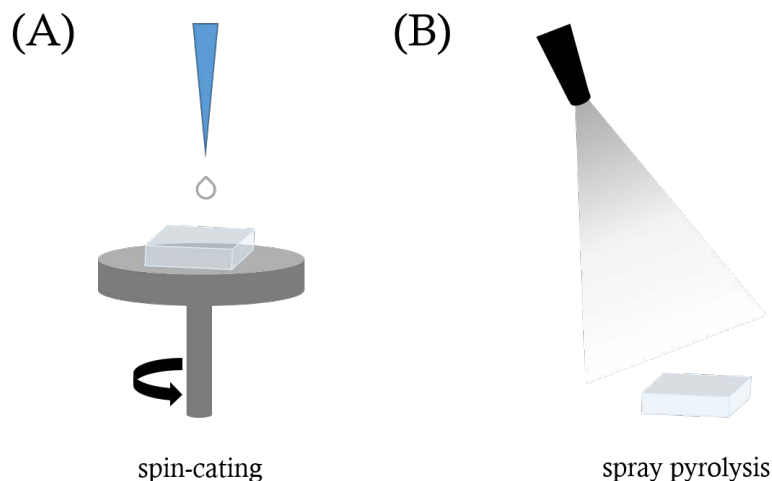
Figure 12 Schematic presentation of spin-coating (A) and spray pyrolysis (B) method of compact TiO₂ layer deposition.

Cleaned samples were put on a hot plate (100 °C) for 1 h if the cleaning was not made on the same day as the compact TiO_2 layer deposition.

Spin-coated TiO₂

In order to prepare titania, the precursor in the form of titanium isopropoxide was diluted in ethanol (0.5 mL in 4.5 mL ethanol – 0.34 M, Sigma-Aldrich). It is important to add titania precursor to ethanol keeping the tip of the pipette in the solution. Before deposition, the fragment of the substrate at the opposite to the etched one was covered with liquid latex or duct tape in order to protect FTO glass for wire electrode connection from removing conducting layer. A volume of 100 µL of the precursor solution was spin-coated on the FTO substrates (speed: 2000 rpm, acceleration: 1000 rpm/s, spinning time: 60 s). After that the substrates were dried at 130 °C for 15 min, then latex was peeled off and the substrates were put in the oven for 30 min at 450 °C (gradually heated for 40 min), to obtain a 150-nm-thick compact layer.

Spray Pyrolysis

Titanium diisopropoxide bis(acetylacetonate) solution (75 % in 2-propanol, Sigma-Aldrich) was diluted in pure ethanol (1 mL in 14 mL ethanol, Sigma-Aldrich). In this method the end of the FTO to be used for electrode connection was protected by metal or glass lamellas on top of a row

of substrates (usually 8 in 2 rows for 15 mL of the precursor solution), as shown in the Figure 13. The substrates were heated gradually (for 30 min) on a hot plate up to 450 ˚C. Then, a spray gun was used with oxygen as a driving gas. The pressure was set directly prior use for creation of nice spread of the solution, without bigger droplets (tested with pure ethanol on a sheet of paper). The precursor solution was sprayed from around 30 cm distance from the substrates, moving very gently from left to the right and reverse with 30 s pause after the full cycle. Start and end of spraying should be made outside stacked substrates to avoid making an uneven layer. After the use of the whole portion of the solution, the samples were heated for next 30 min and then cooled down. The obtained anatase compact layer was of about 50 nm in thickness.
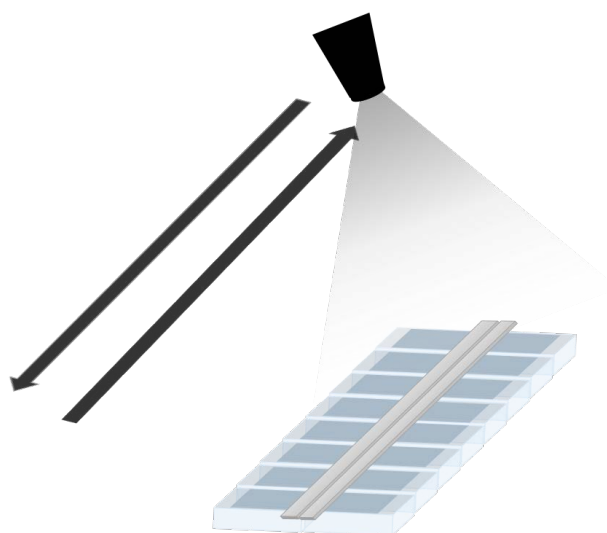
Figure 13 Schematic picture of titania deposition by spray pyrolysis technique.

2.2.4 Mesoporous TiO$_2$ deposition

Mesoporous titania layers were obtained from 30NR-D, GreatCell Solar paste diluted 1:6 in ethanol (wt.:wt.). Nanoparticle solution was stirred for minimum 5 h before use. Substrates were heated for 1 h at 100 ˚C and cooled down before the deposition. Portions of 100 µL of diluted paste per a substrate were spin-coated on top of the compact titania layer (speed: 4000 rpm, acceleration: 2000 rpm/s, spinning time: 10 s), dried for 15 min in 100 ˚C and put in an oven for 30 min at 500 ˚C (gradually heated up for 50 min), to give a 200-nm mesoporous layer.

2.2.5 Perovskite synthesis

Precursor solution preparation recipe for the most efficient perovskite are listed below.

FA$_{0.85}$MA$_{0.15}$Pb(I$_{0.85}$Br$_{0.15}$)$_3$ and FA$_{0.76}$MA$_{0.16}$Cs$_{0.05}$Pb(I$_{0.81}$Br$_{0.19}$)$_3$ precursor solutions

Mixed cation perovskite precursor solution was made using following recipe:

1. **DMF:DMSO:** 4:1 (v:v) mixture of *N,N*-dimethylformamide : dimethyl sulfoxide (DMF:DMSO, Sigma-Aldrich)

2. **1.5 M PbI$_2$ solution:** 1 g of PbI$_2$ (Sigma-Aldrich) dissolved in 1.4409 g of DMF:DMSO

3. **1.5 M PbBr$_2$ solution:** 1 g of PbBr$_2$ (Sigma-Aldrich) dissolved in 1.8100 g of DMF:DMSO

4. **1.5 M CsI solution:** 0.1 g of CsI (Sigma-Aldrich) dissolved in 0.3054 g of DMSO

PbI$_2$, PbBr$_2$ and CsI are hard to dissolve in room temperature. They should be kept in 70 ˚C with stirring if possible. To use them in the next steps, they should be cooled down.

5. **1.5 M FAPbI$_3$ solution (with 9 – 10 % of Pb excess):** 0.2 g of FAI (Sigma-Aldrich) dissolved in 1.427 g PbI$_2$ solution

6. **1.5 M MAPbBr$_3$ solution (with 9 – 10 % of Pb excess):** 0.05 g of MABr (Sigma-Aldrich) dissolved in 0.502 g PbBr$_2$ solution

1.5 M FA$_{0.85}$MA$_{0.15}$Pb(I$_{0.85}$Br$_{0.15}$)$_3$ final solution: Mixture of FAPbI$_3$:MAPbBr$_3$ solution in 85:15 (v:v) ratio.

1.5 M FA$_{0.76}$MA$_{0.16}$Cs$_{0.05}$Pb(I$_{0.81}$Br$_{0.19}$)$_3$ final solution: Mixture of FAPbI$_3$:MAPbBr$_3$:CsI solution in 95:19:6 (v:v) ratio.

Deposition

A volume of 50 μL of the precursor solution was deposited on top of the mesoporous layer by spin-coating (speed: 1000 rpm, acceleration: 120 rpm/s, spinning time: 10 s and then speed: 4000 rpm, acceleration: 2000 rpm/s, spinning time: 20 s) with addition of 200 μL of chlorobenzene as antisolvent at 10 s before the end of spinning. Then, the samples were kept at 110 ˚C for 1 h to obtain a dark perovskite layer.

2.2.6 Spiro-OMeTAD deposition

A volume of 50 μL of 2,2',7,7'-tetrakis-(*N,N*-di-4methoxyphenylamino)-9,9'-spirobifluorene (spiro-OMeTAD, Sigma-Aldrich) solution (72.3 mg/mL in chlorobenzene) with 29 μL 4-tert-buthylpyridine (tBP, Sigma-Aldrich) and 17.5 μL of bis(trifluoromethane)sulfonamide lithium salt (Li-TFSi, 520 mg/mL in acetonitrile, Sigma-Aldrich) as additives were deposited on top of the perovskite layer by spin coating (speed: 4000 rpm, acceleration: 2000 rpm/s, spinning time: 30 s), to give a layer of around 150 nm.

2.2.7 Gold coating

Before electrode deposition, the substrate end opposite to the etched one (with FTO connection) need to be cleaned. First of all, mesoporous, perovskite and spiro-OMeTAD layers were scraped with a razor blade (Figure 14A) and then wiped down with a cotton stick soaked with a very small volume of DMSO or DMF (Figure 14B). Finally, the remaining scraped pieces

on the substrates were blown out with dry air. During scraping it is highly recommended to wear mask to avoid inhalation of toxic substances.

Gold electrodes were deposited by either thermal evaporation or sputtering to a shape provided by a metal mask (Figure 14C). Such a procedure gave a 70 nm Au layer.
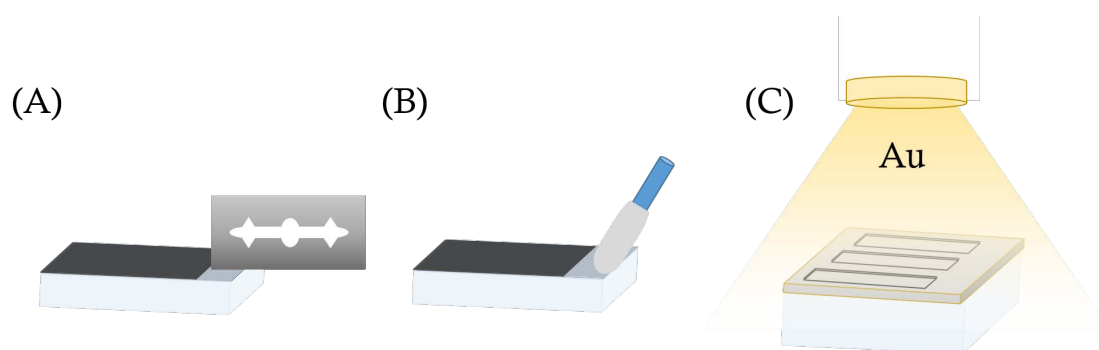
Figure 14 Scraping (A) and cleaning (B) of a cell before deposition of gold electrodes (C)

3 METHODS

3.1 BASIC CHARACTERIZATION TECHNIQUES

3.1.1 Current-Voltage Characteristic

The most basic solar cell characterization technique is measurement of the current-voltage (C-V) characteristics. During the experiment, a solar cell is connected to a potentiostat, which applies particular potential range in steps and measures the current response of the cell [30]. Figure 15 shows C-V curves obtained in this way. The voltage usually applied for this purpose to PSCs ranges from 0 to 1.2 V, at a scanning rate 50 mV/s.
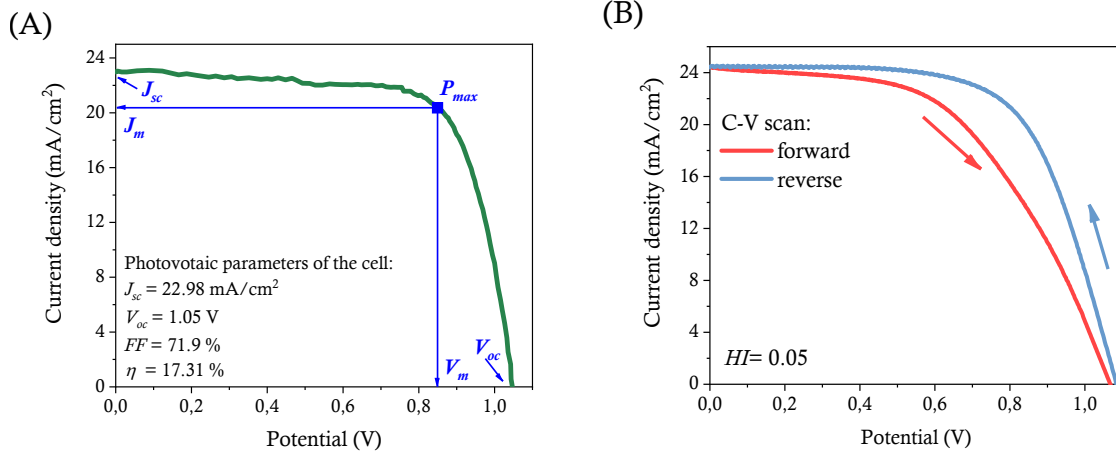
Figure 15 A – Exemplary current-voltage curve of the PSC with marked characteristic points of the curve. J_{sc} – short circuit current density, V_{oc} – open circuit voltage, P_{max} – maximum power point, J_m – current density of maximum power point, V_m – voltage of maximum power point, FF – fill factor, η – efficiency of the cell. The graph is reconstructed from KPB-5. B – Exemplary current-voltage curve of the PSC measured in reverse (blue) and forward (red) scan direction with listed hysteresis index value (HI), taken from KPB-6.

Four basic parameters are used to describe a C-V curve (exemplary ones are listed in Figure 15A). The first two are: current density for the applied potential equal to 0 V, i.e., the short circuit current density (J_{sc}), voltage value for open circuit conditions (no current flow) – the open circuit voltage (V_{oc}). The next one, fill factor (FF), is computed from above two ones and also from the maximum power point (P_{max}) coordinates (J_m and V_m) using the formula [30]:

$$FF = \frac{J_m V_m}{J_{sc} V_{oc}} \tag{4}$$

This value describes ideality of the curve, giving 1 for identical $J_m V_m$ and $J_{sc} V_{oc}$ values. For high quality solar cells it is assumed that FF should be in range 0.6 – 0.9 [42]. The FF is also influenced (deteriorated) by series resistance (due to cell material resistance) and shunt resistance (from leakage of current in a cell).

The most important, the fourth, value characteristic of solar cell is its efficiency (η). It is the energetic efficiency of conversion of incident light (in whole 1Sun spectrum) into electric current energy. It could be computed from equation [30]:

$$\eta = \frac{J_m V_m}{P_s} \qquad (5)$$

or using *FF* from:

$$\eta = \frac{J_{sc} V_{oc} FF}{P_s} \qquad (6)$$

Where P_s is power of incident light, in standard 1Sun (AM1.5) condition, equal to 1000 W/m² [30].

As shown in chapter 1.2, in the best PSCs, $\frac{1}{4}$ of the Sun energy is converted into the electric current energy.

Also, as described in Section 1.4.1, PSCs exhibit C-V hysteresis (Figure 15B). It is the difference in C-V behavior when measured in the reverse direction, from V_{oc} to J_{sc} point (Figure 15B blue, standard direction) and in the forward direction, from J_{sc} to V_{oc} point (Figure 15B red). The parameter characterizing the hysteresis effect, called the hysteresis index (*HI*), is given by [43]:

$$HI = \frac{J_{reverse}\left(\frac{V_{oc}}{2}\right) - J_{forward}\left(\frac{V_{oc}}{2}\right)}{J_{reverse}\left(\frac{V_{oc}}{2}\right)} \qquad (7)$$

Where $J_{reverse}\left(\frac{V_{oc}}{2}\right)$ and $J_{forward}\left(\frac{V_{oc}}{2}\right)$ are current densities at $\frac{V_{oc}}{2}$ points for reverse and forward scan, respectively.

The hysteresis in PSCs allows manipulation of the cell photovoltaic parameters by pre-lighting, scanning rate, starting voltage and scan direction [44]. It is important to measure PSCs in standardized way i.e., without prelighting, at a slow scan rate 50 mV/s, from a voltage very close to V_{oc} (usually 1.2 V) in the reverse scan direction. In the best devices the hysteresis index should be as small as possible.

3.1.2 Incident Photon-to-Current Efficiency (*IPCE*)

To get more detailed information on the photons into electrons conversion (quantum efficiency), a technique called the incident photon-to-current efficiency (*IPCE*) is very helpful. The basis of the experiment is illumination of a cell with a particular wavelength of known intensity and measurement of the generated current [45]. The most common presentation of the *IPCE* data is the wavelength spectrum as presented in Figure 16. As shown in Figure 16, PSCs are excellent photon to current converters in the perovskite absorption region, reaching above 80 % efficiency in the presented example.
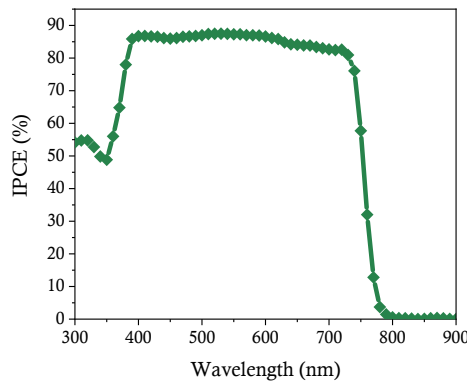
Figure 16 Exemplary incident photon-to-current efficiency spectrum.

3.1.3 Steady-State Absorption Spectroscopy

Another basic technique for characterization of optically active materials is steady-state absorption spectroscopy. The basis of this technique is measurement of particular wavelength light intensity with (I) and without (I_0) sample simultaneously and computation of absorption values using the equation [46]:

$$Abs = -\log\left(\frac{I}{I_0}\right) \tag{8}$$

In the described experiment an additional integrating sphere was used to collect both passing and scattered light.

The steady-state absorption spectroscopy is essential in the PSCs characterization for determination of bandgaps of the perovskite materials (especially perovskite mixes). An exemplary absorption spectrum of perovskite material (triple-cation) is shown in Figure 17. It is characterized by a sharp absorption edge around 770 nm and very high absorption in the region of shorter wavelengths. In NIR region, the interference pattern is dominant, which was a focus of the study reported in KPB-7. Steady-state absorption was also used to estimate the perovskite layer thickness in cells.
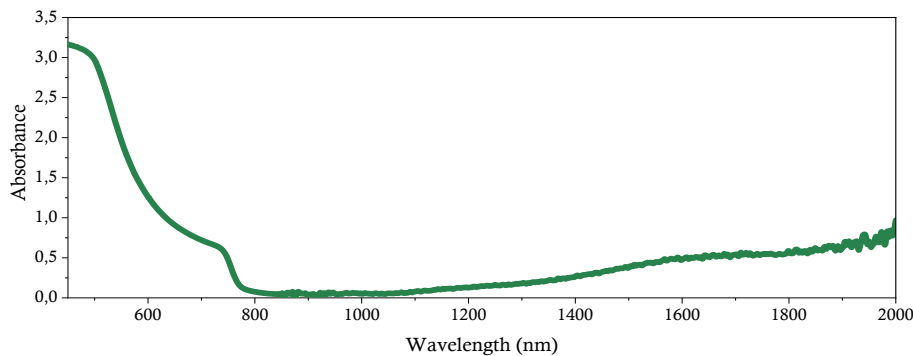
Figure 17 Exemplary absorption spectrum of complete cell with triple-cation perovskite. Taken from KPB-7.

For comparing perovskite materials of various thicknesses, the obtained short circuit current density can be normalized by the number of photons absorbed by the cell (N_{ph}), obtained from the absorption spectrum, multiplied by electric charge e, giving total absorbed photon-to-current efficiency (*TotalAPCE*):

$$TotalAPCE = \frac{J_{sc}}{eN_{ph}} \tag{9}$$

In the publications (KPB-1, KPB-2, KPB-5, KPB-6, KPB-7), although short circuit photocurrents and sunlight conversion efficiencies were varied, the *TotalAPCE* values were close to 100 %, which supported the generalization of the findings to those for very efficient devices.

3.1.4 Scanning Electron Microscopy

The scanning electron microscopy is an imaging technique based on the use of focused high-energy electron beam and providing very high image resolution (up to a few nm). In principle, only electrically conducting samples are measured with this technique. However, if a sample is nonconductive, a very thin layer (several nm) of metal (usually gold) is deposited on top of it. Electrons in a beam interact differently with a studied material giving information mainly about its surface morphology (analysis of backscattered electrons) and differences in material atomic composition (secondary electrons) [47].

In the presented study, the scanning electron microscopy technique was used in determination of the thickness of all layers in PSCs (Figure 18A, articles KPB-4, KPB-6, KPB-7) as well as grain size and layer quality (Figure 18B, publications KPB-3, KPB-5) or gold layer quality (article KPB-7).
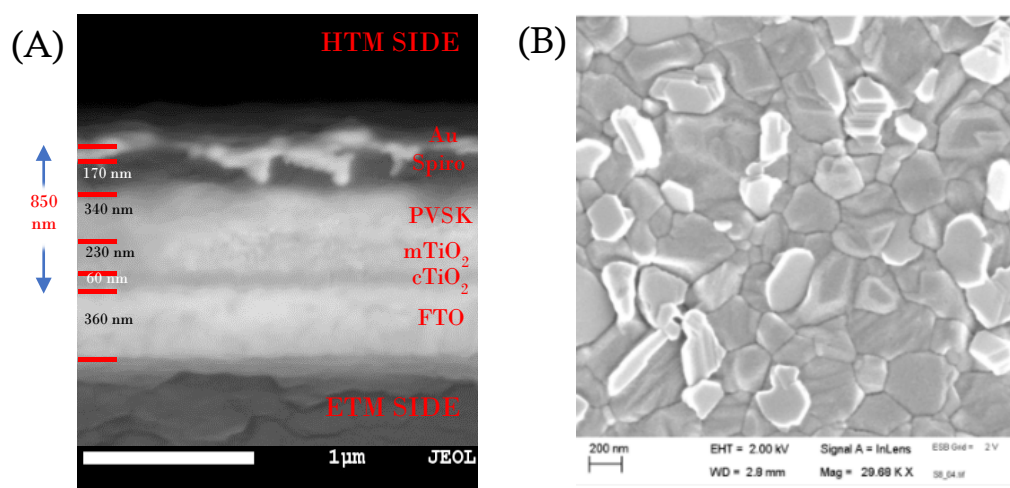
Figure 18 Scanning electron microscopy exemplary images cross-section of a cell with indicated layers and their thicknesses using secondary electrons detection, taken from KPB-7 (A) and perovskite layer from the top obtained from back scattered electrons, taken from KPB-5 (B).

3.2 TIME-RESOLVED TECHNIQUES

As mentioned in Section 1.4.2, the processes contributing to the electric current flow take place in different time scales from femtoseconds to seconds. Therefore different time-resolved techniques are necessary for proper investigation of charge transport dynamics. Figure 19 shows a similar graph as in Figure 9 (Section 1.4.2), presenting three different techniques mostly used in the presented study with their experimental time windows.
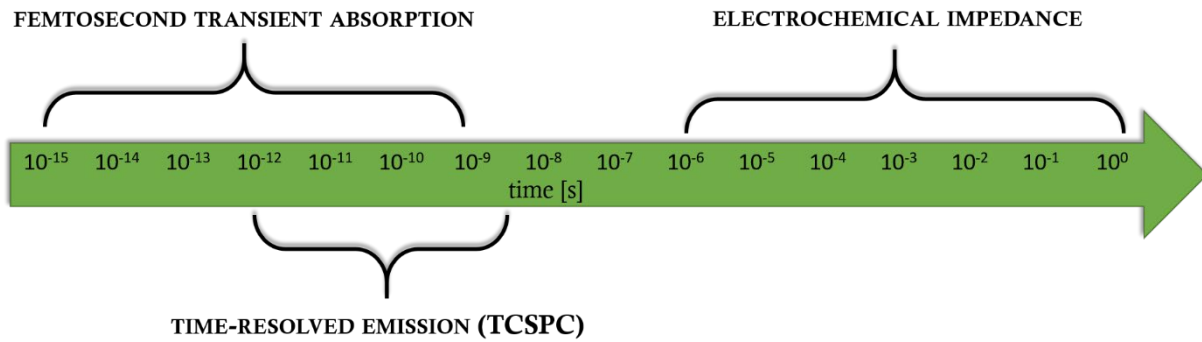
Figure 19 Time scale with marked experimental time widows of used techniques in the research.

3.2.1 Femtosecond Transient Absorption Spectroscopy

Working Principles

The basis of the shortest time range technique used in the presented research, i.e., the transient absorption (TA) spectroscopy, is monitoring of the absorbance spectrum changes (ΔA) after excitation pulse ($A_{with\ pump}$) in reference to that of an unperturbed sample ($A_{w/o\ pump}$) [48]:

$$\Delta A(\lambda, t) = A_{with\ pump}(\lambda, t) - A_{w/o\ pump}(\lambda, t) \qquad (10)$$

As presented in Figure 20, two pulses are involved in the TA experiment. A pump pulse which excites the investigated optically active material and a probe pulse which is delayed by variable period of time in relation to the pump one by a motorized delay stage. The pump pulse is a monochromatic light, while the probe pulse is converted into white light supercontinuum by a nonlinear crystal. The supercontinuum monitors the changes in the optical absorption spectrum caused by the pump pulse in wide spectral (VIS: 430 – 830 nm or NIR: 830 – 1600 nm) and temporal ranges (up to 3 ns, with the instrument response function – IRF – of about 300 fs) [48]. The result of an experiment is a 3D surface of ΔA vs time and vs wavelength as shown in Figure 20.
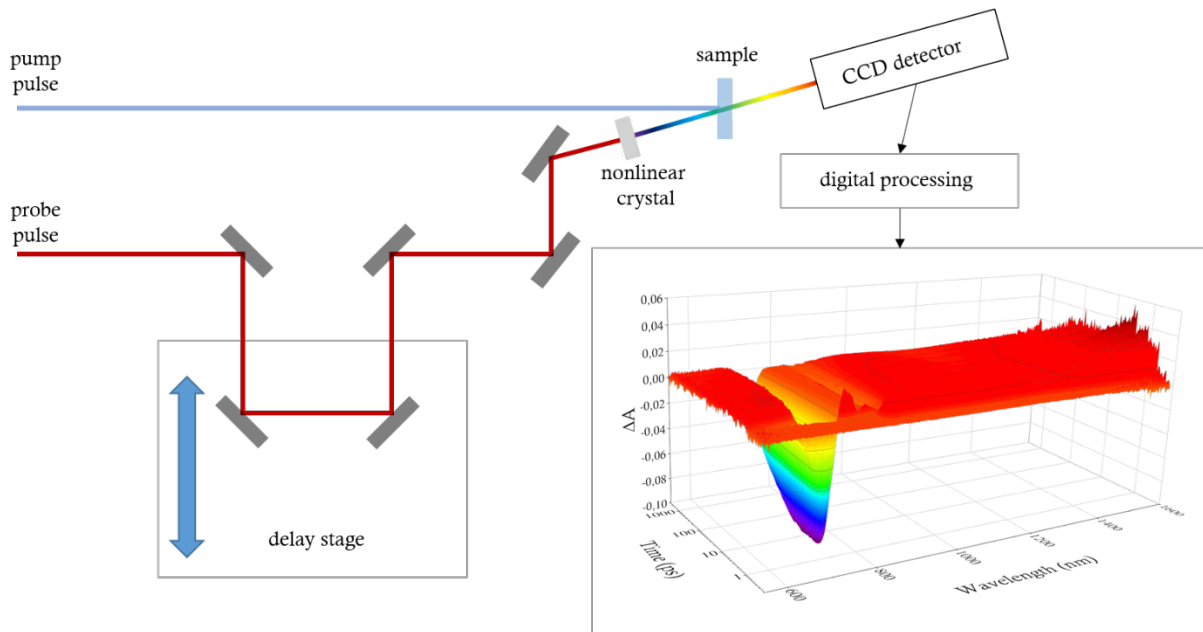
Figure 20 Scheme of the femtosecond transient absorption setup.

Usually, instead of a 3D surface, the TA data are presented as particular spectra after chosen delay times in order to show a signal development, as presented in Figure 21. In the VIS range (up to 800 nm), transient absorption signal of PSCs, at the beginning demonstrates charge cooling as a derivative-like shape of long wavelength steady-state absorption sharp edge. After 1 ps, TA spectrum presents a bleach signal of the absorption edge that decays out of the measurement time widow. The signals below 550 nm were usually not detected due to a too high absorption of the probe pulse in the perovskite. In the NIR range, oscillations at thin layers in a cell are present [49], [50] as well as oxidized spiro-OMeTAD TA signal around 1500 nm [51], [52]. Deconvolution of these two signals was one of the goals of the study reported in KPB-7.
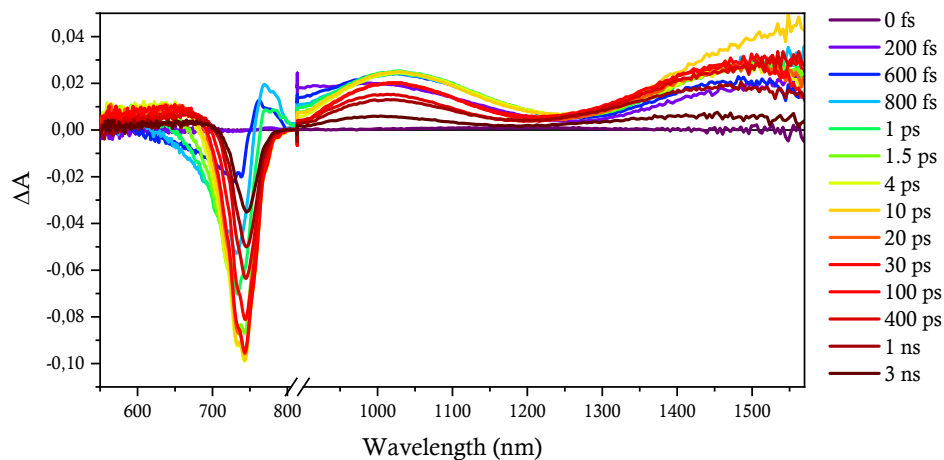
Figure 21 Exemplary time evolution of the TA signal in PSCs. The visible and near-infrared regions were collected separately.
Infrared signal is multiply by 10. Build from data published in KPB-7.

Most of the TA analyzes are performed in the region of the long-wavelength absorption edge bleach (600 – 850 nm). However, in many TA spectra of perovskites, the additional short-wavelength bleach appears below 500 nm (Figure 22). Its nature is not clear. The most common interpretations are that it is related to transitions involving another conduction or valence band [53], [54], molecular-like charge-transfer transition [55], [56] or contribution from PbI_2 [57], [58]. However, due to very high absorption in this region, only in very thin samples the short-wavelength bleach could be observed and analyzed (KPB-2, KPB-3). Also, positive TA signal (photoinduced absorption) in the region between the bleaches is observed and assigned to the changes in refractive index due to photoexcitation [59]. However, it has not been analyzed by us.
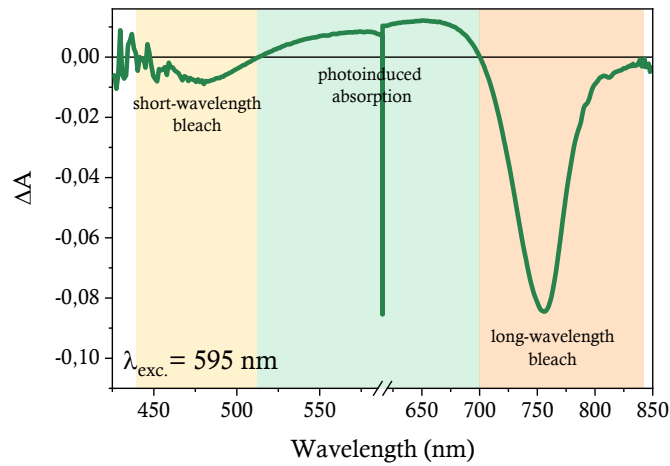
Figure 22 Exemplary TA spectrum of a PSC after 5 ps pump-probe delay with marked main spectral features.
Taken and reconstructed from KPB-3.

Signal Processing

The most common TA data analysis method is global fitting. It is a simultaneous fit of decays by mono- or multi-exponential function in the whole measured spectrum. It can generally be written as [60]:

$$\Delta A(\lambda, t) = A_1 e^{-\frac{t}{\tau_1}} + A_2 e^{-\frac{t}{\tau_2}} + \cdots + A_n e^{-\frac{t}{\tau_n}} \quad , \qquad (11)$$

giving a characteristic time constant (τ_i) and the preexponential factor spectrum ($A_i(\lambda)$) for each component. Global analysis was performed by Surface Xplorer software using the Singular Value Decomposition (SVD) procedure [60]. The SVD creates a matrix product $\Delta A'$ with a set of eigenvectors (consisting of principal kinetics and spectra):

$$\Delta A' = U \times S \times V \qquad (12)$$

Several firsts eigenvectors (with the highest significance coefficient S – singular values, which are diagonal elements of the S matrix) bring the most important information about the ΔA surface.

In the study 2 – 3 first singular value (SV) kinetics were chosen. Then the multi-exponential decay is fitted only to several principal kinetics, which makes the fit very fast as compared to global fits made to all kinetics in the analyzed spectral range.

Figure 23A – C presents global fit results for 2-, 3- and 4-exponential function – preexponential factor spectra, as well as SV kinetics fit quality (Figure 23D – F). In the study simple 2-exponential decay fitting was mostly used to simply characterize the decays and obtain characteristic times for two main processes (charge cooling and bleach decay). The 3- and 4-exponential functions were used for better SV kinetics fitting and to show differences in the dynamics in different bleach regions. The 2-exponential decay function fitting (Figure 23D) is very poor and it is getting better with addition of exponential components. However, addition of more exponential decays to the fitting does not bring additional physical meaning. Also, Burstain Moss effect (described widely in KPB-3) causes bleach narrowing and shifting with time, so pre-exponential factor spectra for a higher number of exponential decays present increasingly shifted and narrowed bleaches.
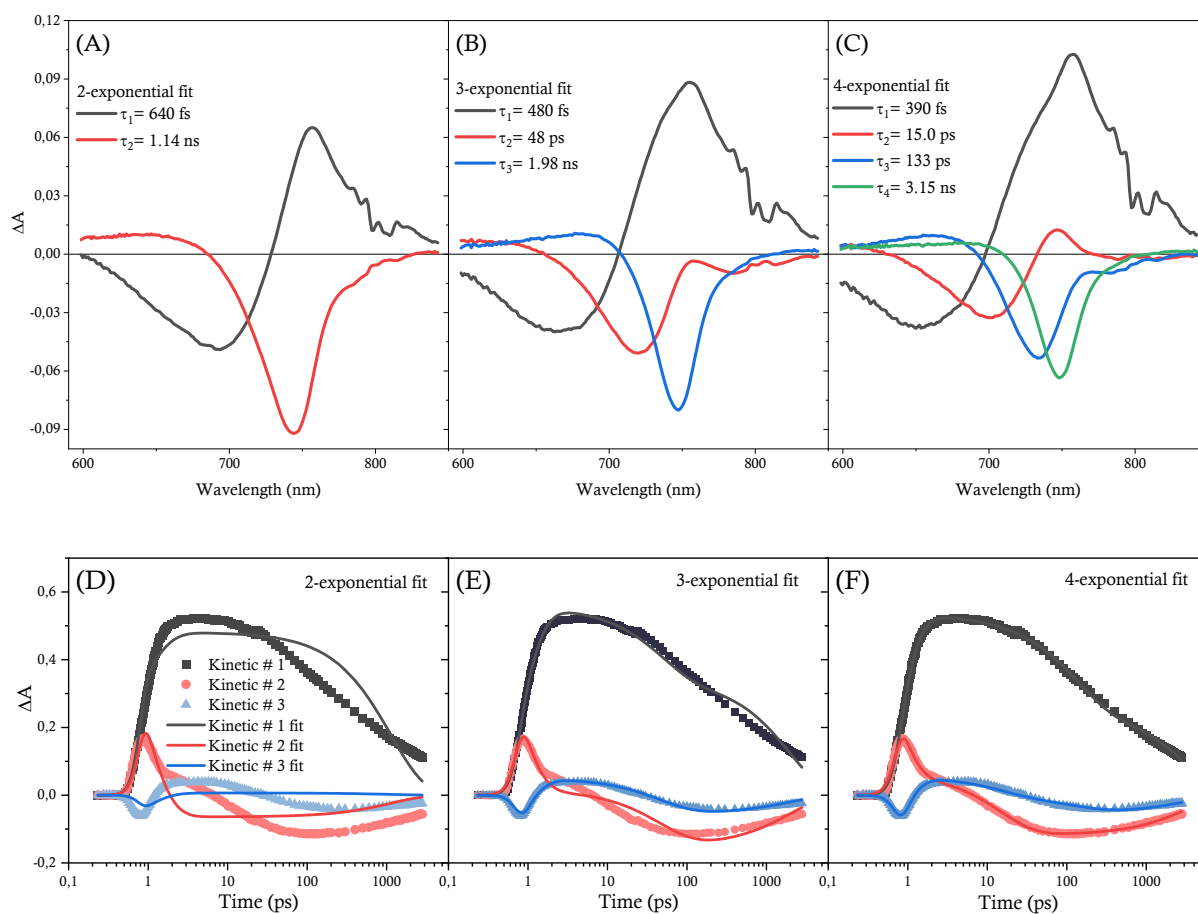
Figure 23 Exemplary 2- (A), 3- (B) and 4-exponential (C) global analysis results – preexponential factor spectra. 3 SV was chosen. D-E fit traces for each fitting. Build from data published in KPB-7.

The solution of differential equation (2) for the number of excited carriers after a short laser pulse is not an exponential function. If only first and second order processes are taken into account, the solution is given by [61]:

$$n(t) = \frac{k_1 n_0}{e^{k_1 t} k_1 - k_2 n_0 + e^{k_1 t} k_2 n_0}$$

(13)

Where, n_0 is the number of excited carriers at $t=0$.

Since, the ΔA of the bleach describes the repopulation of the valence band (decay of the excited carriers), the kinetics at the minimum bleach was fitted by equation (13) giving directly the rate constants of first- and second- order processes, as exemplary shown in Figure 24.
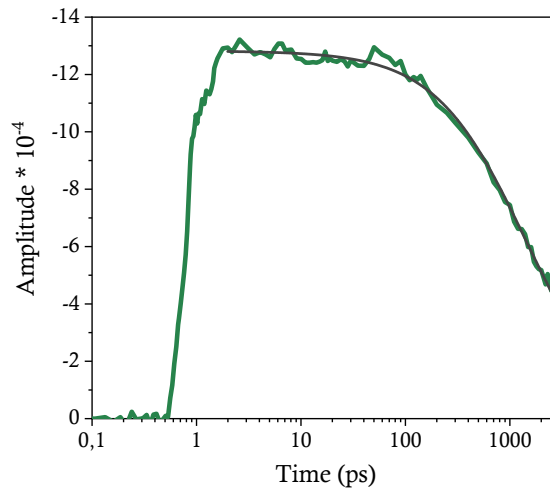
Figure 24 Exemplary minimum bleach kinetic fitted by function from equation (13). Taken from KBP-3.

However, due to the mentioned above Burstain-Moss effect, the bleach minimum shifts in the measured time widow (see Figure 25). The band integral (*BI*), given by [62]:

$$BI(t, \Delta \lambda) = \int \Delta A(t, \lambda) \frac{d\lambda}{\lambda}$$

(14)

was used to collect all bleach decay information in one kinetic which represented a wide spectral range of the signal (marked in Figure 25) and total charge population decay. Analysis of *BI* signal as a basis of our study reported in KPB-3 and since then we have been using it in our analysis (it was also mentioned in supporting information of KPB-2)
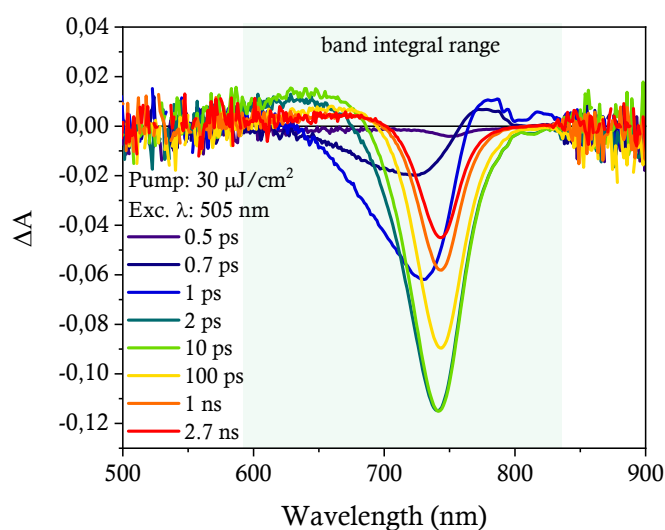
Figure 25 Exemplary TA signal after different pump-probe delay with indicated band integration wavelength range. Taken from KPB-7.

TA spectroscopy conditions for the PSCs

The PSC transient absorption bleach is very narrow in comparison to those of the molecular systems studied by TA (e.g., alternative PV devices – DSSCs).

As mentioned above, perovskite material shows very high absorption coefficient above the bandgap (Figure 17), giving stationary absorbance value at excitation wavelengths (400 – 600 nm) above 1 (90 % absorbed photons). The TA long-wavelength signals in perovskites (~750 nm in the studies presented in this thesis) has very high amplitude (e.g., in comparison to TA of molecular systems), enabling fast measurement even for very small energy density (a few of $\mu J/cm^2$). Moreover, experiments in complete cells with a gold layer (as we show in KPB-7) were possible. Such a high absorption in excitation wavelength range causes that excited carriers are located mostly close to the reaching interface. This allows almost exclusive investigation of volumes close to the interfaces, as shown in Figure 26. Thus, photoexcited charge carriers decays are governed mostly by electrons (when excited from ETM side) or holes (when excited from HTM side).
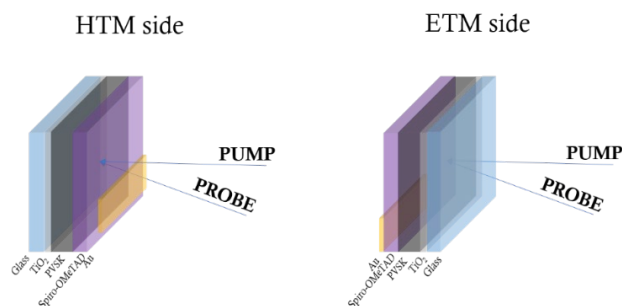
Figure 26 Sample setup in the TA experiment for the HTM and ETM side.

As written above, the decay of excited carriers in the PSC strictly depends on excited carriers density (excitation energy, equation (2)). It is important to keep the excitation energy as low as possible for proper investigation of the first order injection processes. We usually use tens of $\mu J/cm^2$ but also as low energy as a few $\mu J/cm^2$ if we need to minimize the second order recombination influence. To be able to make comparisons between samples, generation of the same conditions (the same excitation energy) in a perovskite material is essential. Also, the decrease in the bleach signal with time observed in PSC is not only caused, as usually for molecules, by photodegradation but is also a result of changes in the perovskite structure such as e.g., ion segregation. In order to average the kinetic and spectral changes during TA experiment (from 5 to 40 min, depending on the number of scans) bidirectional scan mode is used, which means that in every odd scan the delay line goes from the shortest to the longest times and in every even scan in the opposite direction. Also very important in the TA analysis of the PSCs is proper statistics, based on a sufficient number of similar samples checked. Perovskite layer, as we demonstrate e.g., in KPB-7 shows 10 % of thickness dispersion from one point of the sample to another and from sample to sample. The general conclusion should not be never based on only one experiment due to very small femtosecond laser beam focus (250 μm in diameter), which permits investigation of a limited perovskite volume. Therefore, the spread of lifetimes can occur not only between different samples prepared in the same way, but also between the different probing spots of the same sample.

3.2.2 Time-resolved Emission (time-correlated single photon counting)

Working Principles

Analysis of radiative decay of the excited state by a time-resolved emission technique is also helpful in the investigation of charge dynamics in the perovskite material. In our emission setup (based on time-correlated single photon counting detection), under very low intensity of excitation, maximum one photon is emitted from the sample per excitation pulse (Figure 27A). Time resolution is obtained by generation of an electric pulse from the optical one obtained from a laser, which corresponds to time 0, and then the emitted photon is converted in to another electric pulse by an avalanche photodiode (or photomultiplier tube) and stops the timing circuit. This gives the delay time of photon emission from the sample after an excitation at a particular detection wavelength and its result is added to an appropriate channel of time histogram (one of 4096 in our setup). The experiment is conducted in this way repeatedly until a certain counts in maximum of the created decay is reached (usually several thousands) [63]. Figure 27B presents exemplary kinetics for two different excitation powers. Time per channel can be tuned from 0.61 to 12.21 ps giving a time window from 2.5 to 50 ns (with a laser repetition rate of 4 MHz). This setup was also used in the stationary mode to measure stationary fluorescence, the obtained exemplary spectrum of the PSC emission is shown in Figure 27C.
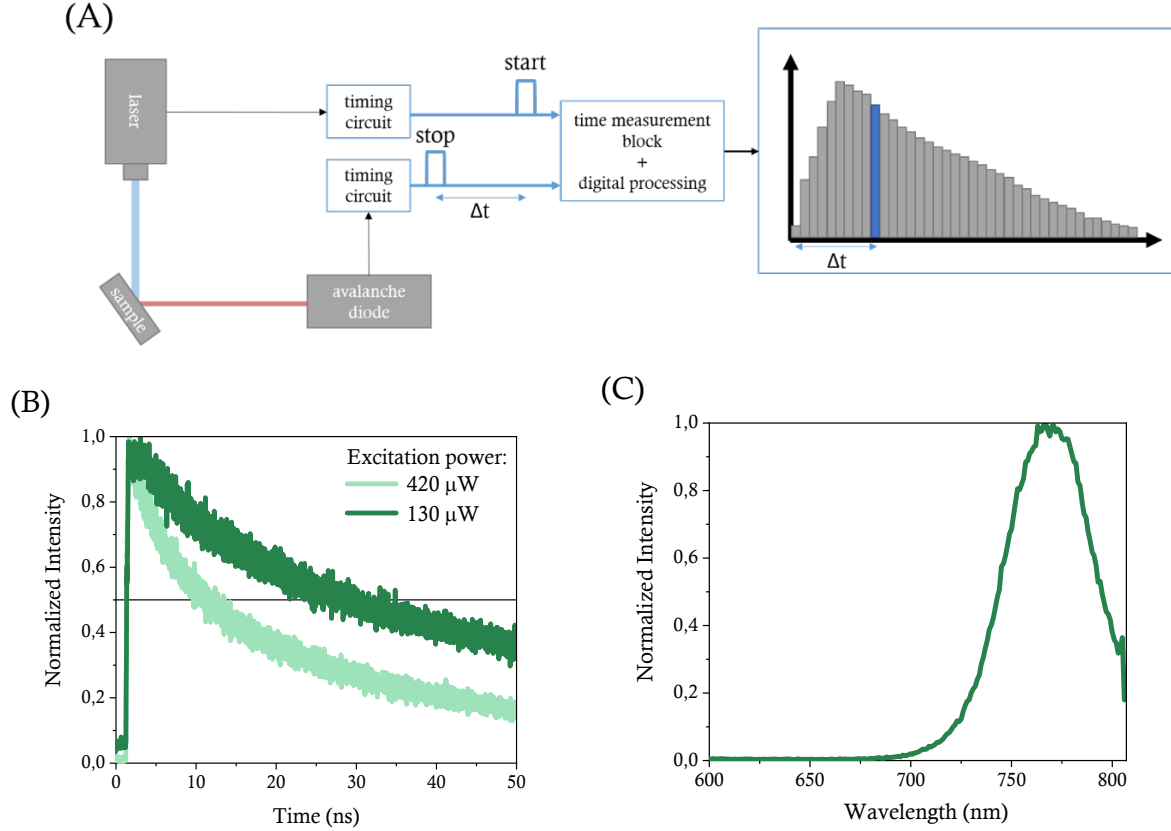
Figure 27 A – Scheme of the TCSPC setup. B,C – Obtained exemplary PSC emission decays for different excitation energy, taken from KPB-4 (B) and stationary emission spectrum of PSC, taken from KPB-5 (C).

Signal processing

The decays were characterized by a simple half-lifetime ($\tau_{1/2}$), which is a time when the amplitude of a decay is equal to half of the initial one (publications KPB-4, KPB-5) or were fitted by stretched exponential function (articles KPB-1, KPB-2, KPB-3, with deconvolution of the instrument response function), given by [60]:

$$I(t) = A_0 e^{-\left(\frac{t}{\tau}\right)^{\beta}} \tag{15}$$

It is a modified exponential function, where β is the diffusion parameter and is equal to 1 when the decay is monoexponential and to 0 when the signal does not decay at all. It is also possible to describe many exponential functions by the stretched function (squeezed) with $\beta<1$ [64].

Averaged decay time (τ_{AVG}) can be obtained from [60] as:

$$\tau_{AVG} = \frac{\tau}{\beta} \Gamma\left(\frac{1}{\beta}\right) \tag{16}$$

Figure 28 shows fitted decays for different emission wavelengths. Moreover in the publication KPB-4 emissions decay were fitted by mixed order decay function (equation (13)), described in Section 3.2.1.
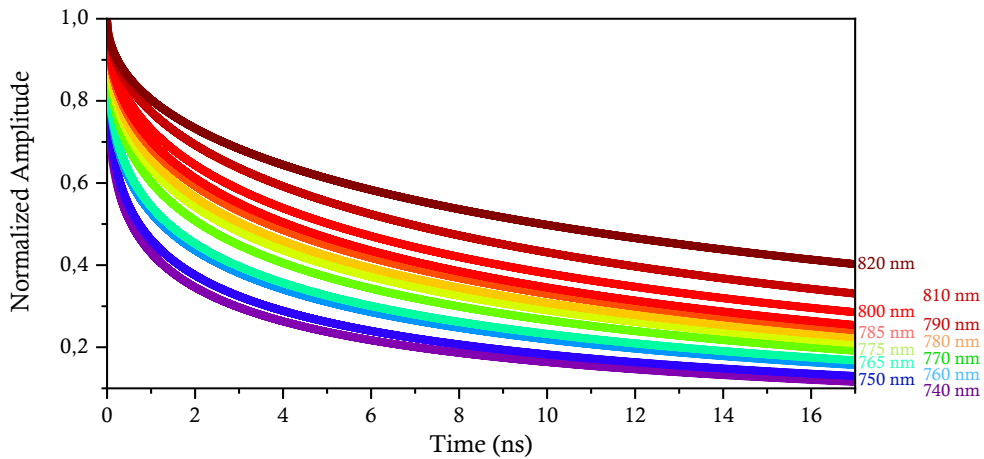
Figure 28 Obtained from experimental decays fitting, stretched exponential functions for indicated wavelengths. Taken from KPB-3.

TCSPC of the PSCs

Time-resolved emission spectroscopy in the time widow 2.5 ps to 50 ns permits investigation of the repopulation of the valence band after excitation. The information provided by the TCSPC setup overlaps that from the femtosecond transient absorption system but with much worse time resolution (orders of magnitude) and only one wavelength can be monitored at once. Stationary emission occurs always from the lowest energy perovskite state so it gives information about ion segregation and trap states [34].

In investigation of PSCs by this technique it is important to provide experimental conditions (proper sample angle) in which the reflection from the cell does not reach the detector. It is necessary to keep excitation energy constant and, as mentioned for the TA experiment, comparison of decays obtained for different excitation fluence, as it is in usual molecular studies, is incorrect because the decay strictly depends on the excited carriers density (equation (2)). Similarly as in the TA spectroscopy, excitation from the ETM and HTM sides was investigated (Figure 29, publication KPB-5). Also the experiment should be repeated at least a few times in different samples or at different sample places.
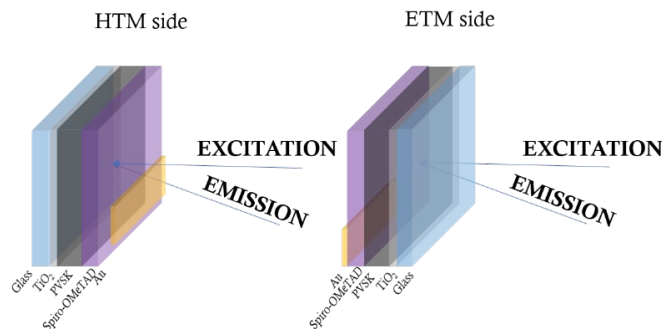
Figure 29 Sample configuration in the TCSPC experiment when measured the HTM and ETM side.

3.2.3 Electrochemical Impedance Spectroscopy

Working Principles

While instead of direct current (DC), alternating current (AC) flows in the solar cell, it meets resistance (energy dissipation) and capacitance (energy storage) in cells' layers which leads to decrease in its amplitude and also change in its phase. The electrochemical impedance spectroscopy (EIS) is a technique based on this phenomenon and uses voltage (E) with very small sinusoidal perturbation in time, described by the expression [65]:

$$E(t) = E_0 \sin(\omega t) \tag{17}$$

Where E_0 – amplitude of the signal, ω – radial frequency ($\omega = 2\pi f$, f – frequency in Herz)

As shown in Figure 30, sinusoidal voltage generate current (I) with phase shift (ϕ):

$$I(t) = I_0 \sin(\omega t + \phi) \tag{18}$$

Where I_0 – amplitude of a signal
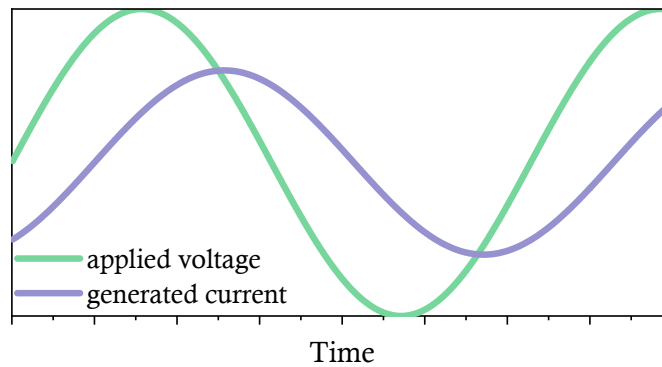
Figure 30 Schematic relation of the applied sinusoidal voltage and current generated by a cell.

Impedance (Z) is a measure of the ability of a system to resist current, defined by formula:

$$Z(\omega) = \frac{E_t(\omega)}{I_t(\omega)} = \frac{E_0 \sin(\omega t)}{I_0 \sin(\omega t + \phi)} = Z_0 \frac{\sin(\omega t)}{\sin(\omega t + \phi)} \tag{19}$$

Using Euler relationship it becomes a complex number:

$$Z(\omega) = Z_0(\cos(\phi) - i\sin(\phi)) \tag{20}$$

giving imaginary (Z'') and real (Z') part of the impedance.

Figure 31 shows two usual representations of the EIS results. Imaginary part of the impedance vs frequency (Figure 31A) and the so-called Nyquist plot – imaginary vs real part of the impedance (Figure 31B) [65]. Usually, two main features are observed in the impedance plot (two semi circles in Z'' vs Z' plot and two peaks in Z'' vs frequency plot), low frequency (LF, $<10^2 – 10^3$ Hz) and a high or sometimes called middle frequency (HF or MF, $\sim10^4 – 10^5$ Hz) signal [66]. The LF

signal reflects dynamics of ion motion, the HF signal represents recombination processes in titania layer and in bulk perovskite [67].
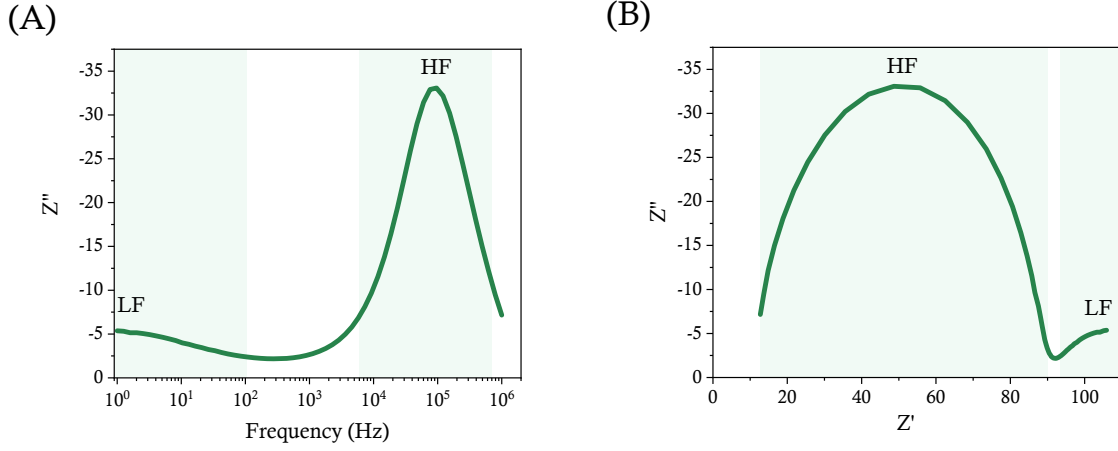
Figure 31 Exemplary Z" vs frequency and Z" vs Z' (called Nyquist) plots of impedance spectroscopy experiments with low (LH) and high (HF) regions indication.

Signal processing

The obtained EIS data are fitted by the so-called equivalent circuit, which usually contains different configurations of resistors, capacitors or/and its alternative, the so-called constant phase element (*CPE*). The latter impedance is given by [65]:

$$Z_{CPE} = \frac{B}{j\omega^n} \tag{21}$$

Where *B* and *n* are frequency independent parameters.

The *CPE* can exist as resistor (for *n*=0) or a capacitor (for *n*=1). For *n* above 0.8 it is treated as capacitor with capacitance described as:

$$C = \frac{(R_{ct}B)^{\frac{1}{n}}}{R_{ct}} \tag{22}$$

Where, R_{ct} is charge transport resistance of the circuit
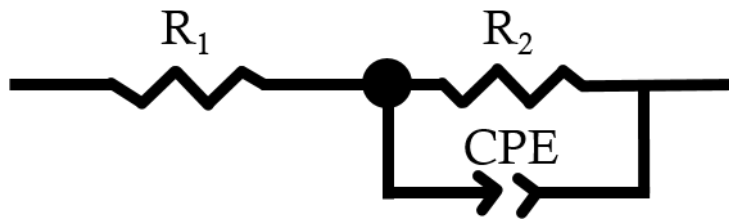
Figure 32 Equivalent circuit used in the study. R₁ is abbreviated as Rₛ and R₂ as Rₜ.

In this thesis, the obtained impedance data were fitted by equivalent circuit shown in Figure 32 (in KPB-5 where only HF range was studied) or connected double RC circuits (KPB-1 and KBP-4 for HF and LF range).

From Kirchoff's circuit laws, the impedance of the circuit from Figure 32 is given by:

$$Z(\omega) = R_s + \left(\frac{1}{R_{ct}} + \frac{B}{j\omega^n}\right)^{-1} \tag{23}$$

From the obtained capacitance and resistance, the time constant of the recombination process (equivalent circuit) can be calculated using the formula:

$$\tau_i = R_i C_i \tag{24}$$

A single resistor in series connection to RC circuit represents series resistance of the cell and it is seen in Nyquist plot as the *Z'* starting value.

If the EIS experiment is performed as a function of applied voltage (*V*), the ideality factor (*m*) can be obtained from the equation [65]:

$$R = R_0 \exp\left(\frac{eV}{m k_B T}\right) \tag{25}$$

Where e – elementary charge, k_B – Boltzmann constant, T – temperature in Kelvin's

Ideality factor gives information about the recombination process path (*m*=1 indicates band-to-band recombination, *m*=2 trap-assisted recombination by mid-gap trap states and values between 1 and 2 indicate superposition of these two) [68].

EIS of PSCs

The perturbation in EIS experiment can be applied in different conditions of a sample e.g., with (light) or without (dark) illumination (by 1Sun or monochromatic), at non-open (NOC) or open circuit (OC) conditions or mix of these conditions in order to obtain different information of the system.

Resistance, capacitance and time constants can be compared for the illuminated and non-illuminated samples to get the information characterizing cell operation (KPB-1, KPB-4). These values can be compared for different ETMs or HTMs (KPB-1), for the cells with different currents (KPB-4) or the cells made under different conditions (KPB-5) to characterize the charge transport in a given cell. The most desired cell is that with the smallest loss of energy, which means that its resistance, capacitance as well as time constant should be as high as possible. Also in conditions with illumination, different wavelengths (e.g., blue and red) of the light can be used to reach different perovskite layer volumes, as in KPB-5 (Figure 33). Due to high absorption of blue light of the perovskite material it probes a region nearby the titania interface. Red light goes deeper into

perovskite material and gives information about the bulk processes or the processes taking place close to spiro-OMeTAD volume.
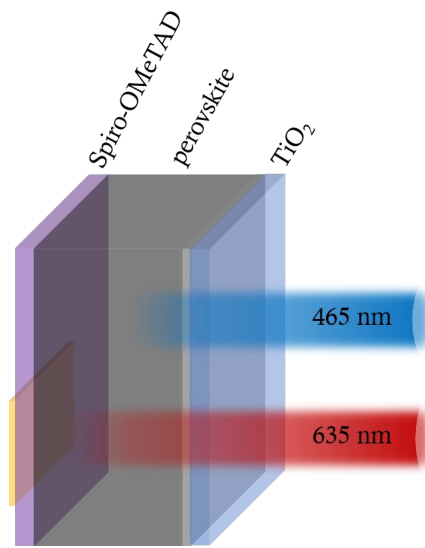
Figure 33 Scheme of blue (465 nm) and red (635nm) light penetration depth in perovskite solar cell used in KPB-5.

4 COMMENTS ON THE PUBLICATIONS

KPB-1

Effects of different small molecule hole transporters on the performance and charge transfer dynamics of perovskite solar cells

In the first article of the presented thesis, MAPbI₃ perovskite sandwiched between titania layer and the most common HTM – spiro-OMeTAD was studied. Very similar in structure, but cheaper than spiro-OMeTAD, X60 (also known as SFX-MeOTAD, 2,2',7,7'-tetrakis(*N,N*-di(4-methoxyphenyl)amino)-spiro-(fluorine-9,9'-xanthene)) and a mixture of both were examined. Their chemical structures are shown in Figure 34. Femtosecond transient absorption spectroscopy (TA), time-resolved photoluminescence and electrochemical impedance spectroscopy (EIS) were used as time resolved techniques to deeply investigate hole transfer dynamic differences between the fabricated cells. Perovskite materials were fabricated under ambient room conditions by one- or two-step method. The novelty of the paper was that the cells with X60 have been studied by transient methods for the first time.
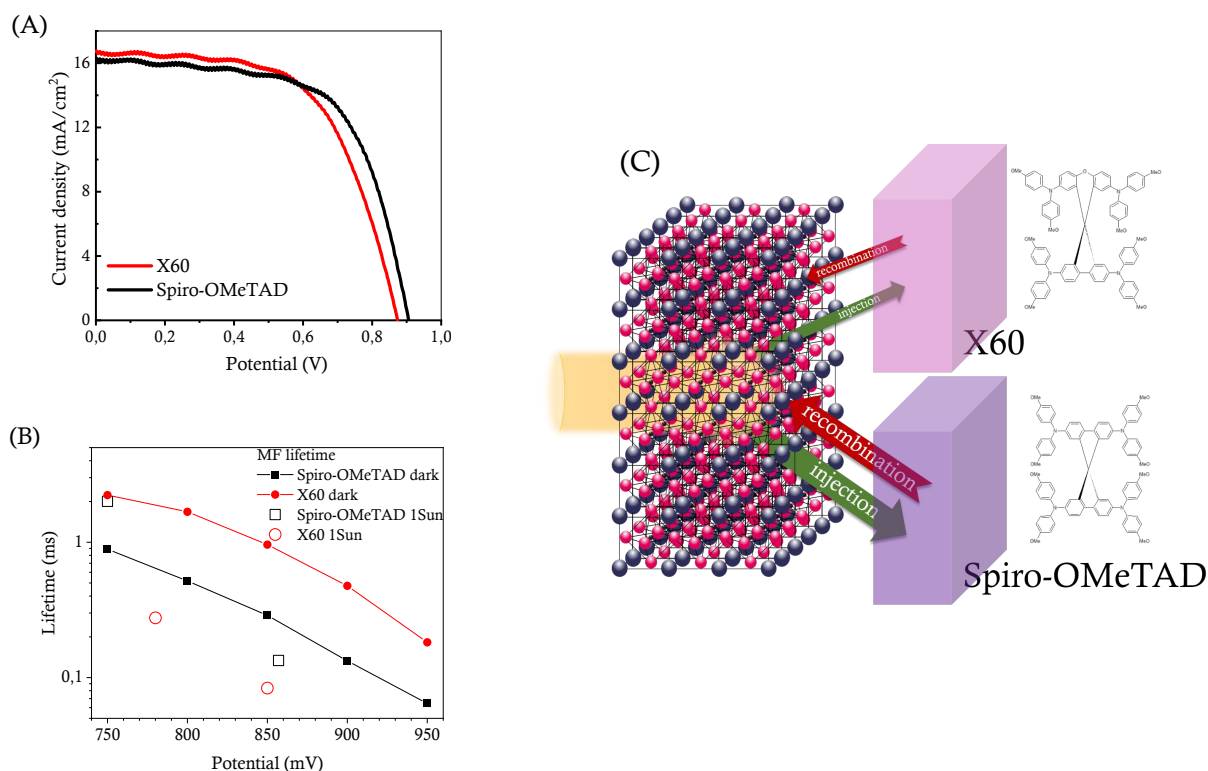
Figure 34 A – Exemplary current voltage curves of X60 and spiro-OMeTAD based cells. B – Time constants obtained from EIS vs applied potential for samples studied under 1Sun illumination and dark. C – Schematic picture of the most important findings from the study.

The *totalAPCE* for both spiro-OMeTAD and X60 based cells reached nearly 100 %. However, the X60 cells exhibited a fill factor smaller by 13 % than that of the spiro-OMeTAD cells (Figure 34A).

The EIS was performed for the best cells, fabricated by the two-step method, in the dark and under 1Sun illumination as a function of the applied potential (600 – 950 mV, Figure 34B). The cells with X60 exhibited longer recombination time constant (sometimes, incorrectly called lifetime in our papers) in the high-frequency region (resulting from higher resistance) in the dark indicating that the recombination from X60 to MAPbI$_3$ is slower than that from spiro-OMeTAD (red arrows in Figure 34).

In TA study we compared the longer rate constant, obtained from 2-exponential global analysis of the results of experiments with the small excitation pulse energy density (from 2.5 to 8 µJ/cm^2) for X60 and spiro-OMeTAD samples. Assuming that the electron transfer to TiO$_2$ and the first order recombination in perovskite remain the same for each pair, the difference in the rate constants reflects only the differences in the interfacial charge transfer to HTM. Averaged difference in the longer TA rate constants *Δk* was equal to 0.036 ± 0.022 ns^{-1}. Taking the hole transfer rate constant from MAPbI$_3$ to spiro-OMeTAD obtained earlier (0.06 ns^{-1}) [69], we deducted that hole transfer to X60 is no more than twice slower than that to spiro-OMeTAD. Additionally, photoluminescence decays supported that findings, the average decay time for X60 was longer than that for spiro-OMeTAD.

The cells made with X60:spiro-OMeTAD (1:1, v:v) mixture exhibited intermediate behavior confirmed by all above techniques.

The results of TA interpreted together with EIS results show that X60 was characterized by a lower recombination rate and a lower hole injection in comparison to those of spiro-OMeTAD, as schematically shown in Figure 34C. Slower injection to X60 can be caused by slightly more positive redox potential of this material in comparison to that of spiro-OMeTAD (about 20 mV), thus, the driving force for charge transfer is smaller.

KPB-2

Differences in photoinduced optical transients in perovskite absorbers for solar cells

In this article, following the hole transporting material study presented in KPB-1, we focused on the perovskite material. The publication reports the investigation of MAPbI$_3$ perovskite films and powdered crystals using the methods of femtosecond transient absorption as well as time-resolved photoluminescence spectroscopy. The perovskite films were made at non-stoichiometric (3:1, **NS**) or stoichiometric (1:1, **S**) MAI:PbI$_2$ molar ratios in precursor solutions. **S** samples exhibited a red-shift of stationary absorption edge and the emission band and also had longer fluorescence lifetime as well as lower relative photocurrent in comparison to those of **NS** sample.
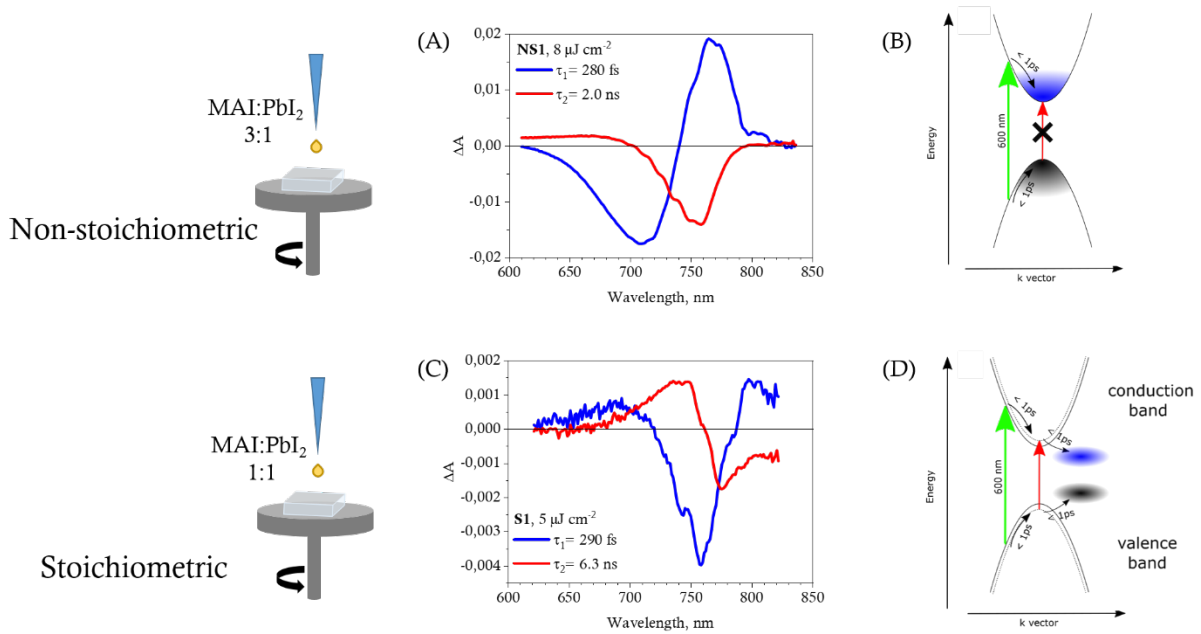
*Figure 35 2-exponential global fit of transient absorption data results for **NS** (non-stoichiometric, A) and **S** (stoichiometric, C) MAI:PbI$_2$ ratio in perovskite precursor solution. Schemes of proposed interpretation of charge behavior for **NS** (B) and **S** (D) samples.*

The TA signal of **S** samples, after initial charge cooling (with a time constant τ_1), had a derivative-like shape as shown in Figure 35C (τ_2), instead of becoming a bleach signal, as for **NS** samples. Negative amplitude in longer and positive in shorter wavelength range of this derivative-like signal can be an indication of a blue shift of the absorption band. Furthermore, TA signal for **S** sample was ten times smaller than that for the **NS** standard bleach signal (Figure 35A, τ_2). Moreover, charge cooling signal (τ_1) of **S** film is also different than that well-known and observed for **NS**. It was dominated by negative bleach signal with a minimum at about 760 nm. The powdered MAPbI$_3$ crystals exhibited the TA spectral shape similar to that of **S** samples, the longest emission lifetime and greater red-shift of steady-state absorption edge. The TA signal dynamics was the same no

matter if MAPbI$_3$ film was prepared directly on FTO glass or sandwiched between TiO$_2$ and spiro-OMeTAD, indicating that charge recombination within perovskite layer brings the greatest contribution.

The proposed explanation of different spectroscopic behavior of the films with different MAI:PbI$_2$ ratios in the precursor solution is shown in Figure 35B,D. The **NS** sample signal obeys the rules described in Section 3.2.1: after excitation, charge cooling process leads to accumulation of electron and holes at band edges, which gives a strong and narrow bleach signal (Figure 35B), then the bleach signal recovers due to charge recombination and injection. In contrast, in **S** samples the carrier cooling process does not finish at band edges but in the local states below the minimum of the conduction band and above the maximum of the valence band (Figure 35D). This accumulation outside the bands due to electric modification of the band-edge transition (Stark effect) causes a derivative-like shape of the spectrum. Another proposed explanation was the existence of a second bandgap (slightly shifted in k-space), which caused charge leakage/transfer from the primary bands.

Additionally, the excitation energy density dependence of the TA signal was also checked, demonstrating that amplitude of the TA signal varied with the excitation energy density. Moreover the temporal and spectral behavior of the signal was different. With increasing excitation energy density the bleach signal is shifted and widened and more exponential components are needed to describe the TA signal. Simpler analysis of global integration of the band has been proposed and further studied in the next papers of the thesis.

Later, in 2019, Leng published his TA study of a perovskite film showing that TA signal can be contaminated by transient reflection, manifesting as derivative-like shape signal [70]. This observation abolishes our interpretation and probably indicates that our stoichiometric samples with poorer quality (more pinholes and other imperfections) reflected a lot of probe light, which led to the appearance of derivative-like shape of ΔA signal. Nevertheless, findings for non-stoichiometric samples are still valid, such as the TA signal excitation energy dependence, which was the starting point for our next research (KPB-3).

KPB-3

Insights into the femtosecond to nanosecond charge carrier kinetics in perovskite materials for solar cells

In the article, complete inverted PSCs with three different ETMs, delivered by Saule Technologies company were investigated. The subject of the study was an inverted cell deposited on an electrode (PET foil) with ITO, PEDOT:PSS as the HTM, $MAPbI_3$ and PCBM as the ETM. PenPTC (also called PDI, N,N'-dipentyl-3,4,9,10-perylene dicarboximide) and SPPO13 (2,7-bis(diphenylphosphoryl)-9,9'-spirobifluorene) organic materials were substitutions for PCBM. The reference samples, with perovskite layer deposited directly on the glass with the above-mentioned ETMs were also examined. Femtosecond transient absorption as well as picosecond to nanosecond time-resolved photoluminescence were used.

The study started with analysis of the perovskite bleach signal behavior described in KPB-2. In our first studies of PSCs in 2016 [69], we proposed that the rate constants of the first and second order processes could be obtained from the plot of the reciprocal of longer time component (τ_2) from 2-exponential global analysis of TA data as a function of pump pulse intensity (I). The first order rate constant was extracted as the intercept value (denoted below as k_1') and the second order rate constant (denoted as k_2') from the slope of the data linear fit. However, in the presented KPB-3 work, we assessed the quality of the above-described 2-exponential approximation of decay by comparing it with simulated second or mixed (first and second) order decay functions with set k_1 (first order) and k_2 (second order) values. In the case of pure second order decay function fitting, k_1' obtained from $1/\tau_2$ vs I plot is very close to 0 and k_2' is equal to 0.3 of the set in simulation value of k_2. For the mixed order decay function fitting, k_1' obtained from linear fit is equal to given k_1 value, while the slope value – k_2', is again different than set in the simulation (k_2'= 0.4 k_2). If the fitting is performed for the simulated decay in cut off temporal widow (kinetic decay to amplitude equal to 25 % of the initial one) k_1 value remains the same, but k_2' value becomes 1.0 k_2. Therefore, although the exponential fit of TA data does not precisely describe the first and second order processes, the simple 2-exponential global approach may be useful in many situations, providing the correct first order rate constants and the slope proportional to the second order rate constant.

Secondly, we focused on determination of a proper kinetics of photoexcited carriers decay in perovskite material. Figure 36A shows three different kinetic curves obtained from the analysis of TA experiment i.e., kinetics at the minimum bleach (black line), 1st Singular Value kinetics from global fit procedure (green line) and the result of integration procedure over a broad spectral range (610 – 850 nm) – in the form of band integral (red line). Only band integral amplitude is a linear function of excitation energy (population of excited carriers) in a wide energy region.

The other two approaches do not correctly take into account the fast decaying charge population related to the blue part of the bleach band.
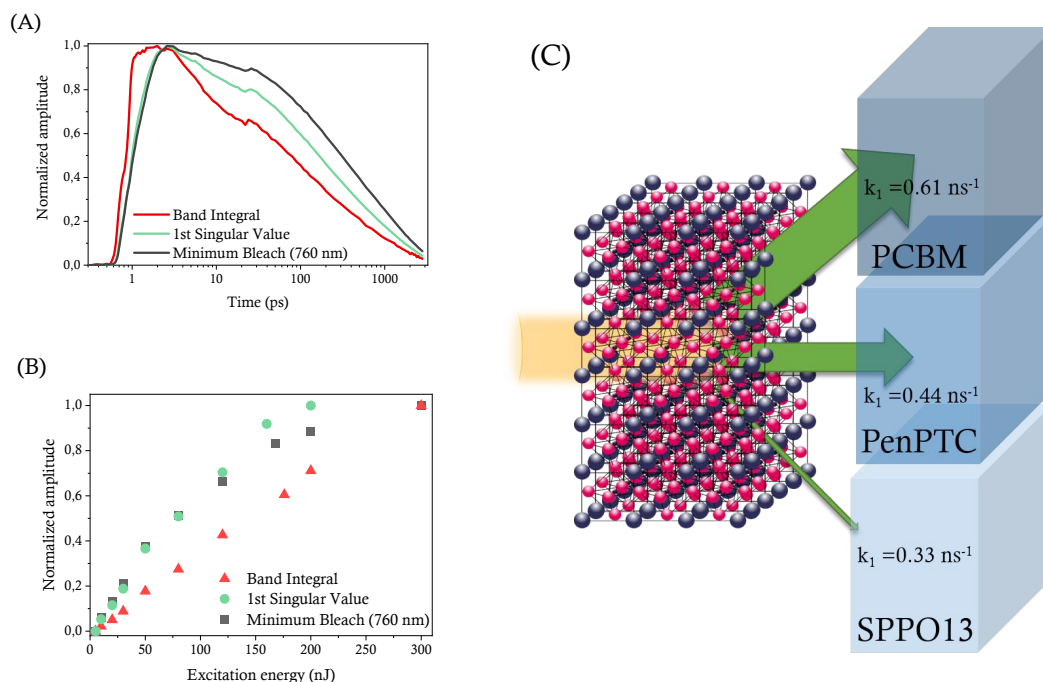
Figure 36 A – Comparison of band integral, 1st singular value and minimum bleach kinetics of a PSC. B – Normalized maximum amplitude of the kinetics obtained in different ways as a function of excitation energy.
C – Schematic presentation of the obtained results.

Thirdly, rate constants for the perovskite with PCBM on glass and complete PSCs decay were determined by fitting the band integral kinetics with a mixed order decay function. For glass samples the fit quality was sufficient only up to the pump pulse intensity of 15 $\mu J/cm^2$, however in PSCs this limit was 40 $\mu J/cm^2$. The perovskite film on the glass was recognized by the SEM images and XRD pattern as of poorer quality than that on top of PEDOT:PSS. It can indicate that in a lower quality structure Auger recombination threshold is placed in the lower excitation energy region. The k_2 value determined for glass samples was equal to $(8.9 \pm 1.0) \times 10^{-10}$ cm^3/s, while the complete solar cells of higher quality exhibited significantly smaller second order rate constant $(3.6 \pm 0.3) \times 10^{-10}$ cm^3/s. Also k_1 values for three different ETMs were compared. The first order rate constant was the highest for PCBM and equal to 0.61 ± 0.10 ns^{-1}, together with the highest photocurrent of the cell. PenPTC exhibited middle values of both photocurrent (two times smaller than for PCBM cells) and k_1 (0.44 ± 0.06 ns^{-1}). The smallest k_1 value: 0.33 ± 0.17 ns^{-1} was determined for SPPO13, included in the cell with negligible photocurrent.

Additionally, the short-wavelength bleach (480 nm) signal was studied. In contrast to the long-wavelength bleach, its amplitude in the minimum of the band depends linearly on the excitation energy. This bleach did not show shifting and widening. It suggests that the short-wavelength bleach signal is caused by different electronic nature than the long-wavelength one.

KPB-4

Understanding the effect of different synthesis conditions on the physicochemical properties of mixed-ion perovskite solar cells

In the article research introduced the first substitution of perovskite MAPbI$_3$ material. We chose mixed-ion, $(FAPbI_3)_{0.85}(MAPbBr_3)_{0.15}$ perovskite for which PSCs performance was better at that time than for MAPbI$_3$. As observed in KPB-3, charge transport rate constants (k_1 and k_2) seem to depend on the perovskite quality. The article describes different quality PSCs obtained in different conditions of synthesis. The time-resolved emission spectroscopy and electrochemical impedance spectroscopy were used to determine the influence of the cell modification on charge transport within the cells. Table 2 collects the synthesis parameters and the corresponding averaged photocurrent of prepared batches.

Table 2 Synthesis parameters and averaged J$_{sc}$ value of prepared batches.
Better mesoporous layer is called SC18dil in KPB-6.

Sample	TiO$_2$ layer	Anti-solvent	O$_2$ [%]	Humidity RH [%]	J_{sc} [mA/cm^2]
WM (No A–S)		No	21	8 – 40	8.5
WM (21% O$_2$; 40% RH)			21	40	8.9
WM (21% O$_2$; 8% RH)	Worse mesoporous		21	8	13.3
WM (<1% O$_2$; 10% RH)		Yes	<1	10	14.9
P (21% O$_2$; 8% RH)	Planar		21	8	14.9
BM (21% O$_2$; 8% RH)	Better mesoporous		21	8	17.8

The cells quality was characterized as a ratio of absorbance at 600 nm (containing the unreacted precursors) to that at 700 nm. The lowest limit of this ratio is equal to 1.41 for the ideal semiconductor with a direct bandgap with the absorption edge corresponding to that of mixed-cation perovskite (775 nm). The samples of the best quality whose ratio of absorbances was the closest to this value, show the highest absorption at 700 nm (Figure 37A). A correlation of the photocurrent of the samples (J_{sc}) with absorbance value at 700 nm has been found. X-ray diffraction revealed that the peak areas ratio of mixed cation (28.5° and 31.8°) over unreacted PbI$_2$ (12.3°) took higher values for the higher absorbance at 700 nm. This indicates that the higher the perovskite layer quality, the higher the photocurrent. A similar correlation has been found for efficiency vs. absorbance at 700 nm value with exception of planar cells which despite contain a high quality perovskite layer, do not extract charges as efficiently as mesoporous titania.

The EIS experiments performed for the cells with different photocurrent under 1Sun illumination revealed that the interfacial charge transfer becomes faster with increasing cell photocurrent.

The first and second order recombination rates, obtained by fitting the time-resolved emission spectroscopy decays by the equation (2), increased with increasing cell quality (absorbance at 700 nm, Figure 37B). The k_1 increase is probably caused by faster injection to ETM or HTM in higher quality cells. On the other hand, increase in k_2 value suggests that maybe the proper perovskite structure exhibits a faster second order recombination process. The second explanation of the increase in both rates is that the injection process is described by the first and second order parameter. For minimization of the effect of possible random fluctuation of the results, the emission measurements were performed at least at two places on the sample, and the results were averaged from two to four samples from the same batch.
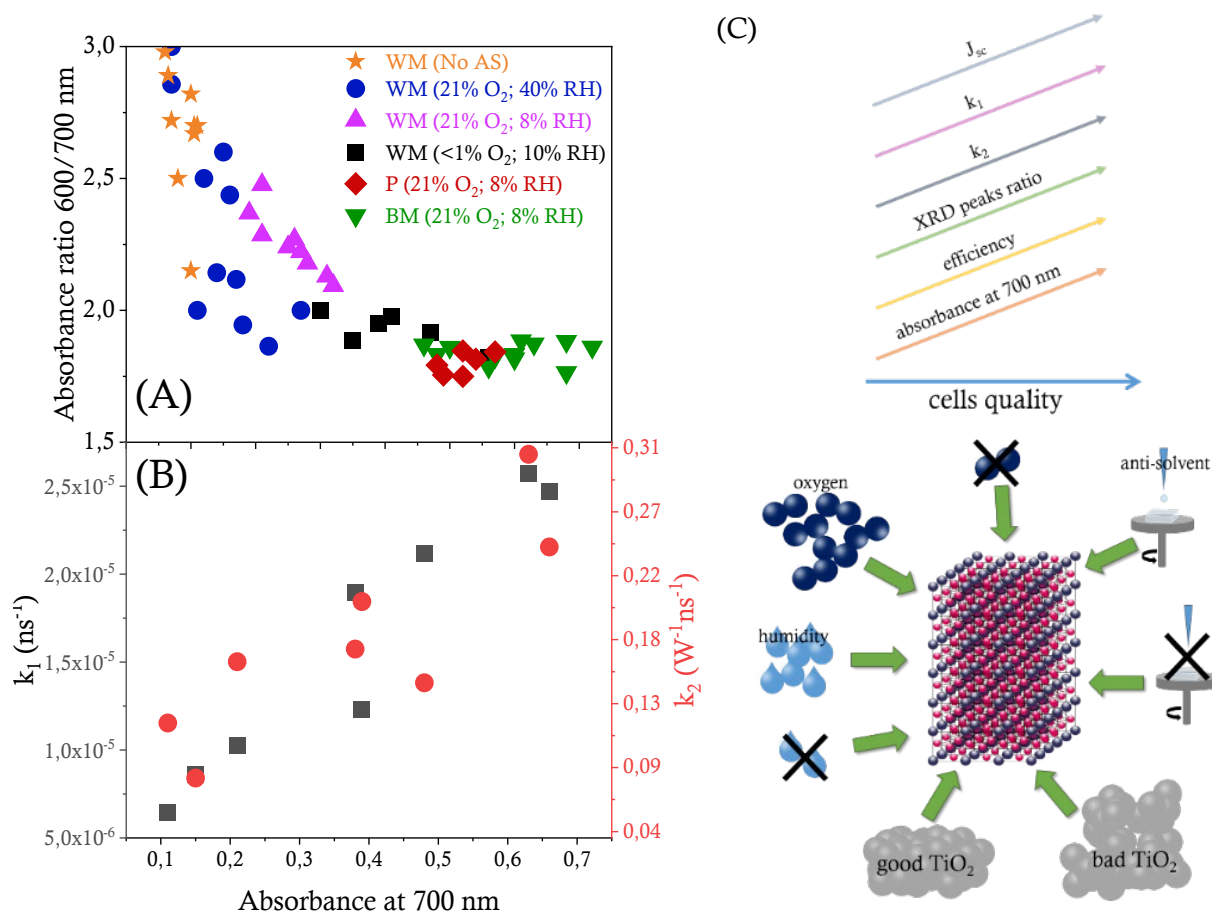
Figure 37 A – Absorbance ratio at 600 nm to that at 700 nm for differently prepared PSCs batched (A) and k_1 and k_2 value for different samples (B) as a function of absorbance value at 700 nm. C – schematic presentation of the different synthesis conditions and the main findings of the study.

KPB-5

Understanding the interfaces between triple-cation perovskite and electron or hole transporting material

The article reports a study of PSCs with benchmark triple-cation perovskite ($FA_{0.76}MA_{0.16}Cs_{0.05}Pb(I_{0.81}Br_{0.19})_3$) sandwiched between layers of titania and spiro-OMeTAD. Cells were made in a drybox under dry (water-free) conditions (**DC**) or under ambient room conditions (**AC**). The **AC** samples were made with varying DMSO:DMF ratio (from 0.24 to 0.4 DMSO content) in the final perovskite precursor solution in different water vapor pressure conditions (WVP, 0.9 – 1.3 kPa). In the study we focused on the differences in photoexcited charge carriers dynamics between that from the ETM side (close to the titania/perovskite interface) and the HTM side (close to the spiro-OMeTAD/perovskite interface). The experimental realization of the way of probing of selected interfaces is described in the Methods section of this thesis. The time-resolved emission spectroscopy, transient absorption spectroscopy and electrochemical impedance spectroscopy with support of scanning electron microscopy, transmission electron microscopy and grazing incident X-ray diffraction were employed to determine charge dynamics and perovskite crystal structure close to the interfaces.

Study of PSCs prepared from the solution with varying DMSO content and under different WVP conditions did not allow drawing general conclusions on the photovoltaic parameters of the devices. Only the ideality factor was clearly influenced by the DMSO concentration (Figure 38A). Its value was about 1.0 – 1.5 for the standard 0.24 DMSO content, and increased with DMSO content. It suggests that for low DMSO concentrations the recombination process is mostly due to bulk recombination and it becomes the surface recombination, when DMSO content is high.

The samples prepared under ambient room conditions (under a fume hood in a laboratory), showed that the photoexcited charge carrier decay is faster from the ETM side than from the HTM side. The emission study showed that half-lifetime of the decay, for the samples of the same thickness, was equal to 1.6 ns and 2.4 ns from the ETM side and HTM side, respectively. The transient absorption experiments results permitted determination of the average decay time constant equal to 3.5 ns for the ETM side and 5.5 ns for HTM side. The electrochemical impedance spectroscopy indicated that the charge recombination loss is lower close to the interface with ETM in comparison to that close to HTM. These observations indicate that for the **AC** samples, the asymmetry in charge transport is governed mostly by electrons from the ETM side and holes from the HTM side, which can be caused by different recombination center distribution.

The PSCs prepared in a drybox showed that the hole injection becomes faster (higher ETM/HTM half-lifetime ratio) for the cells exhibiting higher photocurrent (Figure 38B). It suggest that in highly

efficient PSCs the hole transport rate is crucial in gaining the best efficiencies. The cells were also investigated by grazing incident x-ray diffraction at different incident beam angle, which showed that unreacted PbI_2 is higher close to TiO_2 layer in comparison to that close to spiro-OMeTAD/perovskite interface. This difference can affect the charge dynamics. Stationary emission further indicated a difference in the hole and electron dynamics, a long-wavelength feature close to the ETM was observed, which caused a maximum emission shift from 770 nm at the HTM side to 784 nm at the ETM side.

The study revealed that the perovskite structure and charge dynamics are not uniform within the whole perovskite material. These conclusions were drawn with support of statistic relevance, using Pearson method on numerous experiments.
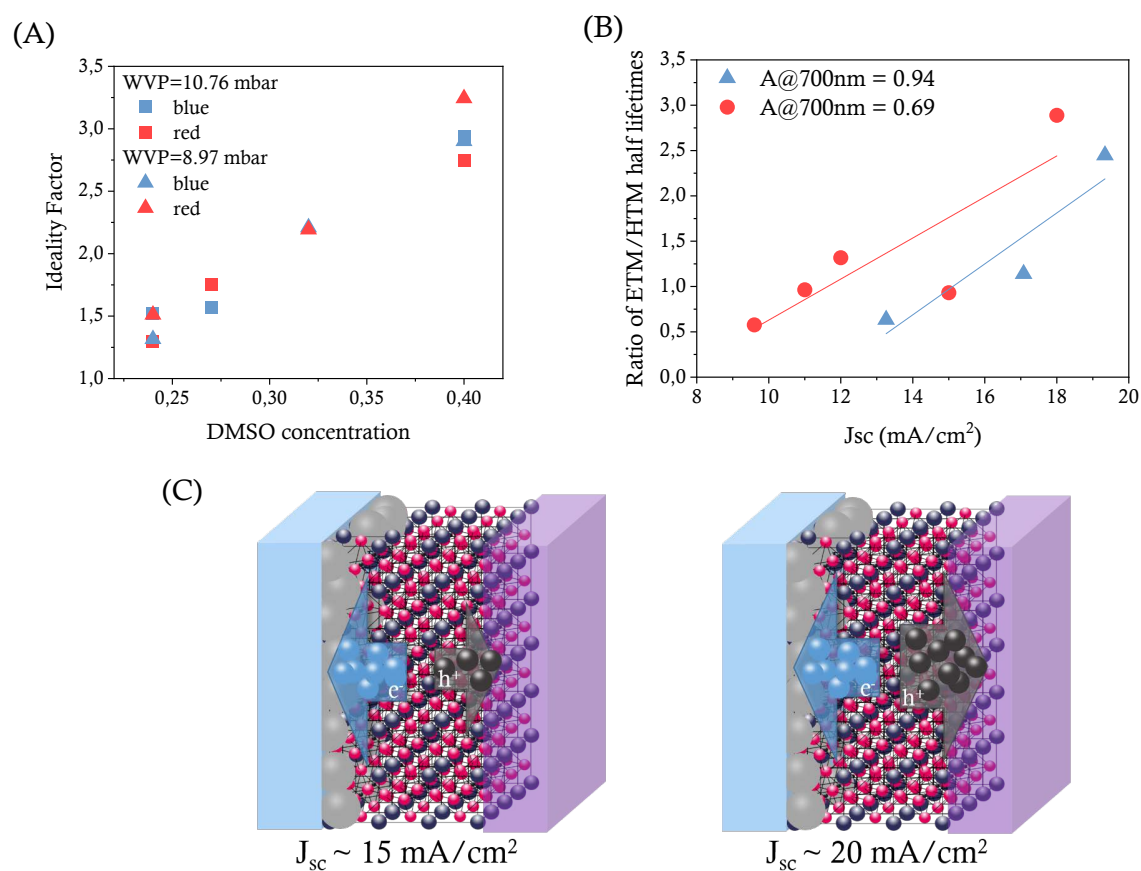
Figure 38 A – Ideality factor vs DMSO concentration in precursor solution, obtained from the EIS measurements with blue or red light for cells prepared under two different WVP conditions. B – ratio of ETM/HTM half lifetimes for cells with different perovskite thickness and different photocurrent. C – schematic picture of the presented findings.

KPB-6

Impact of improvements in mesoporous titania layers on ultrafast electron transfer dynamics in perovskite and dye-sensitized solar cells

The article is focused on improvement in the PSCs and DSSCs performance upon modifications of mesoporous titania layer, investigated using femtosecond transient absorption. The PSCs cells were made of a triple-cation perovskite (the same as in KPB-5), spiro-OMeTAD and two different titania layers: a commonly used one, optimized of about $150 - 200$ nm in thickness (made of 30 nm nanoparticles, called **SC30dil**) and a homogenous layer $300 - 350$ nm thick (made of 18 nm nanoparticles, called **SC18dil**), with poor homogeneity. The **SC30dil** exhibited the efficiency ~18 % (J_{sc} ~24 mA/cm^2, relative photocurrent ~100 %), while **SC18dil** only 11 % (J_{sc} ~17 mA/cm^2, relative photocurrent ~70 %).

Results of the TA experiments of the PSCs excited from the ETM and the HTM side (as conducted in KPB-5) were globally fitted by a 3-exponential decay function. Charge cooling constant rate (τ_1=0.3 ps) was the same for both **SC18dil** and **SC30dil** samples. Two longer-time components, describing charge population decay were always shorter for **SC30dil** samples from both sides. A simpler 2-exponential global fit was also performed, giving mean values collected in Table 2. **SC30dil** cells show faster decays, especially from the ETM side, where the charge carrier dynamics is governed mostly by injection to the titania layer. It indicates that faster electron injection to the optimized TiO_2 is responsible for the higher photocurrent in the studied cells.

Table 3 Averaged values of longer time component from 2-exponential global analysis of PSCs TA data for different excitation sides.

TiO$_2$ layer	Excitation side	τ_{AVG} [ns] error: ± 0.1 ns
SC30dil	ETM	1.9
	HTM	2.5
SC18dil	ETM	3.3
	HTM	3.3

The KPB-5 article revealed that photoexcited charge carrier dynamic is not uniform within the whole perovskite layer, which was further explored in the KPB-6. Additional, red-shifted spectral features were observed in the TA experiments from ETM side. The probable explanation is that the photoinduced ion segregation leads to different concentrations of iodide and bromide ions close to the perovskite interfaces. In the study, the **SC30dil** bleach signal at 100 ps was collected and compared in subsequent cycles of the TA experiment (Figure 39B – C) from the ETM and the HTM sides. Only at the ETM side a shift and decrease in the bleach signal was observed.

The cell with the lower photocurrent (**SC18dil**) as well as **SC30dil** passivated by organic dye (MK2) did not show above changes. The study of this phenomenon was continued and presented in the next paper (KPB-7).

(A)

SC30dil   SC18dil

(B)   (C)
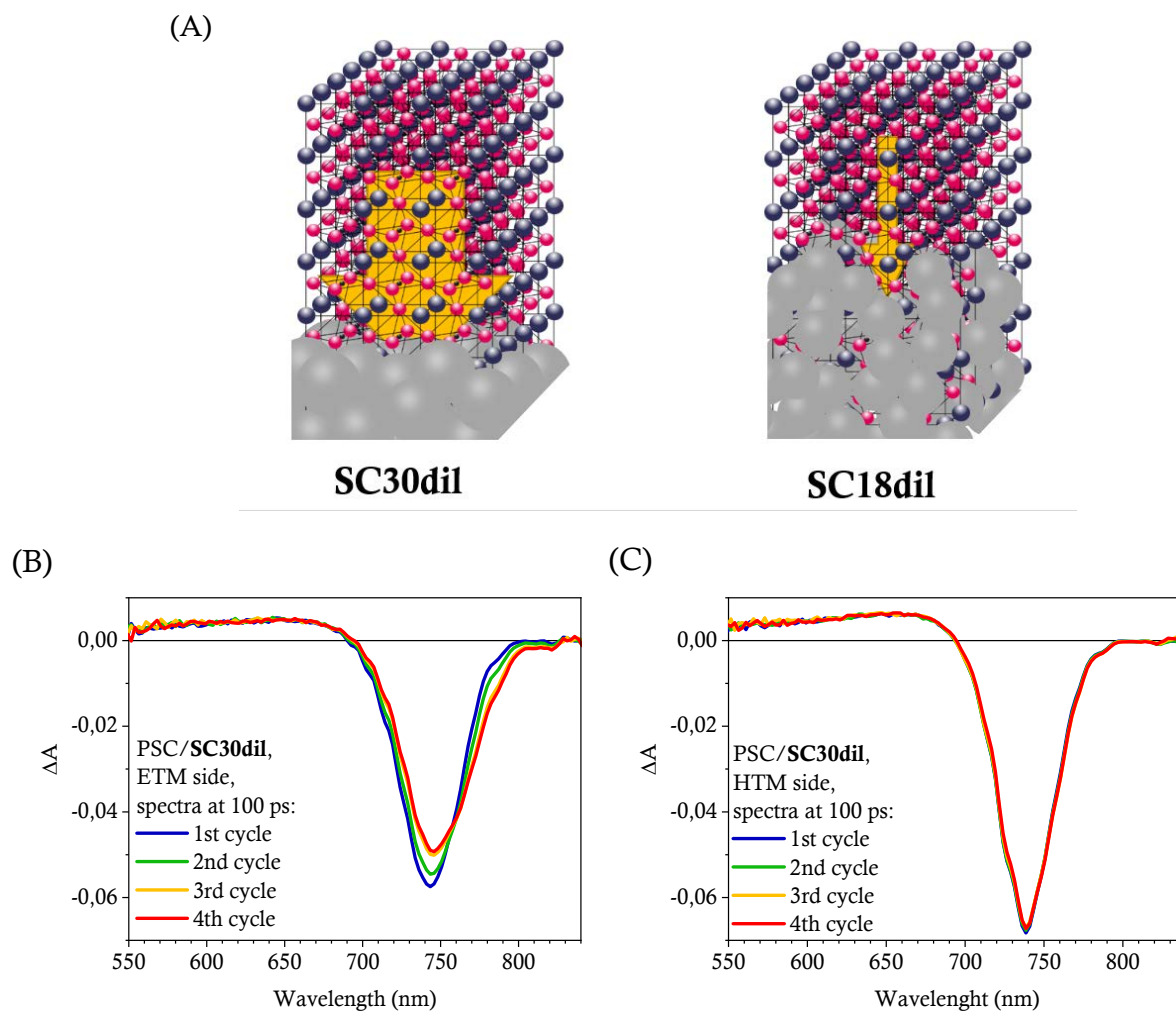
Figure 39 A – Schematic picture of the presented study. B,C – femtosecond transient absorption signal at 100 ps for excitation from the ETM (B) and the HTM side (C) for subsequent scans in the experiment.

Complete perovskite solar cells with gold electrodes studied in the visible and near-infrared range

The last article presents spectroscopic results for the same triple-cation perovskite as in the previous two works in complete PSCs. It shows a novel approach to the TA study, which is an experiment with the applied potential (through the gold electrode at HTM side) and additional 1Sun illumination, schematically shown in Figure 40A. It allows the TA investigation of charge carrier dynamics upon conditions close to the working conditions of the cell.
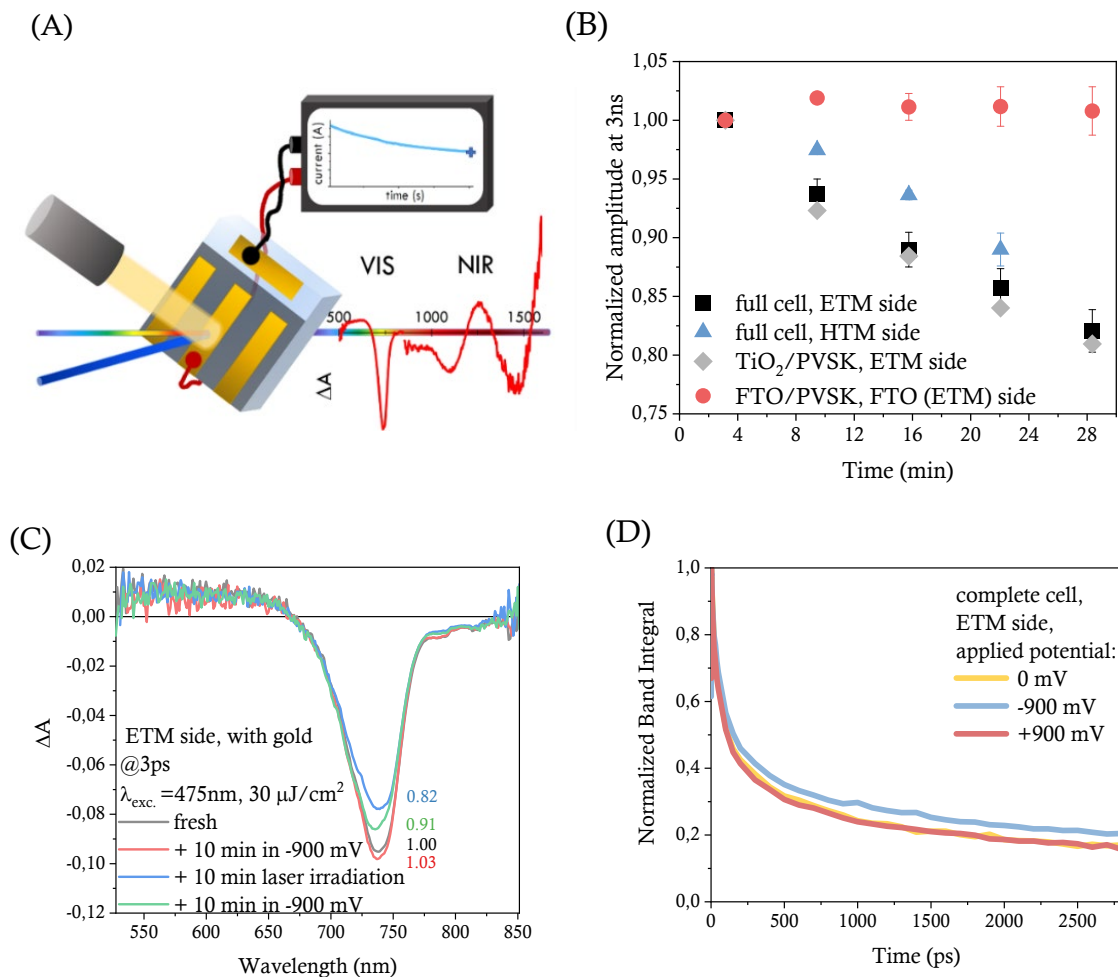
Figure 40 A – Schematic presentation of the study (TOC from the article) B – Normalized amplitude at 3 ns over experiment time for different samples, C – the TA signal at 3 ps for complete PSC under different conditions excited from the ETM side, D – Normalized band integral kinetics for complete PSCs with different applied potential.

Gold electrode effect was studied by the stationary and transient absorption spectroscopy. It was shown that light suppress in a 50 nm gold layer, at 750 nm (TA bleach position) is about 50 – 60 %, which allows a decent noise-to-signal ratio. The gold layer does not show a significant TA signal (50 times smaller than the perovskite bleach amplitude).

The SEM images, on a fresh layer and after 80 days, revealed that the gold layer was smooth just after deposition but changed into a layer of $100 - 140$ nm gold islands with time. Such changes reduce the conductivity of the layer, so they can be the cause of reduced efficiency of the aged cells.

Although, a gold layer TA signal is insignificant, it causes appearance of a new positive absorption signal around $770 - 840$ nm when excited from HTM side, whereas for the cells without gold, the signal is negative due to stimulated emission. The band exhibits also different kinetics than that in the corresponding spectral range for the cells without gold. This phenomenon can be explained by assuming that gold layer suppresses the perovskite stimulated emission caused by the plasmonic effects or by the gold layer enhancement of the absorption coefficient of spiro-OMeTAD.

The TA signal of the PSCs in the NIR region was either reported to be dominated by interference (caused by refractive index changes due to photoexcited carriers) [49], [50] or as dominated by the oxidized HTM materials (e.g., spiro-OMeTAD at 1500 nm) [71]. In this study, we clarified that, despite the domination of the interference signal, the signal from the oxidized spiro-OMeTAD can be also detected. It is manifested as a rise up to 30 ps of the kinetics above 1200 nm from the HTM side, while for the ETM side only the decay is observed.

The experiments with illumination revealed that the red-shift of the long-wavelength absorption band edge upon 1Sun illumination is accompanied by a drop in photocurrent. Reverse, partial changes of TA spectral signal were observed when after illumination the samples were kept in the dark.

The effect of long laser illumination on the TA signal (bleach amplitude) in PSCs, briefly described in KPB-6, was more deeply analyzed. The TA experiments with several scans numbers were performed on complete cells as well as on the samples with excluded particular layers. For the ETM side, the bleach signal was red-shifted, widened and vanished over time. A possible explanation of the red-shift and widening is the rearrangement of ions in the perovskite structure. The bleach amplitude decreases by about 20 % after 35 min for the samples with a TiO_2 layer, excited from the ETM side (complete cell and TiO_2/PVSK, Figure 40B). The complete cell excited from the HTM side exhibits a smaller drop in the bleach amplitude, while for the samples without a TiO_2 layer, the bleach amplitude does not decrease at all, irrespective of the excitation side. It confirmed the findings published for $MAPbI_{1.5}Br_{1.5}$ that only charge extraction by TiO_2 causes ion segregation [72]. Time constants obtained from multi-exponential global analysis showed that except for the fastest-time component, all time constants are lower upon irradiation of the sample with TiO_2, which indicates that the electron injection or/and charge recombination accelerate with increase of ion rearrangement.

Results of investigation on the relation between irradiation with femtosecond laser to that of irradiation with 1Sun on TA results were checked and revealed that the laser pulses at 475 nm, fluence 30 μJ/cm^2 and repetition rate 500 Hz lead to approximately the same decrease in the bleach

signal as the continuous 1Sun illumination, i.e., a reduction of the signal by about 15 % after 25 min.

Finally, thanks to the measurements of the complete cells with gold electrodes, the effect of applied potential during TA experiment was studied. It revealed that the reverse current flow (realized by applied voltage bias of -900 mV in the dark) can reverse the TA bleach signal long-term changes, described above (Figure 40C).

Moreover, application of a bias close to V_{oc} (-900 mV) under irradiation means that almost no current flows through the sample so the charge injection to the contacts is suppressed. Indeed, we observed that bleach band under such applied voltage decays slower than that at short circuit or positive voltage applied (Figure 40D), probably due to the lack of charge injections. Therefore, results of our research have opened the new way to investigate the ultrafast processes in PSCs under different working conditions.

5 SUMMARY

My thesis is based on a series of seven scientific articles. It describes the study of perovskite solar cells conducted from 2016 to 2021. During that time the cells fabricated in the laboratory in Poznań reached 18 % efficiency with small hysteresis, starting from a few percent and huge hysteresis in 2016, when I started to fabricate and study them. Figure 41 shows photos of the cells prepared in 2016 and 2021, highlighting the evolution of the solar cell construction.
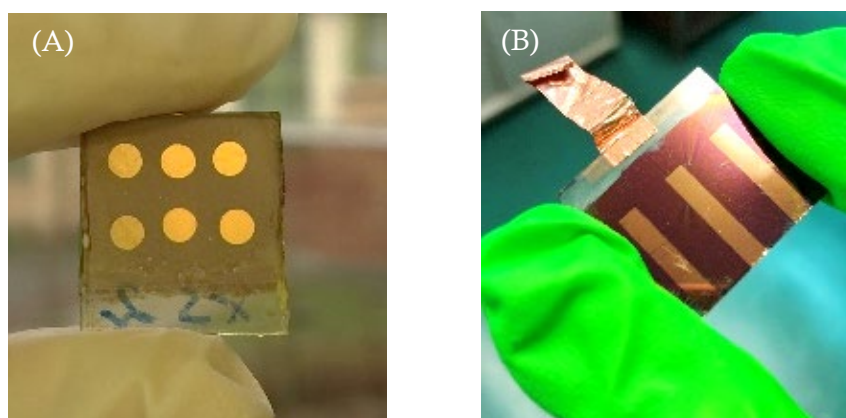
Figure 41 Photos of the PSCs prepared in 2016 (A) and 2021 (B) at the Faculty of Physics, Adam Mickiewicz University, Poznań.

The perovskite material complexity varied from simple $MAPbI_3$ (presented in KPB-1 – KPB-3) through double cation, double halides mixture (($FAPbI_3)_{0.85}(MAPbBr_3)_{0.15}$, studied in KPB-4) up to triple cation, double halides composition ($FA_{0.76}MA_{0.16}Cs_{0.05}Pb(I_{0.81}Br_{0.19})_3$; investigated in KPB-5 – KPB-7).

Apart from the perovskite composition, the synthesis conditions were also changed. Precursor solutions were modified by using various $MAI:PbI_2$ molar ratio (KPB-1, KPB-2) or different DMF:DMSO ratio (KPB-5). The $MAI:PbI_2$ with excess (3:1, non-stoichiometric ratio) of PbI_2 gave the fastest photoexcited carriers decay (KPB-1, KPB-2). Different DMSO concentration in the precursor solutions does not influence ultrafast processes. However, it influences recombination on a greater time scale, changing recombination mechanism from bulk to surface with increase in the DMSO concentration (KPB-5).

We analyzed changes in synthesis conditions, i.e., under open air (with presence of humidity and oxygen, KPB-1, KPB-2, KPB-4, KPB-5) and under dry box conditions (KPB-4 – KPB-7). The best results were obtained for dry-box conditions (KPB-4, KPB-5). However, it has been shown that triple-cation perovskite can be fabricated with high efficiency under ambient room conditions (KPB-5).

Different PSCs structures were investigated, i.e., normal mesoporous (KPB-1, KPB-2, KPB-4 – KPB-7) and planar inverted (KPB-3). Different hole and electron transporting material were used in PSCs, i.e., HTMs: spiro-OMeTAD (KPB-1, KPB-2, KPB-4 – KPB-7), X60 (KPB-1), PEDOT:PSS (KPB-3), ETMs: different quality TiO_2 (KPB-1, KPB-2, KPB-4 – KPB-7), PCBM, SPPO16 and PenPTC (KPB-3). Spiro-OMeTAD exhibits faster electron transfer than X60, but also faster interfacial recombination (KPB-1). The best mesoporous TiO_2 layer for PSCs is a homogenous, 150 – 200 nm layer with 30-nm size nanoparticles. It provided the best perovskite quality and extraction properties (shorter lifetime of the photoexcited charge carriers, KPB-4, KPB-6). The best studied ETM for inverted PSCs was PCBM, exhibiting the highest efficiency and first order rate constant (k_1). The PenPTC has exhibited lower k_1 along with lower efficiency than PCBM. The SPPO16 with the negligible current indicated the smallest k_1 value from those three (KPB-3).

The above combinations of conditions allowed investigation of charge transport in perovskite material with different modifications (KPB-2, KPB-4, KPB-5) and together with selective transporting material (KPB-1, KPB-3, KPB-6) of different qualities or chemical compositions. We also introduced changes in the PSCs by physical, instead of chemical interactions: application of potential bias or additional 1Sun illumination in the experiments (KPB-7).

Based on the research presented in the thesis, the following, general conclusions on charge transport in perovskite material can be drawn.

The higher the efficiency of the PSC, the shorter the time constants of the photoexcited charge carrier decay, assigned to the dynamics of the charge transport to selective transporting material (KPB-3 – KPB-6). It should be stressed that these findings made for complete cells with ETM and HTM materials are in contrast to those observed in isolated perovskite, when longer decay usually means fewer trap states and better quality of perovskite crystals. The differences in the hole and electron dynamics are distinguishable (KPB-5 – KPB-7), moreover photoinduced kinetic and spectral changes are observed close to TiO_2/perovskite interface (KPB-6 – KPB-7).

Examination of incomplete PSCs (without a particular layer or layers) by time-resolved laser spectroscopy (pulsed laser illumination) can be useful in determination of the charge transport dynamics. However, in order to analyze the cell in the working conditions, additional 1Sun illumination and applied potential should be provided (KPB-7) for complete cells with deposited metal electrodes.

The transient bleach signal changes with increasing pump energy density: i.e., shift and widening in the spectral domain and a faster decay in the temporal domain are observed (KPB-2, KPB-3, KPB-5, KPB-7). In some cases, the bleach signal can be outcompeted by the transient reflection signal (KPB-2).

Moreover, optical interference on thin layers can influence the TA spectra (KPB-7). The additional short-wavelength bleach signal exhibits different behavior than the long-wavelength one (KPB-1, KPB-2).

Furthermore, the correct conclusions from the time-resolved studies should be based on proper kinetics analysis: singular value decomposition global analysis is better than single-wavelength kinetics, but it is the band integral analysis that should be performed in order to obtain the proper, complete kinetics of charge carrier decay. In order to characterize the kinetics, the simple half-lifetime (KPB-4, KPB-5), multi-exponential function (KPB-1 – KPB-3, KPB-5 – KPB-7), stretched exponential function (KPB-1, KPB-2, KPB-5) and, the most appropriate, mixed first and second order model (KPB-3 – KPB-5) can be used. Moreover, due to wide spread of kinetics of perovskite samples, it is important to provide statistically significant number of experiments (KPB-1 – KPB-7).

I hope that my contribution to the knowledge of charge transport in perovskite solar cells will help to understand and further develop non-carbon-emissive electric current sources.

LIST OF REFERENCES

[1]   IPCC, *Technical Summary. Contribution of Working Group I to the Sixth Assessment Report of the Intergovernmental Panel on Climate Change*. 2021.

[2]   H. Ritchie, "Sector by sector: where do global greenhouse gas emissions come from?", 2020. [Online]. Available: https://ourworldindata.org/ghg-emissions-by-sector, Access date: 23.06.2022.

[3]   DNV, "Energy Transition Outlook 2021", 2022. [Online]. Available: https://eto.dnv.com/2021/highlights/energy-transition-outlook, Access date: 23.06.2022.

[4]   B. Weston, "Apparatus for utilizing solar radiant energy", US389124A, 1888.

[5]   M. L. Severy, "Apparatus for mounting, and operating thermopiles", US527377A, 1894.

[6]   M. Severy, "Apparatus for generating electricity by solar heat", US527379A, 1894.

[7]   D. M. Chapin, C. S. Fuller, and G. L. Pearson, "A new silicon p-n junction photocell for converting solar radiation into electrical power", *J. Appl. Phys.*, vol. 25, no. 5, pp. 676–677, 1954.

[8]   National Renewable Energy Laboratory, "Best Research Cell Efficiencies Chart," 2022. [Online]. Available: https://www.nrel.gov/pv/cell-efficiency.html, Access date: 23.06.2022.

[9]   J. Y. Kim, J. W. Lee, H. S. Jung, H. Shin, and N. G. Park, "High-Efficiency Perovskite Solar Cells", *Chem. Rev.*, vol. 120, no. 15, pp. 7867–7918, 2020.

[10]   J. H. Noh, S. H. Im, J. H. Heo, T. N. Mandal, and S. Il Seok, "Chemical management for colorful, efficient, and stable inorganic-organic hybrid nanostructured solar cells", *Nano Lett.*, vol. 13, no. 4, pp. 1764–1769, 2013.

[11]   G. E. Eperon, S. D. Stranks, C. Menelaou, M. B. Johnston, L. M. Herz, and H. J. Snaith, "Formamidinium lead trihalide: a broadly tunable perovskite for efficient planar heterojunction solar cells", *Energy Environ. Sci.*, vol. 7, no. 3, p. 982, 2014.

[12]   N. J. Jeon *et al.*, "Compositional engineering of perovskite materials for high-performance solar cells", *Nature*, vol. 517, no. 7535, pp. 476–480, 2015.

[13]   M. A. Green, K. Emery, Y. Hishikawa, W. Warta, and E. D. Dunlop, "Solar cell efficiency tables (version 48)", *Prog. Photovoltaics Res. Appl.*, vol. 24, no. 7, pp. 905–913, 2016.

[14]   M. Saliba *et al.*, "Cesium-containing triple cation perovskite solar cells: improved stability, reproducibility and high efficiency", *Energy Environ. Sci.*, vol. 9, pp. 1989–1997, 2016.

[15]   Y. Hu *et al.*, "Understanding the Role of Cesium and Rubidium Additives in Perovskite Solar Cells: Trap States , Charge Transport , and Recombination", *Adv. Energy Mater.*, vol. 1703057, no. 16, pp. 1–11, 2018.

[16]   J. M. Chem, M. Konstantakou, and T. Stergiopoulos, "A critical review on tin halide perovskite solar cells", *J. Mater. Chem. A*, vol. 5, no. 23, pp. 11518–11549, 2017.

[17]   M. Lyu *et al.*, "Organic-inorganic bismuth(III)-based material: a light-absorber beyond organolead perovskites", *Nano Res.*, vol. 9, no. 3, pp. 692–702, 2016.

[18]   M. Wang *et al.*, *Lead-Free Perovskite Materials for Solar Cells*, vol. 13, no. 1. Springer Singapore, 2021.

[19]   Q. Chen *et al.*, "Under the spotlight: The organic-inorganic hybrid halide perovskite for optoelectronic applications", *Nano Today*, vol. 10, no. 3, pp. 355–396, 2015.

[20]   Z. Hawash, L. K. Ono, and Y. Qi, "Recent Advances in Spiro-MeOTAD Hole Transport Material and Its Applications in Organic–Inorganic Halide Perovskite Solar Cells", *Adv. Mater. Interfaces*, vol. 5, no. 1, 2018.

[21]   F. Behrouznejad, S. Shahbazi, N. Taghavinia, H. P. Wu, and E. Wei-Guang Diau, "A study on utilizing different metals as the back contact of $CH_3NH_3PbI_3$ perovskite solar cells", *J. Mater. Chem. A*, vol. 4, no. 35, pp. 13488–13498, 2016.

[22]   H.-S. Kim *et al.*, "Lead Iodide Perovskite Sensitized All-Solid-State Submicron Thin Film Mesoscopic Solar Cell with Efficiency Exceeding 9%", *Sci. Rep.*, vol. 2, no. 1, p. 591, 2012.

[23]   M. M. Lee, J. Teuscher, T. Miyasaka, and H. J. Snaith, "Efficient Hybrid Solar Cells Based on Meso-Superstructured Organometal Halide Perovskite", *Science*, vol. 338, pp. 643–647, 2012.

[24]   D. Li *et al.*, "A Review on Scaling Up Perovskite Solar Cells", *Adv. Funct. Mater.*, vol. 31, no. 12, pp. 1–27, 2021.

[25]   S. Li, Y. L. Cao, W. H. Li, and Z. S. Bo, "A brief review of hole transporting materials commonly used in perovskite solar cells", *Rare Met.*, vol. 40, no. 10, pp. 2712–2729, 2021.

[26]   L. Xu *et al.*, "Inverted perovskite solar cells employing doped NiO hole transport layers: A review", *Nano Energy*, vol. 63, no. July, p. 103860, 2019.

[27]   A. Andersson, N. Johansson, P. Bröms, N. Yu, D. Lupo, and W. R. Salaneck, "Fluorine tin oxide as an alternate to indium tin oxide in polymer LEDs", *Adv. Mater.*, vol. 10, no. 11, pp. 859–863, 1998.

[28]   K. Mahmood, S. Sarwar, and M. T. Mehran, "Current status of electron transport layers in perovskite solar cells: materials and properties", *RSC Adv.*, vol. 7, no. 28, pp. 17044–17062, 2017.

[29]   X. Lin *et al.*, "Efficiency progress of inverted perovskite solar cells", *Energy Environ. Sci.*, vol. 13, no. 11, pp. 3823–3847, 2020.

[30]   J. Nelson, *The physics of solar cells*. World Scientific Publishing Co Pte Ltd, 2003.

[31]   R. P. Feynman, *The Feynman Lectures on Physics*. Addison-Wesley, 2005.

[32]   E. Raoult *et al.*, "Optical Characterizations and Moddeling of Semitransparent Perovskite Solar Cells for Tandem Applications", in *36th European Photovoltaic Solar Energy Conference and Exhibition, Marseille, France*, 2019, vol. 36, pp. 757–763.

[33]   H. Jin *et al.*, "It's a trap! on the nature of localised states and charge trapping in lead halide perovskites", *Mater. Horizons*, vol. 7, no. 2, pp. 397–410, 2020.

[34]   A. J. Knight and L. M. Herz, "Preventing phase segregation in mixed-halide perovskites: A perspective", *Energy Environ. Sci.*, vol. 13, no. 7, pp. 2024–2046, 2020.

[35]   J. Shi *et al.*, "From Ultrafast to Ultraslow: Charge-Carrier Dynamics of Perovskite Solar Cells", *Joule*, vol. 2, no. 5, pp. 879–901, 2018.

[36]   C. Li *et al.*, "Insights into Ultrafast Carrier Dynamics in Perovskite Thin Films and Solar Cells", *ACS Photonics*, vol. 7, no. 8, pp. 1893–1907, 2020.

[37]   J. Peng, Y. Chen, K. Zheng, T. Pullerits, and Z. Liang, "Insights into charge carrier dynamics in organo-metal halide perovskites: From neat films to solar cells", *Chem. Soc. Rev.*, vol. 46, no. 19, pp. 5714–5729, 2017.

[38]   C. M. Wolff *et al.*, "Orders of Recombination in Complete Perovskite Solar Cells – Linking Time-Resolved and Steady-State Measurements", *Adv. Energy Mater.*, vol. 11, no. 45, 2021.

[39]   T. W. Crothers *et al.*, "Photon Reabsorption Masks Intrinsic Bimolecular Charge-Carrier Recombination in $CH_3NH_3PbI_3$ Perovskite", *Nano Lett.*, vol. 17, no. 9, pp. 5782–5789, 2017.

[40]   M. Zhou, J. S. Sarmiento, C. Fei, and H. Wang, "Charge Transfer and Diffusion at the Perovskite/PCBM Interface Probed by Transient Absorption and Reflection", *J. Phys. Chem. C*, vol. 123, no. 36, pp. 22095–22103, 2019.

[41]   M. Saliba *et al.*, "How to Make over 20% Efficient Perovskite Solar Cells in Regular (n − i − p) and Inverted (p − i − n) Architectures", *Chem. Mater.*, vol. 30, pp. 4193–4201, 2018.

[42] M. Wacławek and T. Rodzeiewicz, *Ogniwa słoneczne wpływ środowiska naturalnego na ich pracę*. Wydawnictwo Naukowo-Techniczne, 2011.

[43] H. W. Chen, N. Sakai, M. Ikegami, and T. Miyasaka, "Emergence of hysteresis and transient ferroelectric response in organo-lead halide perovskite solar cells", *J. Phys. Chem. Lett.*, vol. 6, no. 1, pp. 164–169, 2015.

[44] F. Wu, R. Pathak, and Q. Qiuo, "Origin and alleviation of *J-V* hysteresis in perovskite solar cells: A short review", *Catal. Today*, vol. 374, pp. 86–101, 2021.

[45] G. Palma, L. Cozzarini, E. Capria, and A. Fraleoni-Morgera, "A home-made system for IPCE measurement of standard and dye-sensitized solar cells", *Rev. Sci. Instrum.*, vol. 86, no. 1, 2015.

[46] M. Drozdowski, *Spektroskopia ciała stałego*. Wydawnicto Politechniki Poznańskiej, 1996.

[47] D. McMullan, "Scanning electron microscopy 1928–1965", *Scanning*, vol. 17, no. 3, pp. 175–185, 1995.

[48] R. Naskręcki, *Femtosekundowa spektroskopia absorpcji przejsciowej*. Wydawnictwo Naukowe UAM, 2000.

[49] H. P. Pasanen, P. Vivo, L. Canil, A. Abate, and N. Tkachenko, "Refractive index change dominates the transient absorption response of metal halide perovskite thin films in the near infrared", *Phys. Chem. Chem. Phys.*, vol. 21, no. 27, pp. 14663–14670, 2019.

[50] H. P. Pasanen *et al.*, "Monitoring Charge Carrier Diffusion across a Perovskite Film with Transient Absorption Spectroscopy", *J. Phys. Chem. Lett.*, vol. 11, no. 2, pp. 445–450, 2020.

[51] C. Kulshreshtha, A. Clement, T. Pascher, V. Sundström, and P. Matyba, "Investigating ultrafast carrier dynamics in perovskite solar cells with an extended π-conjugated polymeric diketopyrrolopyrrole layer for hole transportation", *RSC Adv.*, vol. 10, no. 11, pp. 6618–6624, 2020.

[52] G. Grancini *et al.*, "Femtosecond Charge-Injection Dynamics at Hybrid Perovskite Interfaces", *ChemPhysChem*, vol. 18, no. 17, pp. 2381–2389, 2017.

[53] B. Anand *et al.*, "Broadband transient absorption study of photoexcitations in lead halide perovskites: Towards a multiband picture", *Phys. Rev. B*, vol. 93, no. 16, pp. 1–5, 2016.

[54] G. Xing *et al.*, "Long-Range Balanced Electron- and Hole-Transport Lengths in Organic-Inorganic $CH_3NH_3PbI_3$", *Science*, vol. 342, no. 6156, pp. 344–347, 2013.

[55] K. G. Stamplecoskie, J. S. Manser, and P. V. Kamat, "Dual nature of the excited state in organic–inorganic lead halide perovskites", *Energy Environ. Sci.*, vol. 8, no. 1, pp. 208–215, 2015.

[56] J. A. Christians, J. S. Manser, and P. V. Kamat, "Best practices in perovskite solar cell efficiency measurements. Avoiding the error of Making Bad Cells Look Good", *J. Phys. Chem. Lett.*, vol. 6, no. 5, pp. 852–857, 2015.

[57] T. Du, C. H. Burgess, J. Kim, J. Zhang, J. R. Durrant, and M. A. McLachlan, "Formation, location and beneficial role of PbI_2 in lead halide perovskite solar cells", *Sustain. Energy Fuels*, vol. 1, no. 1, pp. 119–126, 2017.

[58] L. Wang, C. McCleese, A. Kovalsky, Y. Zhao, and C. Burda, "Femtosecond time-resolved transient absorption spectroscopy of $CH_3NH_3PbI_3$ perovskite films: Evidence for passivation effect of PbI_2", *J. Am. Chem. Soc.*, vol. 136, no. 35, pp. 12205–12208, 2014.

[59] S. Narra, E. Jokar, O. Pearce, C. Y. Lin, A. Fathi, and E. W. G. Diau, "Femtosecond Transient Absorption Spectra and Dynamics of Carrier Relaxation of Tin Perovskites in the Absence and Presence of Additives", *J. Phys. Chem. Lett.*, vol. 11, no. 14, pp. 5699–5704, 2020.

[60] J. S. Beckwith, C. A. Rumble, and E. Vauthey, "Data analysis in transient electronic spectroscopy–an experimentalist's view", *Int. Rev. Phys. Chem.*, vol. 39, no. 2, pp. 135–216, 2020.

[61] X. Li *et al.*, "A vacuum flash-assisted solution process for high-efficiency large-area perovskite solar cells", *Science*, vol. 353, no. 6294, pp. 58–62, 2016.

[62] S. A. Kovalenko, R. Schanz, V. M. Farztdinov, H. Hennig, and N. P. Ernsting, "Femtosecond relaxation of photoexcited para-nitroaniline: Solvation, charge transfer, internal conversion and cooling", *Chem. Phys. Lett.*, vol. 323, no. 3–4, pp. 312–322, 2000.

[63] J. R. Lakowicz, *Principles of Fluorescence Spectroscopy*. Plenum Press, New York, 1983.

[64] R. Chen, "Apparent stretched-exponential luminescence decay in crystalline solids", *J. Lumin.*, vol. 102–103, no. SPEC, pp. 510–518, 2003.

[65] A. Lasia, *Electrochemical Impedance Spectroscopy and Its Applications, Modern Aspects of Electrochemistry*. Springer, 1999.

[66] E. Von Hauff and D. Klotz, "Impedance spectroscopy for perovskite solar cells: Characterisation, analysis, and diagnosis", *J. Mater. Chem. C*, vol. 10, no. 2, pp. 742–761, 2022.

[67] A. Todinova, L. Contreras-Bernal, M. Salado, and S. Ahmad, "Towards a Universal Approach for the Analysis of Impedance Spectra of Perovskite Solar Cells : Equivalent Circuits and Empirical Analysis", pp. 1–12, 2017.

[68] P. Caprioglio *et al.*, "On the Origin of the Ideality Factor in Perovskite Solar Cells", *Adv. Energy Mater.*, vol. 10, no. 27, pp. 1–9, 2020.

[69] K. Pydzińska *et al.*, "Determination of Interfacial Charge-Transfer Rate Constants in Perovskite Solar Cells", *ChemSusChem*, vol. 9, no. 13, pp. 1647–1659, 2016.

[70] J. Leng, "Artifacts in Transient Absorption Measurements of Perovskite Films Induced by Transient Reflection from Morphological Microstructures", no. 10, pp. 97–101, 2019.

[71] M. E. F. Bouduban, A. Burgos-Caminal, R. Ossola, J. Teuscher, and J. E. Moser, "Energy and charge transfer cascade in methylammonium lead bromide perovskite nanoparticle aggregates", *Chem. Sci.*, vol. 8, no. 6, pp. 4371–4380, 2017.

[72] J. T. Dubose and P. V. Kamat, "TiO$_2$-Assisted Halide Ion Segregation in Mixed Halide Perovskite Films", *J. Am. Chem. Soc.*, vol. 142, no. 11, pp. 5362–5370, 2020.

FULL TEXT OF PUBLICATIONS

CONSTITUTING THE THESIS
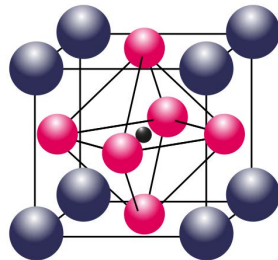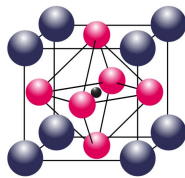
KPB-1

Effects of different small molecule hole transporters on the performance and charge transfer dynamics of perovskite solar cells

K.Pydzińska, P. Florczak, G.Nowaczyk, M.Ziółek

Contents lists available at ScienceDirect

Synthetic Metals

journal homepage: www.elsevier.com/locate/synmet
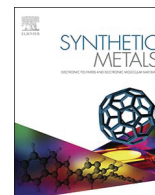
Research paper

Effects of different small molecule hole transporters on the performance and charge transfer dynamics of perovskite solar cells

Katarzyna Pydzińska[a], Patryk Florczak[b], Grzegorz Nowaczyk[b], Marcin Ziółek[a],[*]

[a] Faculty of Physics, Adam Mickiewicz University in Poznań Umultowska 85, 61-614 Poznań, Poland
[b] NanoBioMedical Centre, Adam Mickiewicz University in Poznań, Umultowska 85, 61-614 Poznań, Poland

ARTICLE INFO

ABSTRACT

Perovskite solar cells with popular 2,2′,7,7′-tetrakis(N,N-di-p-methoxyphenylamine)-9,9′-spirobifluorene (spiro-OMeTAD) as the hole transporting material are compared to those prepared with 2,2′,7,7′-tetrakis(N,N-di(4-methoxyphenyl)amino)-spiro-(fluorene-9,9′-xanthene) (X60), its recently proposed new and potentially cheaper alternative, and with a mixture of both materials. The cells with both small-molecule transporters have similar photocurrent and photovoltage, but the cells with X60 exhibit about 13% smaller fill factor than those with spiro-OMeTAD. The dynamics of the interfacial charge transfer occurring on the time scales from femtoseconds to seconds is explored. The overall hole injection is slower from methylammonium lead iodide to X60 than that to spiro-OMeTAD by about 0.04 ns^{-1}. Similarly, slower hole recombination is found for the cells with X60, taking place on the millisecond time scale in the dark. The recombination under illumination is accelerated more for ×60 material, which might explain the differences in fill factor values. The cells with the 1:1 mixture of spiro-OMeTAD and X60 show intermediate behavior in all aspects, revealing that a simple combination of small molecule transporters can be used to tune the properties of HTM.

1. Introduction

Perovskite solar cells (PSC) have been recently the most intensely developed ones from among the emerging photovoltaic systems. The best sunlight conversion efficiencies of PSC have grown exceptionally fast in the latest few years, currently exceeding 22% (certified 22.1%) [1–3]. Among many prospective benefits of PSC, their potential low production costs are one of the most interesting [4,5]. However, not only perovskite material itself, but also the contact materials that extract and transport charges play crucial role in the operation and performance of PSC. The current champion devices use spiro-OMeTAD (2,20,7,70-tetrakis(N,N-di-p-methoxyphenylamine)-9,90-spirobifluorene, Fig. S1A in the Supporting information) as the hole transporting material (HTM) [2,3]. This material, belonging to small molecule hole transporters, is, however, very expensive due to complex synthetic route and purification. Therefore, one of the important points of interest in PSC studies is the search for alternative HTMs [6–10].

Very recently, a low-cost alternative to spiro-OMeTAD − 2,2′,7,7′-tetrakis(N,N-di(4-methoxyphenyl)amino)-spiro-(fluorene-9,9′-xanthene) − has been independently proposed by two different groups (Fig. S1B) [11,12]. This organic HTM, based on a spiro(fluorene-9,90-xanthene), has been denoted as X60 [11] or SFX-MeOTAD [12]. It has

been estimated that the costs of X60 are should be more than five times lower than those of the commonly used spiro-MeOTAD [12]. Therefore, this new spiro-type molecule is promising for large-scale industrial production, and a combination with state-of-the-art perovskite materials (mixed cation perovskite) yielded PSC of almost 20% efficiency [11], very close to that of the champion devices. According to our knowledge, apart from the initial articles [11,12], no other studies of PSC using X60 have been reported so far. Therefore, we decided to compare the performance of ×60 and spiro-OMeTAD in PSC using the standard perovskite material, methylammoinium lead iodide, MAPbI$_3$ (MA = CH$_3$NH$_3$). Besides, recently also the mixtures of spiro-OMeTAD and other organic and inorganic materials have been studied as HTM in order to improve the performance of PSC [13,14]. Therefore, we also checked the effect of using a mixture of spiro-OMeTAD and X60. We focus our attention on the simultaneous studies of basic photovoltaic parameters of PSC and time-resolved spectroscopy measurements of the charge dynamics over the entire time range in which the charges are transported. Thanks to the combination of broadband transient absorption with femtosecond laser system and electrochemical impedance studies, we were able to investigate the hole injection and recombination at the interface between MAPbI$_3$ and HTMs on the time scale from picoseconds to seconds.

[*] corresponding author.
E-mail address: marziol@amu.edu.pl (M. Ziółek).

It should be noted that such comprehensive studies of charge dynamics on different time scales and in complete PSC samples are still very rare. Recently, we have used such an approach to explain the worse performance of PSC made with inorganic CuSCN with respect to those made with spiro-OMeTAD [15]. The initial charge separation (on ns time scale) was observed to be by about 3 times faster for CuSCN system, but the worse photocurrent and photovoltage of this system was explained by the accompanying faster recombination on ms time scale [15]. It should be emphasized that the interpretation of both time-resolved laser spectroscopy and electrochemical impedance spectroscopy results is yet not generally accepted for PSC. In the former, there is still a fundamental controversy whether electron and hole injections from the perovskite to contact materials occur on sub-ps or ns time scale [16–19], as we shortly discussed in our previous paper [15]. In impedance spectroscopy, the assignment of each of the three characteristic response regions (low, mid and high frequency) is also not well established, and it is not clear which of these regions has direct influence on certain photovoltaic parameters [20–22]. Therefore, we believe that our present studies, besides the comparison between X60, spiro-OMeTAD and its mixture, will also bring some contribution to the understanding of the correlation of time-resolved spectroscopy results with the performance of PSC.

Finally, in the present contribution we also show, for the first time, our simplified approach to the preparation of PSC. Instead of using the glovebox, we made the cells under normal room conditions (with the presence of oxygen and moisture). As will be revealed, our cells show good stability and high charge separation efficiency, yet the sunlight conversion efficiency is limited by small thickness of the perovskite layer.

2. Materials and methods

2.1. Solar cell preparation

FTO glass (Sigma Aldrich, 2.2 mm thickness, 13 Ω/sq) was cleaned in soap solution, distilled water and ethanol for 15 min in each step. Then 0.34 M titanium isopropoxide ethanol solution was deposited by spin coating (2000 rpm, 60 s) onto FTO glass to obtain ~150 nm compact TiO_2 layer. After annealing at 100 °C, the water suspension of titanium dioxide nanoparticles (15–20 nm diameter, Solaronix) was spun (5000 rpm, 30s) into a compact layer giving ~100 nm mesoporous structure and then the photoanode was kept at 475 °C for 30 min. Additional ultrathin dense TiO_2 coating was deposited on top of the previous layer by dipping in 0.05 M $TiCl_4$ water solution (70 °C, 20 min) and annealing at 475 °C for 30 min. Perovskite layers were prepared using two different methods, the one- and two-step procedures. The precursor solutions were prepared and spin-coating was performed under normal room conditions (under the presence of oxygen and moisture with laboratory humidity 35–45%).

In the one-step methods, the precursor solution contained dissolved methylammonium iodide (MAI, Dyenamo) and lead iodide (PbI_2, 0.55 M or 1 M) or lead chlorine ($PbCl_2$, 1 M) in dimethylformamide (DMF). Concentration of precursors for one-step method was kept in stoichiometric (1:1) or non-stoichiometric (3:1) molar ratio for MAI:PbI_2 or MAI:$PbCl_2$ and are summarized in Table S1. The solution was spun (2000 rpm, 45 s for MAI:PbI_2 and 3000 rpm, 20 s for MAI:$PbCl_2$ solution) on formerly prepared electrodes and annealed at 100 °C in dry nitrogen flux until obtaining dark brown perovskite structure.

The two-step method consisted of sequential deposition of PbI_2 (0.55 M) in DMF and MAI (0.05 M) in 2-propanol solution. Firstly, PbI_2 (20 µl) was spun (6000 rpm, 5 s) on TiO_2 structure and kept at 40 °C for 3 min, next at 100 °C for 5 min, then MAI (300 µl) was applied and spin coated (4000 rpm, 20 s) after 40 s delay. After that the samples were annealed at 100 °C in dry nitrogen flux.

All HTMs (70 µl) were spin coated at 3000 rpm for 30s. To prepare HTM solutions in chlorobenzene, 4-*tert*-buthylpyridine (TBP, 28.8 µl/ml) and bis(trifluoromethylsulfonyl)imide lithium salt (Li-TFSI, 17.5 µl/ml of 520 mg/ml solution in acetonitrile) were added to spiro-OMeTAD (Sigma-Aldrich, 60 mM), X60 (Dyenamo, 60 mM) or their 1:1 vol mixture (60 mM). Finally, gold electrodes were deposited by sputtering using a mask with several 0.05 cm^2 apertures that defined the active surface of the cells.

2.2. Solar cells characterization

The current–voltage (J–V) curves and incident photon-to-current efficiency (IPCE) spectra were measured using Autolab M101 potentiostat coupled to a photoelectric spectrometer equipped with a solar simulator (Instytut Fotonowy − Photon Institute, Poland). The intensity was adjusted to provide 1Sun illumination (100 mW/cm^2) by using a xenon arc lamp with an AM 1.5G spectral filter and calibrated using a reference cell (15151, ABET). The J–V curves were recorded in two scan directions: "reverse mode" (scanning the potential from values higher than the open-circuit voltage to zero) and "forward mode" (scanning the potential in the opposite direction) at the scan rates 100 or 500 mVs^{-1}. IPCE data were collected in 400–850 nm range with a 10 nm step. The absorption spectra were obtained using a Jasco V-700 spectrophotometer equipped with 150 mm integrating sphere (LN-925). The sample cross sections were analyzed by using an Jeol 7001 TTLS field-emission scanning electron microscope (SEM) operating at 10 kV accelerating voltage.

The setup for ultrafast broadband transient absorption has been described before (Helios spectrometer, Ultrafast Systems, and Spectra Physics laser system) [23]. The instrument response function (IRF, pump–probe cross-correlation function) was about 200 fs (fullwidth at half-maximum (FWHM)) and transient absorption measurements were performed in the time range of up to 3 ns. An important modification of the transient absorption setup with respect to the standard, commercial configuration, was the use of a filter suppressing the residual 800 nm in the white light continuum before the sample, in order to avoid pump-and-dump artifacts [24,25]. Global analysis of the transient absorption data was performed by using the Surface Explorer software (Ultrafast Systems). It was used to fit a multiexponential function (convoluted with IRF) to the kinetic vectors of a selected number of singular values (excluding those due to noise). As a result of the analysis, the characteristic time constants were obtained as well as the wavelength-dependent amplitudes associated with them (also called decay-associated difference spectra or pre-exponential factor spectra).

Electrochemical impedance spectroscopy measurements were carried out in the dark or under 1Sun illumination. A response analyzer module (M101/FRA32 M, Autolab) was used to analyze the frequency response of the devices. For the measurements, a 10 mV voltage perturbation was applied over a frequency range of 10^{-1}–10^6 Hz (from the highest to the lowest). Zview (Scribner) was used for equivalent circuit modeling of the impedance spectra.

3. Results and discussion

3.1. Stationary absorption and photovoltaic parameters

Several SEM cross section images were used to estimate the thickness of all layers in PSC prepared by a two-step method. The exemplary picture is shown in Fig. 1A for the cell prepared by the two-step method. On average, the thicknesses were the following: 350 nm of fluorine-doped tin oxide, 50 nm of compact TiO_2, 250 nm of mixed mesoporous TiO_2 layer and perovskite, 200 nm of HTM and 100 nm of gold. Within experimental error, all thicknesses were the same for all HTMs studied.

The perovskite samples without deposited gold electrodes were investigated by stationary absorption measurements with integrating sphere (to include the effect of the light scattered by TiO_2
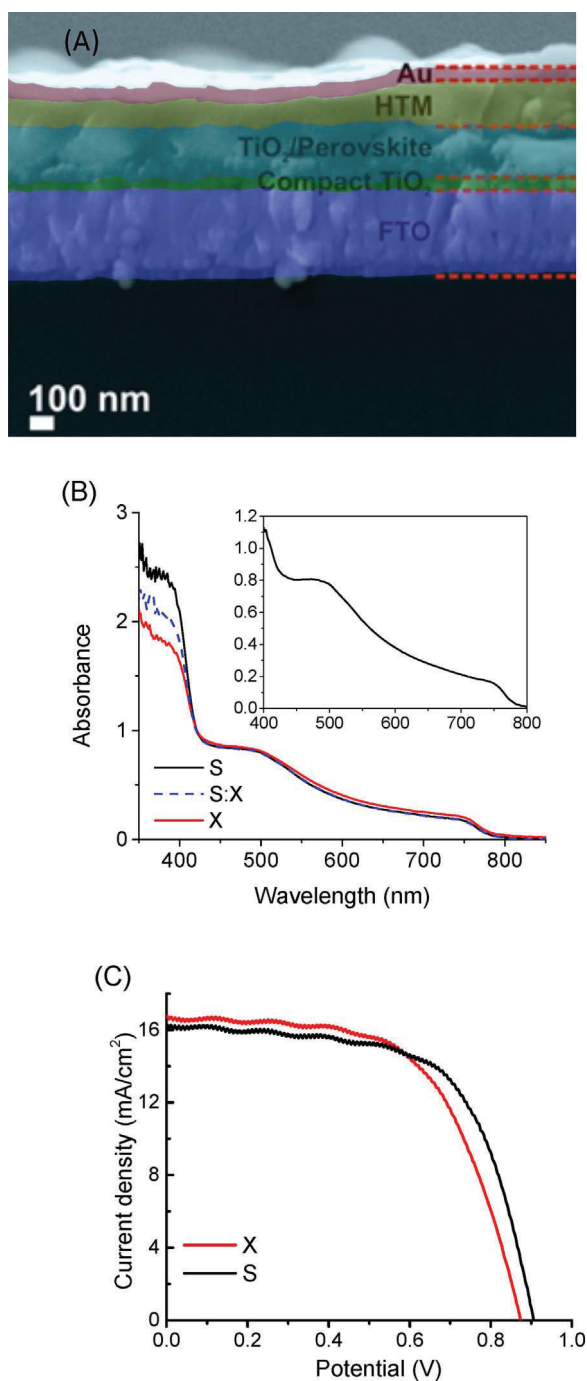
Fig. 1. (A) Scanning electron microscopy cross-section image of the cells prepared with spiro-OMeTAD as HTM. (B) Steady-state absorption spectra of S, S:X and X samples with perovskite obtained by the two-step preparation method after subtraction of TiO$_2$ contribution. The inset shows the absorption spectra after the subtraction of HTM and TiO$_2$ contribution used to calculate N_{ph}. (C) Current-voltage curves of the best perovskite cells based on X60 (**X**) and spiro-OMeTAD (**S**) obtained in the reverse scan at rate of 0.5 V/s.

nanoparticles), and with the baseline measured for TiO$_2$ layers subtracted (samples without perovskite and HTMs). Fig. 1B shows the representative spectra obtained for the sample produced by the two-step perovskite deposition method. The effect of different HTMs is visible below 410 nm: the sample with spiro-OMeTAD (abbreviated as **S**) exhibits higher absorbance (by about 0.5) than that with X60 (abbreviated as **X**), while the intermediate absorption is obtained for the HTMs mixture (spiro-OMeTAD:X60 at the volume ratio 1:1, abbreviated as **S:X**). It can be noted that absorption differences occur only in the

negligible region of 1Sun spectrum, therefore, they should not affect the performance of solar cells. The absorbance above 410 nm is the same for **S**, **X** and **S:X** samples, which confirms that the thickness and morphology of the perovskite layer is not affected by using different HTMs. The absorbance at 750 nm, near the excitonic edge of the perovskite, is about 0.2 for the two-step method, and it allows us to estimate the thickness of the perovskite layer by comparison with our previous report for MAPbI$_3$ (absorbance 0.5-0.6 for 400–500 nm perovskite thickness) [15]. Such an estimation gives the thickness of about 150 nm of the perovskite layer obtained by the two-step method in our current studies, and the measured absorbance and estimated perovskite thicknesses for the layers obtained by the other preparation methods are collected in Table S1. The 150 nm thickness of the perovskite layer produced by the two-step method is also in agreement with the thickness of common mesoporous TiO$_2$ and perovskite layer observed in SEM cross-sections (250 nm), taking into account that the mesoporous TiO$_2$ layer is about 100 nm thick (see Materials and methods section). The relatively small thickness of the perovskite (in comparison to the PSC of the best sunlight conversion efficiencies) is mainly dictated by the requirement of sufficiently transparent samples in transient absorption experiments. The stationary absorption data were also used to calculate the number of photons absorbed by the perovskite layer, N_{ph}, which will be used below to calculate the relative photocurrent of our cells. The value of N_{ph} was obtained from integration of stationary absorptance spectrum (after the subtraction of contributions of both TiO$_2$ and HTM) multiplied by the photon flux spectrum from AM 1.5G data. For the two-step method, $N_{ph} = 8.9 \times 10^{20}\,\mathrm{s}^{-1}\mathrm{m}^{-2}$ (inset in Fig. 1B).

Photovoltaic parameters of the constructed solar cells were extracted from the current-voltage curves measured under 1Sun illumination. They are collected in Table 1 for 0.5 V/s reverse scan for several measurement series of different samples. For each sample, the best within 6 different gold contacts was selected, with typical variation of the photocurrent of about 10% for different contacts. The values of the parameters presented in Table 1 show quite high fluctuations, yet they are explicitly presented to visualize the important trends, which will be discussed below. The fluctuations should be related to the different preparation methods, sensitivity of prepared PSC to the small variations in the handmade construction of the devices, and limited beam homogeneity of our sunlight source with respect to professional solar simulators (thus, additional deviations might be due to sample positioning in the current-voltage measurements in different series). For the method which gave the best results (two-step), the differences between the photocurrents and efficiencies of samples with the same HTM are usually less than 20% (Table 1).

Our cells exhibit severe hysteresis effect [26,27], typical of the

Table 1

Photovoltaic parameters for the best cells from each series with perovskites obtained by different synthesis method and for different precursor concentration: open circuit voltage (V$_{OC}$), fill factor (FF), short-circuit current density (J$_{SC}$) and efficiency. J-V curves were obtained for 500 mVs^{-1} reverse scan rate.

Synthesis method	Sample	Voc (mV)	Jsc (mA/cm^2)	Fill factor	Efficiency (%)
two-step (1st series)	S	903	13.9	0.56	7.0
	X	656	10.5	0.51	3.5
two-step (2nd series)	S	906	16.5	0.64	9.6
	X	875	17.2	0.62	9.3
two-step (3rd series)	S	800	15.8	0.62	7.8
	X	796	17.2	0.57	7.8
	S:X	842	16.9	0.58	8.2
one-step (1:1), 1 M PbI$_2$[a]	S	755	13.6	0.51	5.2
	X	794	13.1	0.43	4.4
one-step (1:1), 0.55 M PbI$_2$[a]	S	906	9.5	0.54	4.7
	X	764	9.7	0.51	3.8
one-step (3:1), 1 M PbCl$_2$[a]	S	665	8.4	0.59	3.3
	X	669	9.6	0.36	2.3

[a] (MAI:PbI$_2$ or MAI:PbCl$_2$ ratio in precursors solution).

selective contacts and the preparation method used. It is illustrated in Table S2, which presents the exemplary photovoltaic parameters measured under different scan speed and direction. One of the most probable explanations of hysteresis effect in PSC is the combined effect of ion migration and charge trapping at perovskite interface [26]. It is especially often observed for the cells with perovskite-titania interface (e.g. the opposite to perovskite-PCBM interface) [27]. Significant overlayer of pure perovskite (for planar TiO_2 or thin mesoporous TiO_2) [28] and small crystal sizes of perovskite [29] also enhance hysteresis effect, which might explain our observations.

The current-voltage curves for the cells with the best sunlight conversion efficiency are presented in Fig. 1C. The efficiency close to 10% is obtained for the cells prepared by the two-step method (9.6% for the cell with spiro-OMeTAD and 9.3% for the cell with ×60). It is more than twice smaller than the best records for PSC (22%), but the small thickness of the perovskite layer should be taken into account. Therefore, we calculated the parameter called *total APCE* (APCE − absorbed photon per current efficiency), describing the relative photocurrent of the cells per the number of absorbed photons. It is defined as the *total APCE* $= J_{SC}/e\, N_{ph}$, where J_{SC} is the short circuit current density, and e is the elementary charge. In our best configurations these values are close to 100%. For example, taking the average $J_{SC} = 14$ mA/cm^2 from the reverse and forward scans (16 mA/cm^2 and 12 mA/cm^2, respectively), and $N_{ph} = 8.9 \times 10^{20}$ s^{-1}m^{-2} the *total APCE* is equal to 98% for the two-step method. Very efficient charge separation at 0 V bias is also confirmed in the independent measurement of IPCE spectra. After the correction for absorption, the APCE spectra show values close to 100% in 600–800 nm range (Fig. S2). For shorter wavelengths these values drop, which might indicate that when the photons are mainly absorbed close to TiO_2 interface, the longer diffusion distance towards HTM decreases the charge separation efficiency. Moreover, our cells exhibit remarkable stability when kept in the dark but under normal atmospheric conditions. It can be seen from Table S3 that the parameters of the cells do not change significantly even 7 weeks after preparation. Therefore, we can conclude that the two-step preparation method under simplified conditions (without glovebox but under the presence of oxygen and moisture during the preparation of precursor solutions and spin-coating, and with only dry nitrogen flow during heating of the samples) led, in our experiment, to stable and relatively efficient $MAPbI_3$ cells, at least for small perovskite layer thickness.

For the other control one-step preparation methods, the relative photocurrent was usually significantly smaller than for the two-step method with 0.55 M PbI_2. Only for the samples with the thinnest perovskite layer of 100 nm (with precursors concentrations of 0.55 M, Table S1) the relative photocurrent, (J_{SC} of about 10 mA/cm^2, Table 1) was similar to that of the two-step method. For higher precursors concentrations, despite thicker perovskite layer (250 or 300 nm, Table S1), the photocurrent was lower than that for the two-step method. This indicates that for thicker perovskite layers the quality of the perovskite film is not good enough, and, probably, in such case more rigorous preparation conditions with the glovebox are required.

The photovoltaic parameters in Table 1 can be used to compare the cells made with spiro-OMeTAD and X60. The spread of the parameters values is significant, like in many PSC studies, however, some clear trends can be observed. Interestingly, the trends are not only present for the best cells prepared by the two-step method, but also for the control cells produced by the one-step method under different MAI:PbI_2 precursor concentrations and compositions (1:1 or 3:1, all iodide or mixed halide). To take advantage of many measurements performed, we calculated and averaged the relative differences of the photovoltaic parameters between **S** and **X** cells from 6 series of experiment presented in Table 1. Within the experimental error, the photocurrent for both HTMs is similar ($\Delta J_{SC}/J_{SC} = 0.2 \pm 5.5$ %, although the best J_{SC} is 16.6 mA/cm^2 for **S** and 17.2 mA/cm^2 for **X**), while the open circuit voltage is higher for the cells with spiro-OMeTAD by $\Delta V_{OC}/V_{OC} = 9.1 \pm 4.8$ %. The largest difference is in the fill factor values,

which are better in **S** cells by $\Delta FF/FF = 13.4 \pm 5.4$ %, thus the overall sunlight conversion efficiency is better by 19.7 ± 7.6 % (relative increase). In the experimental series in which **S:X** cells were also measured, their photovoltaic parameters were placed between those of **S** and **X** cells (Table 1 and Table S3).

3.2. Electrochemical impedance

Electrochemical impedance spectroscopy studies brought the information about the time constants of bulk and interfacial charge recombination, occurring on time scales from sub-milliseconds to seconds. The impedance measurements were performed for the selected cells prepared by the two-step method without illumination or under 1Sun conditions, for different applied bias voltages, spanning from 600 mV to 950 mV in 50 mV increments. Typical Nyquist plots are shown in Fig. S3A. In line with other studies of PSC, three frequency regions with separate semi-arcs can be distinguished: high-frequency (HF), mid-frequency (MF) and low-frequency (LF). The LF part (< 10–100 Hz) is usually interpreted as due to slow ionic motion in the perovskite [30,31]. In our cells the LF signal showed inductance behavior as obtained from measurements in the dark (positive Z" part in Fig. S3A), in line with several reports on PSC [21,32], while under 1Sun illumination the third arc appeared in this region. Therefore, we excluded the LF part from the fit and used equivalent circuit with two RC elements (one for HF and another for MF part) and series resistance. In fact, typically of impedance analysis, constant phase elements were used instead of capacitors for better fit quality, but the fitted exponent (0.8-1.2) was close to the value of the capacitor (1). Moreover, the HF part sometimes extended above the frequency range of our analyzer (> 1 MHz), especially for the experiments with high bias voltage and under illumination, so the extracted HF parameters might be charged with considerable uncertainty. Therefore, below we will concentrate on the analysis of the MF part.

Fig. 2A presents exemplary MF lifetimes under different bias voltages, and similar results for another solar cell series are shown in Fig. S3B. The lifetimes are calculated as the product of MF resistance and MF capacitance. In line with other reports for PSC [15,21], the capacitance values (0.1-0.5 µF) do not exhibit, within experimental error, any voltage dependence. This dielectric capacitance is by about an order of magnitude higher than in our previous studies of PSC with a similar active area [15], which agrees with the difference in the perovskite thickness between the previous and current cells. Thus, the changes in MF lifetimes under different applied voltage reflect the MF resistance behavior. This lifetime in the dark is significantly longer for **X** samples than **S** ones, while the cells made with the mixture of spiro-OMeTAD and ×60 show intermediate behavior (Fig. 2A and S3B). MF lifetime is determined by the charge recombination inside the perovskite layer and at the interfaces with TiO_2 and HTM [15,20,22,33,34]. During the preparation, HTM was deposited on the top of all other layers, so we assume that the bulk recombination and that on TiO_2 interface was the same for **S**, **S:X** and **X** cells. Therefore, the differences in the lifetimes reflect different charge recombination between HTMs and $MAPbI_3$.

Interestingly, slower charge recombination for the cells with X60 does not influence the overall charge separation efficiency, since the photocurrent and photovoltage are similar for **X** and **S** cells. The slower recombination for **X** samples is also hard to explain on the basis of the differences in the parameters of both materials [11]. The redox potential of ×60 was reported to be slightly more positive with respect to that of spiro-OMeTAD (0.65 and 0.63 V vs. NHE), and hole mobility is even higher for X60 (19×10^{-5} cm^2 V^{-1} s^{-1} vs. 8.1×10^{-5} cm^2 V^{-1} s^{-1} for spiro-OMeTAD). Therefore, interfacial factors seem to be more important, which will be also indicated in the next section. However, it should be noted that both X60 and spiro-OMeTAD were deposited using the same method, with the same concentration and with the same amount of additives (TBP and Li-TFSI)
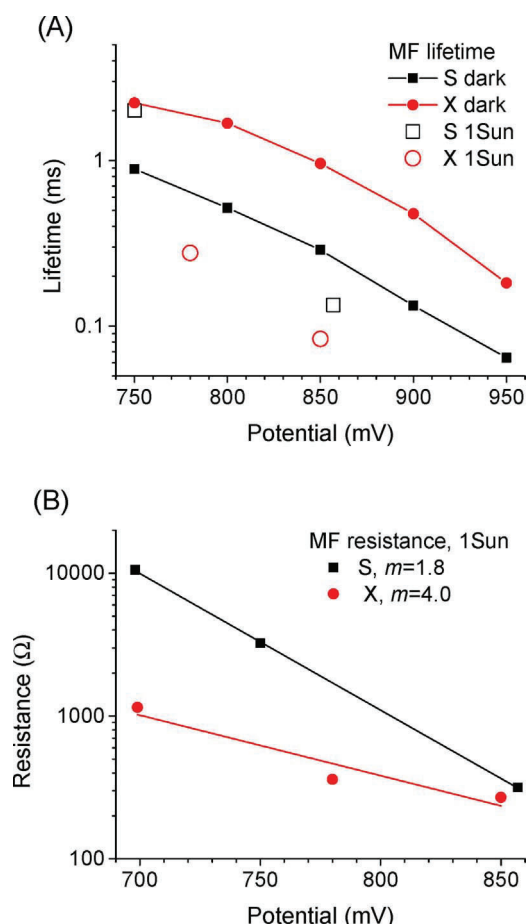
Fig. 2. (A) Mid-frequency (MF) lifetime of **S** and **X** cells (two-step method preparation) measured by electrochemical impedance in the dark and under 1Sun illumination. (B) MF resistance under 1Sun; ideality factors *m* are calculated from fitting (solid lines) the exponential function: $R = R_0 \exp(-Ve/m\,kT)$.

that were used in the previous studies using X60 [11,12]. It should be noted that the concentrations of additives were optimized for spiro-OMeTAD, thus, as suggested, perhaps some improvement in the performance of X60 cells can be obtained by varying the amount of TBP and Li-TFSI [12].

To explain smaller fill factor of the cells with X60, the impedance results under 1Sun conditions must be taken into account, when photoinduced excess carriers are present in the perovskite. Despite more relevance to the operating conditions, the impedance studies of PSC under illumination are relatively rare [15,35], probable due to the problems with sample stability. MF lifetimes under illumination suffer from much higher shortening for **X** than for **S** cells (e.g. Fig. 2A). Moreover, the voltage dependence of MF resistance under 1Sun can be analyzed. As shown in Figs. 2B and S3C, the semi-log plots of resistance vs bias voltage are steeper for **S** than **X** cells, and the fitted exponential function gives better ideality parameter *m* for the former than for the latter cells. In the series of experiments involving the **S:X** solar cells, the values of their *m* parameter lie between those of **S** and **X** (Fig. S3C: *m* = 6.8 for **S**, *m* = 8.1 for **S:X**, and *m* = 23.0 for **X**). Therefore, worse charge separation in the cells with X60 under high bias occurs only when high density of electrons and holes in MAPbI₃ is induced by illumination. It might be related to the different hole injection rate constants, revealed in the next section.

3.3. Transient absorption

Femtosecond transient absorption was performed under excitation at 600 nm in 3 ns time window in the spectral range between 610 and
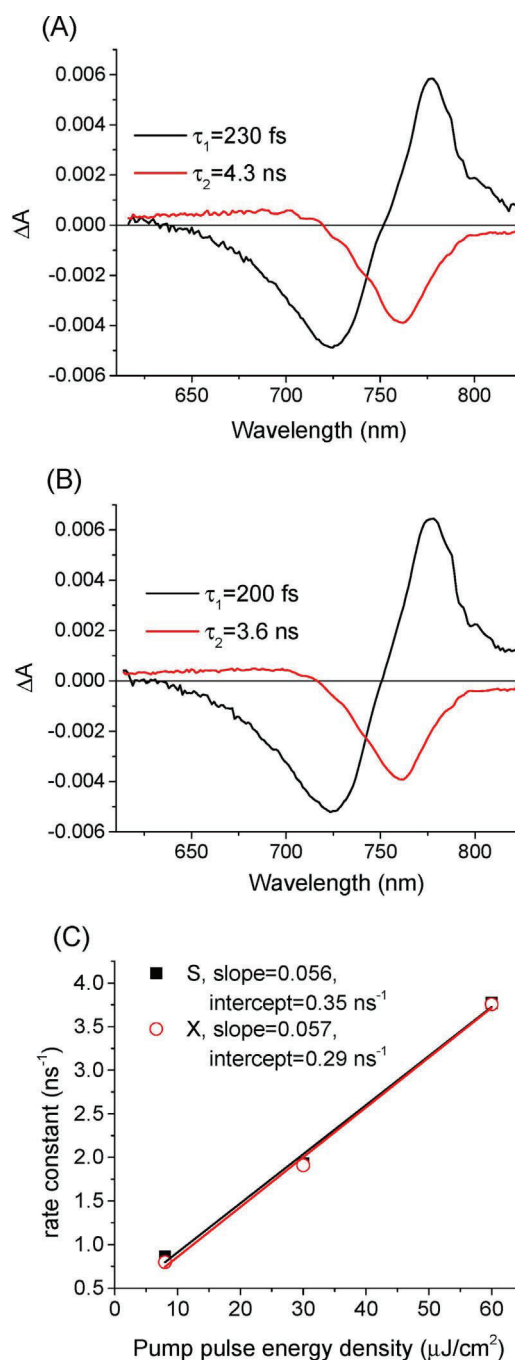
Fig. 3. Femtosecond transient absorption experiment results (pre-exponential factor spectra obtained from two exponential global fit) for (A) X60 and (B) spiro-OMeTAD based solar cells for pump energy density 2.5 μJ/cm². (C) Plots of the rate constants of the longer component in transient absorption global analysis as a function of pump pulse energy density. The solid lines show the linear fits to the data.

850 nm. The measured evolution of the transient absorption spectra was similar as in our previous studies [15], therefore we applied analogous two-exponential analysis of the transient absorption spectra. As a result, we obtained the wavelength-dependent amplitude spectra of the two components, which are shown in Fig. 3A-B for exemplary **S** and **X** cells prepared by the two-step method and for the pump energy density 2.5 μJ/cm² The faster, sub-ps component has a shape characteristic of the band-edge shift (derivative of the absorption band), and it is due to charge cooling and/or exciton dissociation [36–38]. Its values are similar for the cells with spiro-OMeTAD and X60 under the same energy density of the pump pulse. The second component of single

nanoseconds time constants (for the pump energy density below 10 μJ/ cm^2) has a characteristic band dominated by negative bleach of the perovskite long-wavelength excitonic band with a minimum at 760 nm (Fig. 3A–B). This longer time constants represent the decay of the population of excited carriers, whose dynamics is determined by the charge recombination within the perovskite material and charge transfer to TiO$_2$ and HTM [15,39,40]. In our previous work we proposed a method in which recombination contribution could be subtracted by the analysis of the longer component rate constants as a function of pump pulse energy [15]. An example of such an analysis is presented in Fig. 3C for the cells in the current study. As can be seen, a linear relationship confirms that the recombination is dominated by the second order process, at least for energy densities below 60 μJ/cm^2. However, we observed large spread of both slope (due to the second order recombination) and intercept values (due to the first order recombination) of the fitted linear functions, even for the same cell measured at different spots. Most probably, the charge recombination is more heterogeneous in our present samples than those used in the previous studies, so it is difficult to use the intercept values to extract interfacial charge transfer rate constants.

In this study we are only interested in a comparison between the hole transfer rates to different HTMs, therefore we applied a simplified approach. The difference between the rate constants of the longer component in **S** and **X** samples, Δk, is considered as due to different hole transfer rate from the perovskite to HTM. It is based on the assumption that the first order recombination within the perovskite and charge transfer to TiO$_2$ are, on average, the same for the cells with both HTMs, because the thickness and morphology of the TiO$_2$ and perovskite layers are not affected by different HTM's deposited on top of them. Similarly, the contribution of second order recombination should be similar in the samples of different HTMs, yet to minimize the influence of the possible fluctuations in the second order recombination rate constants, the results obtained for the lowest pump pulse energy were only taken into account in each series. Table 2 presents such results obtained in several measurement series for different samples. In most of the sample pairs the time constants were faster for **S** than **X** cells. It is true for both two-

step and one-step preparation methods (in the latter with both 1:1 and 3:1 precursor ratios), which confirms that different dynamics in spiro-OMeTAD and X60 is an universal feature of MAPbI$_3$ perovskite. It should be noted here that for 1:1 one-step method, the pre-exponential factor spectra were different from those presented in Fig. 3 A–B, but two-exponential global analysis with sub-ps and single-ns component was still valid. We will present a more detailed analysis of this effect in our forthcoming contribution.

The variation in Δk shown in Table 2 is significant, probable due to the random variation in the first order recombination within perovskite. However, we again took advantage of statistics, and calculated that the rate constant of hole transfer from MAPbI$_3$ to spiro-OMeTAD was faster than that to X60 by Δk = 0.036 ± 0.022 ns^{-1}. In our previous studies we determined the absolute value of hole transfer rate constant from MAPbI$_3$ to spiro-OMeTAD as 0.06 ns^{-1}. Thus, the hole transfer to X60 is not more than twice slower, assuming that the hole transfer dynamics in the cells with spiro-OMeTAD is the same in the previously and presently studied cells. However, the perovskite thickness in the presently studied cells is smaller than in the previously considered ones, and it was recently shown that charge diffusion dynamics plays an important role in the overall time scale of charge injections to contact materials [41]. Therefore, the relative difference between the hole injection in **S** and **X** samples might be in fact much than twice smaller. Interestingly, the slower hole injection into X60 does not lead to worse efficiency of charge separation, since, as revealed in the first section, the photocurrent is the same for both **S** and **X** cells.

One of the explanations of slower hole injection in X60 cells could be slightly more positive redox potential of X60 with respect to that of spiro-OMeTAD (by about 20 mV [11]), which implies smaller driving force for injection from MAPbI$_3$. On the other hand, slower hole transfer to X60 correlates with slower charge recombination at perovskite/X60 interface, shown by impedance spectroscopy in the dark. This suggest that the interface properties and contact quality have probably more important impact on the charge transfer dynamics [42]. In our previous studies we observed a similar correlation when comparing the performance of the cells with organic spiro-OMeTAD and inorganic CuSCN as HTMs (with faster hole transfers for CuSCN) [15]. Therefore, the present results point to a more universal feature of perovskite/HTM interfaces: higher coupling between the perovskite and HTM results in a faster hole transfer in both directions (hole injection and recombination).

Finally, we have also made some fluorescence control measurements to confirm that the long component obtained in transient absorption really represents the carrier lifetime in MAPbI$_3$ perovskite. The excitation energy was not precisely determined in luminescence tests, so the absolute values of time constants cannot be compared. Despite that, the relations between the lifetimes of **X** and **S** samples were the same as that obtained from bleach decay in transient absorption. In the measurements using streak camera detection over the entire fluorescence spectrum (650–900 nm) and upon excitation with 100 fs pulse at 500 nm, the average lifetimes of 2.5 ns and 2.1 ns were obtained for the cells with X60 and spiro-OMeTAD, respectively (Fig. S4). In time-correlated single photon counting (TCSPC) experiment with 420 nm excitation and detection at 780 nm, the stretched exponential function described the emission decay profile (Table S4). The average time constants were 1.25 ns for **X** sample and 0.93 ns for **S** sample. Additionally, we also measured mixed **S:X** cell, for which the fluorescence lifetime (0.97 ns) was between that of **X** and that of **S** cells.

4. Conclusions

X60 (spiro(fluorene-9,90-xanthene)-based molecule, also called SFX-MeOTAD) has been recently proposed as a cheaper alternative to spiro-OMeTAD as the hole transporting material in perovskite solar cells. We compare the performance of the cells made with a thin (150–200 nm) layer of MAPbI$_3$ as the active perovskite, mesoporous

Table 2
Lifetimes of the listed cells with perovskites obtained by appropriate synthesis methods and PbI$_2$ concentration in precursor solution obtained from femtosecond transient absorption global fit for small pulse energy to neglect second order recombination processes. Rate constants difference for each X and S sample pair and average difference Δk is given.

Synthesis method	Pulse energy density (μJ/ cm^2)	Sample	Lifetime (ns)	Rate constants difference, Δk (ns^{-1})
One-step (3:1), 0.55 M PbI$_2$[a]	8	X	1.25	0.06
		S	1.16	
One-step (3:1), 0.55 M PbI$_2$[a]	8	X	2.2	0.02
		S	2.1	
One-step (1:1), 0.55 M PbI$_2$[a]	5	X	6.7	0.01
		S	6.3	
One-step (1:1), 1 M PbI$_2$[a]	5	X	4.4	0.01
		S	4.3	
Two-step	7	X	2.3	−0.06
		S	2.7	
Two-step	2.5	X	3.9	0.01
		S	3.8	
Two-step	2.5	X	4.3	0.04
		S	3.7	
Two-step	8	X	3.6	0.04
		S	3.1	
Two-step	8	X	2.5	0.19
		S	1.7	
Average difference				0.036 ± 0.022

[a] (MAI:PbI$_2$ ratio in precursors solution).

TiO$_2$ as the electron transporting layer, and X60 or spiro-OMeTAD as HTMs. The dynamics of the interfacial charge transfer occurring on the time scales from femtoseconds to seconds was explored. Our cells were prepared in normal room conditions (with the presence of oxygen and moisture), but the photocurrent of the thin cells was high, of about 14 mA/cm^2, for the given perovskite thickness. As confirmed by steady-state absorption measurements using integrating sphere, it corresponds to the absorbed photon to current efficiency (APCE) close to 100%. Moreover, the cells exhibited remarkable stability over many weeks when kept in the dark.

The cells with both HTMs have similar photocurrent and photovoltage, but the cells with X60 exhibit smaller fill factor than those with spiro-OMeTAD. The overall hole injection from perovskite to HTM was slower for X60 than that for spiro-OMeTAD (rate constant difference of about 0.04 ns^{-1} revealed from the bleach recovery dynamics in transient absorption measurements). On the millisecond time scale (investigated by electrochemical impedance spectroscopy), the charge recombination under bias in the dark was also slower for X60 cells. However, the acceleration of charge recombination under illumination was much more pronounced for the cells with X60 than for those with spiro-OMeTAD, resulting in a worse ideality factor in the former than in the latter cells. The cells with the 1:1 mixture of spiro-OMeTAD and X60 show intermediate behavior in all aspects, revealing that a simple combination of small molecule transporters can be used to tune the properties of HTM. The best sunlight conversion efficiencies were obtained for the two-step perovskite preparation method, but the validity of the differences between X60 and spiro-OMeTAD was also confirmed for other popular one-step methods.

Acknowledgements

Appendix A. Supplementary data

Supplementary data associated with this article can be found, in the online version, at http://dx.doi.org/10.1016/j.synthmet.2017.08.007.

References

[1] www.nrel.gov/pv, National Center for Photovoltaics. National Renewable Energy Laboratory (NREL).
[2] X. Li, D. Bi, C. Yi, J.-D. Décoppet, J. Luo, S.M. Zakeeruddin, A. Hagfeldt, M. Grätzel, Science 353 (2016) 58.
[3] S.S. Shin, E.J. Yeom, W.S. Yang, S. Hur, M.G. Kim, J. Im, J. Seo, J.H. Noh, S.I. Seok, Science 356 (2017) 167.
[4] T.M. Brenner, D.A. Egger, L. Kronik, G. Hodes, D. Cahen, Nat. Rev. Mater. 1 (2016) 15007.
[5] H.S. Jung, N.-G. Park, Small 11 (2015) 10.
[6] Z. Yu, L. Sun, Adv. Energy Mater. 5 (2015) 1500213.
[7] S.F. Völker, S. Collavini, J.L. Delgado, ChemSusChem 8 (2015) 3012.
[8] M. Saliba, S. Orlandi, T. Matsui, S. Aghazada, M. Cavazzini, J.-P. Correa-Baena, P. Gao, R. Scopelliti, E. Mosconi, K.-H. Dahmen, F. De Angelis, A. Abate, A. Hagfeldt, G. Pozzi, M. Graetzel, M.K. Nazeeruddin, Nat. Energy 1 (2016) 15017.
[9] A.E. Shalan, T. Oshikiri, S. Narra, M.M. Elshanawany, K. Ueno, H.-P. Wu, K. Nakamura, X. Shi, E.W.-G. Diau, H. Misawa, ACS Appl. Mater. Interfaces 8 (2016) 33592.
[10] P. Qi, F. Zhang, X. Li, Y. Xiao, J. Guo, S. Wang, Synt. Met. 226 (2017) 1.
[11] B. Xu, D. Bi, Y. Hua, P. Liu, M. Cheng, M. Grätzel, L. Kloo, A. Hagfeldt, L. Sun, Energy Environ. Sci. 9 (2016) 873.
[12] M. Maciejczyk, A. Ivaturi, N. Robertson, J. Mater. Chem. A 4 (2016) 4855.
[13] E. Nouri, Y.-L. Wang, Q. Chen, J.-J. Xu, V. Dracopoulos, L. Sygellou, Z.-X. Xu, M.R. Mohammadi, P. Lianos, Electrochim. Acta 222 (2016) 1417.
[14] M. Li, Z.-K. Wang, Y.-G. Yang, Y. Hu, S.-L. Feng, J.-M. Wang, X.-Y. Gao, L.-S. Liao, Adv. Energy Mater. 6 (2016) 1601156.
[15] K. Pydzińska, J. Karolczak, I. Kosta, R. Tena-Zaera, A. Todinova, J. Idígoras, J.A. Anta, M. Ziółek, ChemSusChem 9 (2016) 1647.
[16] A. Marchioro, J.C. Brauer, J. Teuscher, M. Grätzel, J.-E. Moser, Proc. of SPIE 8811 (2013) 881108.
[17] C.S. Ponseca Jr., E.M. Hutter, P. Piatkowski, B. Cohen, T. r. Pascher, A. Douhal, A. Yartsev, V. Sundström, T.J. Savenije, J. Am. Chem. Soc 137 (2015) 16043.
[18] S.D. Stranks, G.E. Eperon, G. Grancini, C. Menelaou, M.J.P. Alcocer, T. Leijtens, L.M. Herz, A. Petrozza, H.J. Snaith, Science 342 (2013) 341.
[19] S. Makuta, M. Liu, M. Endo, H. Nishimura, A. Wakamiya, Y. Tachibana, Chem. Comm. 52 (2016) 673.
[20] I. Zarazua, G. Han, P.P. Boix, S. Mhaisalkar, F. Fabregat-Santiago, I. Mora-Seró, J. Bisquert, G. Garcia-Belmonte, J. Phys. Chem. Lett. 7 (2016) 5105.
[21] A. Guerrero, G. Garcia-Belmonte, I. Mora-Sero, J. Bisquert, Y.S. Kang, T.J. Jacobsson, J.-P. Correa-Baena, A. Hagfeldt, J. Phys. Chem. C 120 (2016) 8023.
[22] A. Todinova, J. Idígoras, M. Salado, S. Kazim, J.A. Anta, J. Phys. Chem. Lett. 6 (2015) 3923.
[23] J. Idígoras, G. Burdziński, J. Karolczak, J. Kubicki, G. Oskam, J.A. Anta, M. Ziółek, J. Phys. Chem. C 119 (2015) 3931.
[24] T.C. Sum, N. Mathews, G. Xing, S.S. Lim, W.K. Chong, D. Giovanni, H.A. Dewi, Acc. Chem. Res. 49 (2016) 294.
[25] M. Wendel, S. Nizinski, D. Prukala, M. Sikorski, S. Wybraniec, G. Burdzinski, J. Photochem. Photobiol. A: Chem 332 (2017) 602.
[26] S. van Reenen, M. Kemerink, H.J. Snaith, J. Phys. Chem. Lett. 6 (2015) 3808.
[27] H.-S. Kim, I.-H. Jang, N. Ahn, M. Choi, A. Guerrero, J. Bisquert, N.-G. Park, J. Phys. Chem. Lett. 6 (2015) 4633.
[28] H.-W. Chen, N. Sakai, M. Ikegami, T. Miyasaka, J. Phys. Chem. Lett. 6 (2015) 164.
[29] H.-S. Kim, N.-G. Park, J. Phys. Chem. Lett. 5 (2014) 2927.
[30] C.F. Eames, J.M. Barnes, P.R.F. O'Regan, B.C. Walsh, A.M.S. Islam, Nat. Commun. 6 (2015) 7497.
[31] L. Contreras, J. Idigoras, A. Todinova, M. Salado, S. Kazim, S. Ahmad, J.A. Anta, Phys. Chem. Chem. Phys. 18 (2016) 31033.
[32] M. Anaya, W. Zhang, B.C. Hames, Y. Li, F. Fabregat-Santiago, M.E. Calvo, H.J. Snaith, I. Miguez, Mora-Sero, J. Mater. Chem. C 5 (2017) 634.
[33] H.-S.M.-S. Kim, I. Gonzalez-Pedro, F. Fabregat-Santiago, E.J. Park, N.-G. Bisquert, J. Nat. Commun. 4 (2013) 2242.
[34] J. Shi, H. Wei, S. Lv, X. Xu, H. Wu, Y. Luo, D. Li, Q. Meng, ChemPhysChem 16 (2015) 842.
[35] L. Contreras-Bernal, M. Salado, A. Todinova, L. Calio, S. Ahmad, J. Idígoras, J.A. Anta, J. Phys. Chem. C 121 (2017) 9705.
[36] K. Chen, A.J. Barker, F.L.C. Morgan, J.E. Halpert, J.M. Hodgkiss, J. Phys. Chem. Lett. 5 (2015) 153.
[37] F. Deschler, M. Price, S. Pathak, L.E. Klintberg, D.-D. Jarausch, R. Higler, S. Hüttner, T. Leijtens, S.D. Stranks, H.J. Snaith, M. Atatüre, R.T. Phillips, R.H. Friend, J. Phys. Chem. Lett. 5 (2014) 1421.
[38] M.T. Trinh, X. Wu, D. Niesner, X.-Y. Zhu, J. Mater. Chem. A 2 (2015) 9285.
[39] E.M. Hutter, J.-J. Hofman, M.L. Petrus, M. Moes, R.D. Abellón, P. Docampo, T.J. Savenije, Adv. Energy Mater. 7 (2017) 1602349.
[40] R.L. Milot, G.E. Eperon, H.J. Snaith, M.B. Johnston, L.M. Herz, Adv. Funct. Mater. 25 (2015) 6218.
[41] J. Leng, J. Liu, J. Zhang, S. Jin, J. Phys. Chem. Lett. 7 (2016) 5056.
[42] M. Moriya, D. Hirotani, T. Ohta, Y. Ogomi, Q. Shen, T.S. Ripolles, K. Yoshino, T. Toyoda, T. Minemoto, S. Hayase, ChemSusChem 9 (2016) 2634.

Supporting Information

for

Effects of different small molecule hole transporters on the performance and charge transfer dynamics of perovskite solar cells.

Katarzyna Pydzińska, [a] Patryk Florczak, [b]

Grzegorz Nowaczyk [b] and Marcin Ziółek [a] [*]

[a] Faculty of Physics, Adam Mickiewicz University in Poznań,

Umultowska 85, 61-614 Poznań, Poland.

[b] NanoBioMedical Centre, Adam Mickiewicz University in Poznań,

Umultowska 85, 61-614 Poznań, Poland.

Table S1.

Perovskite absorbance, thickness and precursors concentrations used in given solar cell preparation processes. The thickness is estimated from the absorbance value.

Sample	Absorbance at exciton band (750 nm)	Estimated thickness of perovskite layer	Precursors concentrations used in the preparation	
two-step	0.2	150 nm	MAI	0.05 M
			PbI_2	0.55 M
one-step (1:1), 0.55 M PbI_2	0.15	100 nm	MAI	0.55 M
			PbI_2	0.55 M
one-step (1:1), 1 M PbI_2	0.3	250 nm	MAI	1 M
			PbI_2	1 M
one-step (3:1), 0.55 M PbI_2	0.3	250 nm	MAI	1.65 M
			PbI_2	0.55 M
one step (3:1), 1 M $PbCl_2$	0.4	300 nm	MAI	3 M
			$PbCl_2$	1 M

Table S2.

Photovoltaic parameters for given samples for forward and reverse scan direction with different scan rate.

Sample	Scan direction	Scan rate (mV/s)	Voc (mV)	Jsc (mA/cm^2)	Fill factor	Efficiency (%)
S	reverse	0.5	766	15.9	0.60	7.3
		0.1	801	10.8	0.63	5.4
	forward	0.5	771	9.6	0.48	3.5
		0.1	763	14.1	0.51	5.5
X	reverse	0.5	793	14.8	0.44	5.2
		0.1	841	6.5	0.53	2.9
	forward	0.5	772	12.1	0.39	3.6
		0.1	772	7.3	0.43	2.4
S:X	reverse	0.5	800	16.1	0.54	6.9
	forward	0.5	798	13.0	0.45	4.7

Table S3.

Photovoltaic parameters for the cells measured at different time after fabrication: open circuit voltage (V_{OC}), fill factor (FF), short-circuit current density (J_{SC}) and efficiency. J-V curves were obtained for 500 mVs^{-1} reverse scan rate.

Synthesis method	Time after preparation	Sample	Voc (mV)	Jsc (mAcm^{-2})	Fill factor	Efficiency (%)
two-step (1st series)	fresh	S	707	15.2	0.54	5.8
		X	656	10.5	0.51	3.5
	4 days	S	903	13.9	0.56	7.0
		X	726	10.0	0.30	2.2
two-step (2nd series)	fresh	S	906	16.5	0.64	9.6
		X	888	14.7	0.42	5.5
	4 days	S	923	16.6	0.61	9.4
		X	875	17.2	0.62	9.3
	6 days	S	925	14.4	0.66	8.8
		X	895	15.3	0.60	8.2
two-step (3rd series)	fresh	S	800	15.8	0.62	7.8
		X	796	17.2	0.57	7.8
		S:X	842	16.9	0.58	8.2
	3 days	S	815	12.9	0.57	6.0
		X	852	15.7	0.45	6.0
		S:X	873	14.3	0.49	6.1
	13 days	S	859	13.7	0.59	6.9
		X	861	16.3	0.46	6.4
		S:X	892	15.7	0.52	7.2
	39 days	S	847	13.9	0.56	6.6
		X	858	14.2	0.38	4.6
		S:X	889	15.2	0.49	6.6
	47 days	S	900	15.5	0.54	7.5
		X	922	14.9	0.41	5.6
		S:X	888	14.4	0.54	6.9
one-step (1:1), 1 M PbI$_2$	fresh	S	849	7.8	0.56	3.7
		X	823	9.3	0.37	2.9
	4 days	S	755	13.6	0.51	5.2
		X	794	13.1	0.43	4.4
		X	669	9.6	0.36	2.3
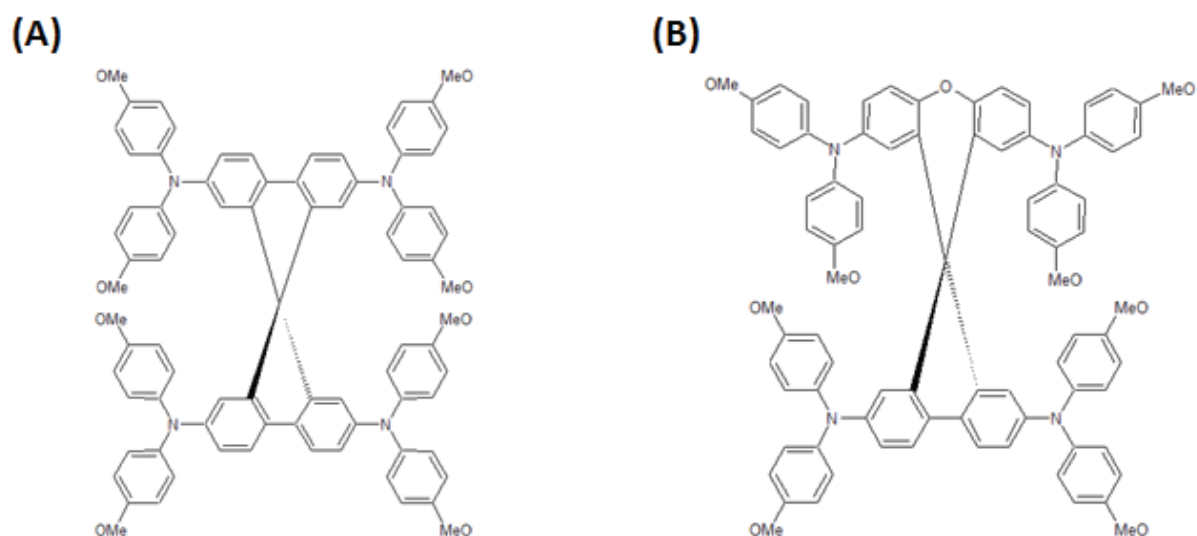
Figure S1. Chemical structure of spiro-OMeTAD (A) and X60 (B).
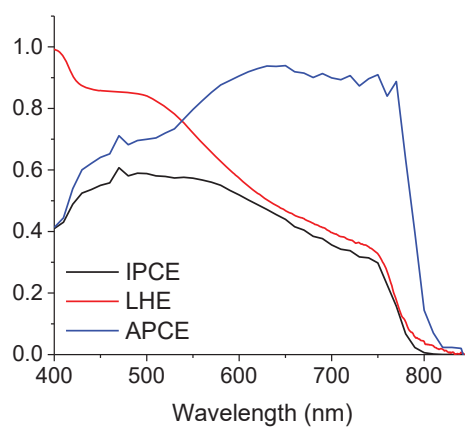
Figure S2. Incident-photon to current efficiency (IPCE), light harvesting efficiency (LHE) and absorbed-photon to current efficiency (APCE) spectra for the best solar cells prepared by two-step method with spiro-OMeTAD as HTM. LHE is calculated as $1-10^{-A}$, where A is absorption from Figure 1B. APCE(λ)=IPCE(λ)/LHE(λ).

(A)

bias 750 mV

(B)

MF lifetime, dark:
- S
- S:X
- X

(C)

MF resistance, 1Sun:
- S, $m=6.8$
- S:X, $m=8.1$
- X, $m=23.0$
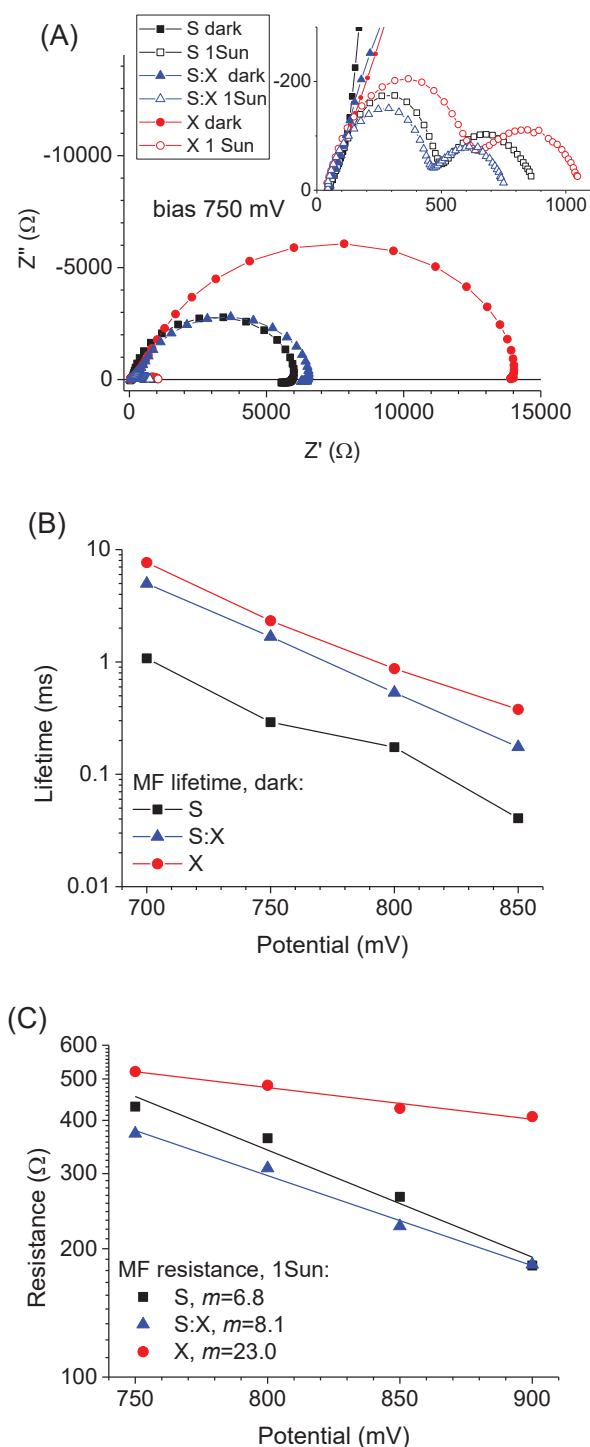
Figure S3. (A) Examples of Nyquist plots for different cells at bias voltage 750 mV measured by electrochemical impedance. (B) Mid-frequency (MF) lifetime of **S. S:X** and **X** cells (two-step method preparation) in the dark. (C) MF resistance under 1Sun; ideality factors m are calculated from fitting (solid lines) the exponential function: $R=R_0 \exp(-Ve/m \, kT)$.
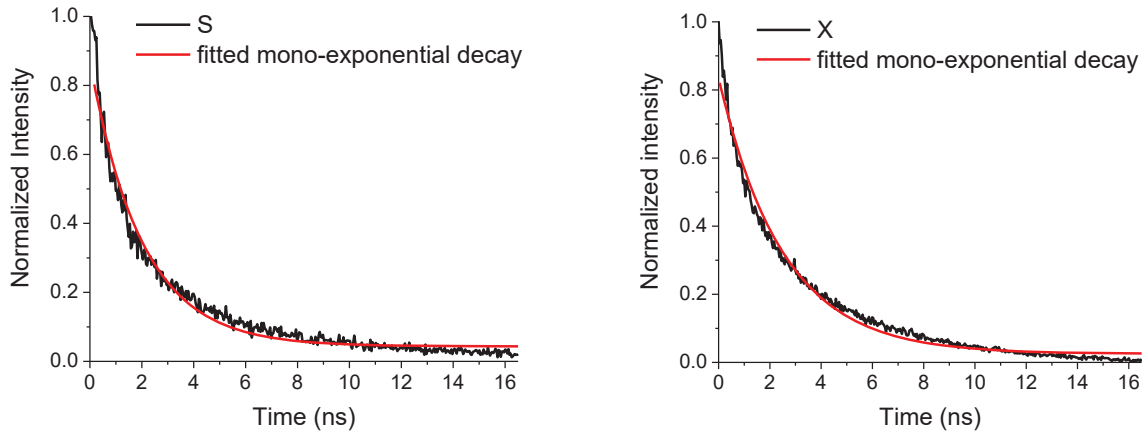
Figure S4. Fluorescence decay (black) measured by streak camera under excitation at 500 nm with 100-fs pulse (the integrated signal over 650-900nm). The fitted one-exponential function (red) gives the time constant 2.1 ns for **S** (left) and 2.5 ns for **X** cell (right).

Table S4.

Results for photoluminescence TCSPC decay fit using stretched exponential function at 780 nm (excitation at 420 nm) with average lifetime for different sample prepared by two-step method. The stretched exponential function is defined as:

$$A(t) = A_0 \ e^{-(t/\tau)^\beta},$$

and the averaged lifetime is calculated as:

$$\tau_{AVG} = \frac{\tau}{\beta} \Gamma\left(\frac{1}{\beta}\right).$$

sample	τ (ps)	β	τ_{AVG} (ps)
X	730	0.55	1 250
S:X	305	0.41	970
S	320	0.42	930

KPB-2
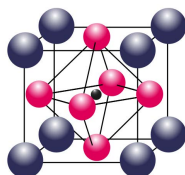
Differences in photoinduced optical transients in perovskite absorbers for solar cells

K.Pydzińska, J.Karolczak, M.Szafrański, M.Ziółek

RSC Advances

PAPER
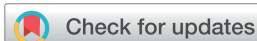
Check for updates

Differences in photoinduced optical transients in perovskite absorbers for solar cells†

Katarzyna Pydzińska, [ID] [a] Jerzy Karolczak, [ab] Marek Szafrański[a] and Marcin Ziółek [ID] *[a]

Methylammonium lead iodide films and powdered crystals were studied by time-resolved absorption and emission spectroscopy on the time scales from femtoseconds to nanoseconds. Strikingly different transient absorption signals were observed, changing from strong long-wavelength band-edge bleach to weak signatures of band-shift, which depended on the absorber form (films or polycrystals) and preparation method (stoichiometric or non-stoichiometric). The observed differences were correlated with the variation in absorption and emission spectra, changes in photo-induced carrier lifetimes and solar cell efficiency. These differences also pointed out that similar perovskite absorbers can provide significantly different transient responses and emphasize that special care must be taken when interpolating the obtained findings to the processes occurring in the most efficient devices.

Introduction

The best sunlight conversion efficiencies of perovskite solar cells (PSC) have improved exceptionally fast in the last few years, currently exceeding 22% (certified 22.7%).[1–3] Among emerging photovoltaic systems, PSCs are the most intensely developed solar cells. Concurrently, there has been a rapid increase in the number of basic studies of the properties of perovskites (particularly organo-metal halide type). These studies are aimed at better understanding the intriguing and complex properties of these organic–inorganic hybrids.[4] One of the most important problems is the variety of preparation methods of perovskite layers in solar cells,[5] which leads to differences in the materials morphology and structure. Different crystallographic phases might exhibit different spectroscopic properties.[6,7] It is also not clear how the findings for isolated perovskite crystals are relevant to the materials properties in solar cell configurations, where thin perovskite films are formed on mesoporous substrates and exposed to light and current flow. Organo-metallic halide perovskites are also widely studied in applications such as lasers and light-emitting diodes.[8–10] Similarly for solar cell efficiency, the morphology of perovskite films are crucial to their luminescence properties; for example, the strong effect of the precursor's stoichiometry on the optical properties has recently been reported for $MAPbBr_3$.[11]

The most characteristic feature in time-resolved absorption studies of perovskite films is the strong bleach signal observed at the long-wavelength band-edge. The formation and recovery dynamics as well as the changes in the spectral shape of this bleach are used to determine many key properties of the perovskites, such as the carrier recombination mechanism, order and dynamics,[12–15] the electron and hole cooling and exciton dissociation times,[16–18] and the carrier diffusion and charge-transfer rate constants with contact materials.[18–22] In general, the bleaching (or ground state depopulation) signals are the most common sample responses in transient absorption measurements, occurring as negative absorption changes (ΔA) due to a decrease in the possible optical transitions after pump excitation. For organic molecules the excitation will block the transitions from the ground state to all electronic excited states, resulting in multiple negative bleach bands resembling the ground state absorption spectrum. However, in semiconductors, due to the delocalized nature of the carriers in valence and conduction bands, after the excitation, the electrons will relax to the conduction band energy minimum and the holes will "move" to the valence band maximum. Therefore, irrespective of the initial excitation transition, after charge cooling only the lowest energy transitions (from the top of the valence band to the bottom of the conduction band) will be blocked. This process, called state-filling, is responsible for the strong bleach at the band-edge of direct bandgap semiconductors.[12,23,24] It has been shown for perovskites that both electrons and holes contribute to the bleach signal.[21,25]

Such band edge bleach dominates in most of the studied perovskites. However, in some works the disappearance of this signal has been reported. For example, a blue shift instead of population bleaching at the band-edge was reported when perovskite dimensionality decreased from 3D to 2D.[26,27] The bleach was observed for the three-dimensional $CH_3NH_3PbI_3$ perovskite, but for the two-dimensional sample

[a]*Faculty of Physics, Adam Mickiewicz University in Poznań, Umultowska 85, 61-614 Poznań, Poland. E-mail: marziol@amu.edu.pl*

[b]*Center for Ultrafast Laser Spectroscopy, Adam Mickiewicz University in Poznań, Umultowska 85, 61-614 Poznań, Poland*

† Electronic supplementary information (ESI) available: Fig. S1–S9. See DOI: 10.1039/c8ra00579f

$(C_4H_9NH_3I)_2(CH_3NH_3I)_{n-1}(PbI_2)_n$, it was only present for $n = 3$. In this study we add more insight into the origin of the bleach signals in perovskites by reporting the cases of its disappearance in 3D perovskite samples. We chose the most commonly studied MAPbI$_3$ (MA = CH$_3$NH$_3$) perovskite and compared the samples prepared by several typically used methods. The obtained results are correlated with changes in the optical spectroscopy properties of the materials.

Experimental section

Sample preparation

Samples of five different perovskite forms were prepared and used for the spectroscopic studies: powdered crystals (C), two films prepared by a non-stoichiometric process (NS) and two films prepared by a stoichiometric method (S). The abbreviation of sample names and the preparation methods are outlined in Table 1. The films were prepared both on FTO glass (glass with a fluorine doped tin oxide layer), FTO glass with titania and in full solar cell configuration. For emission studies, finely powdered crystals were used, but it was not possible to prepare the full solar cell configuration from them.

The MAPbI$_3$ crystals were prepared as described previously[28] and according to the slightly modified method described by Poglitsch and Weber.[29] Briefly, the synthesis was performed in concentrated water solution of MAI and HI. The solution was heated to about 100 °C and then, lead(II) acetate, dissolved in hot water, was slowly added with continuous stirring until a black precipitate was formed. Black crystals of MAPbI$_3$ with well-developed faces grew out of the solution as it slowly cooled down to about 45 °C. At this temperature, the crystals were taken out of the solution and dried to prevent the formation of hydrates. The single-crystal and powder X-ray diffraction experiments evidenced that the crystalline material obtained was pure MAPbI$_3$ in its tetragonal phase of space group $I4/mcm$.[7,28]

The details of the preparation of the perovskite films and the solar cells using a spin coating technique have been described in our previous study.[22] Titania structure on FTO glass (Sigma Aldrich, 13 Ω sq^{-1}) was prepared by sequential deposition of the compact layer (from titanium isopropoxide ethanol solution), ~100 nm mesoporous particles layer (from water suspension of titanium dioxide nanoparticles, 15–20 nm diameter, Solaronix)

and an additional ultrathin dense TiO$_2$ blocking layer (by dipping in 0.05 M TiCl$_4$ water solution). The two-step method was used for the first type of perovskite films (NS1), which consisted of sequential deposition of PbI$_2$ in dimethylformamide (DMF, 0.55 M, Sigma Aldrich) and then, after annealing at 100 °C, deposition of methylammonium iodide (MAI, Dyenamo, 0.05 M) in 2-propanol. The final thickness of the MAPbI$_3$ layer was close to 150 nm. For the second sample prepared via nonstoichiometric method (NS2), we applied the one-step method with the precursor solution of MAI (1.65 M) and PbI$_2$ (0.55 M) in DMF, thus having a precursor molar ratio of (3 : 1). The one-step method was also used to prepare the perovskite layer in the stoichiometric way. For the first sample (S1), 0.55 M of both MAI and PbI$_2$ in DMF were prepared, while for the second sample (S2), we directly dissolved MAPbI$_3$ crystals in DMF at a 1 M concentration, having an exactly (1 : 1) molar ratio. Due to different precursor concentrations, the S1 and S2 samples also differed in their perovskite layer thicknesses, which were about 100 nm and 250 nm, respectively. To make the complete solar cell, 2,2′,7,7′-tetrakis(N,N-di-p-methoxyphenylamine)-9,9′-spirobifluorene (spiro-OMeTAD) was spin coated on the top of the perovskite layer and gold electrodes were deposited by sputtering using a mask with several 0.05 cm^2 apertures that defined the active surface of the cells.

Sample characterization

The current–voltage curves were measured using an Autolab M101 potentiostat coupled to a photoelectric spectrometer equipped with a solar simulator (Instytut Fotonowy-Photon Institute, Poland). The intensity was adjusted to provide 1 sun illumination (100 mW cm^{-2}) using a xenon arc lamp with an AM 1.5G spectral filter and calibrated using a reference cell (15151, ABET). The absorption spectra were obtained using a Jasco V-700 spectrophotometer equipped with a 150 mm integrating sphere (LN-925). The film samples were placed before the integrating sphere; thus, both transmitted and scattered light were measured. The powdered crystal samples were placed after the integrating sphere; thus, the reflected light was collected and the light intensity data were transformed using the Kubelka–Munk function (KM) to compare the data with the absorbance of the films. The time-resolved emission measurements in the ps–ns time window were performed using a time-correlated single photon counting technique (TCSPC).[30]

Table 1 Stationary and transient absorption data for the measured samples

Sample name	Preparation method	Absorption λ_{onset}[b]	ΔA amplitude (at 5 ps)	ΔA lifetime	ΔA shape[c] (at 5 ps)
NS1	Two-step	765 nm	0.02	~2 ns	Band-edge bleach
NS2	One-step (3 : 1)	765 nm	0.02	~2 ns	Band-edge bleach
S1	One-step (1 : 1)	766 nm	0.002	~6 ns	Derivative
S2	Dissolved crystals (1 : 1)	771 nm	0.002	~6 ns	Derivative
C	Crystal powder[a]	808 nm	—	—	—

[a] Not in a solar cell configuration. [b] Position of long-wavelength band, calculated as the maximum of the first derivative of the absorption spectrum. [c] Transient absorption shape in the long-wavelength region (650–850 nm): strong negative signal (band-edge bleach) or derivative-like shape with positive signal in the blue region and negative signal in the red.

The same setup was used to measure steady-state emission spectra. The excitation wavelength was set at 420 nm. The obtained emission decay kinetics were not single-exponential. Therefore, they were fitted with a stretched exponential function: $I(t) = I_0 \exp\left[-\left(\dfrac{t}{\tau}\right)^{\beta}\right]$; then, the average lifetime was calculated using the following equation: $\tau_{\mathrm{AVG}} = \dfrac{\tau}{\beta}\Gamma\left(\dfrac{1}{\beta}\right)$.

The setup for ultrafast broadband transient absorption has been described before (Helios spectrometer, Ultrafast Systems, and Spectra Physics laser system).[31] The instrument response function (IRF, pump–probe cross-correlation function) was of about 200 fs (full width at half-maximum, FWHM). The pump pulse energy of 1 nJ corresponds to the pump pulse energy density of 0.5 μJ cm^{-2}. An important modification of the transient absorption setup with respect to the standard commercial configuration was the use of a filter that suppresses the residual 800 nm white light continuum before the sample in order to avoid pump-and-dump artifacts.[14,32] Femtosecond transient absorption was performed under excitation at 600 nm in a 3 ns time window in the spectral range between 440 and 850 nm. Global analysis of the transient absorption data was performed using the Surface Explorer software (Ultrafast Systems). It was used to fit a multi-exponential function (convoluted with IRF) to the kinetic vectors of a select number of singular values (excluding those due to noise). As a result of the analysis, the characteristic time constants were obtained as well as the wavelength-dependent amplitudes associated with them (also called decay-associated difference spectra or pre-exponential factor spectra). At least two samples of the same type were measured in at least three different spots to confirm the recurrence of the results.

Results and discussion

Stationary spectra, time-resolved emission and photovoltaic properties

Stationary absorption spectra of representative samples are shown in Fig. 1. The third column in Table 1 lists the positions of the long-wavelength absorption edge of each perovskite material. Due to uncertainty in the appropriate measurement of the absorption tail, it is calculated as the maximum of the first derivative of the absorption spectrum; thus, it roughly represents the middle of the rising slope of the absorption onset. The absorption is slightly red-shifted for the samples prepared in stoichiometric proportions and it is significantly red-shifted for the crystals with respect to the film samples. Further differences can be observed when comparing the absorption shape in the shorter wavelength range (Fig. 1). For NS1 and NS2 samples, the absorbance at around 480 nm is about 4 times higher than that at the band-edge with a shape that clearly indicates the presence of another band. The origin of this additional band is under debate in the literature. The most common interpretation is that it is due to the transitions involving higher energy conduction bands or lower energy valence bands.[19,33] Another explanation is that the band represents the molecular-like charge-transfer (from I to Pb) transition in the perovskite inorganic framework[13,34] or that it contains the contribution from PbI$_2$.[35,36] For samples S1 and S2, the band between 450 and 500 nm is much weaker, while for sample C, it is almost absent. This difference can also be visualized in the photos of the samples (Fig. S1 in the ESI†). The samples prepared with a non-stoichiometric precursor ratio are light-brown in color due to some red light that is transmitted through the films. In contrast, both films prepared at (1 : 1) precursor ratio and the powdered crystals are almost black.

Further differences between the samples are revealed from the emission studies. Stationary emission spectra are presented in Fig. S2† and their maxima are listed in Table 2. The spectra are red-shifted from 780 nm to 813 nm for the samples in the following order: NS1 < S1 < S2 < C. In line with the changes in the emission maxima, the fluorescence lifetimes measured at 780 nm also change (Table 2). Influence of the preparation method on the emission maximum shift has also been observed by Mokhtar *et al.* who reported that the red-shifting fluorescence maximum accompanies a two-step to one-step method transition.[37] The lifetime is the shortest for the NS1 sample (1 ns) and the longest for the C sample (6 ns). The differences are also visualized in the decay kinetics presented in Fig. S3.† For the powdered crystal sample, the lifetime is exclusively due to electron–hole recombination, while for the film samples it might also be affected by charge transfer rates to TiO$_2$ and spiro-OMeTAD. In our previous studies we estimated the charge
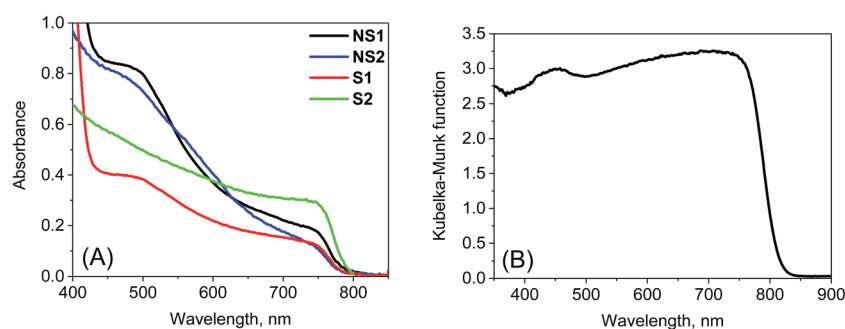
Fig. 1 Stationary absorption spectra of the samples studied after TiO$_2$ film contribution subtraction (A) and Kubelka−Munk function of sample C (B).

Paper

Table 2 Emission and photovoltaic data for the measured samples

Sample name	Preparation method	Emission maximum	Emission lifetime[b] at 780 nm	J_{sc}[c], mA cm^{-2}	Total APCE[d]
NS1	Two-step PVSK	780 nm	1 ns	16.6	98%
S1	One-step (1 : 1)	787 nm	2 ns	9.5	80%
S2	Dissolved crystals (1 : 1)	792 nm	3 ns	13.6	81%
C	Crystal powder[a]	813 nm	6 ns	—	—

[a] Not in a solar cell configuration. [b] Obtained from fitting emission decay kinetics with a stretched exponential function and then calculating the average lifetime. [c] The best obtained short-circuit current density for a given sample. [d] The relative photocurrent of the solar cell defined in the text.

transfer rate constant from MAPbI$_3$ to mesoporous TiO$_2$ to be 0.11 ns^{-1} and the rate constant from MAPbI$_3$ to spiro-OMeTAD to be 0.06 ns^{-1}.[18] If such values are subtracted from the measured fluorescence decay rates, the rate constants due to charge recombination are 0.83 ns^{-1} for NS1, 0.33 ns^{-1} for S1, and 0.17 ns^{-1} for both S2 and C. Thus, charge recombination is significantly faster in the samples prepared by the non-stoichiometric precursor ratio than in either those prepared from the stoichiometric mixture or in the crystals.

In the emission spectra, a small band at 580 nm can be noticed (Fig. S2B†), which probably originates from the absorption band at 480 nm. Its amplitude is several hundred times smaller than that of the main long-wavelength emission. The emission lifetime measured in this short-wavelength range is around 100 ps, which is much shorter than that at 780 nm. However, its presence indicates that the absorption at 480 nm is due to the existence of another band that is not directly coupled to the lowest conduction band in MAPbI$_3$, otherwise all carriers would relax to the lowest energy band and the short-wavelength emission would not be detectable.

Finally, photovoltaic parameters were also measured for the solar cells prepared from MAPbI$_3$ film samples. The best efficiency of about 10% was obtained for the two-step method (sample NS1) as reported in our previous contribution.[22] However, the perovskite film thicknesses were small and different for different samples. Therefore, the more relevant parameter is the one we name total APCE (APCE – absorbed photon per current efficiency), describing the relative photocurrent of the cells per the number of absorbed photons. It is defined as the total APCE = $J_{sc}/(eN_{ph})$, where J_{sc} is the short circuit current density, e is the elementary charge, and N_{ph} is the number of absorbed photons from 1 sun illumination, calculated from integration of the stationary absorptance spectrum

of the film multiplied by the photon flux spectrum from AM 1.5G data. The values of J_{sc} and total APCE are collected in Table 2. As observed for the NS1 sample, the relative photocurrent is close to 100%, while for the samples prepared from the material at stoichiometric precursor ratios (S1 and S2), the relative photocurrent is lower (about 80%). The other photovoltaic parameters and representative C–V curves were reported in our previous contribution (fill factors 0.5–0.6, open circuit voltages 0.75–0.90 V).[22]

In summary, the "stoichiometric" MAPbI$_3$ films exhibit absorption and red-shifted emission and they have longer fluorescence lifetime and lower relative photocurrent when compared to the "non-stoichiometric" samples. The crystals have even greater red-shifted absorption and emission and the longest lifetimes.

Transient absorption

The most important and significant differences between the investigated perovskite samples were observed in transient absorption measurements. The most visible difference is the amplitude of the signal. As shown in Table 1, the maximum transient absorption signal (either negative or positive) is about an order of magnitude smaller for samples S1 and S2 with respect to that for samples NS1 and NS2. It should be noted that the stationary absorbance of the samples at the excitation wavelength 600 nm varied only between 0.2 and 0.4 and the pump pulse energy density was between 5 and 8 μJ cm^{-2}. Hence, it cannot account for the observed changes in the signal amplitude. In addition to the amplitude, the transient absorption signal shape also changes between samples. The exemplary transient absorption spectra measured at 5 ps after excitation are shown in Fig. 2. This time was chosen because after 5 ps, all the carrier relaxation processes should be finished and the
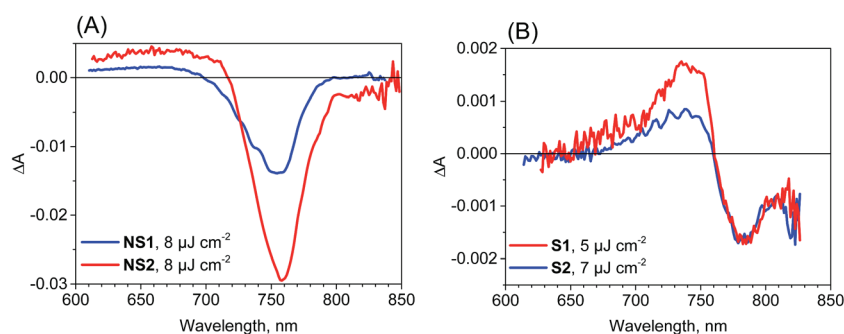
Fig. 2 Transient absorption spectra at 5 ps after excitation (λ_{ex} = 600 nm) for the samples studied and the indicated pump pulse energy density.

photoexcited electron and hole populations will be close to the maximum (recombination times are in the nanosecond or hundreds of picoseconds range). For the samples prepared *via* the non-stoichiometric method (NS1 and NS2, Fig. 2A), the dominant signal is the negative bleach with the minimum at around 760 nm, corresponding to the perovskite absorption edge. It should be noted that such a characteristic signal has been most frequently reported in transient absorption studies of perovskites,[12,14,15,19–21,38] including our recent studies.[18,22] The origin of the positive signal below 700 nm in the second component is not fully understood, but it is not a real transient absorption feature due to electronic transition. The possible explanations are that it is caused by a bandgap renormalization effect[21,39] or by refractive index changes.[40]

In contrast, for the samples prepared *via* the stoichiometric method (S1 and S2, Fig. 2B) the signal at around 760 nm is close to zero with symmetric positive and negative transient bands for the shorter and longer wavelengths, respectively. This shape is characteristic of the first derivative of the absorption edge and represents the transient blue-shift of this long-wavelength absorption band. Thus, the positive signal occurs on the blue side (more absorption upon the shift) and the negative signal on the red (less absorption) side of the maximum of band-edge at 760 nm. We have also tried to measure the transient signals of polycrystalline sample C by depositing the powder on FTO glass *via* spin coating from hexane suspension to allow for measurements in the transmission mode. No strong bleach signal was observed in this preliminary test, similar to samples S1 and S2. However, the deposition method yielded a very inhomogeneous perovskite layer and a noisy transient absorption signal. Therefore, these results need confirmation with

another deposition method, which we plan to conduct in future studies.

No significant differences in the spectroscopic results (except for a small variation in the lifetimes) were observed for the same perovskite films prepared on FTO glass, FTO glass with TiO_2 or in the full solar cell configuration. This indicates that for the pump pulse energies used herein, the charge transfer to TiO_2 and spiro-OMeTAD brings smaller contributions to the lifetime than the charge recombination as discussed above for emission decays. Moreover, for selected samples, we were also able to collect the transient absorption spectra below pump pulse energy (600 nm). As shown in Fig. S4,† for the film samples prepared with the non-stoichiometric ratio, the spectra at 5 ps shows another bleach band at 450–500 nm, which is much weaker than that at around 760 nm. This band is correlated with the stationary absorption band at around 480 nm. Interestingly, this bleach is absent in the spectra of the films prepared with a stoichiometric ratio (Fig. S4†), which is in line with the much less pronounced band at 480 nm in the stationary spectra (Fig. 1).

Further information from transient absorption measurements is obtained through global analysis performed in the range 610–850 nm for all of the samples. The results for the film samples are presented in Fig. 3. For NS1 and NS2, two exponential components can be used to fit the data for pulse energy density below 10 µJ cm^{-2} and the interpretations of the spectra and times are the same as those discussed in our previous studies.[18,22] The faster, sub-ps component (200–300 fs for pump pulse energy density about 8 µJ cm^{-2}) has a shape characteristic of the band-edge shift (derivative of the absorption band, negative for shorter wavelengths and positive for longer
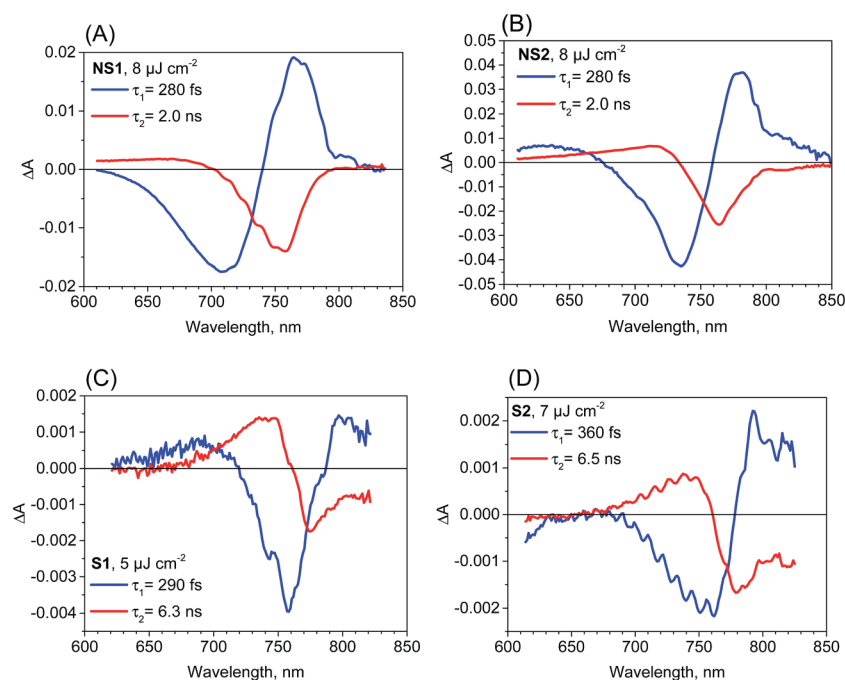
Fig. 3 Femtosecond transient absorption experiment results (pre-exponential factor spectra obtained from a two-exponential global fit) for the perovskite film samples studied and the indicated pump pulse energy density.

wavelengths) due to charge cooling and/or exciton dissociation.[16,17,41] The second component of the time constants of about 2 ns for both samples has a characteristic band dominated by the negative bleach of the perovskite long-wavelength band (Fig. 3A and B). These longer time constants represent the decay of the population of excited carriers, whose dynamics are determined by the charge recombination within the perovskite material and charge transfer to the contact materials. For pump pulse energy below 10 μJ cm^{-2} the bleach recovery can be described by a first order process and well-fitted by a single-exponential function,[18] while for higher energy the bleach kinetics become non-single exponential due to the contribution of second order recombination.[13,16–18]

The two-exponential global analysis was also applied for the film samples prepared *via* the stoichiometric method, but the obtained spectra of the components were different (Fig. 3C and D). The long-timescale decay of the excited carriers was associated with the spectra having the band-edge derivative signal (similar to the signal at 5 ps discussed above). The time constants were about 6 ns for both samples S1 and S2 for the excitation energy density in the range of 5–7.5 μJ cm^{-2}. For higher energy, the time constants become shorter and the one-exponential fit becomes insufficient, indicating that higher order charge recombination processes occur. The shorter component (of time constant 300–400 fs) also has a spectrum different from that observed for the "non-stoichiometric" films. Interestingly, it is dominated by the negative bleach with a minimum at around 760 nm, similar to the spectrum of the longer component in samples NS1 and NS2. The lifetimes for all samples are listed in Table 1. Due to the different excitation conditions (longer excitation wavelength and smaller pulse repetition rate) they are not exactly the same as those obtained from the emission studies (Table 2), but the trends are consistent: the shorter lifetimes are for samples NS1 and NS2 and longer lifetimes for samples S1 and S2.

To account for the observed striking differences between the MAPbI$_3$ samples prepared *via* different methods, we propose that in the samples prepared *via* the stoichiometric method, the photoexcited electrons and holes are somehow gathered outside the edges of the conduction and valence bands, respectively. Our explanation is schematically presented in Fig. 4. For the film samples prepared *via* the most typical non-stoichiometric method, upon excitation at 600 nm, the electrons in the conduction band and holes in the valence band relax to the minimum energy configuration (cooling times < 1 ps, faster component in the global analysis), which causes the band state filling and is responsible for the strong bleach signal observed at the absorption-edge transition (Fig. 4A). The recovery of this bleach follows the dynamics of charge recombination (nanosecond time scale for the small pump energy densities used in our studies). In contrast, for the samples prepared *via* the stoichiometric method, the cooling of electrons and holes is finalized in the local states below the conduction band minimum and valence band maximum (Fig. 4B). Electron cooling is accompanied by short-term filling of the conduction and valence bands. Thus, the spectrum of the fast component in samples S1 and S2 contains a significant contribution from the bleach signal at 760 nm (Fig. 3C and D). When electron and hole are transferred to the trap states, the direct transition to the absorption edge is possible. Therefore, no bleach occurs in long-term transients and only a blue-shift in the absorption transition (derivative-like shape of the spectrum) is observed. This shift is due to the electric field induced by the trapped electrons and holes modifying the band-edge transition (Stark effect).[17,42] Hence, the shift disappears on the nanosecond time scale, according to charge recombination.

A similar explanation has been proposed for the blue-shift signal and the lack of bleach in 2D perovskites as discussed in the introduction.[26,27] Unlike free carrier character for excitation in 3D perovskites, a localization of excitation in 2D perovskite (Mott–Wannier exciton) was proposed, which only exerts
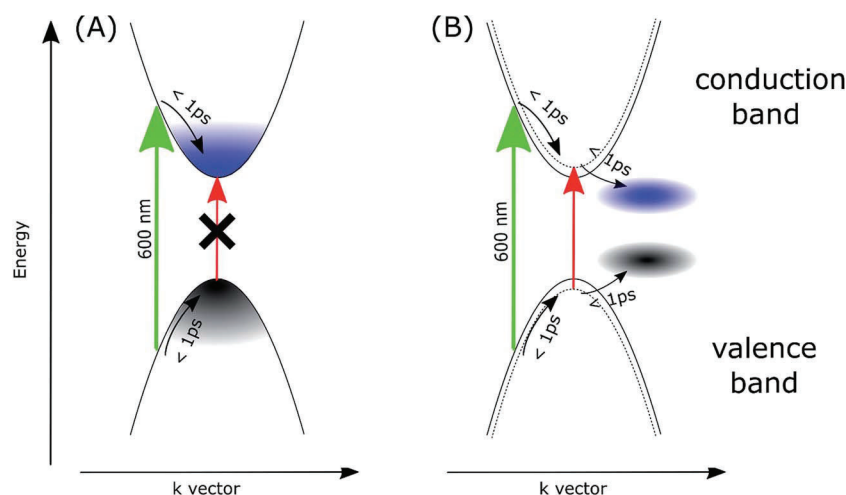
Fig. 4 Scheme of the proposed mechanism explaining the transient absorption signals for the samples prepared in non-stoichiometric (A) and stoichiometric (B) conditions. Green and red arrows represent the excitation (600 nm) and the absorption transition at the long-wavelength edge, respectively. Dotted curves in (B) represents the effect of the blue-shift of the band-edge transition due to the electric field induced by the localized electrons and holes.
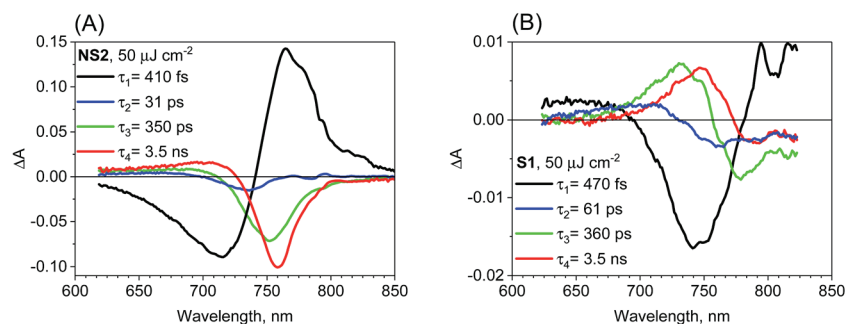
Fig. 5 Four-exponential global analysis results of transient absorption data for sample NS2 (A) and S1 (B) for pump pulse energy density equal to 50 μJ cm^{-2} ($\lambda_{ex} = 600$ nm).

local influence on subsequent optical excitations (screening reduces the exciton binding energy and, thus, results in a blue-shift in the band-edge absorption). In our case, the localized trap states for electrons and holes, which induce charge-screening that affects the band-edge transition, are likely to appear in the S1 and S2 samples. The charge recombination in these samples is not faster than that in the NS1 and NS2 samples, but charge diffusion and separation in the cells made of such perovskites with localized traps should be worse, which is in agreement with the smaller relative photocurrent in the samples prepared *via* the stoichiometric method.

Another possible interpretation is based on the involvement of the indirect bandgap. The appearance of other conduction and valence bands with energy minima/maxima slightly shifted in the *k*-space has been suggested in recent studies of perovskites.[43–49] It is quite probable that the exact position of such bands can be different for samples prepared *via* different methods, whose structures can be distorted as a result of lattice strains at the interfaces and local defects and impurities. If the band position in the samples prepared *via* the stoichiometric method are energetically more favorable than those of the main bands that form a direct bandgap, the photo-excited electrons and holes might be transferred to the main bands, thus emptying the direct band-edge transition, which results in the absence of the bleach signal.

We have also checked the effect of variation in pump pulse energy density between 5 and 50 μJ cm^{-2} and observed that the amplitude of transient absorption spectra varied linearly with the excitation energy. The kinetics become shorter and displayed a non-single exponential due to the second-order charge recombination as mentioned above and discussed previously.[18] To have a sufficiently good fit, additional time components in the global analysis are necessary and their amplitude spectra are different. These spectra are shown in Fig. S5–S7† for different samples and pump pulse energy densities together with the transient absorption spectra for selected pump–probe delay times. In general, with an increase in the energy density, increasingly shorter components appear with the spectral features being blue shifted. A representative global analysis for the pump pulse of high energy density made for the two types of the samples is shown in Fig. 5. The results appear to be in agreement with the proposed model. For the film samples prepared *via* the non-stoichiometric method, the bleach band is

initially broader on the short-wavelength side due to the deeper band state filling. The recombination occurs faster for the higher-energy electrons and holes and the band state filling becomes shallower upon decreasing charge population. That is why faster components in the global analysis have blue shifted amplitude spectra (Fig. 5A). The shift is schematically shown in Fig. S8.† For the film samples prepared *via* the stoichiometric method without a bleach signal, the faster recombination components exhibit a blue-shift of the zero crossing point in the derivative-like spectral shape (Fig. 5B). This result indicates that upon increasing time after excitation and decreasing charge population, the induced shift of the stationary absorption band becomes smaller. It should be noted that the particular time constants obtained in multi-exponential global fits do not have direct relation to the rates of the recombination processes. The mixed first and second order function should be instead used to extract the second order recombination rate (an example of the fit of such a function and a comparison with multi-exponential analysis are shown in Fig. S9†). However, the advantage of our multi-exponential analysis is that it shows the spectral dependence of the recombination kinetics (faster decay for shorter wavelength).

Conclusions

Methylammonium lead iodide perovskite films prepared under non-stoichiometric conditions showed prominent negative bleach signals of the absorption edge on timescales of picoseconds and nanoseconds. However, for the film samples of the same perovskite prepared under stoichiometric conditions and for the powdered crystals, no such signals were observed; only much weaker signals due to band shift were present. The observed differences are associated with the changes in other spectroscopic parameters: the films prepared *via* the non-stoichiometric method have the most blue shifted absorption edge and emission band, the most pronounced short-wavelength band is at 480 nm, and they exhibit better photovoltaic performance. The study presented herein also demonstrates the complex nature of organic–inorganic perovskites for solar cells, and shows that the spectroscopic signatures for the same materials cannot be generalized because many of these signals depend on tiny differences in the perovskite material.

Conflicts of interest

There are no conflicts to declare.

Acknowledgements

References

1 http:/ww.nrel.gov/pv, National Renewable Energy Laboratory (NREL).

2 X. Li, D. Bi, C. Yi, J.-D. Décoppet, J. Luo, S. M. Zakeeruddin, A. Hagfeldt and M. Grätzel, *Science*, 2016, **353**, 58–62.

3 S. S. Shin, E. J. Yeom, W. S. Yang, S. Hur, M. G. Kim, J. Im, J. Seo, J. H. Noh and S. I. Seok, *Science*, 2017, **356**, 167–171.

4 J. S. Manser, J. A. Christians and P. V. Kamat, *Chem. Rev.*, 2016, **116**, 12956–13008.

5 J.-P. Correa-Baena, A. Abate, M. Saliba, W. Tress, T. Jesper Jacobsson, M. Gratzel and A. Hagfeldt, *Energy Environ. Sci.*, 2017, **10**, 710–727.

6 H. Wang, L. Whittaker-Brooks and G. R. Fleming, *J. Phys. Chem. C*, 2015, **119**, 19590–19595.

7 M. Szafrański and A. Katrusiak, *J. Phys. Chem. Lett.*, 2017, **8**, 2496–2506.

8 S. D. Stranks and H. J. Snaith, *Nat. Nanotechnol.*, 2015, **10**, 391–402.

9 H. Zhu, Y. Fu, F. Meng, X. Wu, Z. Gong, Q. Ding, M. V. Gustafsson, M. T. Trinh, S. Jin and X. Y. Zhu, *Nat. Mater.*, 2015, **14**, 636–642.

10 Z. Xiao, R. A. Kerner, L. Zhao, N. L. Tran, K. M. Lee, T.-W. Koh, G. D. Scholes and B. P. Rand, *Nat. Photonics*, 2017, **11**, 108–115.

11 G. Longo, A. Wong, M. Sessolo and H. J. Bolink, *J. Lumin.*, 2017, **189**, 120–125.

12 J. S. Manser and P. V. Kamat, *Nat. Photonics*, 2014, **8**, 737–743.

13 J. A. Christians, J. S. Manser and P. V. Kamat, *J. Phys. Chem. Lett.*, 2015, **6**, 2086–2095.

14 T. C. Sum, N. Mathews, G. Xing, S. S. Lim, W. K. Chong, D. Giovanni and H. A. Dewi, *Acc. Chem. Res.*, 2016, **49**, 294–302.

15 Y. Yang, M. Yang, D. T. Moore, Y. Yan, E. M. Miller, K. Zhu and M. C. Beard, *Nat. Energy*, 2017, **2**, 16207.

16 F. Deschler, M. Price, S. Pathak, L. E. Klintberg, D.-D. Jarausch, R. Higler, S. Hüttner, T. Leijtens, S. D. Stranks, H. J. Snaith, M. Atatüre, R. T. Phillips and R. H. Friend, *J. Phys. Chem. Lett.*, 2014, **5**, 1421–1426.

17 M. T. Trinh, X. Wu, D. Niesner and X.-Y. Zhu, *J. Mater. Chem. A*, 2015, **2**, 9285–9290.

18 K. Pydzińska, J. Karolczak, I. Kosta, R. Tena-Zaera, A. Todinova, J. Idígoras, J. A. Anta and M. Ziółek, *ChemSusChem*, 2016, **9**, 1647–1659.

19 G. Xing, N. Mathews, S. Sun, S. S. Lim, M. Lam, M. Grätzel, S. Mhaisalkar and T. C. Sum, *Science*, 2013, **342**, 344–347.

20 P. Piatkowski, B. Cohen, F. J. Ramos, M. D. Nunzio, M. K. Nazeeruddin, M. Grätzel, S. Ahmad and A. Douhal, *Phys. Chem. Chem. Phys.*, 2015, **17**, 14674–14684.

21 J. Leng, J. Liu, J. Zhang and S. Jin, *J. Phys. Chem. Lett.*, 2016, **7**, 5056–5061.

22 K. Pydzińska, P. Florczak, G. Nowaczyk and M. Ziółek, *Synth. Met.*, 2017, **232**, 181–187.

23 S. Hunsche, K. Leo, H. Kurz and K. Köhler, *Phys. Rev. B*, 1994, **49**, 16565–16568.

24 V. I. Klimov, *Ann. Rev. Phys. Chem.*, 2007, **58**, 635–673.

25 K. Wu, G. Liang, Q. Shang, Y. Ren, D. Kong and T. Lian, *J. Am. Chem. Soc.*, 2015, **137**, 12792–12795.

26 X. Wu, M. T. Trinh, D. Niesner, H. Zhu, Z. Norman, J. S. Owen, O. Yaffe, B. J. Kudisch and X. Y. Zhu, *J. Am. Chem. Soc.*, 2015, **137**, 2089–2096.

27 X. Wu, M. T. Trinh and X. Y. Zhu, *J. Phys. Chem. C*, 2015, **119**, 14714–14721.

28 M. Szafrański and A. Katrusiak, *J. Phys. Chem. Lett.*, 2016, **7**, 3458–3466.

29 A. Poglitsch and D. Weber, *J. Chem. Phys.*, 1987, **87**, 6373–6378.

30 T. Wróżowa, B. Ciesielska, D. Komar, J. Karolczak, A. Maciejewski and J. Kubicki, *Rev. Sci. Instrum.*, 2004, **75**, 3107–3121.

31 J. Idígoras, G. Burdziński, J. Karolczak, J. Kubicki, G. Oskam, J. A. Anta and M. Ziółek, *J. Phys. Chem. C*, 2015, **119**, 3931–3944.

32 M. Wendel, S. Nizinski, D. Prukala, M. Sikorski, S. Wybraniec and G. Burdzinski, *J. Photochem. Photobiol., A*, 2017, **332**, 602–610.

33 B. Anand, S. Sampat, E. O. Danilov, W. Peng, S. M. Rupich, Y. J. Chabal, Y. N. Gartstein and A. V. Malko, *Phys. Rev. B*, 2016, **93**, 161205.

34 K. G. Stamplecoskie, J. S. Manserab and P. V. Kamat, *Energy Environ. Sci.*, 2015, **8**, 208–215.

35 T. Du, C. H. Burgess, J. Kim, J. Zhang, J. R. Durrant and M. A. McLachlan, *Sustainable Energy Fuels*, 2017, **1**, 119–126.

36 L. Wang, C. McCleese, A. Kovalsky, Y. Zhao and C. Burda, *J. Am. Chem. Soc.*, 2014, **136**, 12205–12208.

37 M. Z. Mokhtar, M. Chen, E. Whittaker, B. Hamilton, N. Aristidou, S. Ramadan, A. Gholinia, S. A. Haque, P. O'Brien and B. R. Saunders, *Phys. Chem. Chem. Phys.*, 2017, **19**, 7204–7214.

38 S. D. Stranks, G. E. Eperon, G. Grancini, C. Menelaou, M. J. P. Alcocer, T. Leijtens, L. M. Herz, A. Petrozza and H. J. Snaith, *Science*, 2013, **342**, 341–344.

39 Y. Yang, D. P. Ostrowski, R. M. France, K. Zhu, J. van de Lagemaat, J. M. Luther and M. C. Beard, *Nat. Photonics*, 2015, **10**, 53–59.

40 M. B. Price, J. Butkus, T. C. Jellicoe, A. Sadhanala, A. Briane, J. E. Halpert, K. Broch, J. M. Hodgkiss, R. H. Friend and F. Deschler, *Nat. Commun.*, 2015, **6**, 8420.

41 K. Chen, A. J. Barker, F. L. C. Morgan, J. E. Halpert and J. M. Hodgkiss, *J. Phys. Chem. Lett.*, 2015, **5**, 153–158.

42 V. Roiati, E. Mosconi, A. Listorti, S. Colella, G. Gigli and F. De Angelis, *Nano Lett.*, 2014, **14**, 2168–2174.

43 Y. Zhang, J. Yin, M. R. Parida, G. H. Ahmed, J. Pan, O. M. Bakr, J.-L. Brédas and O. F. Mohammed, *J. Phys. Chem. Lett.*, 2017, **8**, 3173–3177.

44 C. Motta, F. El-Mellouhi, S. Kais, N. Tabet, F. Alharbi and S. Sanvito, *Nat. Commun.*, 2015, **6**, 7026.

45 J.-E. Moser, *Nat. Mater.*, 2017, **16**, 4–6.

46 E. M. Hutter, M. C. Gelvez-Rueda, A. Osherov, V. Bulovic, F. C. Grozema, S. D. Stranks and T. J. Savenije, *Nat. Mater.*, 2017, **16**, 115–120.

47 T. Etienne, E. Mosconi and F. De Angelis, *J. Phys. Chem. Lett.*, 2016, **7**, 1638–1645.

48 T. Kirchartz and U. Rau, *J. Phys. Chem. Lett.*, 2017, **8**, 1265–1271.

49 T. Wang, B. Daiber, J. M. Frost, S. A. Mann, E. C. Garnett, A. Walsh and B. Ehrler, *Energy Environ. Sci.*, 2017, **10**, 509–515.

Supporting Information

for

Differences in photoinduced optical transients in perovskite absorbers for solar cells

Katarzyna Pydzińska, [a] Jerzy Karolczak, [a,b]

Marek Szafrański [a] and Marcin Ziółek [a] [*]

[a] Faculty of Physics, Adam Mickiewicz University in Poznań,

Umultowska 85, 61-614 Poznań, Poland.

[b] Center for Ultrafast Laser Spectroscopy, Adam Mickiewicz University in Poznań,

Umultowska 85, 61-614 Poznań, Poland.

Figure S1. Photos of **NS1** (A left), **S2** (A right) and **C** (B) samples. Powdered crystal sample (sample **C**) was used in emission and steady-state reflectance experiments.
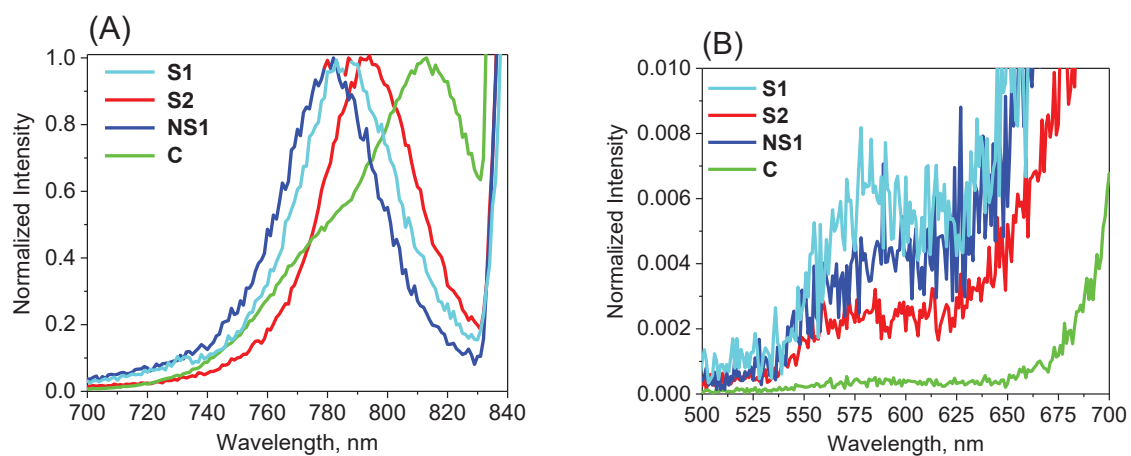
Figure S2. Normalized emission spectra of the samples studied in the long (A) and short (B) wavelengths regions.
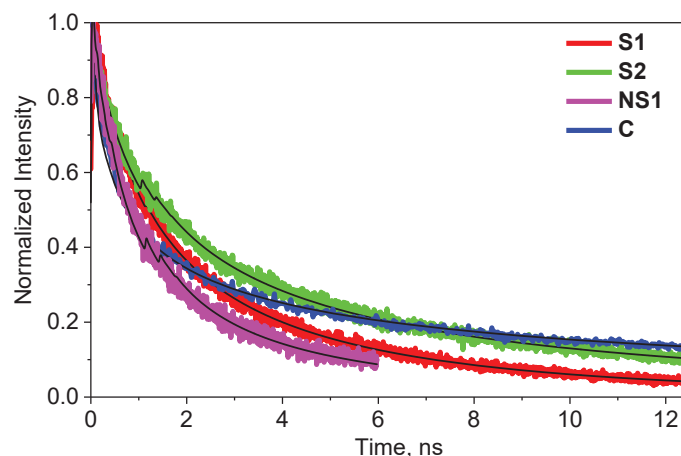
Figure S3. Emission decay kinetics at 780 nm of selected samples with fitted stretched exponential function (black line). Excitation wavelength was equal 420 nm. The initial decay of sample **C** was faster than for other samples, but the overall decay profile was much more stretched (β parameter significantly smaller than for other samples), therefore the average lifetime was the longest for sample **C** (Table 2).
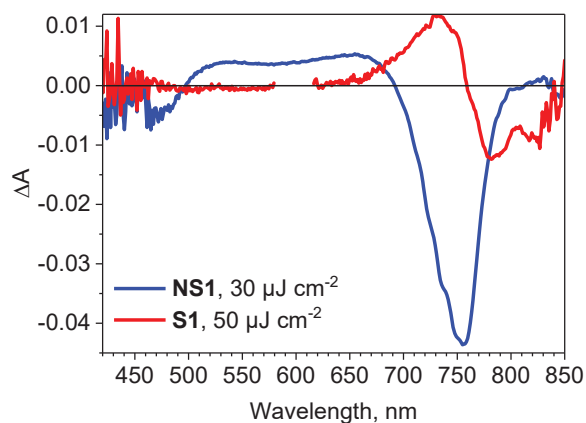
Figure S4. Transient absorption spectra 5 ps after excitation (λ_{ex}=600 nm) for a given sample and pump pulse energy density.
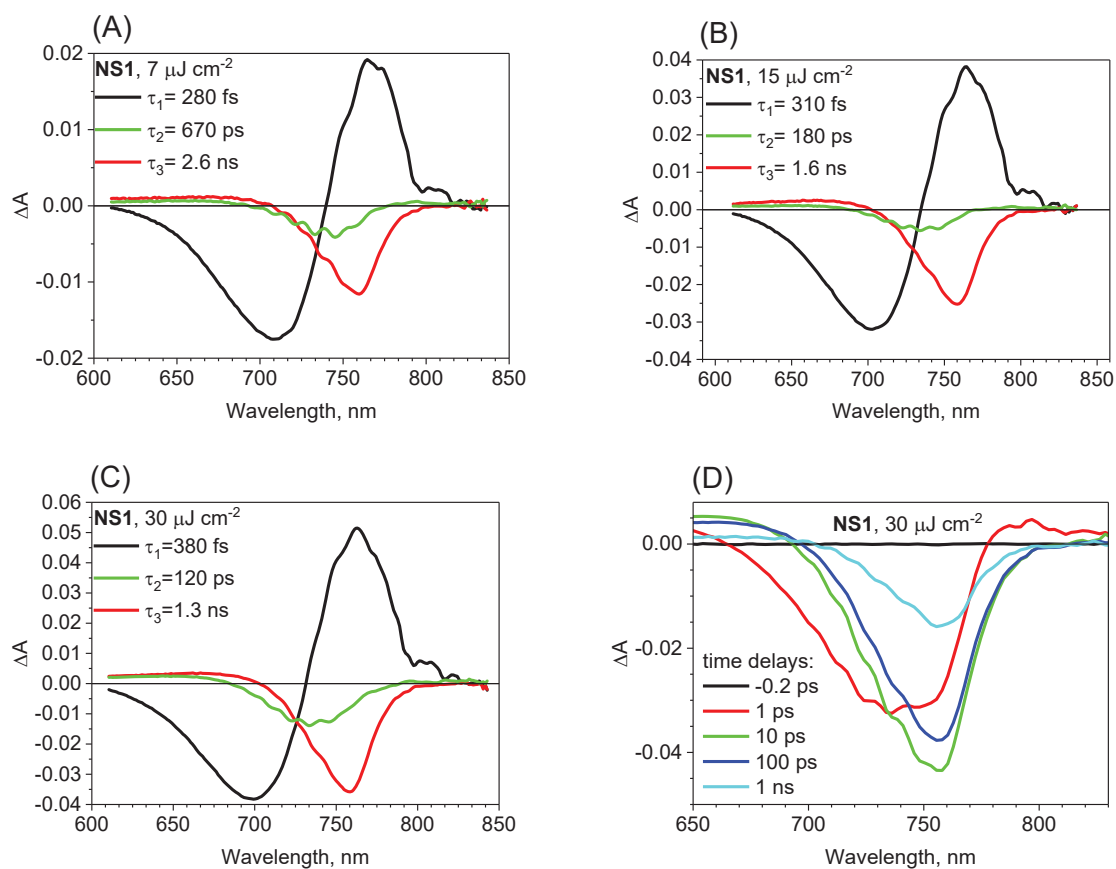
Figure S5. Global analysis of transient absorption for sample **NS1** for different pump pulse energy density (A-C). Selected transient absorption spectra at indicated time delays for the highest pump pulse energy density (D).

4
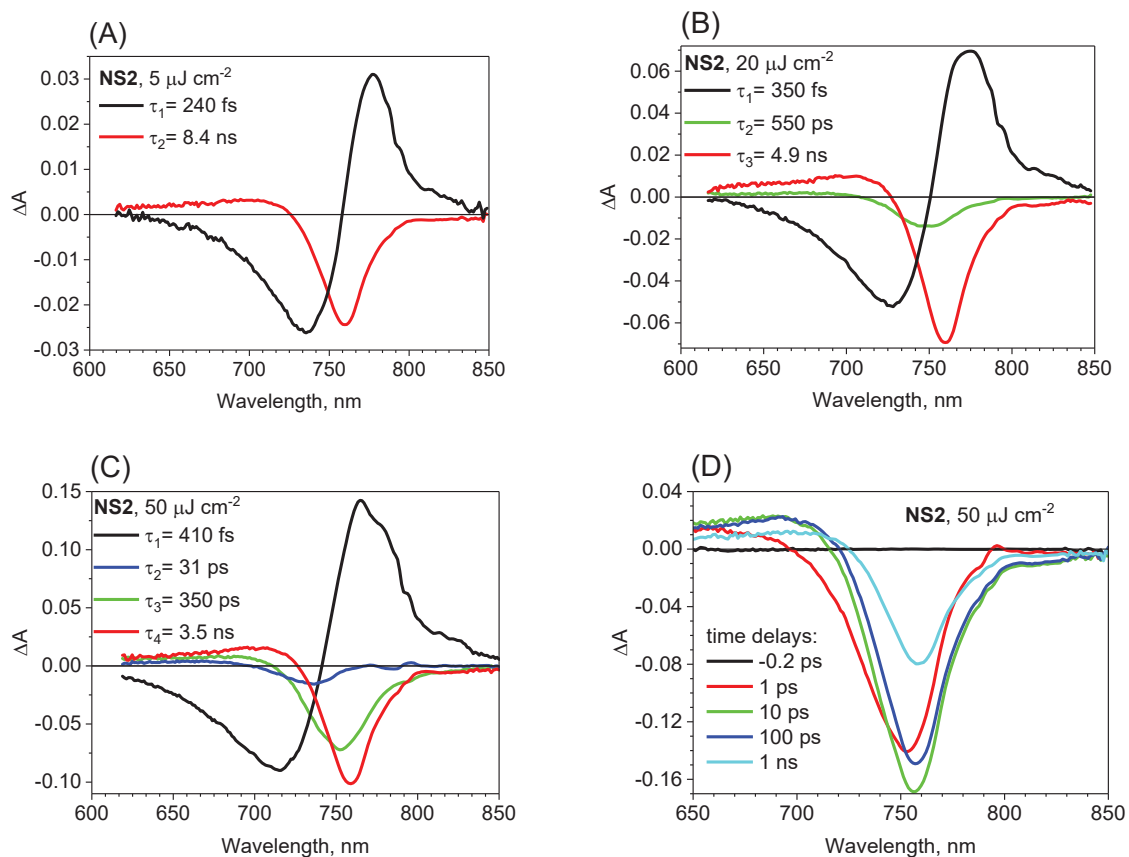
Figure S6. Global analysis of transient absorption for sample **NS2** for different pump pulse energy density (A-C). Selected transient absorption spectra at indicated time delays for the highest pump pulse energy density (D).
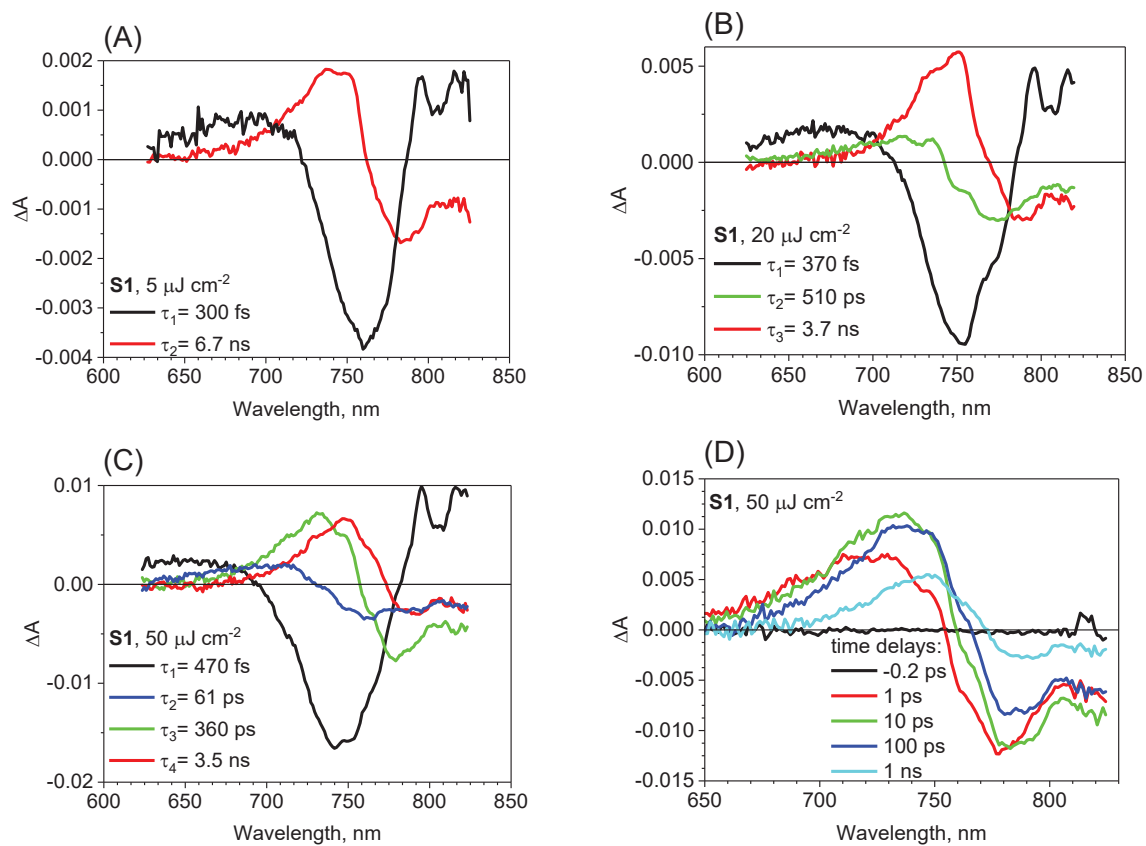
Figure S7. Global analysis of transient absorption for sample **S1** for different pump pulse energy density (A-C). Selected transient absorption spectra at indicated time delays for the highest pump pulse energy density (D).

6
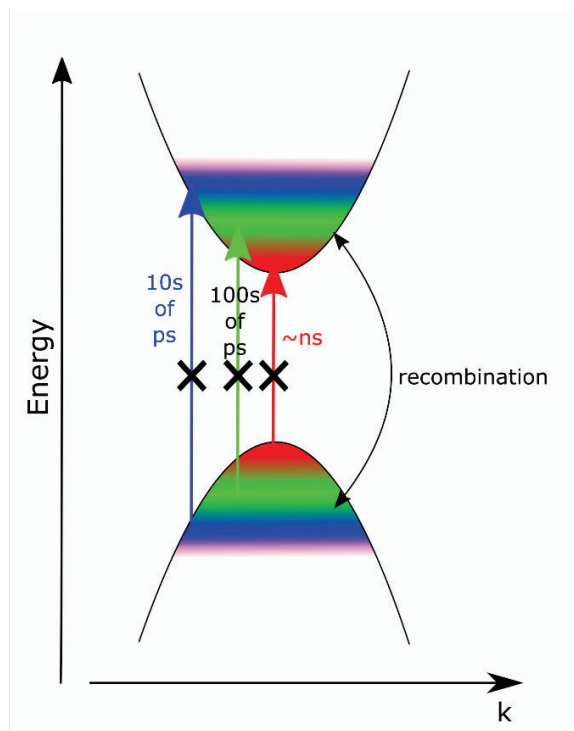
Figure S8. Schematic explanation of observed bleach band shifting due to band filling effect for the samples prepared in the non-stoichiometric way.
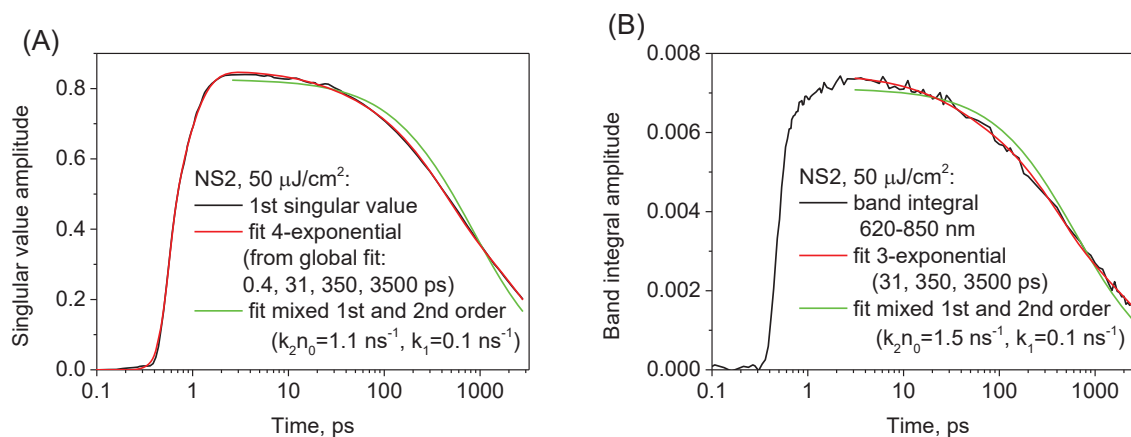
Figure S9. The comparison of the fit of mixed first and second order function and multi-exponential function for the exemplary sample showing second-order recombination (**NS2** at pump pulse energy density 50 $\mu J/cm^2$). The population decay n(t) described by the mixed function is the following: $n(t)=k_1 n_0 /(k_1 e^{k1\ t} + k_2 n_0 (e^{k1t}-1))$, where k_1 is the first order rate constants, k_2 is the second order rate constants, and n_0 is the initial population of the excited state. Figure (A) shows the fit to the first, dominant singular value of the transient absorption data, while in figure (B) the band integral of the same transient absorption data in the spectral range 620-850 nm is used [S.A. Kovalenko, R. Schanz, V.M. Farztdinov, H. Henning, N.P. Ernsting, *Chem. Phys. Lett*. 2000, **323**, 312].

KPB-3
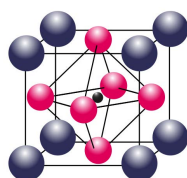
Insights into the femtosecond to nanosecond charge carrier kinetics in perovskite materials for solar cells

K.Pydzińska-Białek, J.Szeremeta, K.Wojciechowski, M.Ziółek

The Journal of Physical Chemistry C, 123 (2019), 110 – 119

Insights into the Femtosecond to Nanosecond Charge Carrier Kinetics in Perovskite Materials for Solar Cells

Katarzyna Pydzińska-Białek,[†] Janusz Szeremeta,[‡] Konrad Wojciechowski,[‡,§] and Marcin Ziółek*,[†]

[†]Faculty of Physics, Adam Mickiewicz University in Poznań, Umultowska 85, 61-614 Poznań, Poland

[‡]Saule Technologies and [§]Saule Research Institute, Wrocław Technology Park, Duńska 11, Sigma Building, 54-427 Wrocław, Poland

Ⓢ *Supporting Information*

ABSTRACT: In this work, we analyze a few simple methods that permit getting insight into the charge dynamics in methylammonium lead iodide (MAPbI$_3$) perovskites, on the basis of femtosecond transient absorption and fluorescence studies. We show that proper determination of the charge population decay kinetics requires broad spectral integration of the long-wavelength bleach signal (~760 nm) assigned to the band-filling effect, which can be realized, e.g., by band integral analysis. On the contrary, the kinetics related to a shorter-wavelength bleach band (~480 nm) behave differently: a single-wavelength decay is sufficient to probe charge population. Moreover, both the shorter-wavelength excitation and higher pump pulse intensities result in significantly longer charge cooling times, which might be important in efficient hot carrier extraction. The validity of our previously proposed easy approach for the elimination of higher-order recombination rates is also discussed and confirmed in terms of proper estimation of first-order decay rate constants. As an example, the rate constants of electron injection from MAPbI$_3$ to standard (6,6)-phenyl-C$_{61}$-butyric acid methyl ester (PCBM) material and the alternative PenPTC (also called PDI) and SPPO13 polymers are extracted and compared in inverted solar cells on the flexible substrate.
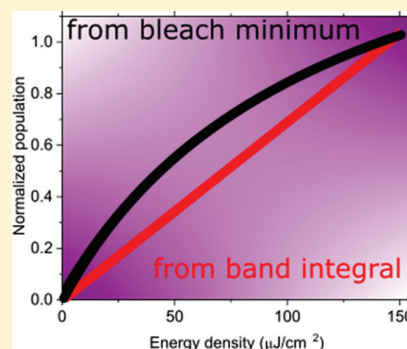
INTRODUCTION

Perovskite solar cells (PSCs) caught the attention of the scientific world through the revelation of their outstanding optoelectronic properties in 2009 by Miyasaka and co-workers.[1] Since that time, the knowledge about the nature of perovskite materials has greatly expanded and several milestone improvements in PSC operation led to reaching the certified efficiency equal to 23.3%.[2] However, many aspects of PSC operation are still not fully understood. Some of the important features that need further studies are the detailed dynamics of charge transfer after excitation[3−5] and the role of perovskite band-gap structure in charge separation.[6]

In a PSC, after light absorption, an electron is transferred to the conduction band (CB) of the perovskite, leaving a hole in the valence band (VB). The exciton dissociates relatively rapidly (<1 ps) into free charges, which cool down to the lowest energies in CB and VB, resulting in the bleach at long-wavelength absorption edge (band-filling mechanism, Scheme S1 in the Supporting Information).[7] The potential involvement of deeper CBs and VBs at short-wavelength excitation is also considered in the cooling mechanism.[8] It is essential that both electron transfer to electron-transporting material (ETM) and hole transfer to hole-transporting material (HTM) occur faster than various charge recombination processes within the perovskite material: first- (trap-assisted), second- (free carriers), or third-order (Auger).[3] Determination of kinetics of these processes is important to optimize the whole system and reach high efficiency of charge separation.

Ultrafast laser spectroscopy techniques such as transient absorption or time-resolved emission spectroscopy are commonly used to study charge recombination processes within perovskites[7,9−11] or the rates of carrier transfers to ETM and HTM.[12−16] However, there is a large spread of approaches to such studies, both in the selection of proper experimental data and application of the correct model to fit these data. As for the representative data, in the simplest methods, single kinetics at minimum bleach or maximum emission are considered,[7,17,18] whereas broad-band analysis, frequently supported by global analysis and the set of measurements under different pump fluences, is employed in other studies.[19−22] Moreover, the data treatment can be based on multiexponential analysis,[23] analytical solutions of kinetic equations of higher-order reactions,[22,24−26] or much more complex models using numerical integration of rate equations,[24] including charge diffusion in perovskite material,[12] and, very recently, reabsorption effect.[27] Despite more strict considerations, the complex models are often not easy to implement and require a lot of additional parameters that might influence the final results. Therefore, one of the main objectives of our current study is to test a couple of simplified protocols to determine charge carrier dynamics in methylammonium lead iodide (MAPbI$_3$) perovskites on the time

Article

scale from femtoseconds to nanoseconds, and to check to which extent they can provide correct results.

In this contribution, we tested MAPbI$_3$-based inverted PSCs with different ETM such as (6,6)-phenyl-C$_{61}$-butyric acid methyl ester (PCBM), N,N'-dipentyl-3,4,9,10-perylene dicarboximide (PenPTC), 2,7-bis(diphenylphosphoryl)-9,9'-spiro-bifluorene (SPPO13), and poly(3,4-ethylenedioxythiophene):-polystyrene sulfonate (PEDOT:PSS) as HTM on the conductive foil. Additionally, samples without HTM (perovskite was deposited on a nonconductive glass) were measured. Charge-transfer rates to different ETMs and second-order recombination rates were determined. According to our knowledge, SPPO13 polymers have been studied for the first time in inverted perovskite cells, whereas PenPTC (called also PDI) has been recently introduced.[28] The efficiency of such solar cells with PenPTC was even slightly higher than those with PCBM, but the introduction of methylammonium bromide to MAPbI$_3$ was necessary to better align the energy levels.[28]

In our previous contribution, we proposed a simple transient absorption protocol to determine charge injection rates and radiative recombination in a PSC system, through the collection of appropriate rate constants as a function of pulse energy.[23] In this work, we test this approach through a simulation of mixed-, first- and second-order decay and fit with a monoexponential decay function.

■ MATERIALS AND METHODS

Solar Cell Preparation. Two kinds of samples were prepared: full solar cells on a poly(ethylene terephthalate) (PET) foil and reference samples without hole-transporting material on a nonconductive glass. For solar cell devices, substrates cut out from 60 Ω/sq indium tin oxide (ITO) on a PET foil were cleaned by sonication in detergent, isopropanol, and deionized (DI) water; dried on a hotplate; and O$_2$ plasma-treated for 1 min, and then coated with ca. 40 nm thick poly(3,4-ethylenedioxythiophene:polystyrene sulfonate (PE-DOT:PSS), Heraeus Al4083) layer spun at 3000 rpm for 30 s in air. The layer was annealed on the hotplate at 95 °C for 1 h, and then the substrates were transferred to the glovebox. MAPbI$_3$ layers (perovskite precursor ink composition: Saule Technologies proprietary information) were deposited in N$_2$ atmosphere by one-step spin-coating process from the precursor solution, followed by an annealing step to induce crystallization and obtain ca. 150 nm brownish shining perovskite layers. Then, a 30 nm (6,6)-phenyl-C$_{61}$-butyric acid methyl ester (PCBM, Lumtec), 10 nm N,N'-dipentyl-3,4,9,10-perylene dicarboximide (PenPTC, Lumtec), or 30 nm 2,7-bis(diphenylphosphoryl)-9,9'-spirobifluorene (SPPO13, Lumtec) layer was spin-coated at 2000 rpm for 30 s from chlorobenzene solution. Concentrations of the as-prepared PCBM and SPPO13 solutions were 20 mg/mL, while for PenPCT it was 5 mg/mL because of its lower solubility. Solutions were filtered by PTFE 0.45 μm syringe filters prior to application on the samples. Then, the devices were finished by thermal evaporation of 5 nm of bathocuproine and 100 nm of Ag through a shadow mask at a base pressure of 10^{-6} bar. The surface area of each device was 0.12 cm^2 with four devices per substrate. Glass substrates for the reference samples were prepared by cleaning by ultrasonication in detergent, acetone, and DI water; drying on a hotplate; and plasma-treating before deposition. Then, a perovskite layer was spun in inert atmosphere inside a glovebox directly on the glass and a

PCBM, PenPTC, or SPPO13 layer was spin-coated on the top. Spin-coating conditions were analogous as for the tested devices. The perovskite layer thickness was equal to 150 nm for full devices as determined by a Bruker Dektak XT profilometer. The thickness of the perovskite on glass samples was estimated to be 110 nm from the comparison of the absorbance values at 600 nm. Highest occupied molecular orbital and lowest unoccupied molecular orbital levels of examined ETM were −6.1 and −3.7 eV (vs vacuum) for PCBM,[29] −6.56 and −2.91 eV for SPPO13,[30] and −5.83 and −3.82 for PenPTC, respectively.[28]

Solar Cell Characterization. J−V curves of the cells were measured using a 2400 Keithley source meter under 1 sun AM1.5G illumination (100 mW/cm^2) by a solar simulator (ABET Technologies Sun 2000, class AAA). The lamp was calibrated with a silicon reference cell RR-208 with a KG5 filter window from ReRa Solutions. The active area of the device was defined by a metal mask with the aperture area of 0.0914 cm^2. The highest efficiency obtained for the device with PCBM was 10.2%, whereas the efficiency of the devices with PenPTC was up to 2.6% (Figure S1 and Table S1). All samples with SPPO13 were isolated and did not show diode characteristics.

Ultrafast dynamics were determined using a broad-band transient absorption setup (Helios spectrometer, Ultrafast Systems, and Spectra Physics laser system), described before.[31] The IRF (pump−probe cross correlation function) was about 200 fs (full width at half-maximum), and transient absorption measurements were performed in the time range of up to 3 ns. Two excitation wavelengths were tested: 485 and 600 nm, and the spectra were probed in the range of 440−820 nm. The studies were performed for the pump pulse energy varying from 5 to 300 nJ, which corresponded to the pump pulse energy density changes from 2.5 to 150 μJ/cm^2.

Supplementary time-resolved emission measurements were performed using two different setups based on time-correlated single-photon counting technique (TCSPC). The first had a temporal resolution of tens of picosecond for perovskite materials studies,[32] with the excitation at 420 nm, and perovskite emission was detected from 740 to 820 nm. The same setup was used to record steady-state emission spectra. The second setup (Edinburg Instruments Spectrophotometer FS5 with a 5 mW, 52 ps laser diode EPL-405) with nanosecond resolution was used to measure the long-time-scale kinetics. The excitation wavelength was set at 405 nm, and the emission was observed at 775 nm. The emission decays showed non-single-exponential character; therefore, the averaged lifetimes were determined either from a stretched exponential fit[23] or from amplitude-weighted average of three-exponential decay components.

■ RESULTS AND DISCUSSION

Simulations. The general formula for the decay of the charge population density n in perovskites due to charge recombination is the following[3,7]

$$-\frac{dn}{dt} = k_1 n + k_2 n^2 + k_3 n^3 \tag{1}$$

where k_1, k_2, and k_3 are the first-, second- and third-order recombination rate constants. The neglect of the third-order (Auger) recombination leads to the simplified equation[25]

$$-\frac{dn}{dt} = k_1 n + k_2 n^2 \tag{2}$$

111
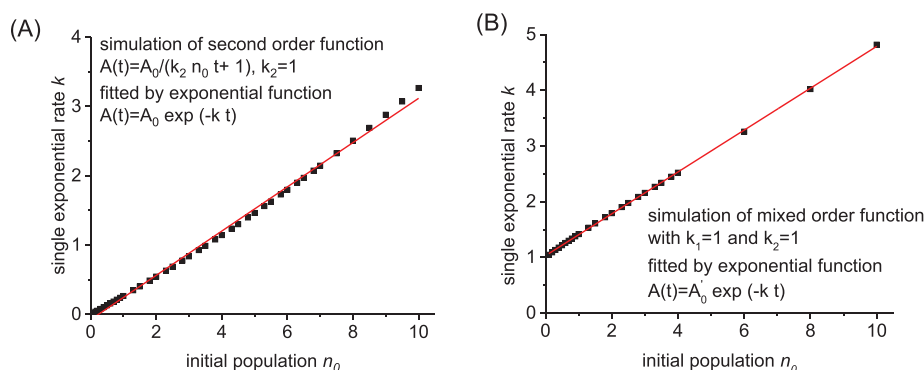
Figure 1. Results of rate constants obtained by fitting the simulated (A) second-order and (B) mixed-order decay functions by a single-exponential function (black squares). The linear fit is also shown (red line).

The first-order decay is related to the trap-assisted recombination (Shockley−Read−Hall recombination), whereas the second-order process to free carrier recombination. It should be noted that recently much more complex equations have been proposed that include the effects of charge diffusion and reabsorption.[7,27] However, their solution requires the numerical integration approach, whereas eq 2 can be solved in the form of the analytical function that can be easily implemented in kinetic fitting procedures. Charge transfer to contact materials is usually considered as a first-order process[3,7,33] so its rate constants increase the apparent values of k_1.

In our previous contribution, we have proposed a simple way to separate the first- and second-order decay observed in perovskite samples by broad-band transient absorption measurements.[23] This method was based on the determination of the average rate constant k of the transient absorption signal decay as a function of pump pulse intensity I (proportional to the created initial charge population density n_0), where the rate k was calculated as the reciprocal of time constant obtained in the global analysis using singular value decomposition (SVD) and fitting of one-exponential function to the principal kinetic vectors. (Strictly speaking, two-exponential function was fitted, but the faster, sub-picosecond component of transient absorption shift was due to charge cooling and was easily separated from the transient absorption decay.) The simplicity of this method relies on the fast and common multiexponential fitting routines implemented in broad-band global analysis. The dependence of $k(I)$ on I was shown to be linear up to the intensities of 100 μJ/cm^2.[23] Therefore, by fitting with the simple linear function

$$k(I) = k_1' + k_2'I \tag{3}$$

the separation of first-order rate constant k_1' from the second-order processes could be achieved. We used the intercept values k_1' for the determination of the charge-transfer rate constants from the perovskite to contact hole- and electron-transporting materials.[23]

However, the above simple formula 3 is not a strict solution of the rate eq 2. Therefore, here we performed simulations to establish the relations between the rate constants k_1', k_2' in eq 3 and the true first- and second-order rate constants k_1 and k_2 in eq 2. At first, we simulated the decay of the signal amplitude according to the second-order process only ($k_1 = 0$), which is given by the analytical formula

$$A(t) = \frac{A_0}{(n_0 k_2 t + 1)} \tag{4}$$

In this and further formulas, the amplitude of the initial signal A_0 is proportional to the initial population n_0. Such second-order decays with varying initial population n_0 were fitted with the single-exponential function $A(t) = A_0'\exp(-kt)$, yielding average rates k. The plot of $k(n_0)$ presented in Figure 1A shows a good linear correlation. The intercept (k_1') is close to zero, which means that $k_1' \approx k_1$, whereas the slope (k_2') is smaller than k_2 ($k_2' \approx 0.3\ k_2$ in this case).

Next, the analytical solution for eq 2 in the form of mixed first- and second-order kinetics was simulated

$$A(t) = \frac{A_0 k_1}{(k_1 \exp(k_1 t) + n_0 k_2(\exp(k_1 t) - 1))} \tag{5}$$

This function has been recently used to fit the emission decay in efficient perovskite cells.[24,25] Figure 1B shows the rate constants of single-exponential fit to the above mixed-order function for different n_0. Similarly as for a pure second-order function shown in Figure 1A, the plot of $k(n_0)$ is to a good approximation linear. The intercept close to k_1 value ($k_1' \approx k_1$), see Figure 1B. However, the slope is again different from k_2 ($k_2' \approx 0.4k_2$).

The above simulations were performed for the second- or mixed-order kinetics decaying to zero. We also checked the influence of the narrowing of the time window available for fitting when the simulated function did not decay to zero. It corresponds to the situation when the decay of charge population in perovskites (approximated by a single-exponential function fit) exceeds the temporal range of the transient absorption experiment. In such a situation, the intercept values were still similar to k_1 but the slope values increased with an increasing residual signal because the second-order decay was flattened at a longer time with respect to the first-order decay. For example, $k_2' \approx 0.6k_2$ for residual amplitude equal to 5% of the initial one, and $k_2' \approx 1.0k_2$ if the analyzed mixed-order function decayed to 25% of the initial amplitude (see Table S2 for more values).

To summarize this part, although the exponential function does not properly describe the nonlinear processes given by eq 2, the approximation based on the single-exponential fit at different pump pulse intensities and analysis based on eq 3 may be useful in many situations. The intercept values (k_1') of linear fits from eq 3 properly estimate the first-order rate constant k_1. However, the values of slope (k_2') are not equal to

117

Article
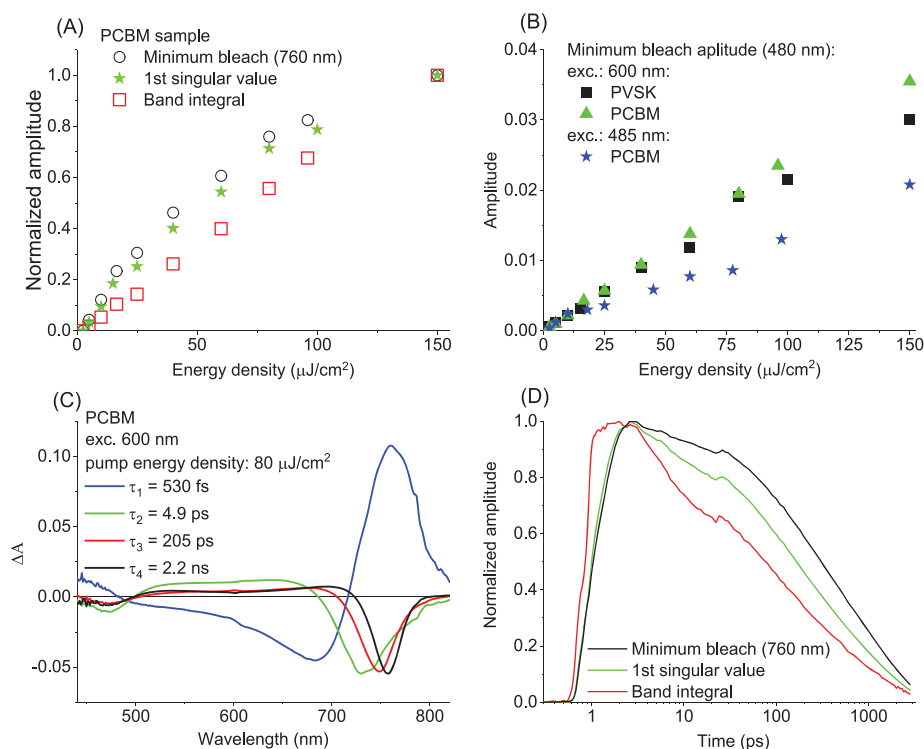
Figure 2. (A) Comparison of the amplitudes at minimum red bleach wavelength after 2 ps (circles), band integral (BI, squares), and first singular value multiplied by maximum of its kinetics (stars) for full devices with PCBM as ETM. (B) Dependence of the amplitude of a bleach (~480 nm) signal on the excitation energy for different devices and the excitation wavelength. (C) Pre-exponential factor spectra obtained from global analysis for a device with PCBM as ETM. (D) Example kinetics obtained for the glass sample for the excitation energy equal to 40 $\mu J/cm^2$; band integral was calculated from 610 to 850 nm wavelength range.

the second-order rate constants. They are approximately proportional to k_2, but if the observed decay goes beyond the temporal window, the proportionality coefficient changes.

Proper Kinetics. For precise determination of the second-order recombination rate constant k_2 using the analytical formula 5, a proper kinetics describing the charge population decay in perovskites is necessary. We have tested several approaches to find an appropriate signal processing method using the MAPbI$_3$ perovskite samples both deposited on glass (without hole-transporting material, HTM) and in a full inverted cell configuration. The typical kinetics used in transient absorption analysis of perovskites are probed at the strong bleach signal at the long-wavelength absorption onset, assigned to the band-filling mechanism (also called the state filling or Burstein−Moss shift).[7] It was shown that an amplitude of this signal depends both on the population of photoexcited electrons in the conduction band and the population of holes in the valence band.[12,34,35] It is because, in the case of band filling, the transient bleach occurs because of either the lack of electrons in the valence band or their occupation of the conduction band, which both block the possible electronic transition from the high-energy states in the valence band to the low-energy states in the conduction band. A difference in the nature of the bleach signal in perovskites and the typical bleach signal in molecular spectroscopy (mimicking the whole ground-state absorption spectrum) should be emphasized.

Thus, the kinetics at the minimum of the negative bleach band signal in transient absorption spectrum is frequently used for the charge population analysis. However, we have observed

that the amplitude at bleach minimum changes linearly with the pump pulse intensity only for small intensities (up to ~20 $\mu J/cm^2$), and for higher intensities, saturation takes place (Figure 2A). This means that such a kinetics is not proportional to the population of photoexcited carriers. It is because the band filling occurs at higher-energy states with an increasing charge population (see Scheme S1), so the bleach band minimum shifts and the bleach bandwidth changes. Figure S2 shows the examples of the shift of the initial bleach band minimum to a shorter wavelength and the broadening of the bleach bandwidth with increasing excitation intensity. We have observed that the bleach bandwidth (in energy units) grows approximately linearly with the pump pulse intensity. For example, at pump intensity 100 $\mu J/cm^2$, the initial bleach minimum (measured 5 ps after excitation) is shifted to the blue by 10 nm and the band is broadened about twice with respect to that at low intensities (Figure S2). Moreover, the bleach broadening occurs on the short-wavelength part (Figure S2).

To better explain the mechanism of the bleach band changes, we again took advantage of the multiexponential global analysis of transient absorption spectra. The results are presented in Figure 2C for relatively high excitation intensity. The fastest component (sub-picosecond) having bleach band derivative shape is due to charge cooling and will be discussed later. The other, longer components have the typical bleach band shape but with minima at different wavelengths; the shorter the component, the greater the blue shift of the spectrum. That is because at shorter times, the band filling affects the more short-wavelength transitions. During recombination, the charge population decreases and the band filling
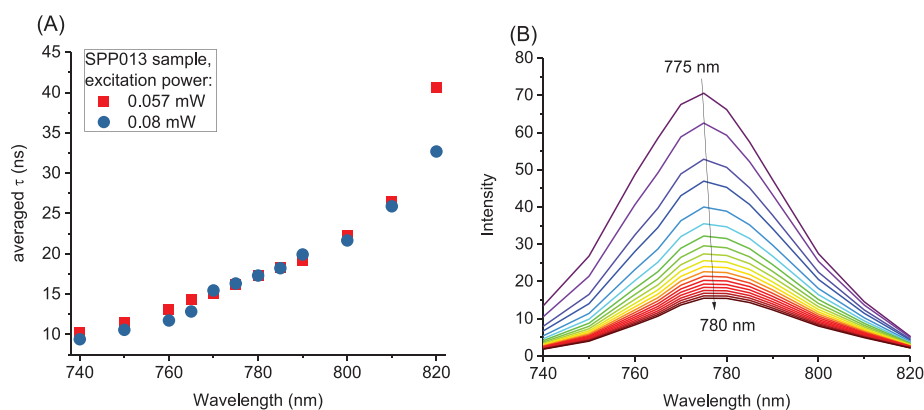
Figure 3. (A) Averaged fluorescence lifetimes and (B) time-resolved emission spectra for delays from 5 ps to 17 ns (delay times shown: 5, 100, and 500 ps and 1−17 ns with 1 ns increment) for full device with SPPO13 as ETM.

influencing the higher transition energies disappears, so the fastest recombination kinetics appear on the blue side of the bleach band. Therefore, the kinetics at the bleach band minimum (around 760 nm at low excitation intensities) might not show the fastest deactivation processes when measured above sufficiently high excitation intensity.

A similar situation might occur in the emission analysis. We have performed the TCSPC measurements at different emission wavelengths within the perovskite fluorescence band (Figures 3 and S3). The averaged lifetime (from a stretched exponential fit[23]) shows a continuous increase from ~10 to ~30 ns when changing the observation wavelength from 740 to 820 nm (the half decays increase from ~1 to ~10 ns), and the maximum of time-resolved emission spectra shifts from 775 nm just after excitation to 780 nm at the end of the temporal window of the experiment (17 ns). Similarly, as in the transient absorption experiment, our explanation is that at different wavelengths, the band filling at different stages is probed (more energetic transitions are monitored at shorter wavelengths). The effect is less pronounced than in transient absorption and is visible on a longer time scale, probably because of lower excitation intensity in the TCSPC experiment. Nevertheless, it shows that, in principle, single-wavelength analysis might not be correct also in the emission studies.

Therefore, if one wants to get the precise information about charge population decay in perovskites, the proper integration of the bleach band in transient absorption or the emission band in time-resolved fluorescence studies is necessary. One way of getting the spectrally averaged kinetic evolution of the transient absorption signal is the determination of the principal kinetic vector by singular value decomposition (SVD) analysis, which is often implemented in global analysis routines.[36,37] We investigated the dependence of the amplitude of the kinetic component associated with the first principal value on the pump pulse intensity (Figure 2A). The linearity is maintained up to higher intensities ($\sim$50 μJ/cm^2) than for the amplitude at bleach minimum, but still for higher intensities, the saturation takes place. It means that for those intensities more principal components must be considered to properly describe the charge population decay; thus, having the single representative kinetic is also not possible in this approach.

Finally, we calculated the so-called band integral (BI) of the transient absorption spectra in the range 610−850 nm. BI is defined as[38]

$$BI(t, \Delta\lambda) = \int \Delta A(t, \lambda) \frac{d\lambda}{\lambda} \quad (6)$$

where the integration of the transient absorption signal ΔA is performed over the spectral range $\Delta\lambda$. This quantity was introduced to classical transient absorption studies of molecules in solution.[38] The integral calculated over the entire band is insensitive to the spectral shift of the band, and reflects population dynamics if the oscillator strengths of optical transitions do not change. For our perovskite samples, we observed that the initial BI amplitude undergoes linear changes with the excitation intensity in the whole investigated intensity range (Figure 2A). Therefore, BI analysis is the most proper way to show the single kinetics representing the photoexcited charge population decay in perovskites. It should be noted that the analysis based only on the amplitude at the bleach minimum often brought about the conclusion about the saturation of carrier concentration,[7,39] which might not be correct, so the band integral analysis or equivalent broad-band integration should be rather used. Figure 2D presents a comparison of the kinetics obtained in the three investigated approaches, obtained for relatively high pump pulse intensity. The decay of a transient absorption signal at bleach minimum is the slowest because it loses the information about the fast population decay contributing to the blue part of the bleach signal. The principal kinetic vector from SVD analysis shows faster decay because it is more spectrally averaged, but it still does not take into account the fastest charge recombination dynamics occurring at high excitation intensities. The fastest, true charge population kinetics is obtained by BI in 610−850 nm range. Therefore, analytical function 5 should be fitted to this kinetics to determine the true second-order recombination rate constant, and the results will be presented in the next section.

Determination of Rate Constants. As concluded in the previous section, the mixed first- and second-order function, given by eq 5, was used to fit the BI transient absorption data calculated from eq 6. The aim was to determine the second-order rate constant k_2. The initial charge population density n_0 for different samples of transmittance T (which is related to absorbance according to $A = -\log(T)$) measured at different excitation densities I was calculated from

$$n_0 = \frac{I(1 - R - T)}{lh\nu} \quad (7)$$
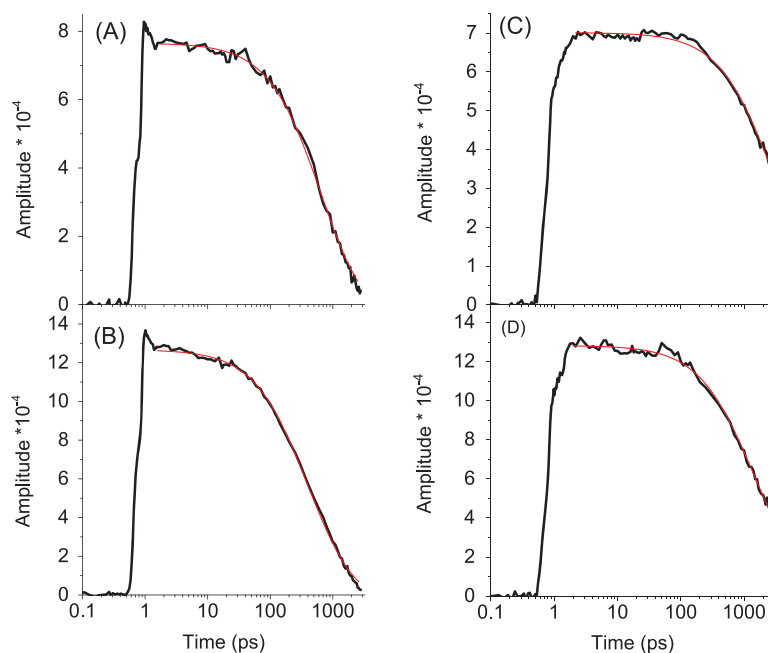
Figure 4. Mixed-order functions (red) fitted to BI in the range 610−850 nm (black) of a PCBM sample (A, B) on the glass and (C, D) in full devices for the excitation energy equal to (A, C) 10 $\mu J/cm^2$ and (B, D) 15 $\mu J/cm^2$.

where the penetration depth l for excitation at 600 nm was taken as the sample thickness, reflectance was taken as $R = 0.1$, and $h\nu$ is the photon energy of a pump.

Figure 4 presents the exemplary fits. Important differences were observed for the two sample series. The first series (glass/MAPbI$_3$/ETM) was prepared by direct deposition of a perovskite layer on glass, and covered with different electron-transport materials (ETM): PCBM, PenPTC, or SPPO13. The second series were full cells in an inverted configuration (ITO/PEDOT:PSS/MAPbI$_3$/ETM), where the perovskite layers were formed on hole-transporting materials. In both series, the test samples without any ETM were also prepared. The crystallinity and homogeneity of the perovskite layer were much better in full devices. On the XRD pattern (Figure S4) recorded for the first series of samples, one can observe a PbI$_2$ peak, which is not visible for the full cells. This lead iodide can originate from not fully converted precursors and passivate the surface of crystal domains creating the trap states. Additionally, peaks of the (110) and (220) planes are about twice as intense for full devices than for the perovskite on glass, which suggests larger and better developed crystals. Scanning electron microscopy (SEM) images taken with a Phenom ProX Desktop Scanning Electron Microscope can be found in the Supporting Information section (Figure S5). Pictures were taken with 5 kV acceleration speed, and the resolution is not good enough to quantify the size of the crystal domains, but the homogeneity of the perovskite layer in full devices is much better than in the case of glass samples. For the first series, the fit quality was sufficient for excitation intensities only up to 15 $\mu J/cm^2$, whereas for the second series, eq 5 could be used up to much higher intensities, 40 $\mu J/cm^2$. Most probably, above these intensities, the third-order recombination should be taken into account (full eq 1 holds instead of eq 2). Interestingly, if it is true, it means that in the higher-quality perovskite layers, the energy threshold at which the Auger recombination occurs is higher.

Similarly, the determined second-order recombination rates were also different. In the first sample series, the averaged k_2 values were $k_2 = (8.9 \pm 1.0) \times 10^{-10}$ cm^3/s when both k_1 and k_2 in eq 5 were left free during the fitting procedure. A slightly smaller relative error in the second-order rate constant was found when a fixed k_1 was used: $k_2 = (7.7 \pm 0.6) \times 10^{-10}$ cm^3/s. In this case, k_1 values were determined from the intercept points of $k(I)$ plots, according to the linear fit with eq 3. As we proved in the first section, the intercept points showed correct k_1 values of the decay modeled by function 5. The examples of such plots are given in Figure S6. In contrast, the second-order rate constants were found to be significantly (more than twice) smaller for the second series of samples. The averaged value of the rate constants was $k_2 = (3.6 \pm 0.3) \times 10^{-10}$ cm^3/s. This difference can also be visualized in the plots of d(BI)/dt versus BI for the two sample series (Figure S7). Again, the better crystal morphology of the perovskite material in full cells (second series) could account for the smaller contribution of second-order recombination processes. Another possibility is that in full cells the probability of recombination decreases. It is because of the generated built-in potential, the holes and electrons are stronger shifted toward the respective contact materials, which decreases the concentration of the electrons and holes being in close proximity (that would lead to recombination). It can also account for the occurrence of the third-order recombination at higher intensities in the full cells, as observed above. The difference in averaged perovskite thickness in both our sample series should also be considered (110 vs 150 nm). Decrease in extracted k_2 values with increasing layer thickness has been reported previously,[12] and recently, reabsorption effects were shown to play an important role in the charge distribution, spreading the charge population over a larger volume in thicker samples, making the apparent second-order recombination rate smaller.[27]

One of the purposes of our work was also the determination of the electron transfer rate constants from MAPbI$_3$ to
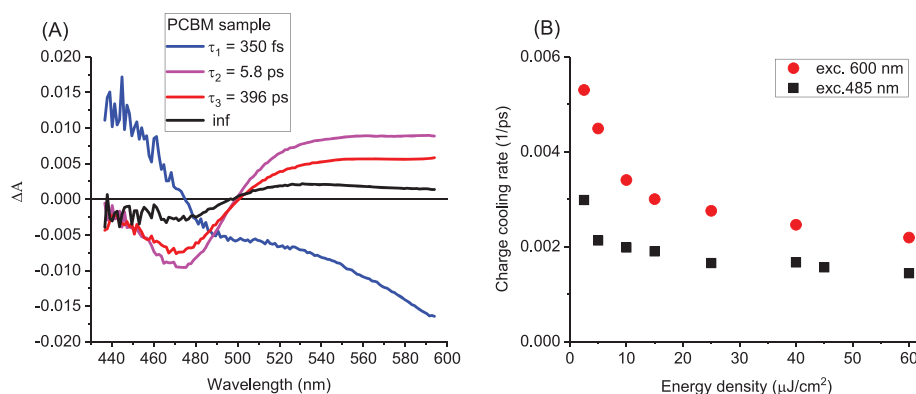
Figure 5. (A) Pre-exponential factor spectra obtained from multiexponential global analysis of blue-bleach (~480 nm) region for full cell with PCBM as ETM (for λ_{ex} = 600 nm and energy was equal to 80 $\mu J/cm^2$). (B) Charge cooling rate (the highest constant rate from global analysis) as a function of excitation energy for 600 nm (dots) and 485 nm (squares) excitation wavelengths.

different contact materials studied. It can be performed by comparison of the first-order rate constants.[23] It should be pointed out that the charge-transfer rate constants determined in this way contain both the contribution of charge diffusion to the interfaces and the intrinsic interfacial electron injection.[12] The rate constants in the first series of samples were the following: k_1 (no ETM) = 0.37 ± 0.13 ns^{-1}, k_1 (PCBM) = 0.61 ± 0.10 ns^{-1}, k_1 (PenPTC) = 0.44 ± 0.06 ns^{-1}, and k_1 (SPPO13) = 0.33 ± 0.17 ns^{-1}. The perovskite samples covered with SPPO13 can be treated as the reference materials because the energy levels of this material do not allow electron transfer. That is why we can calculate that the electron transfer rate constant to PCBM (equal to k_1(PCBM) − k_1(SPPO13) = 0.28 ns^{-1}) is about 2.5 times higher than that to PenPTC (k_1(PenPTC) − k_1(SPPO13) = 0.11 ns^{-1}). The k_1 values for the test sample, which was not covered by any material, were higher than those for SPPO13 probably because the direct contact of $MAPbI_3$ with air resulted in the generation of additional recombination centers on the perovskite outer surface. On the contrary, the passivation effect of processing SPPO13 on the top of perovskites could result in the reduction of surface defects in perovskites and surface recombination in this sample.[40] The obtained transient absorption results were further supported by the supplementary emission studies on much longer, nanosecond time scale, probing the residual kinetics not observed in the transient absorption window (up to 3 ns). The obtained averaged rates were the following: k_1 (no ETM) = 0.06 ns^{-1}, k_1 (PCBM) = 0.34 ns^{-1}, k_1 (PenPTC) = 0.03 ns^{-1}, and k_1 (SPPO13) = 0.02 ns^{-1}. They confirm the slowest decay for SPPO13 with a contribution of components of tens of ns, and the fastest rate for PCBM (a small contribution of slow emission decay components).

The obtained electron transfer rate constant from $MAPbI_3$ to PCBM in our samples (0.28 ns^{-1}) is in general agreement with previous reports. In the previous photoluminescence studies, the perovskite lifetime, upon addition of the PCBM contact, was shortened from 280 to 6 ns (for a mixed-halide perovskite) and from 10 to 3 ns (for a tri-iodide perovskite), which gave an electron transfer rate constant of 0.16 and 0.23 ns^{-1}, respectively.[41] The photoluminescence lifetimes of glass/ $MAPbI_3$/PCBM samples were also shown to decay on the nanosecond time scale.[42] Time-resolved microwave conductivity experiments revealed the electron transfer rate constants of 0.3 ns^{-1}.[43] Time constants of electron transfer to PCBM

were reported to be from hundreds of picoseconds to several nanoseconds on the basis of terahertz spectroscopy studies.[44] The transient absorption studies showed the electron transfer time constants of 0.4 ns.[8] Partial electron injection to PCBM with much faster time constants (single picosecond) was also reported in other transient absorption experiments.[45] The relatively large spread of the reported values can be probably explained by the fact that the intrinsic interfacial electron injection rate constant to PCBM might be as fast as 170 ns^{-1}, whereas the apparent rate constants might be limited by the electron diffusion in the perovskite material.[12] Therefore, it can strongly depend on the perovskite film thickness and quality.

Surprisingly lower first-order rate constants were found in the second series when the perovskite was prepared on HTM material. In this case, we obtained k_1 (no ETM) = 0.19 ± 0.02 ns^{-1}, k_1 (PCBM) = 0.15 ± 0.02 ns^{-1}, k_1 (PenPTC) = 0.18 ± 0.02 ns^{-1}, and k_1 (SPPO13) = 0.17 ± 0.02 ns^{-1}. The average perovskite thickness in these samples was greater, which might partly explain lower rates. However, the presence of HTM might have a crucial impact. If the holes are mainly located near the $MAPbI_3$/HTM interface, then the conditions for electron injection on the ETM side might be different. For example, the presence of holes near the ETM interface in first sample series (without an HTM substrate) could provide additional recombination channels that decreases charge population lifetime. The different built-in potentials at contact layers might also influence the slower charge-transfer dynamics. Finally, it might also be that in the full devices the hole extraction is significantly faster than electron transfer and it predominantly sets k_1 values. (After the hole extraction, remaining carriers live longer, beyond the temporal window of the experiment.) This could explain the similar k_1 values for the full cells with different ETMs.

Other Considerations. In the last section, we would like to discuss several other interesting findings following from the transient absorption experiments of the studied samples. At first, we have analyzed the second, smaller bleach signal located at around 480 nm. The origin of this second bleach band is still not clear. The most common interpretation is that it is due to the transitions involving another conduction band or valence bands.[8,46] Another explanation is that the band represents the molecular-like charge-transfer transition[47,48] or that it contains a contribution from PbI_2.[49,50] We have analyzed the dependence of the amplitude of this bleach as a function of excitation

intensity, and we have found that it is linear in the whole range of investigated intensities (Figure 2B). It is in contrast to the observation for the main bleach in the red side of the transient spectrum (Figure 2A). In agreement with that, there is no shift of the blue-bleach minimum for different intensities (Figure S2), and the different components of multiexponential global analysis have the same spectrum, without any shift, near 480 nm (Figures 2C and 5A). This means that no band integral is necessary to probe the population decay at this blue bleach, but only the kinetics at the band minimum are sufficient. However, it also means that the band-filling mechanism explaining the bleach shift at high intensities is not necessary, unlike for the red bleach. Thus, most probably, the transition observed at ~480 nm can involve neither the lowest conduction band nor the highest valence band responsible for the bleach at ~760 nm. Furthermore, we have observed that the decay of the blue bleach is slightly slower than that of the red bleach. For example, for excitation intensities up to 0.5 $\mu J/cm^2$ and approximated by one-exponential decay, the average lifetime is 1.3 ± 0.1 times lower for the blue bleach than for the red one. For higher intensities, it is also lower, but in the temporal range above 10 ps. The differences in the kinetics measured in these two spectral regions have been previously reported.[48] Together with the lack of characteristic behavior for band filling, they indicate different nature of the transition responsible for the bleach at ~480 nm than that at ~760 nm. The difference might be due to the molecular-like nature of the transition at ~480 nm, which can be, e.g., due to previously mentioned charge-transfer character (from I to Pb)[47,48] or the contribution from isolated PbI_2.[49,50] However, it should be noted that the bleach at ~760 nm is the most important one from the point of view of the majority population of the photoexcited carriers in $MAPbI_3$.

We have also compared the effects of different excitation wavelengths by repeating some of the transient absorption experiments for pump pulse at 485 nm in addition to that at 600 nm. Under the two-exponential approximation (first component for charge cooling and second one for population decay), the charge population decay is on average 1.36 ± 0.14 times faster for excitation at 485 nm than that at 600 nm for the same excitation intensities measured in $\mu J/cm^2$. It can be explained by higher initial charge density at shorter-wavelength excitation. For the second sample series, the absorbance of the $MAPbI_3$ layer was ~1.5 at 485 nm versus ~0.5 at 600 nm, which gives ~1.38 more total absorbed photons for a shorter wavelength; on the other hand, the number of photons per energy unit is 600/485 = 1.24 times smaller for shorter-wavelength excitation. The resultant factor of 1.11 is small; thus, probably the photoexcited charge density is higher at 485 nm because the initial distribution is closer to the entrance part of the absorber layer because of three times higher absorbance than that at 600 nm. We have compared the values for k_2 measured for the same sample sets excited at 485 and 600 nm, by fitting eq 5 to the band integral kinetics, as described in the previous section. Assuming the whole sample thickness as the penetration depth for excitation at 600 nm, see eq 7, we got k_2 = (3.4 ± 0.2) × 10^{-10} cm^3/s, whereas for the excitation at 485 nm, a similar value k_2 = (3.5 ± 0.2) × 10^{-10} cm^3/s was obtained, but when the penetration distance was assumed to be three times shorter than the sample thickness because of the differences in the absorbance.

Finally, important results have been obtained when analyzing the charge cooling dynamics as a function of pump pulse wavelength and intensity. Recently, it has been proposed that relatively slow cooling times in perovskites might be used for extracting hot carriers, which could improve the solar cell efficiency by overcoming the Shockley−Quisser limit.[51,52] Thus, it is crucial to know which factors influence the charge relaxation dynamics. As we have mentioned earlier and reported before,[22,23] the charge cooling times can be determined from the fastest component in multiexponential global analysis. Its amplitude has the shape of a derivate of the bleach band and represents the band-edge shift due to charge screening or band-gap renormalization effect. The times are longer for shorter excitation wavelength and higher pump intensities. Figure 5B collects the charge cooling rate constants for excitations at 485 and 600 nm at different intensities up to 60 $\mu J/cm^2$. For higher pump pulse energy density, the cooling process should be described by two-exponential kinetics. The rate constants are smaller by about 50% for the pump at 485 nm versus the pump at 600 nm, and become about twice smaller for intensities 60 $\mu J/cm^2$ with respect to those at small fluence (2.5 $\mu J/cm^2$) at the same wavelength. It should be noted that we have not observed any differences in cooling times among the samples with different ETMs and between both series of perovskite samples that we studied (on glass and on HTM).

■ CONCLUSIONS

Proper determination of the charge carrier dynamics from femtoseconds to nanoseconds is essential to understand the basis of efficient charge separation in perovskite solar cells, which allows to achieve rapid progress in this photovoltaic technology. However, the analysis based on oversimplified models can often lead to wrong conclusions. In this work, we show that the band filling in $MAPbI_3$ perovskites implies that the bleach transient absorption and emission kinetics cannot, in principle, be analyzed at a single wavelength, which is often used. We compare this approach with single value decomposition (SVD) and band integral (BI) global analyses and find out that the correct determination of the charge population dynamics requires the proper spectral averaging of the signals, e.g., by BI approach or SVD with more than one principal kinetic vectors. Furthermore, although the exponential functions do not properly describe the nonlinear processes in perovskite materials, the approximation based on a single-exponential fit at different pump pulse intensities proposed by us before may be useful in many situations. We show here that when the extracted rate constants are plotted versus pump intensities, the intercept values properly estimate the first-order rate constant, but the values of slope are not equal to the second-order rate constants.

Next, we test the proper determination of the electron injection rate constants from $MAPbI_3$ to different ETM: standard PCBM and the alternative PenPTC and SPPO13 polymers. The photocurrent of the cells with PCBM is about two times higher than that with PenPTC, whereas that for the cells with SPPO13 is negligible. The photocurrent is correlated with the extracted first-order rate constant k_1 for the reference $MAPbI_3$/ETM configurations on a glass substrate, which shows the faster electron injection from the perovskite to more efficient ETM materials: k_1 (PCBM) = 0.61 ± 0.10 ns^{-1}, k_1 (PenPTC) = 0.44 ± 0.06 ns^{-1}, and k_1 (SPPO13) = 0.33 ± 0.17 ns^{-1}. Interestingly, in a full inverted solar cell configuration, the k_1 values are smaller and within the experimental error similar for all samples, at least in the temporal window used (3 ns).

Finally, we compare the excitation effects and transient absorption bleach signals at long- and short-wavelength MAPbI$_3$ absorption bands. Unlike the main bleach at around 760 nm, the smaller bleach signal at 480 nm does not show a spectral shift and thus can be analyzed by simple single-wavelength decay kinetics. Moreover, excitation at 485 nm results in ~50% slower sub-picosecond charge cooling dynamics than that at 600 nm excitation, and in both cases, the dynamics is slower for higher pump fluence. These results point the possible different electronic nature of the short-wavelength perovskite absorption band.

■ ASSOCIATED CONTENT

Ⓢ Supporting Information

The Supporting Information is available free of charge on the ACS Publications website at DOI: 10.1021/acs.jpcc.8b09390.

> Bandwidth of band-edge bleach; photovoltaic parameters for the best cells; current−voltage curves; bleach bandwidth analysis; emission kinetics; XRD patterns; SEM pictures; the rate constants versus energy density; and band integral kinetics (PDF)

■ AUTHOR INFORMATION

Corresponding Author
*E-mail: marziol@amu.edu.pl.

ORCID Ⓞ
Marcin Ziółek: 0000-0003-1882-6022

Notes
The authors declare no competing financial interest.

■ ACKNOWLEDGMENTS

■ REFERENCES

(1) Kojima, A.; Teshima, K.; Shirai, Y.; Miyasaka, T. Organometal Halide Perovskites as Visible-Light Sensitizers for Photovoltaic Cells. *J. Am. Chem. Soc.* **2009**, *131*, 6050−6051.

(2) NREL. National Renewable Energy Laboratory. https://www.nrel.gov/pv/assets/images/efficiency-chart-20180716.jpg (accessed Aug 6, 2018).

(3) Herz, L. M. Charge-Carrier Dynamics in Organic-Inorganic Metal Halide Perovskites. *Annu. Rev. Phys. Chem.* **2016**, *67*, 65−89.

(4) Manser, J. S.; Saidaminov, M. I.; Christians, J. A.; Bakr, O. M.; Kamat, P. V. Making and Breaking of Lead Halide Perovskites. *Acc. Chem. Res.* **2016**, *49*, 330−338.

(5) Yoon, S. J.; Kuno, M.; Kamat, P. V. *Shift Happens*. How Halide Ion Defects Influence Photoinduced Segregation in Mixed Halide Perovskites. *ACS Energy Lett.* **2017**, *2*, 1507−1514.

(6) Manser, J. S.; Christians, J. A.; Kamat, P. V. Intriguing Optoelectronic Properties of Metal Halide Perovskites. *Chem. Rev.* **2016**, *116*, 12956−13008.

(7) Manser, J. S.; Kamat, P. V. Band Filling with Free Charge Carriers in Organometal Halide Perovskites. *Nat. Photonics* **2014**, *8*, 737−743.

(8) Xing, G.; Mathews, N.; Sun, S.; Lim, S. S.; Lam, Y. M.; Gratzel, M.; Mhaisalkar, S.; Sum, T. C. Long-Range Balanced Electron- and Hole-Transport Lengths in Organic-Inorganic CH$_3$NH$_3$PbI$_3$. *Science* **2013**, *342*, 344−347.

(9) Davies, C. L.; Filip, M. R.; Patel, J. B.; Crothers, T. W.; Verdi, C.; Wright, A. D.; Milot, R. L.; Giustino, F.; Johnston, M. B.; Herz, L. M. Bimolecular Recombination in Methylammonium Lead Triiodide Perovskite Is an Inverse Absorption Process. *Nat. Commun.* **2018**, *9*, No. 293.

(10) Richter, J. M.; Abdi-Jalebi, M.; Sadhanala, A.; Tabachnyk, M.; Rivett, J. P. H.; Pazos-Outón, L. M.; Gödel, K. C.; Price, M.; Deschler, F.; Friend, R. H. Enhancing Photoluminescence Yields in Lead Halide Perovskites by Photon Recycling and Light Out-Coupling. *Nat. Commun.* **2016**, *7*, No. 13941.

(11) Trinh, M. T.; Wu, X.; Niesner, D.; Zhu, X.-Y. Many-Body Interactions in Photo-Excited Lead Iodide Perovskite. *J. Mater. Chem. A* **2015**, *3*, 9285−9290.

(12) Leng, J.; Liu, J.; Zhang, J.; Jin, S. Decoupling Interfacial Charge Transfer from Bulk Diffusion Unravels Its Intrinsic Role for Efficient Charge Extraction in Perovskite Solar Cells. *J. Phys. Chem. Lett.* **2016**, *7*, 5056−5061.

(13) Grancini, G.; Viola, D.; Lee, Y.; Saliba, M.; Paek, S.; Cho, K. T.; Orlandi, S.; Cavazzini, M.; Fungo, F.; Hossain, M. I.; et al. Femtosecond Charge-Injection Dynamics at Hybrid Perovskite Interfaces. *ChemPhysChem* **2017**, *18*, 2381−2389.

(14) Li, W.; Zhang, W.; Van Reenen, S.; Sutton, R. J.; Fan, J.; Haghighirad, A. A.; Johnston, M. B.; Wang, L.; Snaith, H. J. Enhanced UV-Light Stability of Planar Heterojunction Perovskite Solar Cells with Caesium Bromide Interface Modification. *Energy Environ. Sci.* **2016**, *9*, 490−498.

(15) Kim, H.-S.; Lee, C.-R.; Im, J.-H.; Lee, K.-B.; Moehl, T.; Marchioro, A.; Moon, S.-J.; Humphry-Baker, R.; Yum, J.-H.; Moser, J. E.; et al. Lead Iodide Perovskite Sensitized All-Solid-State Submicron Thin Film Mesoscopic Solar Cell with Efficiency Exceeding 9%. *Sci. Rep.* **2012**, *2*, No. 591.

(16) Jacobsson, T. J.; Correa-Baena, J. P.; Halvani Anaraki, E.; Philippe, B.; Stranks, S. D.; Bouduban, M. E. F.; Tress, W.; Schenk, K.; Teuscher, J.; Moser, J. E.; et al. Unreacted PbI$_2$ as a Double-Edged Sword for Enhancing the Performance of Perovskite Solar Cells. *J. Am. Chem. Soc.* **2016**, *138*, 10331−10343.

(17) Piatkowski, P.; Cohen, B.; Javier Ramos, F.; Di Nunzio, M.; Nazeeruddin, M. K.; Grätzel, M.; Ahmad, S.; Douhal, A. Direct Monitoring of Ultrafast Electron and Hole Dynamics in Perovskite Solar Cells. *Phys. Chem. Chem. Phys.* **2015**, *17*, 14674−14684.

(18) Mosconi, E.; Grancini, G.; Roldan-Carmona, C.; Gratia, P.; Zimmermann, I.; Nazeeruddin, M. K.; De Angelis, F. Enhanced TiO$_2$/MAPbI$_3$ Electronic Coupling by Interface Modification with PbI$_2$. *Chem. Mater.* **2016**, *28*, 3612−3615.

(19) Augulis, R.; Franckevičius, M.; Abramavičius, V.; Abramavičius, D.; Zakeeruddin, S. M.; Grätzel, M.; Gulbinas, V. Multistep Photoluminescence Decay Reveals Dissociation of Geminate Charge Pairs in Organolead Trihalide Perovskites. *Adv. Energy Mater.* **2017**, *7*, No. 1700405.

(20) Brauer, J. C.; Lee, Y. H.; Nazeeruddin, M. K.; Banerji, N. Ultrafast Charge Carrier Dynamics in CH$_3$NH$_3$PbI$_3$: Evidence for Hot Hole Injection into Spiro-OMeTAD. *J. Mater. Chem. C* **2016**, *4*, 5922−5931.

(21) Pydzińska, K.; Florczak, P.; Nowaczyk, G.; Ziółek, M. Effects of Different Small Molecule Hole Transporters on the Performance and Charge Transfer Dynamics of Perovskite Solar Cells. *Synth. Met.* **2017**, *232*, 181−187.

(22) Pydzińska, K.; Karolczak, J.; Szafrański, M.; Ziółek, M. Differences in Photoinduced Optical Transients in Perovskite Absorbers for Solar Cells. *RSC Adv.* **2018**, *8*, 6479−6487.

(23) Pydzińska, K.; Karolczak, J.; Kosta, I.; Tena-Zaera, R.; Todinova, A.; Idígoras, J.; Anta, J. A.; Ziółek, M. Determination of Interfacial Charge-Transfer Rate Constants in Perovskite Solar Cells. *ChemSusChem* **2016**, *9*, 1647−1659.

(24) Handa, T.; Tex, D. M.; Shimazaki, A.; Wakamiya, A.; Kanemitsu, Y. Charge Injection Mechanism at Heterointerfaces in CH$_3$NH$_3$PbI$_3$ Perovskite Solar Cells Revealed by Simultaneous Time-Resolved Photoluminescence and Photocurrent Measurements. *J. Phys. Chem. Lett.* **2017**, *8*, 954−960.

Article

(25) Li, X.; Bi, D.; Yi, C.; Décoppet, J.-D.; Luo, J.; Zakeeruddin, S. M.; Hagfeldt, A.; Grätzel, M. A Vacuum Flash-Assisted Solution Process for High-Efficiency Large-Area Perovskite Solar Cells. *Science* **2016**, *353*, 58−62.

(26) Yoon, S. J.; Stamplecoskie, K. G.; Kamat, P. V. How Lead Halide Complex Chemistry Dictates the Composition of Mixed Halide Perovskites. *J. Phys. Chem. Lett.* **2016**, *7*, 1368−1373.

(27) Crothers, T. W.; Milot, R. L.; Patel, J. B.; Parrott, E. S.; Schlipf, J.; Müller-Buschbaum, P.; Johnston, M. B.; Herz, L. M. Photon Reabsorption Masks Intrinsic Bimolecular Charge-Carrier Recombination in $CH_3NH_3PbI_3$ Perovskite. *Nano Lett.* **2017**, *17*, 5782−5789.

(28) Karuppuswamy, P.; Hanmandlu, C.; Moorthy Boopathi, K.; Perumal, P.; Liu, C. ching; Chen, Y. F.; Chang, Y. C.; Wang, P. C.; Lai, C. S.; Chu, C. W. Solution-Processable Electron Transport Layer for Efficient Hybrid Perovskite Solar Cells beyond Fullerenes. *Sol. Energy Mater. Sol. Cells* **2017**, *169*, 78−85.

(29) Meijer, E. J.; De Leeuw, D. M.; Setayesh, S.; Van Veenendaal, E.; Huisman, B. H.; Blom, P. W. M.; Hummelen, J. C.; Scherf, U.; Klapwijk, T. M. Solution-Processed Ambipolar Organic Field-Effect Transistors and Inverters. *Nat. Mater.* **2003**, *2*, 678−682.

(30) Wang, J.; Xu, X.; Tian, Y.; Yao, C.; Liu, R.; Li, L. A Novel Blue Fluorescent Polymer for Solution-Processed Fluorescent-Phosphorescent Hybrid WOLEDs. *J. Mater. Chem. C* **2015**, *3*, 2856−2864.

(31) Idígoras, J.; Burdziński, G.; Karolczak, J.; Kubicki, J.; Oskam, G.; Anta, J. A.; Ziółek, M. The Impact of the Electrical Nature of the Metal Oxide on the Performance in Dye-Sensitized Solar Cells: New Look at Old Paradigms. *J. Phys. Chem. C* **2015**, *119*, 3931−3944.

(32) Wróżowa, T.; Ciesielska, B.; Komar, D.; Karolczak, J.; Maciejewski, A.; Kubicki, J. Measurements of Picosecond Lifetimes by Time Correlated Single Photon Counting Method: The Effect of the Refraction Index of the Solvent on the Instrument Response Function. *Rev. Sci. Instrum.* **2004**, *75*, 3107−3121.

(33) Lin, Q.; Wang, Z.; Snaith, H. J.; Johnston, M. B.; Herz, L. M. Hybrid Perovskites: Prospects for Concentrator Solar Cells. *Adv. Sci.* **2018**, *5*, No. 1700792.

(34) Yang, F.; Graciani, J.; Evans, J.; Liu, P.; Hrbek, J.; Sanz, J. F.; Rodriguez, J. A. CO Oxidation on Inverse $CeO_x/Cu(111)$ Catalysts: High Catalytic Activity and Ceria-Promoted Dissociation of O_2. *J. Am. Chem. Soc.* **2011**, *133*, 3444−3451.

(35) Wu, X.; Trinh, M. T.; Niesner, D.; Zhu, H.; Norman, Z.; Owen, J. S.; Yaffe, O.; Kudisch, B. J.; Zhu, X. Y. Trap States in Lead Iodide Perovskites. *J. Am. Chem. Soc.* **2015**, *137*, 2089−2096.

(36) Idígoras, J.; Sobus, J.; Jancelewicz, M.; Azaceta, E.; Tena-Zaera, R.; Anta, J. A.; Ziółek, M. Effect of Different Photoanode Nanostructures on the Initial Charge Separation and Electron Injection Process in Dye Sensitized Solar Cells: A Photophysical Study with Indoline Dyes. *Mater. Chem. Phys.* **2016**, *170*, 218−228.

(37) Kuang, D.; Ito, S.; Wenger, B.; Klein, C.; Moser, J. E.; Humphry-Baker, R.; Zakeeruddin, S. M.; Grätzel, M. High Molar Extinction Coefficient Heteroleptic Ruthenium Complexes for Thin Film Dye-Sensitized Solar Cells. *J. Am. Chem. Soc.* **2006**, *128*, 4146−4154.

(38) Kovalenko, S. A.; Schanz, R.; Farztdinov, V. M.; Hennig, H.; Ernsting, N. P. Femtosecond Relaxation of Photoexcited Para-Nitroaniline: Solvation, Charge Transfer, Internal Conversion and Cooling. *Chem. Phys. Lett.* **2000**, *323*, 312−322.

(39) Wang, H.; Valkunas, L.; Cao, T.; Whittaker-Brooks, L.; Fleming, G. R. Coulomb Screening and Coherent Phonon in Methylammonium Lead Iodide Perovskites. *J. Phys. Chem. Lett.* **2016**, *7*, 3284−3289.

(40) Noel, N. K.; Abate, A.; Stranks, S. D.; Parrott, E. S.; Burlakov, V. M.; Goriely, A.; Snaith, H. J. Enhanced Photoluminescence and Solar Cell Performance via Lewis Base Passivation of Organic-Inorganic Lead Halide Perovskites. *ACS Nano* **2014**, *8*, 9815−9821.

(41) Stranks, S. D.; Eperon, G. E.; Grancini, G.; Menelaou, C.; Alcocer, M. J. P.; Leijtens, T.; Herz, L. M.; Petrozza, A.; Snaith, H. J. Electron-Hole Diffusion Lengths Exceeding. *Science* **2013**, *342*, 341−344.

(42) Heo, J. H.; Han, H. J.; Kim, D.; Ahn, T. K.; Im, S. H. Hysteresis-Less Inverted $CH_3NH_3PbI_3$ Planar Perovskite Hybrid Solar Cells with 18.1% Power Conversion Efficiency. *Energy Environ. Sci.* **2015**, *8*, 1602−1608.

(43) Hutter, E. M.; Hofman, J. J.; Petrus, M. L.; Moes, M.; Abellón, R. D.; Docampo, P.; Savenije, T. J. Charge Transfer from Methylammonium Lead Iodide Perovskite to Organic Transport Materials: Efficiencies, Transfer Rates, and Interfacial Recombination. *Adv. Energy Mater.* **2017**, *7*, No. 1602349.

(44) Ponseca, C. S., Jr.; Hutter, E. M.; Piatkowski, P.; Cohen, B.; Pascher, T.; Douhal, A.; Yartsev, A.; Sundstrom, V.; Savenije, T. J. Mechanism of Charge Transfer and Recombination Dynamics in Organo Metal Halide Perovskites and Organic Electrodes, PCBM, and Spiro-OMeTAD: Role of Dark Carriers. *J. Am. Chem. Soc.* **2015**, *137*, 16043−16048.

(45) Horn, J.; Minda, I.; Schwoerer, H.; Schlettwein, D. Direct Observation of Charge Injection From $CH_3NH_3PbI_{3-x}Cl_x$ to Organic Semiconductors Monitored With Sub-Ps Transient Absorption Spectroscopy. *Phys. Status Solidi B* **2018**, No. 1800265.

(46) Anand, B.; Sampat, S.; Danilov, E. O.; Peng, W.; Rupich, S. M.; Chabal, Y. J.; Gartstein, Y. N.; Malko, A. V. Broadband Transient Absorption Study of Photoexcitations in Lead Halide Perovskites: Towards a Multiband Picture. *Phys. Rev. B* **2016**, *93*, 1−5.

(47) Christians, J. A.; Manser, J. S.; Kamat, P. V. Best Practices in Perovskite Solar Cell Efficiency Measurements. Avoiding the Error of Making Bad Cells Look Good. *J. Phys. Chem. Lett.* **2015**, *6*, 852−857.

(48) Stamplecoskie, K. G.; Manser, J. S.; Kamat, P. V. Dual Nature of the Excited State in Organic−inorganic Lead Halide Perovskites. *Energy Environ. Sci.* **2015**, *8*, 208−215.

(49) Du, T.; Burgess, C. H.; Kim, J.; Zhang, J.; Durrant, J. R.; McLachlan, M. A. Formation, Location and Beneficial Role of PbI_2 in Lead Halide Perovskite Solar Cells. *Sustainable Energy Fuels* **2017**, *1*, 119−126.

(50) Wang, L.; McCleese, C.; Kovalsky, A.; Zhao, Y.; Burda, C. Femtosecond Time-Resolved Transient Absorption Spectroscopy of $CH_3NH_3PbI_3$ Perovskite Films: Evidence for Passivation Effect of PbI_2. *J. Am. Chem. Soc.* **2014**, *136*, 12205−12208.

(51) Guo, Z.; Wan, Y.; Yang, M.; Snaider, J.; Zhu, K.; Huang, L. Long-Range Hot-Carrier Transport in Hybrid Perovskites Visualized by Ultrafast Microscopy. *Science* **2017**, *356*, 59−62.

(52) Bretschneider, S. A.; Laquai, F.; Bonn, M. Trap-Free Hot Carrier Relaxation in Lead-Halide Perovskite Films. *J. Phys. Chem. C* **2017**, *121*, 11201−11206.

124

Supporting Information

for

Insights into the Femtosecond to Nanosecond Charge Carrier Kinetics in Perovskite Materials for Solar Cells

Katarzyna Pydzińska-Białek [a] , Janusz Szeremeta [b] , Konrad Wojciechowski [b,c] and Marcin Ziółek [a] [*]

[a] *Faculty of Physics, Adam Mickiewicz University in Poznań,*
Umultowska 85, 61-614 Poznań, Poland.

[b] *Saule Technologies, Wrocław Technology Park, Duńska 11, Sigma building,*
54-427 Wrocław, Poland

[c] *Saule Research Institute, Wrocław Technology Park, Duńska 11, Sigma building,*
54-427 Wrocław, Poland
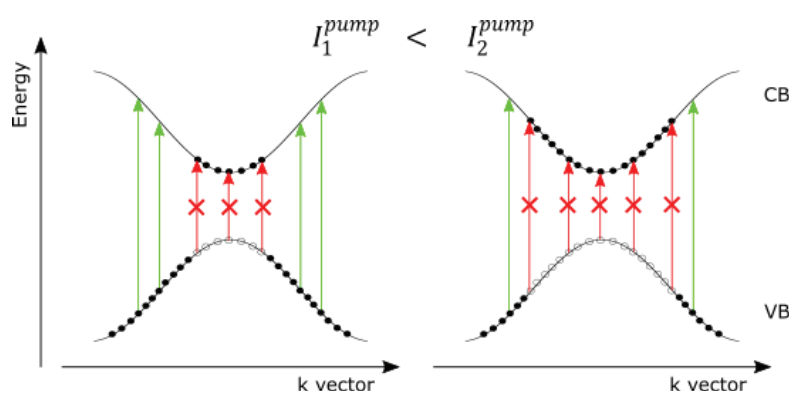
Scheme S1. Schematic presentation of pump energy influence on bandwidth of band-edge bleach.

Table S1. Photovoltaic parameters obtained for the best sample

(Eff – efficiency, FF – fill factor, Jsc – short-circuit current, Voc – open circuit voltage).

	Eff [%]	FF [%]	J_{sc} [mA/cm^2]	V_{oc} [mV]
PCBM	10.2	77.3	14.7	899.5
PenPCT	2.6	34.6	9.7	769.1
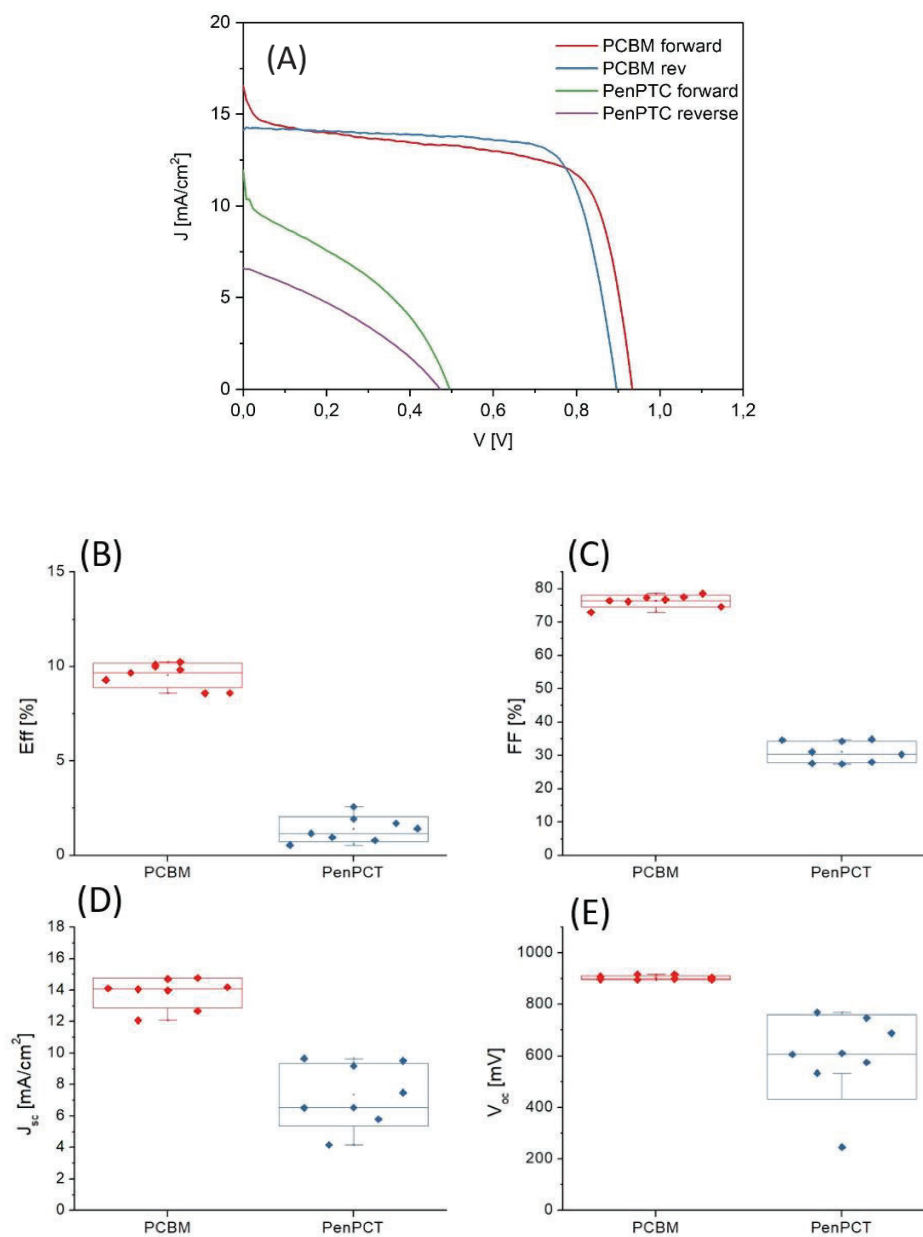
Figure S1. Current-voltage curves (A) and photovoltaic parameters (B-E) of prepared samples as efficiency (B), fill factor (C), short-circuit current (D) and open-circuit voltage (E).
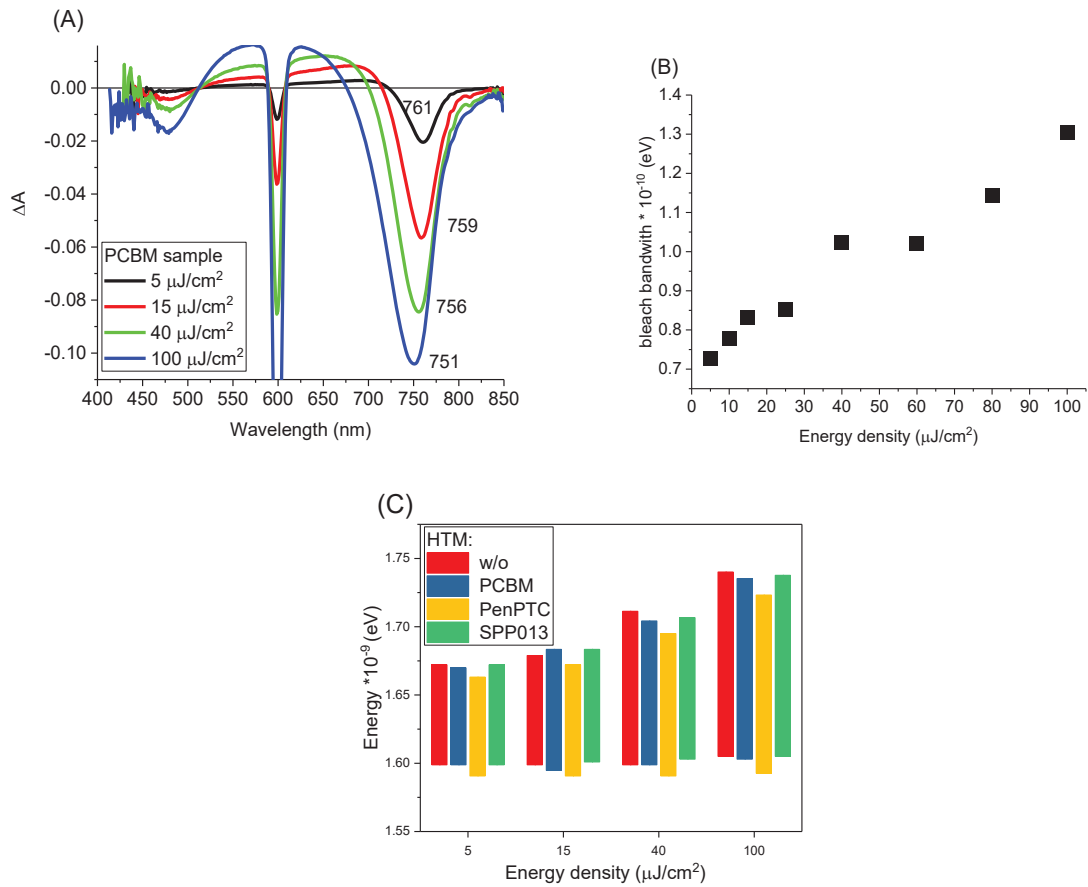
Figure S2. Signal after 5 ps for PCBM sample (A), red bleach (~760 nm) bandwidth of PenPTC sample from the first series (B) and red bleach position for different devices (C) for different excitation energy.

Table S2. Relation between the k_2'and k_2 values for different cutoffs of the temporal window for the analysis of the decays (in % of the initial amplitude).

Cutoffs (in % of the initial amplitude)	Relation between the k_2'and k_2
0	$k_2' \approx 0.3\, k_2$
2	$k_2' \approx 0.5\, k_2$
5	$k_2' \approx 0.6\, k_2$
10	$k_2' \approx 0.7\, k_2$
20	$k_2' \approx 0.9\, k_2$
25	$k_2' \approx 1.0\, k_2$
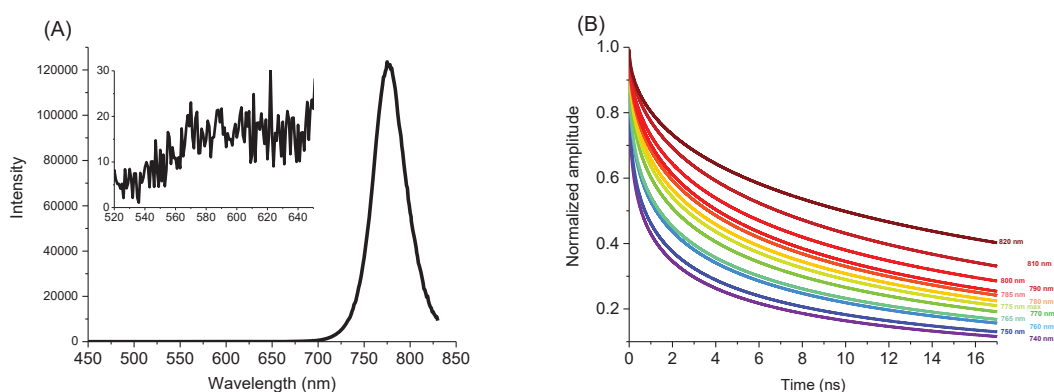
Figure S3. Stationary emission and kinetics at different wavelengths for sample with SPPO13 as ETM (excitation power was equal to 0.057 mW).
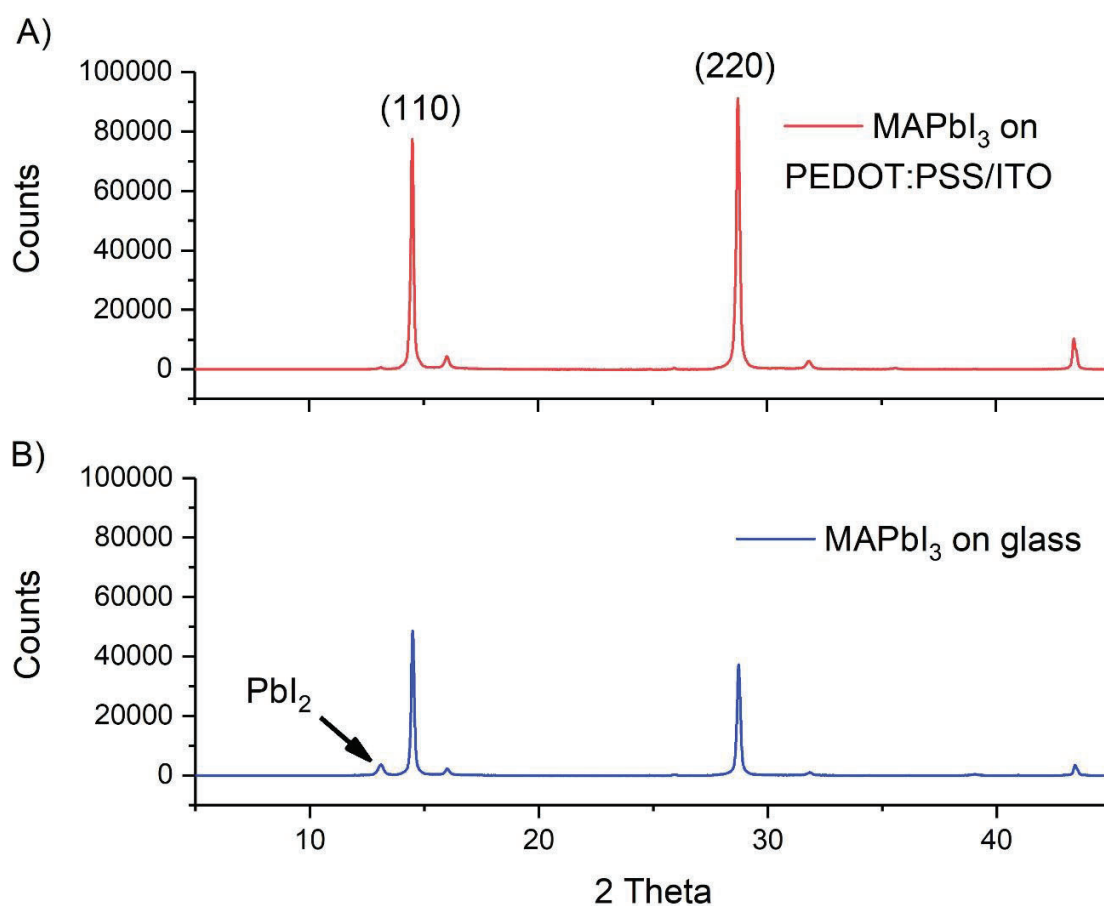
Figure S4. XRD pattern (CuKα) of the MAPbI$_3$ deposited on (A) glass and (B) PEDOT:PSS layer deposited on ITO. Spectra were taken with Rigaku MiniFlex600 X-ray diffractometer.
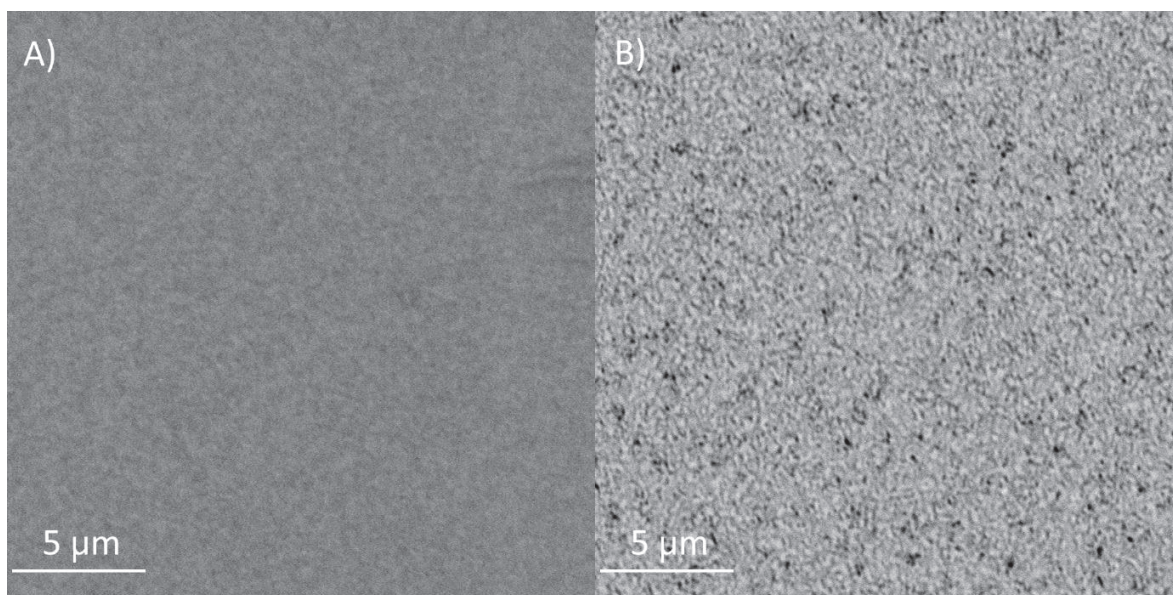
Figure S5. SEM images taken at 5kV with 12k magnification. A) MAPbI$_3$ on PEDOT:PSS/ITO and B) MAPbI$_3$ deposited directly on glass.
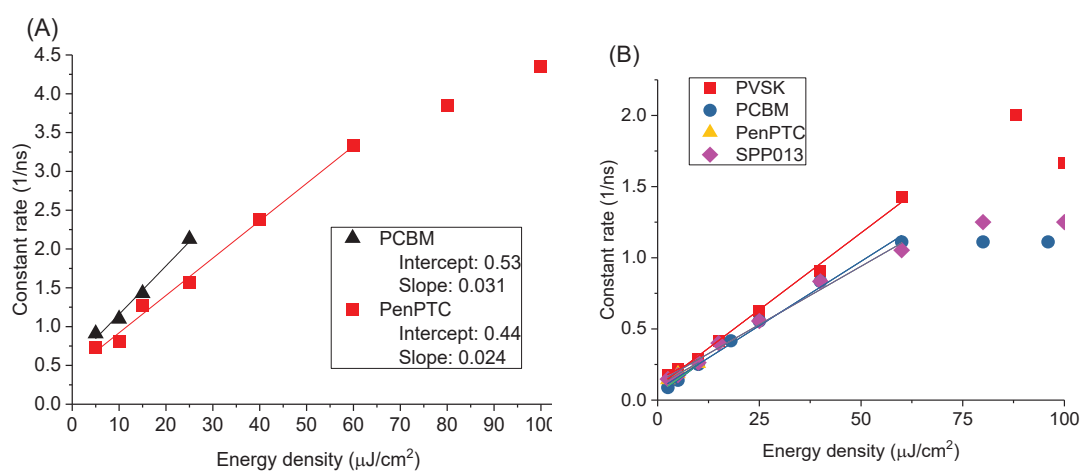
Figure S6. The rate constants of the longer component obtained from two-exponential global analysis as function of excitation energy for samples without HTM (A, first series) and full cells (B, second series).
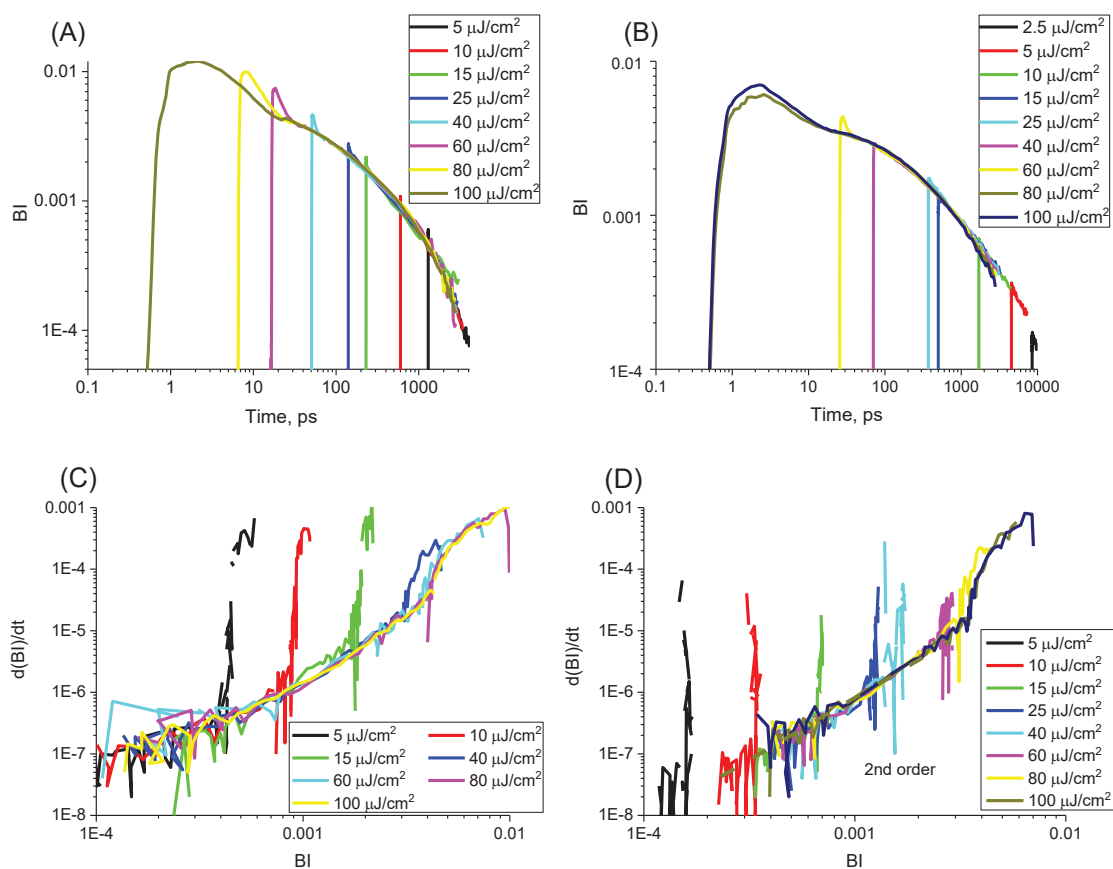
Figure S7. Band integral kinetics of MAPbI$_3$ in glass samples (A) and full devices (B). Time zero for different excitation intensities was shifted to overlap higher intensity decay. Rate of band integral (BI) change as a function of BI values, which is equivalent to the plots of recombination rate dn/dt vs n (BI value is proportional to carrier density n) for glass (C) and full devices (D) samples.

KPB-4
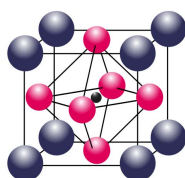
Understanding the effect of different synthesis conditions on the physicochemical properties of mixed-ion perovskite solar cells

B.Quere, **K.Pydzińska-Białek**, J.Karolczak, G.Nowaczyk, E.Coy, M.Ziółek

Perovskites

Understanding the Effect of Different Synthesis Conditions on the Physicochemical Properties of Mixed-Ion Perovskite Solar Cells

Brian Quere,[a] Katarzyna Pydzińska-Białek,[a] Jerzy Karolczak,[a, b] Grzegorz Nowaczyk,[c] Emerson Coy,[c] and Marcin Ziółek*[a]

Abstract: Perovskite solar cells, composed of a mixture of methylammonium (MA) and formamidinium (FA) cations [in the benchmark proportions of $(FAPbI_3)_{0.85}(MAPbBr_3)_{0.15}$] and titania as an electron-accepting material, are prepared under different conditions, with the objective of finding correlations between the solar cell performance and several important stationary and dynamical parameters of the material. The effects of humidity, oxygen, the use of anti-solvent, and the presence and quality of a mesoporous titania layer are investigated. It is found that an increase in the photocurrent corresponds to a higher content of the desired cubic perovskite phase and to increased long-wavelength absorption of the sample. On the contrary, for poorer-quality cells, addi-

tional short-wavelength bands in both absorption and emission spectra are present. Furthermore, a higher photocurrent of the cells is correlated with faster interfacial charge-transfer dynamics. For the highest photocurrent of $>20\ mA\,cm^{-2}$, the characteristic times of about 1 µs are observed by electrochemical impedance spectroscopy, and emission half-lifetimes of about 6 ns by time-resolved fluorescence spectroscopy (upon excitation with 420 nm pulses of $\approx 0.5\ mW$ power). Both first- and second-order rate constants, extracted from the emission measurements, are greater for the cells showing higher photocurrents, probably owing to a more rapid charge injection.

Introduction

One of the most important steps in the rapid development of perovskite solar cells (PSCs) in recent years has been the discovery of the beneficial role of partial substitution of different ions in standard, methylammonium lead iodide ($MAPbI_3$) perovskite, such as formamidinium (FA) in the methylammonium (MA) position, or bromide instead of iodide. This substitution led to the benchmark composition of $(FAPbI_3)_{0.85}$-$(MAPbBr_3)_{0.15}$[1,2] with improved efficiency and stability of PSCs. This discovery permitted the achievement of an efficiency exceeding 20%.[3] The certified efficiency of 22.1% has been reported for a mixture of MA and FA.[4] Other, even more complex compositions, were proposed later, including triple-cation

mixed halide perovskite, allowing an efficiency above 21%.[5] Further incorporation of additional rubidium cations has also been proposed in efficient devices.[6] At present, the best certified PSC efficiency is reported to be 23.3% (achieved at the Institute of Semiconductors, Chinese Academy of Science), which recently exceeded the previous record of 22.7% reached at the Korea Research Institute of Chemical Technology.[7]

Despite huge progress in the stability and efficiency of mixed-ion PSCs, basic studies of such materials are still quite rare compared with the numerous studies of standard $MAPbI_3$ perovskite.[8–14] In particular, only a few time-resolved studies of the charge dynamics have been reported so far for the mixture of MA and FA. Ultrafast interfacial charge injection was studied for devices with 20% efficiency.[15] A long component of the photoluminescence decay of about 2 µs was assigned to the bulk carrier lifetime in the inverted solar cell configuration.[16] Rate constants around four times lower were observed for the nonradiative luminescence decay processes for perovskite material made in vacuum flash-assisted solution processing compared with that produced from conventional one-step solution deposition.[10] Similarly, longer emission decays were observed upon applying meniscus-assisted solution printing instead of the spin-coating method to form the perovskite layer.[17] Perovskites in PbI_2-rich grains exhibited a longer lifetime owing to the suppression of defect trapping.[18] Similarly, longer lifetimes of isolated perovskite layers have also been observed for lower temperatures of anti-solvent (chlorobenzene), indicating a higher crystal quality of the perovskite grains.[19] Emission quenching has been observed if the $(FAPbI_3)_{0.85}(MAPbBr_3)_{0.15}$

[a] B. Quere, K. Pydzińska-Białek, Dr. J. Karolczak, Dr. M. Ziółek
Faculty of Physics
Adam Mickiewicz University in Poznań
Umultowska 85, 61-614 Poznań (Poland)
E-mail: marziol@amu.edu.pl

[b] Dr. J. Karolczak
Center for Ultrafast Laser Spectroscopy
Adam Mickiewicz University in Poznań
Umultowska 85, 61-614 Poznań (Poland)

[c] Dr. G. Nowaczyk, Dr. E. Coy
NanoBioMedical Centre
Adam Mickiewicz University in Poznań
Umultowska 85, 61-614 Poznań (Poland)

Supporting information and the ORCID identification numbers for the authors of this article can be found under https://doi.org/10.1002/chem.201900310.

135

perovskite layer was in contact with different charge-selective materials.[20,21] This process has been also observed upon passivation of perovskite with an additional $FAPbBr_{3-x}I_x$ layer.[22]

Therefore, in this work, we focused on PSCs made of $(FAPbI_3)_{0.85}(MAPbBr_3)_{0.15}$ and studied them by employing several complementary techniques, including basic photovoltaic characterization [current–voltage (CV) curves, incident photon-to-current efficiency (IPCE) spectra], studies of perovskite structure and morphology [X-ray diffraction (XRD), scanning electron microscopy (SEM)], optical properties measurements (stationary absorption and emission), and time-resolved measurements of charge dynamics (electrochemical impedance spectroscopy and time-resolved fluorescence of the full cells). One of the objectives was to test the effect of several deposition conditions (humidity, oxygen, the use of anti-solvent, and the presence and quality of a mesoporous titania layer) on the results of characterization of the samples. More importantly, we intended to check the correlations between the results obtained in structural, optical, dynamical, and photovoltaic studies for the cells showing different performances. In many studies of PSCs, only the material parameters of the best cells are explored. However, on the basis of their values, it is often hard to conclude whether or not these parameters are important in solar cell optimization. On the contrary, in this work, we do not pay much attention to achieving top efficiencies of solar cells, but our objective was the systematic investigation of changes in certain active material parameters and interfacial charge-transfer time constants in the cells of higher and lower photocurrent. Thus, we hope to gain more insight into the role of the basic characterization of perovskite materials in the understanding of PSC performance.

Results and Discussion

Stationary absorption and emission study

Table 1 collects the labels of all samples measured and summarizes the preparation conditions (see Experimental Section for details). The bandgap of the mixed cation perovskite material of the composition $(FAPbI_3)_{0.85}(MAPbI_3)_{0.15}$ is reported to be from 1.55 to 1.6 eV,[2,23,24] which gives a wide absorption spectrum with the edge in the range 775–800 nm (see Figure 1A).

Table 1. Synthesis parameters of prepared solar cell batches.

Sample	TiO₂ layer	Anti-solvent	O₂ [%]	Humidity RH [%]
WM No A-S	Worse mesoporous	No	21	8–40
WM 21O₂ 40RH	Worse mesoporous	Yes	21	40
WM 21O₂ 8RH	Worse mesoporous	Yes	21	8
WM <1O₂ 10RH	Worse mesoporous	Yes	<1	10
P 21O₂ 8RH	Only planar	Yes	21	8
BM 21O₂ 8RH	Better mesoporous	Yes	21	8
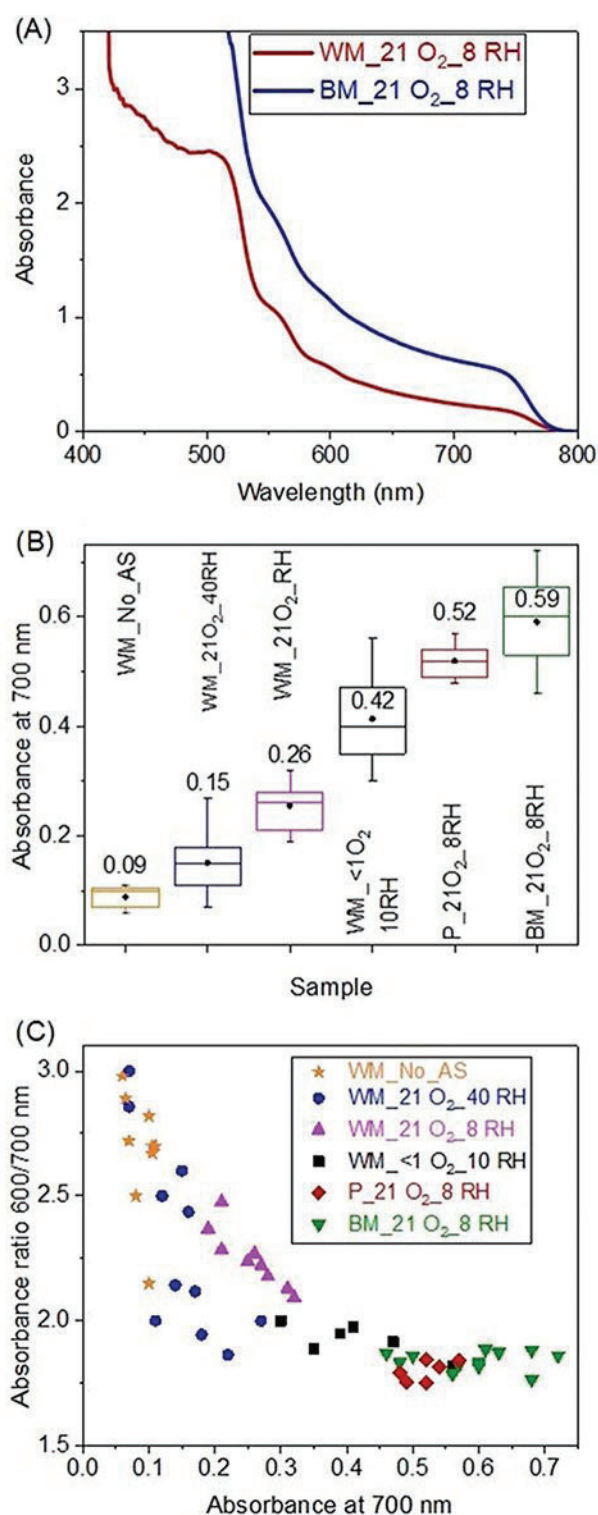
Figure 1. Absorbance of PSC made with two different TiO₂ layers under the same conditions (A), absorbance values at 700 nm for different batches (B), absorbance ratio at 600 and 700 nm as a function of absorbance value at 700 nm (C).

For highly efficient PSCs, it is important to prepare a thick and high-quality layer of perovskite material that would absorb as much sunlight as possible. Figure 1A shows a comparison of the absorbance of samples prepared with worse (WM) and

better (BM) mesoporous titania layers (see Experimental Section for details), prepared under the same conditions (oxygen content 21%, relative humidity 8%). All batches of PSCs were examined in this way to check the influence of the preparation method on the active material absorption, and the statistics for absorbance at 700 nm are presented in Figure 1B. Note that the same amount of perovskite precursor was deposited on all samples, but the long-wavelength absorbance varied significantly depending on the deposition conditions. The highest long-wavelength absorbance was found for BM and planar cells, whereas the lowest was that for the cells without anti-solvent. The samples with lower absorption at 700 nm are expected to exhibit smaller photocurrents owing to poorer light harvesting, which will be discussed in the next sections.

Besides the long-wavelength absorption at 700 nm, we also monitored the absorbance at shorter wavelength (600 nm), which might contain the contribution from other undesired phases (e.g., attributable to unreacted precursors), and calculated the A(600 nm)/A(700 nm) ratio (Figure 1C). For the ideal semiconductor with a direct bandgap, the absorption coefficient at a certain wavelength can be written as in Equation (1), in which B is a constant.[25]

$$\alpha(\lambda) = B\lambda h\left(\frac{1}{\lambda} - \frac{1}{\lambda_{E_g}}\right)^{\frac{1}{2}} \qquad (1)$$

Assuming the absorption edge at 775 nm (λ_{E_g}) in Equation (1), we can calculate the absorbance ratio as in Equation (2).

$$\frac{A\,(600\,\text{nm})}{A\,(700\,\text{nm})} = \frac{\alpha_{600\text{nm}}}{\alpha_{700\text{nm}}} = 1.41 \qquad (2)$$

If the absorbance edge is at 800 nm, the ratio is equal to 1.33. The closer this value is approached, the purer the compound. Ratios of absorbance at 700 and 600 nm are plotted as a function of the absorption at 700 nm in Figure 1C. One can see that the samples showing the highest absorption and the lowest ratios of absorbance are those with only the planar (P) or non-aggregated scaffold TiO$_2$ substrate (BM). These two ho-

mogeneous surfaces would enhance the uniform distribution and crystallization of the perovskite. On the contrary, the low absorbers [A(700 nm) < 0.3] are the samples prepared under conditions restraining crystallization: high humidity or without anti-solvent. These samples exhibit high ratios of A(600 nm)/A(700 nm), which means that there is extra absorption at 600 nm by other phases, added to the perovskite phase absorption, but this is not present at 700 nm.

Additional short-wavelength features observed in the absorption spectra of poor-quality crystals are also validated by stationary emission. As presented in Figure S1 (Supporting Information), the samples with a high ratio of A(600 nm)/A(700 nm) exhibit additional short-wavelength emission (between 700 and 750 nm) upon excitation at 420 nm. This emission might originate from the poorly crystallized parts of the active layer material.

X-ray diffraction characterization

XRD was used to detect different phases present in the active layer. Figure 2A shows selected XRD patterns obtained for perovskite layers deposited on WM and BM TiO$_2$ layers. Not all observed peaks are characteristic of the cubic (FAPbI$_3$)$_{0.85}$(MAPbBr$_3$)$_{0.15}$ perovskite layers at 14°, 28.5°, and 31.8° (Figure 2A, triangles), corresponding to diffraction peaks [001], [002], and [012], respectively.[16,24] The intense peak at 12.3° corresponds to another phase (Figure 2A, star), which is probably attributable to some unreacted precursors. The XRD [001] peak assigned to unreacted PbI$_2$ has been reported to be at 12.6°,[24] and another one corresponding to the perovskite δ-FAPbI$_3$ has been detected at 11.6°.[1] It should be noted that the presence of a small amount of unreacted PbI$_2$ has been reported to improve the efficiency.[26–28] The samples produced with the better quality mesoporous TiO$_2$ under low humidity are characterized by a much higher ratio of the content of perovskite over unreacted phase than the samples prepared with the poorer quality mesoporous TiO$_2$ under the same conditions (BM 21 O$_2$ 8RH vs. WM 21O$_2$ 8RH). For these and two other samples we have calculated the ratio of the area of each of
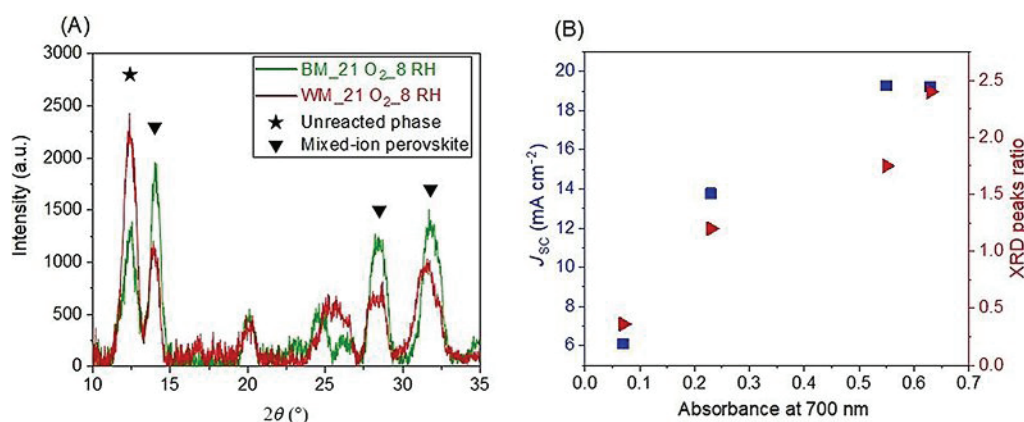
Figure 2. X-ray diffraction pattern for different samples with indicated unreacted and mixed-ion perovskite phase peaks (A). Short-circuit current density and XRD peak area ratio at 28.5° and 31.8° (mixed-ion perovskite phase diffraction peaks [002] and [012], respectively) over 12.3° (unreacted precursors phase) as a function of absorbance at 700 nm (B).

the two peaks at 28.5° and 31.8° (the most intense and well separated peaks of the cubic phase) to the area of the unreacted phase peak at 12.3° as an indication of the amount of desired mixed-ion perovskite phase. This ratio is presented versus the absorbance at 700 nm in Figure 2B (red triangles). It is observed that the higher the absorption at 700 nm, the higher the perovskite content (high peak ratio) in the cell. Moreover, a higher absorption also corresponds to a higher photocurrent density (J_{sc}) for these samples. More details on the photovoltaic parameters of the samples are presented below.

Scanning electron microscopy study

Cross-section images were also obtained using SEM (Figure 3). Different layers, including the active perovskite layer, can be distinguished. The average perovskite thickness observed in the pictures was equal to 600 and 540 nm for BM and WM titania paste, respectively (Figure 3A,B). This small difference does not sufficiently explain the large difference in light absorption (Figure 1A), and implies that the absorption coefficient in the long-wavelength range is higher for the BM samples. Therefore, the long-wavelength light absorption (e.g., at 700 nm) must depend strongly on the quality and purity of the crystallized mixed-ions perovskite, and not only on the thickness of the active layer. The mesoporous titania layer for the WM sample is much thicker than for the BM one, as shown in Figure 3, probably owing to aggregated TiO_2 nanoparticles. However, the SEM image at smaller magnification shows that the thickness of the WM layer is very uneven, whereas that of BM is much more uniform (Figure S2, Supporting Information). Such an irregularity in the WM layer could consequently cause poor crystallization of the mixed ions. Finally, note that the SEM image of the sample prepared with high humidity (of the small long-wavelength absorption, Figure 3C) exhibits a blurred structure without clear grains of the active layer, which may indicate a very small amount of the proper perovskite phase.

Current–voltage and electrochemical impedance examination

The samples studied were characterized by CV measurements to extract the basic photovoltaic parameters of the cells. Figure 4A displays the selected CV curves of the best cells from the BM series, which exhibit an open-circuit voltage (V_{OC}) of more than 1 V and a short-circuit current density (J_{SC}) above 20 mA cm^{-2}, fill factor (FF) of 0.60 (blue) and 0.64 (red), and efficiency of 13.2% (blue) and 13.6% (red). It should be noted that the limits in the efficiency are attributed mainly to the relatively low FF values, whereas our best photocurrents (the most important parameter that we correlate with the other results) is comparable ($>$85%) to that of the most efficient devices with $(FAPbI_3)_{0.85}(MAPbBr_3)_{0.15}$. The hysteresis index of the cells is between 0.33 and 0.41 (Figure S3, Supporting Information).

The efficiencies of all the cells from different batches are given in Figure 4B (with the errors indicated) and their aver-
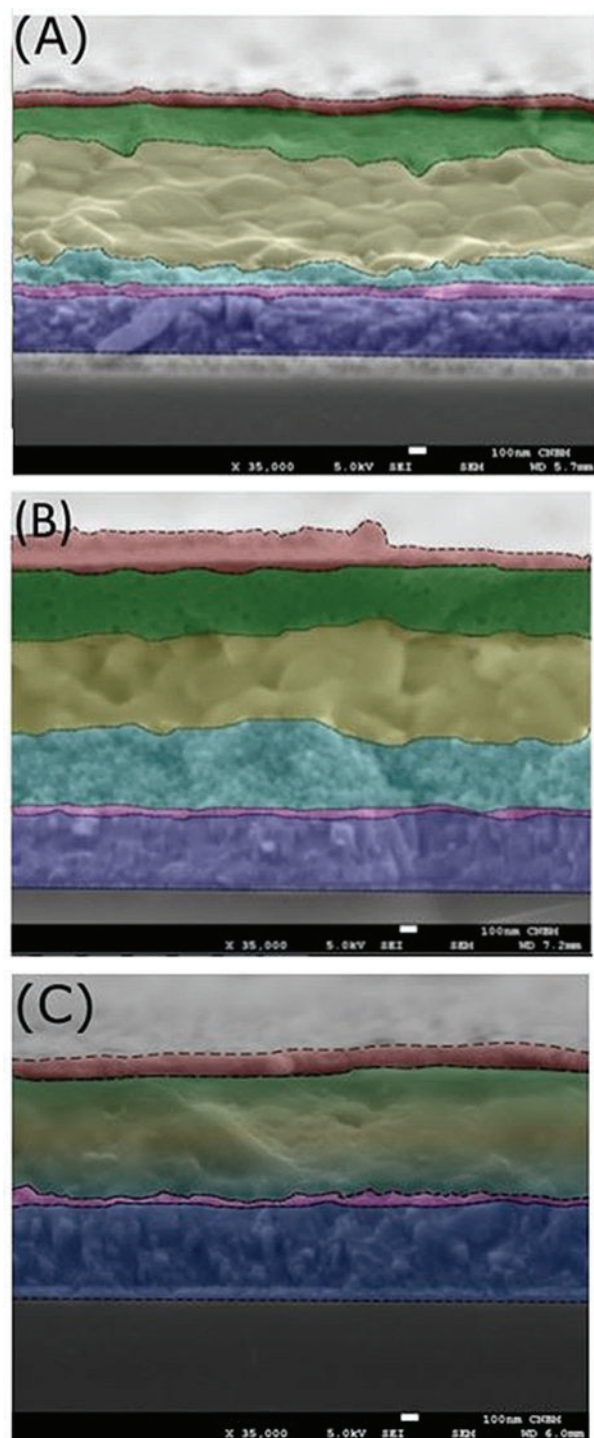
Figure 3. Cross-section SEM images of the cells: BM 21O$_2$ 8RH (A), WM 21O$_2$ 8RH (B), and WM 21O$_2$ 40RH (C): red: gold electrode; green: spiro-OMeTAD; yellow: mixed ion perovskite; cyan: mesoporous TiO$_2$; pink: planar TiO$_2$; purple: FTO glass.

aged photovoltaic parameters are summarized in Table 2. The efficiencies are generally higher for the samples that showed greater absorbance at 700 nm (compare with Figure 1B). The highest photocurrent, FF, and efficiency are found for BM 21O$_2$ 8RH samples. This is also consistent with the XRD findings, as the greater the degree of perovskite crystallization,

Table 2. Averaged current–voltage parameters of prepared batches measured under 0.9 Sun illumination in reverse direction. V_{oc}: open-circuit voltage; J_{sc}: short-circuit current density; FF: fill factor.

Sample	V_{oc} [V]	J_{sc} [mA cm^{-2}]	FF	Efficiency [%]
WM No AS	0.81	8.5	0.42	2.9
WM 21O$_2$ 40RH	0.84	8.9	0.32	2.5
WM 21O$_2$ 8RH	0.93	13.3	0.51	6.3
WM <1O$_2$ 10RH	0.98	14.9	0.49	7.2
P 21O$_2$ 8RH	0.86	14.9	0.38	4.8
BM 21O$_2$ 8RH	0.97	17.8	0.61	10.5
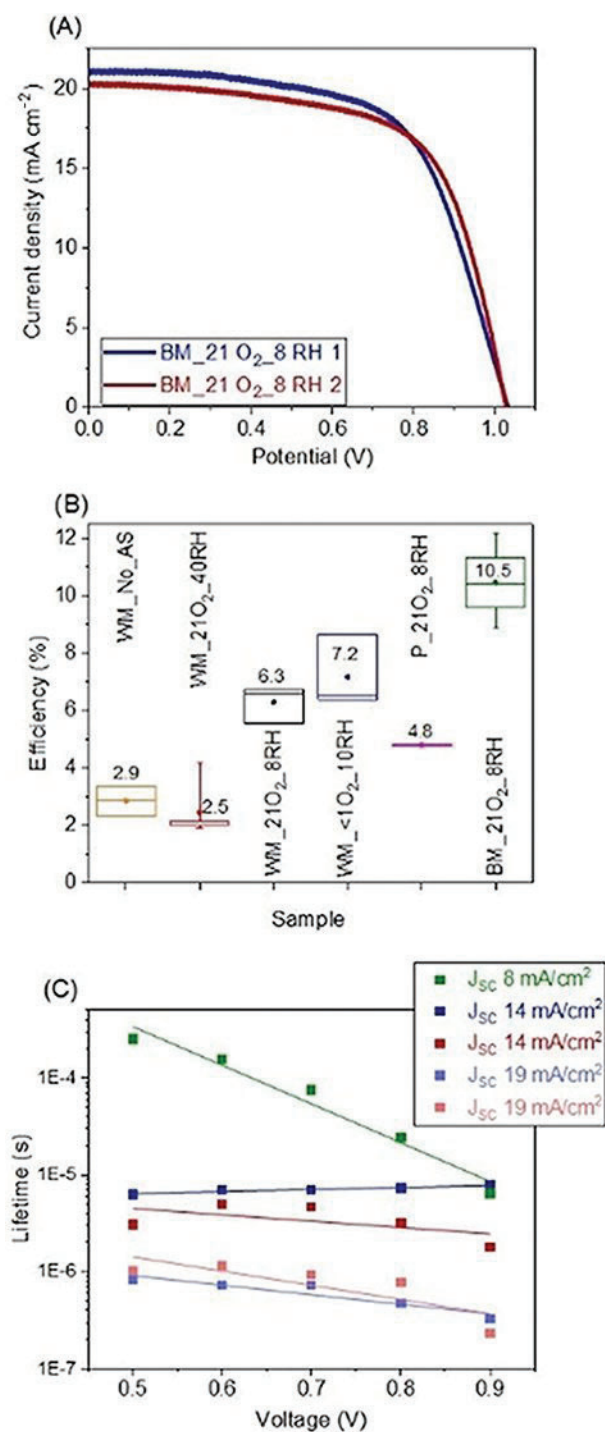
Figure 4. Current density–voltage curves for the best cells under 1 Sun illumination (A) and efficiency values obtained for different batches under 0.9 Sun illumination (B). Comparison of current density–voltage curves recorded in reverse and forward scan direction is shown in Figure S3 (Supporting Information). Electron lifetime as a function of applied voltage obtained from the impedance measurement under 0.9 Sun illumination for the samples of different photocurrent (C). Electron lifetime was obtained by multiplication of resistance and capacitance values of high-frequency semicircle. Selected Nyquist plot and equivalent circuit are shown in Figure S4 (Supporting Information).

the higher the cell efficiency. However, the planar sample P 21O$_2$ 8RH contained, on average, a similar amount of synthesized perovskite to BM 21O$_2$ 8RH (Figure 1 B), whereas the efficiency of the former was about half that of the latter (Figure 4 B), mainly because of the lower photocurrent and lower fill factor. This highlights the role of the mesoporous TiO$_2$ layer in better carrier extraction. Moreover, we also compared the IPCE spectra of the samples with BM and WM layers (Figures S5, Supporting Information). The lower IPCE values for poorer quality layers can be observed for wavelengths below 500 nm, for which more carriers are excited close to the TiO$_2$ layers owing to the higher absorbance.

To obtain more detailed information on charge transport in the investigated cells, we performed electrochemical impedance spectroscopy (EIS) measurements. The electrochemical response of perovskite solar cells contains the resonance response at two or three different frequencies, related to different timescales of the charge-transfer processes.[29–31] The Nyquist plots of the cells studied in this work (Figure S4 A, Supporting Information) exhibit two distinct time constants, so they are modelled by two resistor-constant phase element (R-CPE) circuits put in series with a resistance (R_s). The product of CPE and the corresponding resistance has the meaning of charge lifetime related to certain charge-transfer processes. The first circuit illustrates the short lifetime (µs) of electrons. The second one represents the longer diffusion of ions (tenths of second) processes, in line with the hysteresis effect observed (Figure S3, Supporting Information).[32]

The EIS results, measured under illumination conditions, are shown in Figure 4 C. The decrease in the shorter lifetime accompanies an increase in J_{sc}. This decrease indicates that the shorter lifetime under illumination is associated with faster (more efficient) charge extraction to contacts before competing recombination occurs. In the dark, this lifetime increases significantly (Figure S4 B) and is dependent on the applied voltage (reduced by one order of magnitude as the voltage changes from 0.5 to 0.9 V). Similar behavior has been reported previously by some of us for MAPbI$_3$ cells with spiro-OMeTAD.[31] There are no photoinduced charges in the dark, and thus, in such conditions, the obtained lifetime should be associated with the charge transfer from contact materials to perovskite, showing the timescale of the charge recombination process. It should be noted that in most EIS studies of PSCs, the experiments are only performed in the dark, and typically, longer lifetimes indicate better cells with slower recombina-

tion. Our results indicate that, on the contrary, the experiment under illumination shows the influence of charge extraction, which is faster for the more efficient samples.

The EIS studies also allowed the extraction of the series resistance, the average value of which was $R_S = 90\ \Omega$ for the prepared cells. We calculated that if such series resistance is eliminated, the FF of the best sample would increase from 0.64 to 0.70, leading to an efficiency of 14.9%, an improvement of a factor of around 1.1.

Time-resolved emission investigation

Finally, the samples were investigated using time-resolved emission spectroscopy. The obtained decays were first characterized in the simplest way by half-lifetime (the time after which the amplitude is equal to half the initial value), presented in Figure 5A (for the excitation from spiro-OMeTAD side, planar samples are not included). Generally shorter lifetimes are observed for the cells with higher long-wavelength absorbance. The half-lifetime decreases from around 14 ns for the samples prepared under room conditions (lower absorption at 700 nm) to 6 ns for that prepared at low humidity with the BM layer (higher absorption). This indicates that in more efficient cells (with higher absorbance and purer perovskite phase) the charge transfer to selective contacts is faster.

Then, we analyzed the fluorescence decays in more detail. The decay of photoexcited carriers in perovskites proceeds in two main ways: recombination, and injection of carrier to selective transporting material.[13,31,33] The contribution of a specific type of recombination of carriers depends on the density of states, and thus, on the excitation energy (laser pulse power). Decay of excited carriers (n) in a perovskite is described by Equation (3), in which k_1 is the first-order rate constant (which consists of trap-assisted Shockley–Read–Hall recombination and charge injection) and k_2 is the second-order recombination rate constant (free carrier recombination).[34,35]

$$-\frac{dn}{dt} = k_1 n + k_2 n^2 \tag{3}$$

In Equation (3), the third-order Auger recombination was neglected, as it usually occurs for high excitation intensity. Analytical solution of the Equation (3) is as given in Equation (4), in which n_0 is the initial charge carriers population and t_0 is the time of excitation (maximum amplitude in fluorescence decays).[10]

$$n(t) = \frac{n_0 k_1}{k_1 \exp(k_1(t - t_0)) + n_0 k_2 [\exp(k_1(t - t_0)) - 1]} \tag{4}$$

First, we investigated the influence of excitation pulse intensity (laser power) on the recombination rate constants to check the validity of the above model. The expected slowing down of fluorescence decays with decreasing excitation power (the example shown in Figure S6, Supporting Information) was observed. The decays were fitted with Equation (4) with the initial charge population n_0 varied proportionally to the excita-
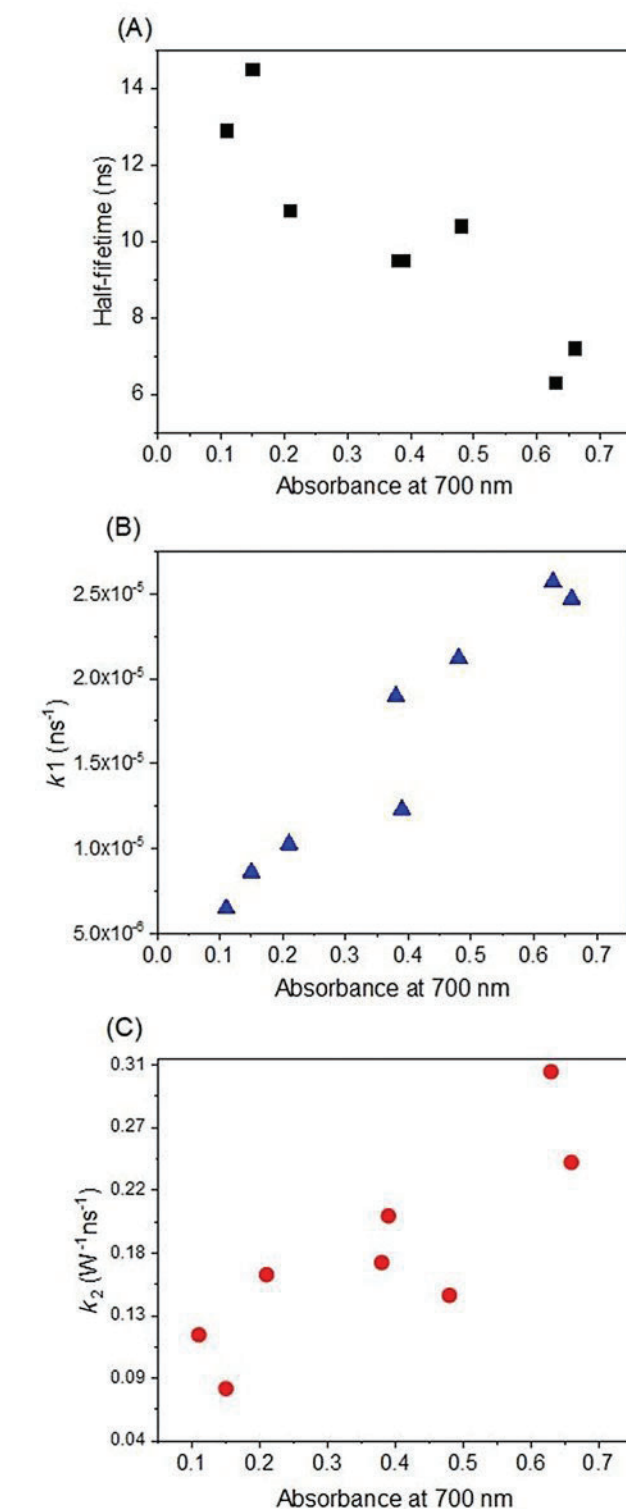
Figure 5. Half amplitude lifetime (A), and first- (B) and second-order (C) recombination rate constants as a function of absorbance at 700 nm.

tion power (determination of exact n_0 value is difficult). The obtained first- and second-order rate constants (parameters k_1 and k_2) for the selected samples are shown in Table 3, and their similar values for all excitation power values means that Equation (4) can describe the kinetics properly.

140

Table 3. First- (k_1) and second-order (k_2) recombination rate constants as a function of excitation laser power for sample WM <1O_2 10RH, obtained from fitting emission decays with Equation (4).

Excitation laser power [µW]	k_1 [10^{-5} ns^{-1}]	k_2 [W^{-1} ns^{-1}]
450	0.90	0.19
150	1.12	0.18
50	1.07	0.17

The first- and second-order recombination rate constants obtained for the studied samples versus the long-wavelength absorbance are shown in Figure 5B,C. The increase in k_1 with more efficient (with higher absorbance at 700 nm) cells can be explained by the faster carriers transfer to selective transporting material, which should be the first-order process.[36] On the other hand, the increase in k_2 values with the sample absorbance is more difficult to clarify. It can be explained by a higher second-order recombination process in the desired perovskite phase with respect to those in the samples with more unreacted precursors. Another possibility is that the charge transfer to contact materials is described by both the k_1 and k_2 parameters, at least if the simple Equation (3) is used to simulate the charge population decay.

Conclusion

We focused on mixed ion perovskite (FAPbI_3)_{0.85}(MAPbBr_3)_{0.15} prepared under different conditions to obtain active layers of different qualities. We used several techniques such as steady-state absorption and emission, X-ray diffraction, scanning electron microscopy, photovoltaic measurements, electrochemical impedance spectroscopy, and time-resolved fluorescence to determine a correlation between the layer quality and the solar cell performance.

The same amount of perovskite precursor was deposited on all samples, but the long-wavelength absorbance (at 700 nm) of the resultant active layer was different depending on the deposition conditions (humidity and oxygen content, use of anti-solvent, presence and quality of mesoporous titania layer). Lower absorbance at long wavelength corresponded to additional absorption features in the short-wavelength range. We propose that the absorbance ratio of longer (700 nm) to shorter (600 nm) wavelengths provides a good description of the layer quality. We confirmed this assumption by observing no significant difference in the thickness of the active layer from SEM cross-section images. In addition, the XRD analysis showed a correlation between the absorbance at 700 nm and the peak ratio of mixed-ion perovskite and unreacted precursor phases. The efficiency of the prepared batches increased with increasing absorbance at 700 nm. The EIS investigation under illumination revealed that the interfacial charge transfer becomes faster with increasing photocurrent of the cells. Finally, the charge population decays were studied by using time-resolved fluorescence spectroscopy to understand the relation between the photovoltaic efficiency and the charge dynamics. For the most efficient samples, emission half-lifetimes of about

6 ns were observed (upon excitation with 420 nm pulses of ≈0.5 mW power). Both first- and second-order rate constants were found to increase with increasing long-wavelength absorption of the perovskite layer and device efficiencies, probably owing to a more rapid charge injection. This is in contrast to many studies of the isolated perovskite material, in which better quality is related to longer lifetimes owing to slower charge recombination.

Experimental Section

Sample preparation

Plates of 1.4×1.9 cm were cut from FTO glass (≈13 Ω/sq, Sigma Aldrich) and cleaned in a soap solution, distilled water, and ethanol in an ultrasound bath for 15 min each. Finally, a UV ozone cleaner was used. A 0.34 M solution of titanium isopropoxide (100 µL, Sigma-Aldrich) in anhydrous ethanol (PoCH) was spin-coated at 2000 rpm for 1 min and then dried at 125 °C for 5 min to obtain a compact TiO_2 layer (c-TiO_2). A mesoporous TiO_2 (mp-TiO_2) layer was provided by spin-coating of mesoporous titania paste at 5000 rpm for 30 s. In our research, two kinds of mesoporous paste were used. The first was the original 15–20 nm particle paste (T600, Solaronix), and the second was 18–20 nm TiO_2 particle nanopaste (screen-printable paste, DN-GPS-18TS, Dyenamo), diluted in ethanol (TiO_2/EtOH 1:5 w/w, PoCH). The first paste gave poorer quality (worse) mesoporous layers (probably owing to aggregations in the original package as a result of aging), so it is abbreviated as "WM", whereas the second paste (freshly prepared by dilution of a denser one) gave a higher-quality (better) mesoporous structure, and is abbreviated as "BM".

After drying at 100 °C for 5 min, the samples were heated at 450 °C for 30 min. They were then dipped into a solution of 140 µL of TiCl_4 (Sigma-Aldrich) diluted in H_2O (25 mL) and heated at 70 °C for 20 min. Finally, they were heated at 475 °C for 30 min. Formamidinium iodide (FAI, 1.275 M, Dyenamo), lead iodide (PbI_2, 1.275 M, Sigma-Aldrich), methylammonium bromide (MABr, 0.225 M, Dyenamo), and lead bromide (PbBr_2, 0.225 M, Sigma-Aldrich) were dissolved in anhydrous N,N-dimethylformamide (DMF, Sigma) and dimethyl sulfoxide (DMSO, PoCH) (4:1, vol/vol) and deposited on the samples by spin-coating (3000 rpm for 60 s or with additional 5000 rpm for next 40 s). An anti-solvent (toluene, 300 µL, Merck) was applied 8 s before the end of the spinning. The cells were annealed on a hot plate at 110 °C for 1 h. Different conditions of deposition and annealing of mixed-cation perovskite films are described in Table 1. The hole-transporting material layer was deposited by spin-coating from a solution consisting of 2,2′,7,7′-tetrakis[N,N-di(4-methoxyphenyl)amino]-9,9′-spirobifluoren (spiro-OMeTAD, 72.3 mg mL^{-1}, Sigma-Aldrich), 4-tert-butylpyridine (TBP, 28.8 µL mL^{-1}, Aldrich), and a solution of lithium bis(trifluoromethanesulfonyl) imide (LiTFSI, 17.5 µL mL^{-1}, Sigma-Aldrich), all dissolved in chlorobenzene (1 mL, Sigma-Aldrich). Perovskite layer synthesis and spiro-OMeTAD deposition were conducted under controlled conditions in a glovebox. Finally, gold electrodes (area $S = 0.05$ cm^2) were deposited by sputtering (using a mask).

Sample characterization

The current–voltage measurements were performed under standard sunlight simulation conditions (delivered by 150 W Xe lamp and AM1.5G filter) with an Autolab M101 potentiostat coupled with a photoelectric spectrometer with the option of a solar simu-

lator (Instytut Fotonowy—Photon Institute, Poland). The intensity was adjusted to provide 1 Sun illumination (100 mW cm^{-2}) by using a calibrated silicon solar cell (15151, ABET). However, it should be noted that most of the measurements were performed under irradiation slightly below 1 Sun conditions (0.9 Sun); only upon presenting the most efficient cells was the condition of 1 Sun intensity well respected. The perovskite active layer area was about 2 cm^2 and the best of the several deposited gold electrodes of active area 0.05 cm^2 was used for the current–voltage measurements. Current–voltage curves were collected for the reverse scan (from open-circuit voltage to zero), and the scan rate was equal to 200 mV s^{-1}. For some samples, the forward scan with the same rate was applied to determine the hysteresis of the cells. The photovoltaic parameters were averaged from —three to six samples. Impedance spectroscopy data were analyzed by an M101/FRA32 M response analyzer module (Autolab) under 1 Sun illumination (near short-circuit conditions) and in the dark. A voltage perturbation of 10 mV was used, in the frequency range from 10^{-1} to 10^6 Hz. Zview (Scriber) was applied to fit the equivalent circuit of the obtained spectra. IPCE spectra were measured with the photoelectric spectrometer mentioned above (without bias light and without chopping of the monochromatic light).

UV/Vis absorption spectra were recorded with a JASCO V-770 spectrometer equipped with 150 mm integrating sphere (LN-925). The absorbance values were averaged from —six to twelve samples. The cross-section images were delivered by a Jeol 7001 TTLS field-emission scanning electron microscope (SEM) working at an acceleration voltage of 5 kV. X-ray diffraction (XRD) experiments were performed using X'pert^3 Panalytical with a Cu X-ray source ($\lambda =$ 1.5406 Å). The time-resolved emission data were collected using the time-correlated single photon counting technique (TCSPC) in the time range from picosecond to nanosecond.[37] TCSPC measurements were performed at the magic angle with a pump pulse repetition rate of 4 MHz and time per channel of 24.4 ps. This setup was also used to measure the stationary emission spectra. The excitation wavelength was equal to 421 nm. For minimization of the effect of possible random fluctuation of the results, the emission measurements were performed for at least two places on the sample, and the results were averaged from —two to four samples from the same batch.

Acknowledgements

Conflict of interest

The authors declare no conflict of interest.

[1] N. J. Jeon, J. H. Noh, W. S. Yang, Y. C. Kim, S. Ryu, J. Seo, S. Il Seok, *Nature* **2015**, *517*, 476–480.

[2] W. S. Yang, J. H. Noh, N. J. Jeon, Y. C. Kim, S. Ryu, J. Seo, S. I. Seok, *Science* **2015**, *348*, 1234–1237.

[3] L. K. Ono, E. J. Juarez-Perez, Y. Qi, *ACS Appl. Mater. Interfaces* **2017**, *9*, 30197–30246.

[4] W. S. Yang, B. Park, E. H. Jung, N. J. Jeon, Y. C. Kim, D. U. Lee, S. S. Shin, J. Seo, E. K. Kim, J. H. Noh, S. I. Seok, *Science* **2017**, *356*, 1376–1379.

[5] M. Saliba, T. Matsui, J.-Y. Seo, K. Domanski, J.-P. Correa-Baena, M. K. Nazeeruddin, S. M. Zakeeruddin, W. Tress, A. Abate, A. Hagfeldt, M. Grätzel, *Energy Environ. Sci.* **2016**, *9*, 1989–1997.

[6] M. Saliba, T. Matsui, K. Domanski, J.-Y. Seo, A. Ummadisingu, S. M. Zakeeruddin, J.-P. Correa-Baena, W. Tress, A. Abate, A. Hagfeldt, M. Grätzel, *Science* **2016**, *354*, 206–209.

[7] NREL, "National Renewable Energy Laboratory", can be found under https://www.nrel.gov/pv/assets/images/efficiency-chart-20180716.jpg, **2018**.

[8] T. W. Crothers, R. L. Milot, J. B. Patel, E. S. Parrott, J. Schlipf, P. Müller-Buschbaum, M. B. Johnston, L. M. Herz, *Nano Lett.* **2017**, *17*, 5782–5789.

[9] S. J. Yoon, K. G. Stamplecoskie, P. V. Kamat, *J. Phys. Chem. Lett.* **2016**, *7*, 1368–1373.

[10] X. Li, D. Bi, C. Yi, J.-D. Décoppet, J. Luo, S. M. Zakeeruddin, A. Hagfeldt, M. Grätzel, *Science* **2016**, *353*, 58–62.

[11] C. L. Davies, M. R. Filip, J. B. Patel, T. W. Crothers, C. Verdi, A. D. Wright, R. L. Milot, F. Giustino, M. B. Johnston, L. M. Herz, *Nat. Commun.* **2018**, *9*, 293.

[12] M. T. Trinh, X. Wu, D. Niesner, X. Y. Zhu, *J. Mater. Chem. A* **2015**, *3*, 9285–9290.

[13] J. Leng, J. Liu, J. Zhang, S. Jin, *J. Phys. Chem. Lett.* **2016**, *7*, 5056–5061.

[14] T. J. Jacobsson, J. P. Correa-Baena, E. Halvani Anaraki, B. Philippe, S. D. Stranks, M. E. F. Bouduban, W. Tress, K. Schenk, J. Teuscher, J. E. Moser, H. Rensmo, A. Hagfeldt, *J. Am. Chem. Soc.* **2016**, *138*, 10331–10343.

[15] G. Grancini, D. Viola, Y. Lee, M. Saliba, S. Paek, K. T. Cho, S. Orlandi, M. Cavazzini, F. Fungo, M. I. Hossain, A. Belaidi, N. Tabet, G. Pozzi, G. Cerullo, M. K. Nazeeruddin, *ChemPhysChem* **2017**, *18*, 2381–2389.

[16] Y. Huang, Y. Zhang, J. Sun, X. Wang, J. Sun, Q. Chen, C. Pan, H. Zhou, *Adv. Mater. Interfaces* **2018**, *5*, 1800224.

[17] M. He, B. Li, X. Cui, B. Jiang, Y. He, Y. Chen, D. O'Neil, P. Szymanski, M. A. Ei-Sayed, J. Huang, Z. Lin, *Nat. Commun.* **2017**, *8*, 16045.

[18] S. Chen, X. Wen, J. S. Yun, S. Huang, M. Green, N. J. Jeon, W. S. Yang, J. H. Noh, J. Seo, S. Il Seok, A. Ho-Baillie, *ACS Appl. Mater. Interfaces* **2017**, *9*, 6072–6078.

[19] Y.-K. Ren, X.-H. Ding, Y.-H. Wu, J. Zhu, T. Hayat, A. Alsaedi, Y.-F. Xu, Z. Li, S.-F. Yang, S.-Y. Dai, *J. Mater. Chem. A* **2017**, *5*, 20327–20333.

[20] Y. Kim, E. H. Jung, G. Kim, D. Kim, B. J. Kim, J. Seo, *Adv. Energy Mater.* **2018**, *8*, 1801668.

[21] S. Paek, P. Qin, Y. Lee, K. T. Cho, P. Gao, G. Grancini, E. Oveisi, P. Gratia, K. Rakstys, S. A. Al-Muhtaseb, C. Ludwig, J. Ko, M. K. Nazaeeruddin, *Adv. Mater.* **2017**, *29*, 1606555.

[22] K. T. Cho, S. Paek, G. Grancini, C. Roldán-carmona, P. Gao, Y. Lee, M. K. Nazeeruddin, *Energy Environ. Sci.* **2017**, *10*, 621–627.

[23] J.-P. Correa-Baena, M. Saliba, T. Buonassisi, M. Grätzel, A. Abate, W. Tress, A. Hagfeldt, *Science* **2017**, *358*, 739–744.

[24] K. Sveinbjörnsson, K. Aitola, J. Zhang, M. B. Johansson, X. Zhang, J. P. Correa-Baena, A. Hagfeldt, G. Boschloo, E. M. J. Johansson, *J. Mater. Chem. A* **2016**, *4*, 16536–16545.

[25] A. Luque, S. Hegedus, *Handbook of Photovoltaic Science and Engineering*, Willey, New York, **2003**.

[26] T. Du, C. H. Burgess, J. Kim, J. Zhang, J. R. Durrant, M. A. McLachlan, *Sustainable Energy Fuels* **2017**, *1*, 119–126.

[27] C. Roldán-Carmona, O. Malinkiewicz, R. Betancur, G. Longo, C. Momblona, F. Jaramillo, L. Camacho, H. J. Bolink, *Energy Environ. Sci.* **2014**, *7*, 2968–2973.

[28] B. Park, N. Kedem, M. Kulbak, D. Y. Lee, W. S. Yang, N. J. Jeon, J. Seo, G. Kim, K. J. Kim, T. J. Shin, G. Hodes, D. Cahen, S. Il Seok, *Nat. Commun.* **2018**, *9*, 3301.

[29] P. Lopez-Varo, J. A. Jiménez-Tejada, M. García-Rosell, S. Ravishankar, G. Garcia-Belmonte, J. Bisquert, O. Almora, *Adv. Energy Mater.* **2018**, *8*, 1702772.

[30] A. Todinova, L. Contreras-Bernal, M. Salado, S. Ahmad, N. Morillo, J. Idigoras, J. A. Anta, *ChemElectroChem* **2017**, *4*, 2891–2901.

[31] K. Pydzińska, J. Karolczak, I. Kosta, R. Tena-Zaera, A. Todinova, J. Idígoras, J. A. Anta, M. Ziółek, *ChemSusChem* **2016**, *9*, 1647–1659.

[32] C. Eames, J. M. Frost, P. R. F. Barnes, B. C. O'Regan, A. Walsh, M. S. Islam, *Nat. Commun.* **2015**, *6*, 7497.

142

[33] L. M. Herz, *Annu. Rev. Phys. Chem.* **2016**, *67*, 65 – 89.

[34] J. S. Manser, P. V. Kamat, *Nat. Photonics* **2014**, *8*, 737 – 743.

[35] T. Handa, D. M. Tex, A. Shimazaki, A. Wakamiya, Y. Kanemitsu, *J. Phys. Chem. Lett.* **2017**, *8*, 954 – 960.

[36] Q. Lin, Z. Wang, H. J. Snaith, M. B. Johnston, L. M. Herz, *Adv. Sci.* **2018**, *5*, 1700792.

[37] T. Wrózowa, B. Ciesielska, D. Komar, J. Karolczak, A. Maciejewski, J. Kubicki, *Rev. Sci. Instrum.* **2004**, *75*, 3107 – 3121.

143

CHEMISTRY
A European Journal

Supporting Information

Understanding the Effect of Different Synthesis Conditions on the Physicochemical Properties of Mixed-Ion Perovskite Solar Cells

Brian Quere,[a] Katarzyna Pydzińska-Białek,[a] Jerzy Karolczak,[a, b] Grzegorz Nowaczyk,[c] Emerson Coy,[c] and Marcin Ziółek*[a]

chem_201900310_sm_miscellaneous_information.pdf
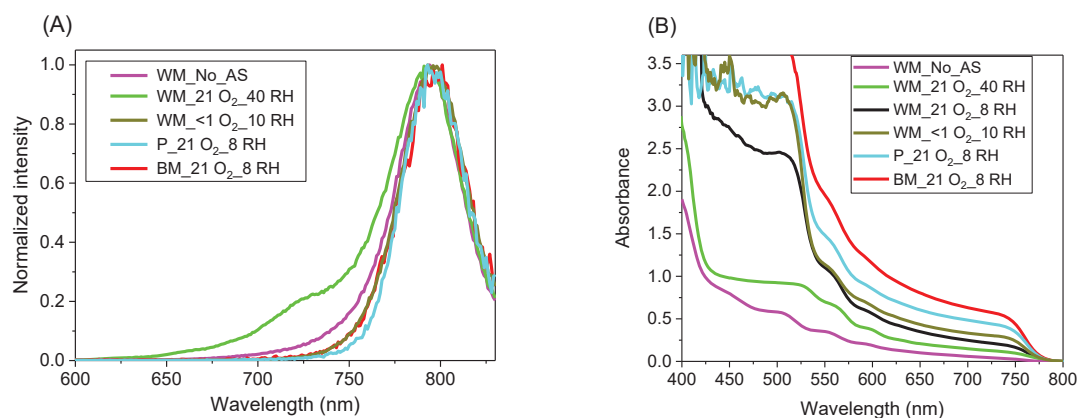
Figure S1. Steady-state emission (A) and absorbance (B) spectra and of PSCs prepared under different conditions.
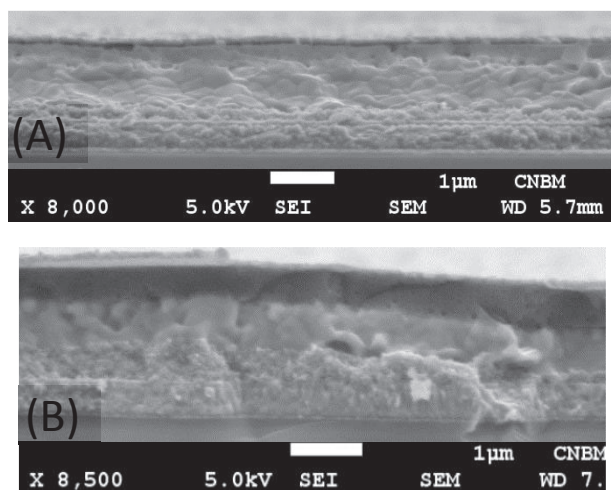
Figure S2. SEM cross-section images of sample BM_21O$_2$_8RH (A) and WM_21O$_2$_8RH (B).

1
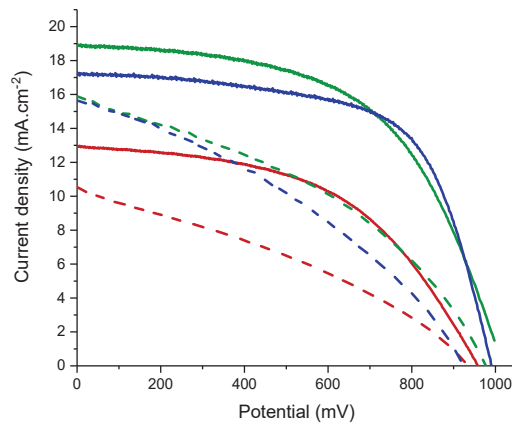
Figure S3. Current density vs. voltage curves for different BM_21O$_2$_8RH samples collected for reverse (solid lines) and forward (dashed lines) scanning directions (scan rate 200 mV/s in both cases). Hysteresis indexes HI obtained from the above graph ($HI = \frac{J_{rev}\left(\frac{V_{oc}}{2}\right) - J_{for}\left(\frac{V_{oc}}{2}\right)}{J_{rev}\left(\frac{V_{oc}}{2}\right)}$) vary from 0.33 to 0.41.
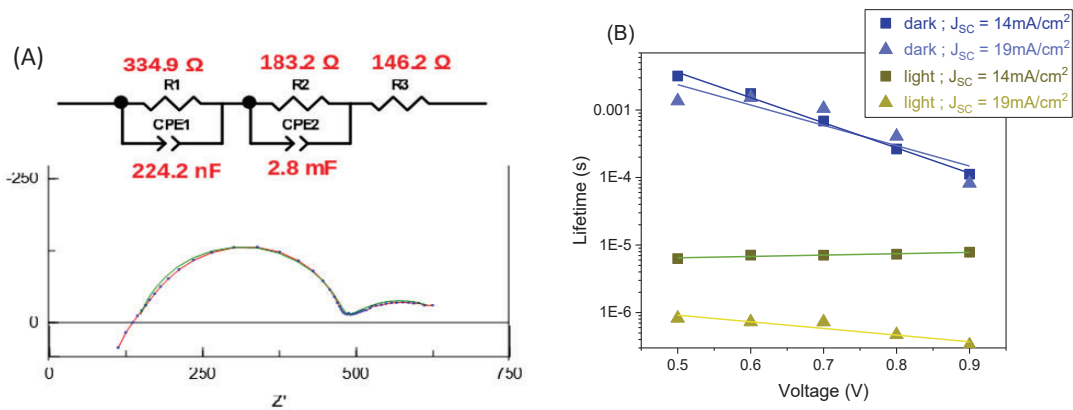
Figure S4. Exemplary Nyquist plot obtained from electrochemical impedance spectroscopy experiment (blue dots) fitted by equivalent circuit, shown above (green line) (A) and the results of fitting, lifetime values obtained for different applied potential for the samples exhibiting different current, measured in the dark (squares) and under 1 Sun illumination (triangles) (B).
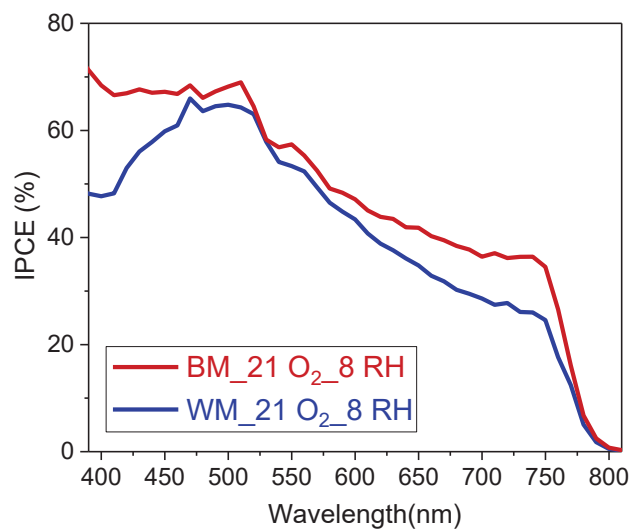
Figure S5. Incident photon-to-current efficiency (IPCE) spectra for samples prepared using two different titania layers. The photocurrent calculated from integrated IPCE spectra under AM1.5G conditions is 20.5 mA/cm^2 for BM_21O$_2$_8RH sample and 17.3 mA/cm^2 for WM_21O$_2$_8RH.
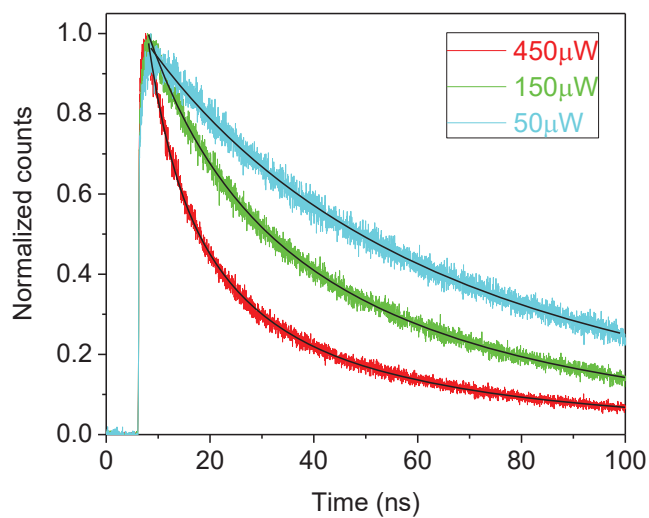
Figure S6. Emission decays fitted by eq. 3 (red line) of sample WM_<1O$_2$_10RH for different excitation power.
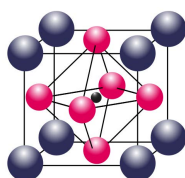
3

KPB-5

Understanding the interfaces between triple-cation perovskite and electron or hole transporting material

K.Pydzinska-Białek, V.Drushliak, E.Coy, K.Załęski, J.Flach, J.Idigoras, L.Contreras-Bernal, A.Hagfeldt, J.A.Anta, M.Ziółek

www.acsami.org

Research Article

Understanding the Interfaces between Triple-Cation Perovskite and Electron or Hole Transporting Material

Katarzyna Pydzińska-Białek, Viktoriia Drushliak, Emerson Coy, Karol Załęski, Jessica Flach, Jesus Idígoras, Lidia Contreras-Bernal, Anders Hagfeldt, Juan Antonio Anta, and Marcin Ziółek*

Cite This: *ACS Appl. Mater. Interfaces* 2020, 12, 30399−30410

Read Online

ACCESS | 📊 Metrics & More | 📖 Article Recommendations | 🆂🅸 Supporting Information

ABSTRACT: The properties of efficient solar cells fabricated with triple-cation perovskite placed between a mesoporous titania layer and a spiro-OMeTAD layer are studied by using devices either prepared under water-free drybox conditions or fabricated under ambient room humidity. The morphological studies indicate that the content of unreacted PbI_2 phase in the perovskite structure is much higher near the interface with titania than near the interface with spiro-OMeTAD. The stationary emission spectra and transient bleach peaks of perovskites show additional long-wavelength features close to the titania side. Time-resolved techniques ranging from femtoseconds to seconds reveal further differences in charge dynamics at both interfaces. The population decay is significantly faster at the titania side than at the spiro-OMeTAD side for the cells prepared under ambient conditions. An increased hole injection rate correlates with higher photocurrent seen in the devices prepared under drybox conditions. The charge recombination loss on the millisecond time scale is found to be slower at the interface with titania than at the interface with spiro-OMeTAD. The ideality factor of the cells is found to increase with increasing DMSO content in the precursor solution, indicating a change in recombination mechanism from bulk to surface recombination. We also found that the charge dynamics are not uniform within the whole perovskite layer. This feature has significant implications for understanding the operation and optimizing the performance of solar devices based on mixed cation perovskites.

KEYWORDS: *perovskite solar cells, triple-cation perovskite, perovskite−TiO₂ interface, perovskite−HTM interface, ultrafast time-resolved optical spectroscopy, impedance spectroscopy*
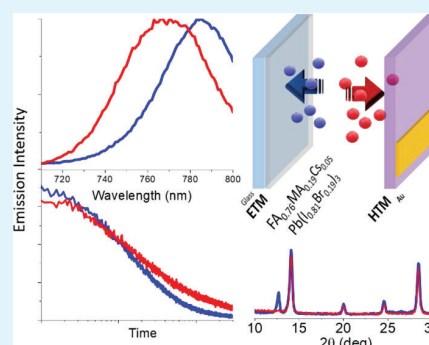
INTRODUCTION

Perovskite solar cells (PSCs) have undergone a tremendous increase in efficiency from 3.8% in 2009[1] to an outstanding 25.2% certificated only 10 years later in 2019.[2] The initial and the most studied perovskite structure for PSC is methyl-ammonium lead triiodide ($MAPbI_3$).[1] However, the $MAPbI_3$ absorber suffers from instability under ambient conditions; therefore, compositions with substitutions made for MA and I have been investigated. The additions of the larger formamidinium (FA) cation and bromide ion, with the optimized configuration $(FAPbI_3)_{0.85}(MAPbBr_3)_{0.15}$, made the structure more thermally stable, increased the band gap, and provided higher tolerance for humidity.[3] Further incorporation of small amounts of cesium atoms brings humidity resistance and less susceptibility for structural impurities.[4,5] Many other substitutions have been tried, for example, tin or bismuth to reduce toxicity[6,7] or rubidium to enhance charge mobility.[5] However, the benchmark triple-cation configuration of $FA_{0.76}MA_{0.19}Cs_{0.05}Pb(I_{0.81}Br_{0.19})_3$, which we study in the present work, is frequently used when one wants to get both stable and very efficient PSCs. Despite

all of that, most fundamental studies of PSCs are still mainly limited to the standard $MAPbI_3$ structure.

Most of the time-resolved studies of PSC, including those implemented in this work, require taking into account the complex response of the perovskite layer to the light excitation. Upon light absorption, pairs of electrons in the conduction band and holes in the valence band are formed, followed by fast processes on the subpicosecond time scale such as charge cooling and exciton dissociation. These processes are accompanied by a band-edge shift due to charge screening or band-gap renormalization effects.[8,9] After charge thermalization to the valence and conduction band edges, the population of the charges is governed by the interplay of charge recombination and injection of electrons or holes into the electron transporting material (ETM) or hole transporting

30399
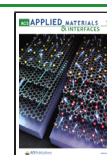
material (HTM), respectively.[10] In the simplest approximation (i.e., neglecting Auger recombination valid in the low range of excited carriers concentration), the change of the population of the excited carriers (n) in the bulk can be described by[11]

$$-\frac{dn}{dt} = k_1 n + k_2 n^2 \tag{1}$$

The first-order decay with the rate constant k_1 is related to the trap-assisted recombination (Shockley−Read−Hall recombination). The second-order process described by the rate constant k_2 is due to free carrier recombination (band-to-band radiative recombination).

The injection of charges into the ETM or HTM contributes to the first-order processes.[12] However, in many cases the apparent charge population decay can be affected by reabsorption and/or diffusion processes, the inclusion of which in eq 1 requires one to numerically solve the kinetic equation.[13,14] Therefore, the observed kinetics of the charge population can be affected not only by the perovskite, HTM, and ETM materials but also by the excitation wavelength, excitation fluence, or the perovskite layer thickness.

Besides the properties of the perovskite absorber, the crucial parts in the optimized operation of PSC are the perovskite/ETM and perovskite/HTM interfaces. For standard MAPbI$_3$, time-resolved techniques were employed to study not only the charge injection dynamics but also the influence of interfacial recombination, interface trap states, and band bending.[14−17] Therefore, one of the main goals of our work is to investigate the interfaces of the benchmark triple-cation perovskite with ETM and HTM, focusing on the differences in the dynamics (probed by time-resolved techniques) and absorber structure close to both interfaces. The absorption properties of perovskite material allow us to probe the ETM or HTM interfaces in the fully assembled PSC either by illumination from different sides[18] or by tuning the illumination wavelength.[19] Although electronic transport is known to be very fast in perovskites, an effect on the initial spatial distribution of photocarriers is still expected[18,19] because interfacial charge injection is much faster than transport.[14] Also, with electron/hole diffusion coefficients on the order of 0.5 cm^2/s,[20] the carriers will travel distances on the order of 200 nm in a time span of nanoseconds. Thus, for typical absorber thicknesses in PCSs of several hundreds of nanometers, the diffusion process can still be observed by using optical time-resolved techniques.[14]

Reducing the fabrication costs is a very important aspect in PSC development. Typically, PSCs are prepared in a highly controlled environment in a glovebox, which makes the procedure expensive and less available. Perovskite crystallization and solar cell preparation can be transferred into an open-air environment; however, a procedure to deal with and control the amount of water content in open air should be developed. Only a few papers have been published on this subject so far: for the simple MAPbI$_3$ case[21,22] and also using a more complicated formulation for triple-cation perovskite.[23] The presence of water can clearly affect both perovskite and ETM/HTM materials. For example, it is well-known that water triggers the perovskite decomposition to produce PbI$_2$.[24] It was observed that perovskite contact with a humid environment produced faster recombination, a tendency to favor surface recombination, and slower transport.[25] The layer of spiro-OMeTAD can be also strongly affected by water, mainly due to the high hygroscopicity of the dopants.[26]

Therefore, in this work we focus on triple-cation perovskite prepared under highly controlled dry conditions in a drybox (DC) or under ambient conditions (AC) present under a fume hood in the laboratory. It is expected that the performance of AC samples is lower than those of DC ones, but it is also interesting to study devices prepared at ambient conditions for industrial reasons. Thus, another goal is to understand charge dynamics (recombination and charge injection to interfaces) for two state-of-the-art methods of perovskite preparation. For that we take advantage of the information provided by stationary and time-resolved optical spectroscopy techniques as well as impedance spectroscopy measurements in the frequency domain.

■ MATERIALS AND METHODS

Sample Preparation. Two different sample preparation protocols were used. In the first method, the perovskite precursor and spiro-OMeTAD solutions were prepared in an argon-filled glovebox and then transported to drybox where the spin coating of precursors, heating, and spin coating of spiro-OMeTAD took place. These samples are abbreviated as DC. In the second method, the solutions were prepared in a nitrogen-filled glovebox and then transferred to a fume hood under ambient air conditions for further processing; these samples are abbreviated as AC.

Samples were prepared from 2.5 × 2.3 cm^2 (for AC samples) or 2.5 × 1.7 cm^2 (for DC samples) conducting glass (FTO) substrates. The substrates were cleaned with detergent, distilled water, ethanol, and isopropanol for 15 min each. A compact layer of titania (TiO$_2$) was applied by using the spray pyrolysis technique from titanium diisopropoxide (6.67% in EtOH v/v). On the top, mesoporous TiO$_2$ paste (Greatcellsolar, 30NR-D, diluted 1:6 w/w in EtOH) was deposited by spin coating (10 s, 2000 rpm). The FA$_{0.76}$MA$_{0.19}$Cs$_{0.05}$Pb(I$_{0.81}$Br$_{0.19}$)$_3$ perovskite precursor solution was obtained by mixing 1.5 M formamidinium lead triiodide (FAPbI$_3$) with 1.5 M methylammonium lead tribromide (MAPbBr$_3$) solutions, both in 4:1 dimethylformamide:dimethyl sulfoxide (DMF:DMSO, with 10% Pb excess), and 1.5 M cesium iodide (CsI) in DMSO with ratio 95:19:6 (v/v/v). The perovskite layer was deposited by two-step spin coating (10 s at 2000 rpm and then 20 s at 4000 rpm) with chlorobenzene (ChB) as antisolvent (10 s before the end). 2,2′,7,7′-Tetrakis[N,N-di(4-methoxyphenyl)amino]-9,9′-spirobifluorene (Spiro-OMeTAD, 72.3 mg/mL in ChB) with additives, i.e., 17.5 μL of lithium bis(trifluoromethanesulfonyl)imide (LiTFSI, 520 mg/mL in acetonitrile) and 29 μL 4-*tert*-butylpyridine (TPB), was used as hole transporting material, deposited by spin coating (30 s at 4000 rpm). Finally, 80 nm thick gold electrodes were evaporated on top of spiro-OMeTAD layer. For the AC case, different DMSO:DMF ratios were applied in 1.5 M FAPbI$_3$ solution to create 0.4, 0.32, 0.27, or 0.24 DMSO content (v/v) in final solution. For DC samples only standard 0.24 DMSO content (v/v) was used.

It has been shown recently that the absolute content of water measured in the form of partial water vapor pressure (WVP) is the determining lab parameter that needs to be considered during preparation of PSCs at ambient conditions.[27] This parameter is given by the formula

$$WVP = \frac{RH}{100} P_{ws} \tag{2}$$

where RH is the relative percent humidity and P_{ws} is saturation vapor pressure (in kPa) for a given temperature. Therefore, the WVP parameter has been also controlled for the cells prepared under ambient conditions.

Sample Characterization. For spectral characterization of PSC, a steady-state absorption setup (Jasco V-770) coupled with an integrating sphere (Jasco ILN-925) was used. In the studies of the solar cells with different absorption values for the active material, it is often helpful to compare the relative corrected photocurrent of the cells, which gives the information about the total efficiency of the

charge separation. Therefore, in our works we introduce the parameter called total APCE (APCE is absorbed photon to current efficiency).[28] It can be calculated based on the measured short-circuit current of the cell, J_{SC}, and the number of absorbed photons, N_{ph} (obtained from integration of stationary absorptance spectrum multiplied by the photon flux spectrum from AM1.5G data):

$$\text{total APCE} = \frac{J_{SC}}{eN_{ph}} \tag{3}$$

where e is the elementary charge. In the present work we consider the correlation between total APCE and time constants or perovskite layer thickness. We also use the corrected photocurrent to compare the charge separation efficiency in the cells of different thicknesses.

A femtosecond transient absorption setup (Spectra-Physics laser system and Helios spectrometer, Ultrafast Systems) was used to measure ultrafast dynamics.[29] The excitation wavelength was set at 505 nm (1 kHz repetition rate), and two different pump pulse energy densities (10 or 30 $\mu J/cm^2$) were used. The instrument response function was 0.4 ps (FWHM). Emission decays as well as stationary fluorescence spectra were obtained by using the time-correlated single photon counting technique (TCSPC) with temporal resolution from pico- to nanoseconds, detection range from 450 to 820 nm, and excitation wavelength equal to 407 nm (power 400 μW at repetition rate 4 MHz).[30] The kinetics of time-resolved emission and absorption studies were analyzed by determination of half-lifetimes or by fitting with an analytical function. The solution of eq 1 can be given by the function[11,31]

$$n(t) = \frac{n_0 k_1}{k_1 \exp(k_1 t) + n_0 k_2 (\exp(k_1 t) - 1)} \tag{4}$$

where n_0 is the initial charge population density. The transient absorption data were also investigated by using global analysis, the band integral, and the stretched exponential function (the details will be given in the Results and Discussion section). The lifetimes are given as averaged values from 5 to 10 samples along with the estimated errors as standard deviation.

For AC samples, current density–voltage ($J–V$) curves were measured under a solar simulator (ABET-Sun2000) with an AM1.5 filter by using a scan rate of 100 mV/s and a sweep delay of 20 s. Samples prepared in DC conditions were characterized by an LED solar simulator (VeraSol-2, Newport). A Keithley Model 2400 digital source meter was used to apply external bias and record photocurrent. The active area was 0.16 cm^2 in both cases. Impedance spectroscopy (IS) measurements were provided by red and blue LEDs (blue, 465 nm; red, 635 nm) over a range of direct current intensities. This allows for probing the devices with two distinct optical penetration depths.[19] The impedance response was measured by using a potentiostat (PGSTAT302N/FRA2, Autolab), and NOVA 1.7 software was used to analyze the data. For these experiments, a 20 mV perturbation in the 10^6–10^{-1} Hz range was applied. To avoid voltage drop due to the series resistance, IS measurements were performed at open-circuit potential under varying illumination intensities to achieve different positions of the Fermi level in the semiconductor.

Sample cross sections were prepared by focused ion beam (FIB) using a JEOL JIB-4000 instrument. First, a carbon thin film was deposited to protect the area of interest—one of the sample's gold top electrodes. This process protects the delicate surface from damage during the FIB milling. Then a series of cuts by Ga$^+$ beam were made, with acceleration voltage between 5 and 30 kV. Finally, the cross section was transferred *ex situ* onto a commercial Cu grid by a sharp glass probe. The lamella was expose to air for a total of ~5 min between preparation and transference to the TEM column. Transmission electron microscopy (TEM) images were collected on a JEOL ARM-200F microscope working at 80 kV equipped with an energy dispersive X-ray spectroscopy (EDX) detector. Electron energy-loss spectroscopy (EELS) and selected area electron diffraction (SAED) were used to study the diffraction pattern and the distribution of nitrogen and carbon elements. Grazing incident X-

ray diffraction experiments (Gi-XRD) were performed on a X'Pert^3 PANAlytical instrument, operating at 45 kV and 40 mA. Samples were measured from 10° to 45° 2θ, sweeping the incident angle between 0.05° and 5° ω. Data were corrected and presented in a 2D topographical map by using OriginLab2017 software.

■ RESULTS AND DISCUSSION

Stationary Absorption and Photovoltaic Parameters. The triple-cation perovskite solar cells were prepared by two methods: under drybox conditions (DC) or under ambient air conditions (AC), as described in the Materials and Methods section. In both cases the electron transporting material (ETM) consists of combined compact and mesoporous TiO$_2$ layers, while the hole transporting material (HTM) is spiro-OMeTAD. The best current–voltage curves and representative stationary absorption spectra for each type of sample are presented in the Supporting Information (Figure S1). The obtained efficiencies of the best cells were equal to 17.3% and 14.3% for DC and AC samples, respectively (Figure S1A). For DC samples two batches of cells were prepared (manufactured by two different people), and they differed slightly by the perovskite thickness, as revealed in the absorption spectra (Figure S1B). However, within the same batch the absorption spectra were very similar to each other. The DC samples selected for further time-resolved studies varied significantly in photocurrent; therefore, the correlations between dynamic parameters and photovoltaic performances could be explored. For AC samples, a much higher variety in the perovskite layer thickness was observed (Figure S1B shows the absorption spectra of the thickest and the thinnest AC sample). However, the corrected photocurrent was similar for most of the AC cells (total APCE = 90 ± 4%). Therefore, in contrast to DC samples, AC cells serve to explore the effect of the perovskite thickness on the observed dynamics. For further time-resolved studies, complete solar cells with measured photovoltaic parameters were used as the samples.

The AC samples were prepared with varying DMSO:DMF ratios (0.24, 0.27, 0.32, and 0.40 v/v) in precursor solution for different WVP conditions (0.9, 1.0, 1.1, and 1.3 kPa). Recently, these parameters were shown to influence the performance and aging effects of MAPbI$_3$ solar cells prepared under ambient air.[27] However, within our experimental errors, no such correlations could be observed in the case of triple-cation perovskite, at least for the studied DMSO:DMF ratio range. Figure S2 presents the photovoltaic parameters of the cells for different DMSO:DMF ratios and WVP conditions. The thickness of the prepared perovskite layer does not seem to be significantly influenced by the DMSO:DMF ratio or WVP condition. As an example, Figure S3A presents the statistics of the sample thickness for different DMSO:DMF ratios based on over 60 samples.

The hysteresis index for AC samples is relatively low (HI = 0.10 ± 0.03). Figure S3B presents the exemplary current–voltage curve for forward and reverse direction, and the definition of HI is given in its caption.

Structural and Morphological Analysis. SEM, TEM, and Gi-XRD measurements were used to determine and understand the structure, thickness, morphology, and perovskite phase content in the AC cells. Figure 1 shows a cross-section TEM image of a lamella cut of the cells with different absorbance values (lower A(700 nm) = 0.95 and higher A(700 nm) = 1.30). The values of absorbance at 700 nm correspond well to the observed thickness of the perovskite layer, which
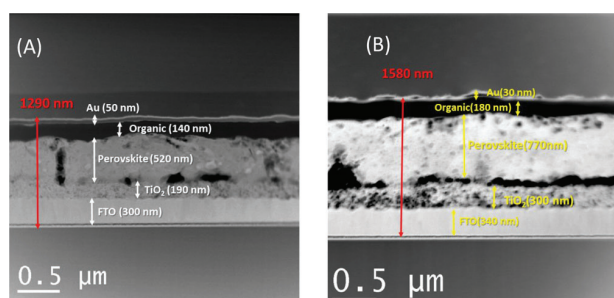
Figure 1. Cross-section transmission electron microscopy images of the thinner (A) and thicker (B) AC samples with the indicated layer thicknesses.

allows us to directly relate the absorbance to the width of the active layer. TEM-EELS-SAED experiments (Figure S4) revealed that the distribution of nitrogen and carbon is homogeneous between the top organic layer (spiro-OMeTAD) and the titania layer. Diffraction patterns show a polycrystalline structure of the perovskite layer with interplanar distances comparable to those observed in XRD pattern. TEM-EDX experiments (Figure S5) show a homogeneous distribution of Pb and Cs atoms and their mixing within the TiO_2 porous layer. Slightly porous and empty areas resembling bubbles or cavities can also be observed. We have verified that these inhomogeneities do not originate from the way the lamella are cut.

Figure S6 presents the SEM top-view images of the perovskite structure for one batch of AC samples at WVP = 0.9 kPa and different DMSO:DMF ratios. Crystal grains ranging from 100 to 400 nm can be recognized. A smoother and more homogeneous perovskite surface at the HTM contact yields slightly better photovoltaic parameters. In this particular batch, the best performing cells were made with 0.32 DMSO:DMF content. However, for other batches this result was not confirmed, so no general conclusions about this particular DMSO:DMF ratio can be drawn.

The most important findings of this section come from the Gi-XRD studies which give information about the perovskite structure at different penetration depths from the top gold electrode (HTM side) obtained with different angles of the incident beam. Figure 2 presents the maps of X-ray diffraction patterns (2θ angle) as a function of the X-ray beam grazing angle (ω) for the same samples shown in Figure 1. The simulated calibration plots to convert the incident angle into the attenuation depth[32] for Au and perovskite are shown in Figure S7. The characteristic diffraction peaks for the perovskite ($2\theta = 14.1°$, $28.5°$, and $31.9°$, black dots), unreacted PbI_2 phase ($2\theta = 12.7°$, red diamonds), and Au ($2\theta = 38.1°$, brown triangles) are indicated in Figure 2. For the thinner sample in Figure 2A, the pattern due to pure perovskite appears just below the HTM surface (~4 nm, corresponding to $\omega = 0.12$), while the unreacted PbI_2 phase occurs around 60 nm ($\omega = 0.43$). It should be noted that the Au (111) peak from the top layer appears at $\omega = 0.31$ (1.5 nm from the top) due to the different density of the materials. Figure S8A shows the XRD patterns for selected penetration depth, and Figure S8B shows the extracted ratio of the PbI_2 to perovskite peaks for the same sample. They show that the deeper the X-ray beam reaches, the higher the content of PbI_2, with the maximum PbI_2 content occurring in the perovskite layer ~150 nm below the HTM interface. Based on Figure 1A with a perovskite layer thickness of ~500 nm, unreacted PbI_2 is present ~350 nm from the bottom TiO_2 interface. For the second sample with the perovskite layer being thicker by about 250 nm (~750 nm total perovskite thickness, Figure 1B), the unreacted PbI_2 phase does not appear until a penetration depth of 200−300 nm (it becomes present only for $\omega > 2.5$, Figure 2B). These measurements suggest that the presence of PbI_2 is found in all samples within a similar distance from the bottom titania interface.

The role of unreacted PbI_2 is widely described in the literature.[33−35] A small amount of unreacted PbI_2 has been reported to improve the efficiency.[36−38] It was shown that PbI_2-rich grains exhibit a longer lifetime because of the suppression of defect trapping,[33,39] and PbI_2 excess leads to a
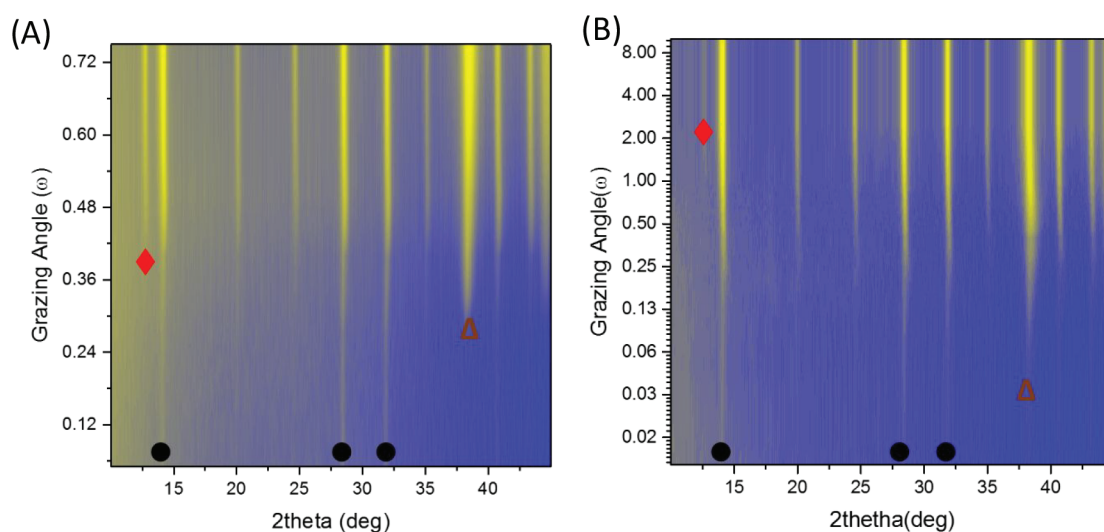
Figure 2. Diffraction pattern vs different grazing angle ω maps with pointed characteristic peaks for thinner (A) and thicker sample (B). Black dots (●) indicate the occurrence of the perovskite peaks (14.1°, 28.5°, and 31.9°), red diamonds (◆) indicate the PbI_2 phase (12.7°), and brown triangles (△) indicate Au(111) (38.1°).
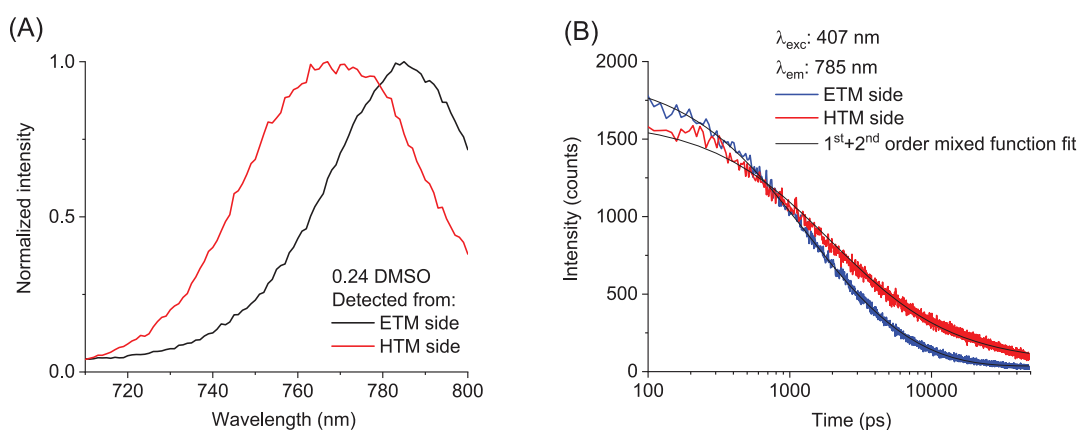
Figure 3. Emission spectra measured from ETM (black) and HTM (red) side (λ_{ex} = 407 nm) (A) and photoluminescence decays measured from ETM (blue) and HTM (red) side with fit first- and second-order decay mixed function (black) (B) for the exemplary AC samples.

more efficient electron injection to TiO_2.[35] However, too large of a contribution of PbI_2 has a detrimental effect on the solar cell performance.[34,40−42] Too thick a PbI_2 layer (>20 nm) at the perovskite/HTM interface lowered the photocurrent.[42] An excess of PbI_2 content had undesirable effects on the PSCs stability as well as on device hysteresis.[34,41] Our results indicate that the content of unreacted PbI_2 phase in the perovskite structure is much higher near the interface with titania (ETM) than near the interface with spiro-OMeTAD (HTM). This means that the perovskite layer is not homogeneous, and the difference observed in spectroscopic experiments described in the next sections could be caused by higher concentration of the unreacted phase in the region closer to the ETM.

Emission. We took advantage of the strong absorption of the perovskite in the short-wavelength range to selectively probe two different interfaces of the cells as the excitation light is absorbed nearest to the illuminated surface. In our samples more than 80% of light is absorbed within the first 100 nm of perovskite layer for the excitation wavelength below 500 nm. In the emission measurements the pump was set at 407 nm, and the laser pulses were directed through either the ETM or HTM side. The stationary emission and fluorescence decay time constants scaling from hundreds of picoseconds to tens of nanoseconds were measured by the time-correlated single photon counting technique. In the case of excitation from the HTM side, the areas of the devices without gold electrodes were used. Figure 3A presents the representative stationary emission results. The spectra were measured up to 800 nm because the second-order diffraction of the pump wavelength obscured the emission signals at longer wavelength. As can be seen, the emission detected from the ETM side results in a red-shifted emission peak with respect to that from HTM side. On average for the AC cells the emission maximum is shifted from 770 ± 3 nm at the HTM side to 784 ± 2 nm at the ETM side. The difference in emission from each side indicates that the perovskite structure and/or composition is different for the layers closest to HTM or ETM, which correlates with the XRD results discussed in the previous section.

Further differences between the excitation from the ETM and HTM side were observed in the kinetics of fluorescence decay measured close to the band maximum (at 785 nm). For AC samples a significantly longer decay at the HTM side was always observed, which is presented in Figure 3B. The kinetics were first analyzed in the simplest way by taking the decay half-

lifetime. The first 100 ps was not analyzed as they contained the contribution from the scattering artifact; this contribution was higher on the HTM side, causing the difference in initial intensities in Figure 3B. The emission half-lifetime statistics for cells of similar perovskite thickness (absorbance around 1.0 at 700 nm) show that the average half-lifetime is equal to 1.61 ± 0.12 and 2.37 ± 0.30 ns for ETM and HTM sides, respectively. The other parameters of all samples (15 in total), including those with different thicknesses, were further studied and compared. Table 1 presents the Pearson correlations between

Table 1. Pearson Correlations between the Parameters of Emission, Corrected Photocurrent (Total APCE), Absorbance (A) (Corresponding to the Sample Thickness), and DMSO Content in Precursor Solution

	ETM half-lifetime	HTM half-lifetime	A(700 nm)	total APCE	DMSO content
ETM half-lifetime	1	0.38	0.55[a]	−0.13	−0.33
HTM half-lifetime	0.38	1	0.82[a]	−0.46	−0.14
A(700 nm)	0.55[a]	0.82[a]	1	−0.36	−0.25
total APCE	−0.13	−0.46	−0.36	1	0.18
DMSO content	−0.33	−0.14	−0.25	0.18	1

[a]The correlation is statistically significant at the 0.05 level (a 95% confidence interval).

half-lifetimes and relative photocurrent, perovskite thickness (absorption), or DMSO:DMF ratio for AC samples. As can be seen, significant correlations can only be found between half-lifetimes and the stationary absorbance at 700 nm (0.55 for ETM-side half-lifetime and 0.82 for HTM-side half-lifetime). The visualization of such correlations is presented in Figure S9A,B. The apparent longer emission decay for thicker samples agrees with recent reports and can be explained by the reabsorption effect.[13] Moreover, the charge population lifetime in thicker samples can also increase due to diffusion effects because there is a longer pathway for electron and holes to reach the contact materials.[14] To exclude the effect of the sample thickness, we performed an analogous analysis limited only to the cells of similar thickness, which confirmed that the DMSO:DMF ratio had no effect on the lifetimes (Table S1). It should be noted that the effect of different probe wavelengths
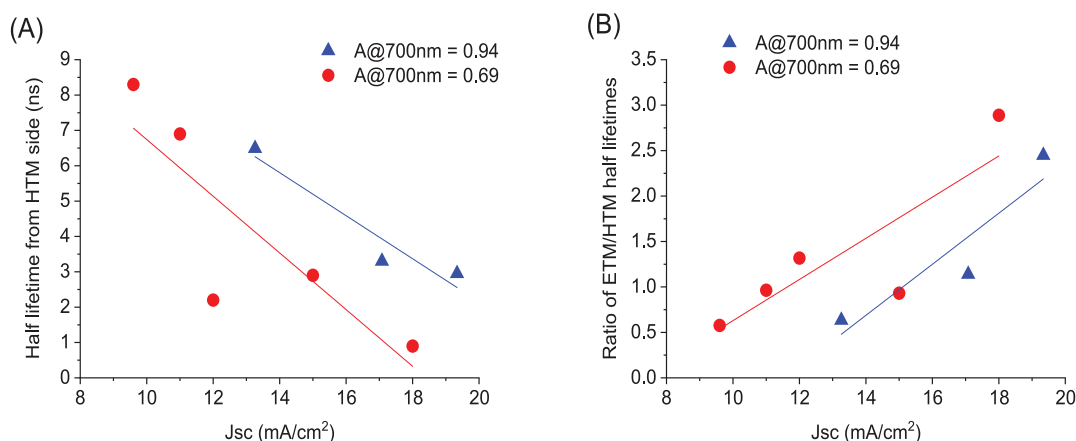
Figure 4. TCSPC results, half-lifetime from HTM side (A), and ratio of ETM/HTM half-lifetimes (B) as a function of short-circuit current for two different thickness of the DC samples.

was also checked (Table S2), and the variation of the emission lifetime within the emission band was not higher than the differences between HTM and ETM.

We have performed a more rigorous analysis by fitting the mixed first- and second-order decay model (eq 4) to the fluorescence kinetics. A good fit quality (correlation $r^2 > 0.99$) was obtained, and an example is presented in Figure 3B. For AC samples of similar thicknesses the average second-order rate constant was higher from the ETM side ($k_{2,ETM} = (13.5 \pm 1.9) \times 10^2$ ns^{-1} W^{-1}, standard error of the mean for five samples is given) than from the HTM side ($k_{2,HTM} = (10.7 \pm 1.7) \times 10^2$ ns^{-1}W^{-1}), in agreement with the half-lifetime analysis. The first-order rate constant (k_1) was negligible from the HTM side, while from the ETM side a random distribution around the small value of $k_{1,ETM} = 1 \times 10^{-4}$ ps^{-1} was observed. Significant Pearson correlations were found between $k_{2,ETM}$ and absorbance at 700 nm (−0.57) and between $k_{2,HTM}$ and the absorbance (−0.65), which confirms the findings from half-lifetimes. However, the Pearson coefficients are not any closer to 1 than those obtained from half-lifetime analysis. Therefore, the parameters of eq 4 do not correlate better with the sample thickness than half-lifetimes.

Differences between the dynamics at HTM and ETM sides were also observed for the DC samples; however, the fluorescence decay at the HTM side was not always longer than from the ETM side. Figure 4A presents half-lifetime data for two different batches with different thickness characterized by indicated absorbance value at 700 nm. Clearly, the decay from the HTM side is getting faster with increasing short-circuit current of the measured cell. For the thicker cells (blue triangles) the decays are slightly slower in comparison to the thinner ones (red dots) due to reabsorption processes[13] and in line with the results for AC samples, but the trend in the correlation with the photocurrent is the same as for thinner cells. The fluorescence decay measured closer to the HTM side is governed more by hole injection into the spiro-OMeTAD layer than electron injection into TiO$_2$. Therefore, for DC cells we can clearly see the correlation between the short-circuit photocurrent and hole injection dynamics: the faster the hole injection, the higher the short-circuit current of the cell. Similar findings have been reported in our recent studies of the mixed MA and FA solar cells.[40] The ratios of half-lifetimes measured from ETM and HTM side are shown in Figure 4B. A significant asymmetry in the half-lifetimes from both sides is

observed. Holes are transported about 3 times faster than electrons in the highest performing cells with photocurrent close to 20 mA/cm^2. It indicates that the crucial part responsible for the variation of the solar cell efficiency for our DC cells is the interface between perovskite and spiro-OMeTAD. Moreover, for efficient charge separation, the hole transfer to spiro-OMeTAD needs to be faster than electron transfer to TiO$_2$. It should be noted that we also observed the same trends for the test perovskite cells prepared in planar configuration (only a compact TiO$_2$ layer without the mesoporous layer), but in that case the best photocurrents were significantly smaller.

The lifetimes obtained for AC and DC samples can be compared for samples of similar perovskite layer thickness (absorbance around 1.0 at 700 nm). Lifetimes are always shorter for the cells prepared under ambient conditions. From the HTM side, the DC cells with the best photocurrent show half-lifetimes of about 3 ns (Figure 4A), while for AC cells it is about 2.4 ns. An even larger difference is found for the excitation from ETM side: half-lifetimes are about 6 ns for the best DC cells (Figure 4) and 1.6 ns for AC cells. As the photocurrent for AC cells is about 20% smaller than that for DC cells, it is unlikely that the shorter lifetimes seen in AC samples are due to faster charge injection to the contact materials. The shorter lifetimes are more likely due to the presence of more defects in the AC samples originating from traces of water during fabrication. These defects will decrease the lifetime due to increased trap-assisted recombination. Interestingly, the comparison of the lifetimes suggests that difference in the defect density between AC and DC samples is larger closer to the ETM side where there is a higher concentration of PbI$_2$. An alternative explanation is that the density of defects is similar, but hole injection is significantly slowed due to the humidity-affected spiro-OMeTAD layer in AC cells.[26]

Transient Absorption. Femtosecond transient absorption was measured upon excitation at 505 nm (at two intensities 10 or 30 μJ/cm^2) in the spectral range from 670 to 830 nm and in the temporal range up to 3 ns. The solar cells were probed in transmission mode in the areas without gold electrodes from either the ETM or HTM side. Similar to the emission measurements, the absorbance at the pump wavelength is so high ($A > 3$) that most of the light absorption in the perovskite
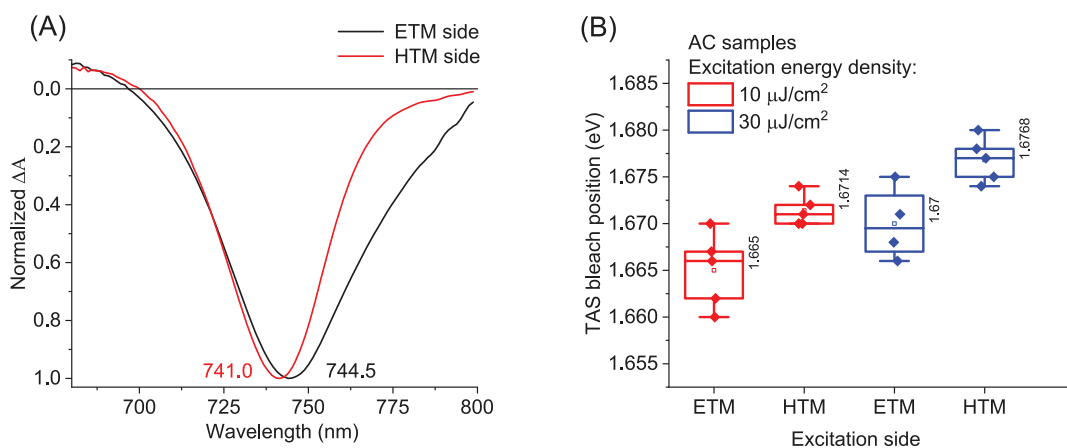
Figure 5. Representative bleach signals from ETM and HTM side observed in transient absoprtion at pump intensity 10 μJ/cm^2 (A). Statistics of bleach maximum for the two excitation intensities (B).
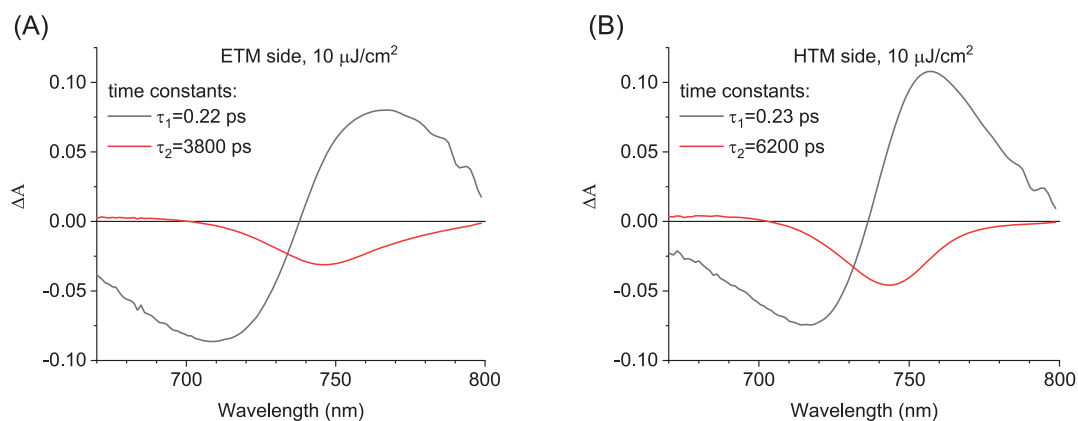
Figure 6. Examples of the global analysis of transient absorption data using two-exponential fit for ETM (A) and HTM (B) side. The graphs present pre-exponential factor spectra associated with the indicated time constants. The pump fluence was 10 μJ/cm^2.

takes place close to the ETM or HTM interface, allowing these interfaces to be selectively probed.

Figure S10 presents the representative transient absorption spectra of the selected time delays between the pump and probe pulses. The observed features of this triple-cation perovskite look similar to many previous reports on the standard MAPbI$_3$ perovskite, including those reported by us earlier.[43,44] After the initial charge carrier relaxation, the signals are dominated by the strong and sharp negative bleach peak at 740–745 nm, close to the absorption edge. This bleach appears due to the band-filling mechanism,[45] where its amplitude represents the population of the excited carriers[14] and, in the simplest approximation, should follow eq 1. Figure 5A shows the representative comparison between the bleach signal measured at ETM and HTM sides and the clear additional negative feature in the long-wavelength range observed for the ETM side. We have observed these differences for both AC and DC samples. Moreover, Figure 5B presents the statistics of the bleach maximum for the two excitation intensities, and it is always red-shifted for the ETM interface with respect to the HTM one. It can be noted that for the increased pump pulse intensity the maximum of the bleach band moves slightly to the blue for the corresponding interfaces (with simultaneous broadening of the bleach band), which is also in line with the band-filling mecha-

nism.[44−46] The red-shift of the bleach signal for the ETM side agrees with the red-shifted emission from this side reported in the previous section (Figure 3A), which might be explained by differences in the conduction and valence band alignment of perovskite layers closer to titania with respect to those closer to spiro-OMeTAD. In particular, the additional red-shifted features on the ETM side in both the stationary emission and transient absorption bleach bands can originate from the perovskite structure disturbed by the unreacted PbI$_2$ phase as described earlier (e.g., by introducing additional trap states responsible for the red-shifted absorption and emission). Another possibility is that there is a different ratio of bromide/iodide content at the interfaces, which could modify the band gap.[47] However, the latter hypothesis could not be verified in our TEM-EDX analysis because the signals of these elements overlap with copper (from the grid), carbon, nitrogen, and oxygen. Interestingly, ion migration was found to be obstructed in the PbI$_2$-deficient samples, which both decreased the current voltage hysteresis and increased the photostability.[34,41] Therefore, it is possible that ion segregation leading to different ratios of bromide/iodide is only possible close to the ETM where we observe an excess of PbI$_2$ content in our samples.

Our analysis of the transient absorption dynamics started with the simplest approach of global fitting using a two-exponential function.[43] Examples of these global fits (pre-

exponential factor spectra and associated time constants) are shown in Figure 6 and Figure S11. The first subpicosecond component has a shape characteristic of the band-edge shift, which is due to charge cooling and/or exciton dissociation. We have not observed any influence of the excitation side or the solar cell parameters on the time constant of this component. The second, longer component dominated by the bleach band represents the average decay of the charge population. This time constant is always longer on the HTM than on the ETM side for AC samples, which is in agreement with the findings from the emission decays and further endorses the asymmetry in the electron and hole injection dynamics. It is also possible that the presence of PbI_2 affects the recombination and/or charge injection rates, which contributes to the differences in the charge population dynamics between HTM and ETM sides. For AC samples of similar thickness, the average time constants are equal: $\tau_{2,ETM} = 3.50 \pm 0.69$ ns, $\tau_{2,HTM} = 5.52 \pm 0.61$ ns for 10 $\mu J/cm^2$ and $\tau_{2,ETM} = 1.59 \pm 0.15$ ns, $\tau_{2,HTM} = 2.02 \pm 0.18$ ns for 30 $\mu J/cm^2$ pump intensity. The shortening of the time constants at higher pump intensity (and also the differences between the time constant values in transient absorption and emission measurements reported in the previous section) is due to the second-order processes (eq 1) which accelerate the charge population decay for higher charge density.

Table 2 presents the Pearson correlations between the longer time constants of the two-exponential global fit at lower

Table 2. Pearson Correlations between the Parameters of Transient Absorption, Corrected Photocurrent (Total APCE), Absorbance (A) (Corresponding to the Sample Thickness), and DMSO Content in Precursor Solution[a]

	τ_2(ETM)	τ_2(HTM)	A(700 nm)	total APCE	DMSO content
τ_2(ETM)	1	0.46	0.78[a]	−0.85[a]	−0.43
τ_2(HTM)	0.46	1	0.50	−0.29	−0.40
A(700 nm)	0.78[a]	0.50	1	−0.38	−0.26
total APCE	−0.85[a]	−0.28	−0.38	1	0.49
DMSO content	−0.43	−0.40	−0.26	0.49	1

[a]The correlation is statistically significant at the 0.05 level (a 95% confidence interval).

intensity and relative photocurrent, perovskite thickness (absorption), or DMSO:DMF content ratio for AC samples. As can be seen, significant correlations can only be found between the time constants and the stationary absorbance at 700 nm (0.78 for the ETM side) or total APCE (−0.85 for the ETM side). This agrees with the findings presented in the emission section that the apparent lifetime increases for higher perovskite thickness and that the lifetime decreases for better relative photocurrent. The visualization of the correlations of the transient absorption lifetime with the absorbance is presented in Figure S9C,D. Similar to the emission study, the Pearson's correlations limited to the samples of the same thickness are shown in Table S3, again showing no effect of the DMSO content on the lifetimes.

To get further insights into the electron dynamics, a more complex analysis of the transient absorption dynamics was performed. In the multiexponential global analysis, a four-exponential function gives a better fit, especially for a higher pump pulse intensity. As we have previously reported, the

additional fit components better describe the initial decay of the charges occupying higher energy levels in the conduction and valence bands.[44,48] Examples of two- or four-exponential fits are shown in Figure S11. The time constants are always longer for the HTM side, and the additional red-shifted features appear for the pre-exponential factor spectra on the ETM side.

We have recently reported that for $MAPbI_3$ perovskite the charge population is most properly described by the band integral (BI).[44] The integral calculated over the entire band is insensitive to the spectral shift of the band (e.g., caused by the Burstein−Moss effect in perovskites)[45] and reflects population dynamics if the oscillator strengths of optical transitions do not change.[49] Therefore, such BIs were calculated for the triple-cation perovskite samples studied in this work (Figure S12A), and we have fit them with a stretched exponential function, mixed first- and second-order decay function (eq 4), and its modification. The details of the fits are presented in the Supporting Information (Tables S4 and S5, Figure S13A). In the stretched exponential analysis, the characteristic times (τ) values are smaller on the ETM than on the HTM side, while the values of the stretch parameter (β) are significantly smaller on the ETM side than on the HTM side (Figure S12B), which indicates more stretched kinetics at ETM side. However, the Pearson correlations were not better than those for two-exponential approximation shown in Table 2. Equation 4 was poorly fitted to BI of the transient absorption, especially for the higher pump pulse intensity (30 $\mu J/cm^2$). Interestingly, quite a good fit was observed when the mixed first- and second-order function given by eq 4 was "stretched" by raising it to a power lower than 1. We have found the best fits with the power equal to 0.3 (Figure S13B), though its physical meaning is rather hard to explain, and higher k_2 values from ETM than HTM side (Table S5). Overall, the fits of the different analytical functions to BI kinetics confirm the findings from the simple two-exponential global analysis (Table 2), but more physical insights cannot be deduced from the fitted parameters. The true kinetics are most likely described by a more complex model including charge diffusion and reabsorption of the light,[13,14] which requires the fits to the numerical solutions of the differential charge population equations. A more complex model would result in a more precise determination of the first- and second-order rate constants and their correlations with other solar cell parameters; however, it was beyond the scope of this work.

Electrochemical Impedance Spectroscopy. AC samples prepared under different DMSO:DMF ratios and WVP values have been studied by electrochemical impedance spectroscopy at open-circuit potential in the frequency range 10^6−10^{-1} Hz. Two different LED bias wavelengths were used (465 nm (blue) and 635 nm (red)) to establish the impact of different optical penetration depths in the perovskite layer.[19] Because of the high perovskite absorption in the blue region, the 465 nm LED light is absorbed in the 200 nm closest to the titania/perovskite interface. In contrast, the 635 nm LED light has a longer penetration depth, so information obtained by red light bias characterizes charge behavior in the perovskite regions further from the titania layer.[19] The impedance spectra were mainly characterized by a high-frequency (HF) signal at 10^5 Hz (Figure S14), which has been associated with electronic transport and recombination processes in the perovskite layer.[19,50−54] The HF signal was analyzed by fitting to a Voight equivalent circuit (inset in Figure S14A). The HF
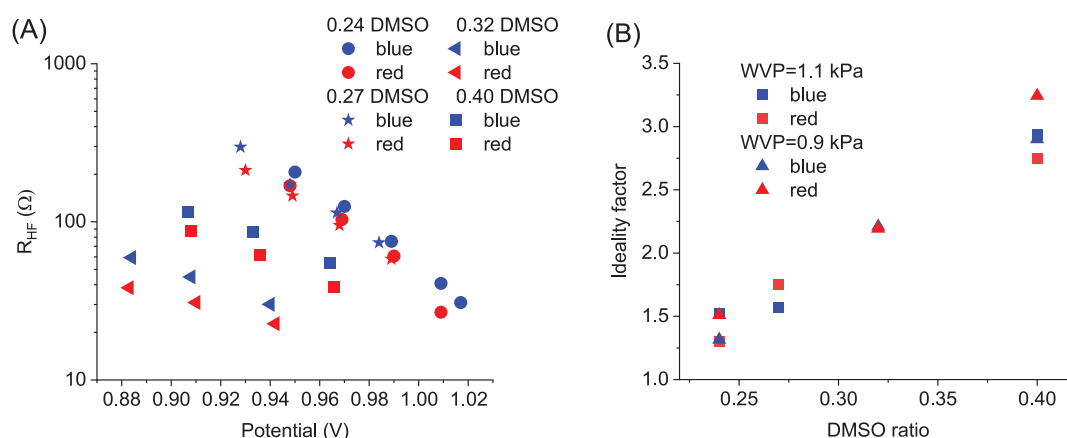
Figure 7. Impedance spectroscopy analysis results (high-frequency region fit by R-CPE equivalent circuit) in open circuit condition with blue (435 nm) and red (635 nm) light bias for WVP = 1.1 kPa. Recombination resistance (A) and the ideality factor for different WVP (B) for the samples prepared with different DMSO ratios.

resistance (R_{HF}) extracted from the impedance results are given in Figure 7A as a function of open-circuit potential, while HF capacitance (C_{HF}) and time constant are shown in Figure S15. In the case of C_{HF}, blue and red signals agree, showing small ($\sim 10^{-8}$ F) and almost constant values for all bias voltages close to V_{OC} (Figure S15A) which are typical for perovskite solar cells.[53] By contrast, R_{HF} varies exponentially with the open-circuit potential following eq 5. From Figure 7A, lower values of R_{HF} are observed with red light illumination than those for those with blue light regardless of DMSO ratio. However, when the R_{HF} is compared for different DMSO ratios, higher values of R_{HF} are obtained for the lowest DMSO concentration. Taking into account that the red light illumination produces photogenerated charged carriers further away from titania/perovskite interface compared to blue light illumination, the lower R_{HF} values can be analyzed as a magnification of charge recombination loss close to the perovskite/HTM interface and/or a shorter diffusion length due to a global acceleration of the recombination rate.

The ideality factors (m) were obtained from the slopes of the graphs of the resistance (R_{HF}) vs potential (V) according to the following equation:[19,50,55]

$$R_{HF} = R_{00HF} \exp\left[\frac{eV}{mk_B T}\right] \tag{5}$$

where R_{00HF} is the resistance at bias potential equal to zero, k_B is the Boltzmann constant, and T is temperature. We can clearly see from Figure 7B that the ideality factor becomes higher with higher DMSO concentration. The smallest and best values of the ideality factor (m between 1 and 1.5) are obtained for 0.24 DMSO:DMF ratio. These ideality factor values are in line with those previously obtained for pure MAPbI$_3$ in AC conditions.[21] The variation of the ideality factor with DMSO concentration can be interpreted as a change of the recombination mechanism (from bulk to surface recombination). This interpretation is supported by a larger shift between red and blue excitation data for a cell with a lower ideality factor.[19]

Finally, we have also measured the electrochemical impedance for DC samples. In this case a different configuration was used—the cells were measured both in the dark and under 1 sun illumination at different bias voltages in non-open-circuit conditions, permitting the flow of the charges through the circuit. At such conditions the time constants obtained in the dark correspond to the recombination processes, while those under illumination contain an additional contribution from the transfer of the photogenerated carriers to ETM and HTM. The exemplary results for the cells that differ in photocurrent are presented in Figure S16. The time constants in the dark are similar for all cells, but time constants measured under illumination are significantly shorter for the cells with higher photocurrent. We have observed similar behavior in our recent studies of the mixed MA and FA solar cells,[40] which can be explained by faster carrier injection in better performing cells. This agrees with the findings of time-resolved emission and transient absorption studies probing injection at shorter time scales as discussed in the previous sections.

■ CONCLUSIONS

One of the most efficient configurations of third-generation solar cells is the triple-cation perovskite (methylammonium, formamidinium, and cesium) placed between the mesoporous titania layer (ETM) and spiro-OMeTAD (HTM). In this work a detailed investigation of the properties of such perovskites in contact with both materials is provided, including the studies of charge transfer dynamics at the interfaces using time-resolved fluorescence and femtosecond transient absorption techniques. The results are verified for perovskite solar cells prepared with standard procedure under water-free drybox conditions as well as those fabricated under ambient room humidity. For the samples prepared under ambient room conditions, the charge population decay is significantly faster at the ETM side than at the HTM side. For example, emission half-lifetimes are 1.6 ns at the ETM side vs 2.4 ns at the HTM side for excitation 400 μW at 407 nm, and transient absorption average decay is 3.5 ns vs 5.5 ns for excitation 10 μJ/cm^2 at 505 nm. This indicates asymmetry in the electron and hole injection dynamics induced by the presence of water and/or a different distribution of recombination centers close to the two interfaces. The charge recombination loss observed by electrochemical impedance spectroscopy is found to be slower at the interface with ETM than with HTM (times on the order of milliseconds). For the solar cells prepared under drybox conditions, the hole injection becomes faster for the solar cells

with higher photocurrent (with the fastest decay emission half-lifetime about 1 ns from HTM side). Grazing incident X-ray diffraction experiments indicate that the content of unreacted PbI$_2$ phase in the perovskite structure is much higher near the interface with ETM than near the interface with HTM. The stationary emission spectra and transient bleach peaks of perovskites show additional long-wavelength features close to the titania side (e.g., emission maximum shifts from 770 nm at HTM to 784 nm at ETM side). Finally, the effects of varying the DMSO content in the precursor solution or perovskite thickness on the properties of the solar cells prepared under ambient room conditions are also investigated. The ideality factor of the cells is found to increase with increasing DMSO concentration. This can be interpreted as a change of the recombination mechanism from bulk to surface recombination. Our findings reveal that the perovskite structure and charge dynamics are not uniform within the whole perovskite layer, which has significant implications for understanding the operation and optimizing the performance of devices based on this efficient mixed-cation perovskite material.

■ ASSOCIATED CONTENT

Supporting Information

The Supporting Information is available free of charge at https://pubs.acs.org/doi/10.1021/acsami.0c07095.

> Figures S1−S16: C−V curves, absorption spectra, TEM-EELS-SAED, TEM-EDX, SEM, and XRD analysis, additional transient absorption spectra, BI kinetics, additional impedance spectroscopy data; Tables S1−S5: Pearson correlations for the cells of similar thickness; emission lifetimes at different wavelength, parameters of the BI fit (PDF)

■ AUTHOR INFORMATION

Corresponding Author

Marcin Ziółek − *Faculty of Physics, Adam Mickiewicz University Poznań, 61-614 Poznań, Poland;* orcid.org/0000-0003-1882-6022; Email: marziol@amu.edu.pl

Authors

Katarzyna Pydzińska-Białek − *Faculty of Physics, Adam Mickiewicz University Poznań, 61-614 Poznań, Poland*

Viktoriia Drushliak − *Faculty of Physics, Adam Mickiewicz University Poznań, 61-614 Poznań, Poland*

Emerson Coy − *NanoBioMedical Centre, Adam Mickiewicz University, 61-614 Poznań, Poland;* orcid.org/0000-0002-4149-9720

Karol Załęski − *NanoBioMedical Centre, Adam Mickiewicz University, 61-614 Poznań, Poland;* orcid.org/0000-0002-4728-2119

Jessica Flach − *Laboratory of Photomolecular Science, Institute of Chemical Sciences and Engineering, Ecole Polytechnique Federale de Lausanne, Lausanne CH-1015, Switzerland; Department of Chemistry, University of Wisconsin—Madison, Madison, Wisconsin 53706, United States;* orcid.org/0000-0002-5824-5575

Jesus Idígoras − *Area de Quimica Fisica, Universidad Pablo de Olavide, E-41013 Sevilla, Spain*

Lidia Contreras-Bernal − *Area de Quimica Fisica, Universidad Pablo de Olavide, E-41013 Sevilla, Spain;* orcid.org/0000-0002-0261-0828

Anders Hagfeldt − *Laboratory of Photomolecular Science, Institute of Chemical Sciences and Engineering, Ecole Polytechnique Federale de Lausanne, Lausanne CH-1015, Switzerland;* orcid.org/0000-0001-6725-8856

Juan Antonio Anta − *Area de Quimica Fisica, Universidad Pablo de Olavide, E-41013 Sevilla, Spain;* orcid.org/0000-0002-8002-0313

Complete contact information is available at:
https://pubs.acs.org/10.1021/acsami.0c07095

Notes

The authors declare no competing financial interest.

■ REFERENCES

(1) Kojima, A.; Teshima, K.; Shirai, Y.; Miyasaka, T. Organometal Halide Perovskites as Visible-Light Sensitizers for Photovoltaic Cells. *J. Am. Chem. Soc.* **2009**, *131* (17), 6050−6051.

(2) NREL. National Renewable Energy Laboratory, https://www.nrel.gov/pv/cell-efficiency.html.

(3) Jeon, N. J.; Noh, J. H.; Yang, W. S.; Kim, Y. C.; Ryu, S.; Seo, J.; Seok, S. Il. Compositional Engineering of Perovskite Materials for High-Performance Solar Cells. *Nature* **2015**, *517* (7535), 476−480.

(4) Saliba, M.; Matsui, T.; Seo, J.-Y.; Domanski, K.; Correa-Baena, J.-P.; Nazeeruddin, M. K.; Zakeeruddin, S. M.; Tress, W.; Abate, A.; Hagfeldt, A.; Grätzel, M. Cesium-Containing Triple Cation Perovskite Solar Cells: Improved Stability, Reproducibility and High Efficiency. *Energy Environ. Sci.* **2016**, *9* (6), 1989−1997.

(5) Hu, Y.; Hutter, E. M.; Rieder, P.; Grill, I.; Hanisch, J.; Aygüler, M. F.; Hufnagel, A. G.; Handloser, M.; Bein, T.; Hartschuh, A.; Tvingstedt, K.; Dyakonov, V.; Baumann, A.; Savenije, T. J.; Petrus, M. L.; Docampo, P. Understanding the Role of Cesium and Rubidium Additives in Perovskite Solar Cells: Trap States, Charge Transport, and Recombination. *Adv. Energy Mater.* **2018**, *8* (16), 1−11.

(6) Lyu, M.; Yun, J.; Cai, M.; Jiao, Y.; Bernhardt, P. V.; Zhang, M.; Wang, Q.; Du, A.; Wang, H.; Liu, G.; Wang, L. Organic − Inorganic Bismuth (III) -Based Material: A Light-Absorber beyond Organolead Perovskites. *Nano Res.* **2016**, *9* (3), 692−702.

(7) Konstantakou, M.; Stergiopoulos, T. A Critical Review on Tin Halide Perovskite Solar Cells. *J. Mater. Chem. A* **2017**, *5* (23), 11518−11549.

(8) Deschler, F.; Price, M.; Pathak, S.; Klintberg, L. E.; Jarausch, D. D.; Higler, R.; Hüttner, S.; Leijtens, T.; Stranks, S. D.; Snaith, H. J.; Atatüre, M.; Phillips, R. T.; Friend, R. H. High Photoluminescence Efficiency and Optically Pumped Lasing in Solution-Processed Mixed Halide Perovskite Semiconductors. *J. Phys. Chem. Lett.* **2014**, *5* (8), 1421−1426.

(9) Trinh, M. T.; Wu, X.; Niesner, D.; Zhu, X.-Y. Many-Body Interactions in Photo-Excited Lead Iodide Perovskite. *J. Mater. Chem. A* **2015**, *3* (17), 9285−9290.

(10) Herz, L. M. Charge-Carrier Mobilities in Metal Halide Perovskites: Fundamental Mechanisms and Limits. *ACS Energy Lett.* **2017**, *2* (7), 1539−1548.

(11) Li, X.; Bi, D.; Yi, C.; Décoppet, J.-D.; Luo, J.; Zakeeruddin, S. M.; Hagfeldt, A.; Grätzel, M. A Vacuum Flash-Assisted Solution

Process for High-Efficiency Large-Area Perovskite Solar Cells. *Science* **2016**, *353* (6294), 58−62.

(12) Lin, Q.; Wang, Z.; Snaith, H. J.; Johnston, M. B.; Herz, L. M. Hybrid Perovskites: Prospects for Concentrator Solar Cells. *Adv. Sci.* **2018**, *5* (4), 1−8.

(13) Crothers, T. W.; Milot, R. L.; Patel, J. B.; Parrott, E. S.; Schlipf, J.; Müller-Buschbaum, P.; Johnston, M. B.; Herz, L. M. Photon Reabsorption Masks Intrinsic Bimolecular Charge-Carrier Recombination in CH3NH3PbI3 Perovskite. *Nano Lett.* **2017**, *17* (9), 5782−5789.

(14) Leng, J.; Liu, J.; Zhang, J.; Jin, S. Decoupling Interfacial Charge Transfer from Bulk Diffusion Unravels Its Intrinsic Role for Efficient Charge Extraction in Perovskite Solar Cells. *J. Phys. Chem. Lett.* **2016**, *7* (24), 5056−5061.

(15) Wojciechowski, K.; Stranks, S. D.; Abate, A.; Sadoughi, G.; Sadhanala, A.; Kopidakis, N.; Rumbles, G.; Li, C. Z.; Friend, R. H.; Jen, A. K. Y.; Snaith, H. J. Heterojunction Modification for Highly Efficient Organic-Inorganic Perovskite Solar Cells. *ACS Nano* **2014**, *8* (12), 12701−12709.

(16) Hutter, E. M.; Hofman, J. J.; Petrus, M. L.; Moes, M.; Abellón, R. D.; Docampo, P.; Savenije, T. J. Charge Transfer from Methylammonium Lead Iodide Perovskite to Organic Transport Materials: Efficiencies, Transfer Rates, and Interfacial Recombination. *Adv. Energy Mater.* **2017**, *7* (13), 1−8.

(17) Baloch, A. A. B.; Alharbi, F. H.; Grancini, G.; Hossain, M. I.; Nazeeruddin, M. K.; Tabet, N. Analysis of Photocarrier Dynamics at Interfaces in Perovskite Solar Cells by Time-Resolved Photoluminescence. *J. Phys. Chem. C* **2018**, *122* (47), 26805−26815.

(18) Bi, D.; Tress, W.; Dar, M. I.; Gao, P.; Luo, J.; Renevier, C.; Schenk, K.; Abate, A.; Giordano, F.; Correa Baena, J.-P.; Decoppet, J.-D.; Zakeeruddin, S. M.; Nazeeruddin, M. K.; Gra tzel, M.; Hagfeldt, A. Efficient Luminescent Solar Cells Based on Tailored Mixed-Cation Perovskites. *Sci. Adv.* **2016**, *2* (1), e1501170−e1501170.

(19) Contreras-Bernal, L.; Salado, M.; Todinova, A.; Calio, L.; Ahmad, S.; Idigoras, J.; Anta, J. A. Origin and Whereabouts of Recombination in Perovskite Solar Cells. *J. Phys. Chem. C* **2017**, *121*, 9705−9713.

(20) Wehrenfennig, C.; Eperon, G. E.; Johnston, M. B.; Snaith, H. J.; Herz, L. M. High Charge Carrier Mobilities and Lifetimes in Organolead Trihalide Perovskites. *Adv. Mater.* **2014**, *26* (10), 1584−1589.

(21) Contreras-Bernal, L.; Aranda, C.; Valles-Pelarda, M.; Ngo, T. T.; Ramos-Terrón, S.; Gallardo, J. J.; Navas, J.; Guerrero, A.; Mora-Seró, I.; Idígoras, J.; Anta, J. A. Homeopathic Perovskite Solar Cells: Effect of Humidity during Fabrication on the Performance and Stability of the Device. *J. Phys. Chem. C* **2018**, *122* (10), 5341−5348.

(22) Aranda, C.; Cristobal, C.; Shooshtari, L.; Li, C.; Huettner, S.; Guerrero, A. Formation Criteria of High Efficiency Perovskite Solar Cells under Ambient Conditions. *Sustain. Energy Fuels* **2017**, *1* (3), 540−547.

(23) Singh, T.; Miyasaka, T. Stabilizing the Efficiency Beyond 20% with a Mixed Cation Perovskite Solar Cell Fabricated in Ambient Air under Controlled Humidity. *Adv. Energy Mater.* **2018**, *8*, 1−9.

(24) Yang, J.; Siempelkamp, B. D.; Liu, D.; Kelly, T. L. Investigation of CH3NH3PbI3degradation Rates and Mechanisms in Controlled Humidity Environments Using in Situ Techniques. *ACS Nano* **2015**, *9* (2), 1955−1963.

(25) Salado, M.; Contreras-Bernal, L.; Caliò, L.; Todinova, A.; López-Santos, C.; Ahmad, S.; Borras, A.; Idígoras, J.; Anta, J. A. Impact of Moisture on Efficiency-Determining Electronic Processes in Perovskite Solar Cells. *J. Mater. Chem. A* **2017**, *5* (22), 10917−10927.

(26) Hawash, Z.; Ono, L. K.; Qi, Y. Recent Advances in Spiro-MeOTAD Hole Transport Material and Its Applications in Organic−Inorganic Halide Perovskite Solar Cells. *Adv. Mater. Interfaces* **2018**, *5* (1), 1700623.

(27) Contreras-Bernal, L.; Riquelme, A.; Gallardo, J. J.; Navas, J.; Idígoras, J.; Anta, J. A. Dealing with Climate Parameters in the Fabrication of Perovskite Solar Cells under Ambient Conditions. *ACS Sustainable Chem. Eng.* **2020**, *8* (18), 7132−7138.

(28) Gierszewski, M.; Glinka, A.; Gradzka, I.; Jancelewicz, M.; Ziółek, M. Effects of Post-Assembly Molecular and Atomic Passivation of Sensitized Titania Surface: Dynamics of Electron Transfer Measured from Femtoseconds to Seconds. *ACS Appl. Mater. Interfaces* **2017**, *9* (20), 17102−17114.

(29) Idígoras, J.; Burdziński, G.; Karolczak, J.; Kubicki, J.; Oskam, G.; Anta, J. A.; Ziółek, M. The Impact of the Electrical Nature of the Metal Oxide on the Performance in Dye-Sensitized Solar Cells: New Look at Old Paradigms. *J. Phys. Chem. C* **2015**, *119* (8), 3931−3944.

(30) Wrózowa, T.; Ciesielska, B.; Komar, D.; Karolczak, J.; Maciejewski, A.; Kubicki, J. Measurements of Picosecond Lifetimes by Time Correlated Single Photon Counting Method: The Effect of the Refraction Index of the Solvent on the Instrument Response Function. *Rev. Sci. Instrum.* **2004**, *75* (10), 3107−3121.

(31) Handa, T.; Tex, D. M.; Shimazaki, A.; Wakamiya, A.; Kanemitsu, Y. Charge Injection Mechanism at Heterointerfaces in CH3NH3PbI3 Perovskite Solar Cells Revealed by Simultaneous Time-Resolved Photoluminescence and Photocurrent Measurements. *J. Phys. Chem. Lett.* **2017**, *8* (5), 954−960.

(32) Henke, B. L.; Gullikson, E. M.; Davis, J. C. X-Ray Interactions: Photoabsorption, Scattering, Transmission, and Reflection at E = 50−30,000 EV, Z = 1−92. *At. Data Nucl. Data Tables* **1993**, *54* (2), 181−342.

(33) Wang, L.; McCleese, C.; Kovalsky, A.; Zhao, Y.; Burda, C. Femtosecond Time-Resolved Transient Absorption Spectroscopy of $CH_3NH_3PbI_3$ Perovskite Films: Evidence for Passivation Effect of PbI2. *J. Am. Chem. Soc.* **2014**, *136* (35), 12205−12208.

(34) Jacobsson, T. J.; Correa-Baena, J. P.; Halvani Anaraki, E.; Philippe, B.; Stranks, S. D.; Bouduban, M. E. F.; Tress, W.; Schenk, K.; Teuscher, J.; Moser, J. E.; Rensmo, H.; Hagfeldt, A. Unreacted PbI2 as a Double-Edged Sword for Enhancing the Performance of Perovskite Solar Cells. *J. Am. Chem. Soc.* **2016**, *138* (32), 10331−10343.

(35) Mosconi, E.; Grancini, G.; Roldan-Carmona, C.; Gratia, P.; Zimmermann, I.; Nazeeruddin, M. K.; De Angelis, F. Enhanced TiO2/MAPbI3 Electronic Coupling by Interface Modification with PbI2. *Chem. Mater.* **2016**, *28* (11), 3612−3615.

(36) Roldán-Carmona, C.; Malinkiewicz, O.; Betancur, R.; Longo, G.; Momblona, C.; Jaramillo, F.; Camacho, L.; Bolink, H. J. High Efficiency Single-Junction Semitransparent Perovskite Solar Cells. *Energy Environ. Sci.* **2014**, *7* (9), 2968−2973.

(37) Park, B.; Kedem, N.; Kulbak, M.; Lee, D. Y.; Yang, W. S.; Jeon, N. J.; Seo, J.; Kim, G.; Kim, K. J.; Shin, T. J.; Hodes, G.; Cahen, D.; Seok, S. Il. Understanding How Excess Lead Iodide Precursor Improves Halide Perovskite Solar Cell Performance. *Nat. Commun.* **2018**, *9*, 1−8.

(38) Du, T.; Burgess, C. H.; Kim, J.; Zhang, J.; Durrant, J. R.; McLachlan, M. A. Formation, Location and Beneficial Role of PbI 2 in Lead Halide Perovskite Solar Cells. *Sustain. Energy Fuels* **2017**, *1* (1), 119−126.

(39) Chen, S.; Wen, X.; Yun, J. S.; Huang, S.; Green, M.; Jeon, N. J.; Yang, W. S.; Noh, J. H.; Seo, J.; Seok, S. Il; Ho-baillie, A. Spatial Distribution of Lead Iodide and Local Passivation on Organo- Lead Halide Perovskite. *ACS Appl. Mater. Interfaces* **2017**, *9*, 6072−6078.

(40) Quere, B.; Pydzińska-Białek, K.; Karolczak, J.; Nowaczyk, G.; Coy, E.; Ziółek, M. Understanding the Effect of Different Synthesis Conditions on the Physicochemical Properties of Mixed-Ion Perovskite Solar Cells. *Chem. - Eur. J.* **2019**, *25* (23), 5978−5986.

(41) Gujar, T. P.; Unger, T.; Schönleber, A.; Fried, M.; Panzer, F.; Van Smaalen, S.; Köhler, A.; Thelakkat, M. The Role of PbI2 in CH3NH3PbI3 Perovskite Stability, Solar Cell Parameters and Device Degradation. *Phys. Chem. Chem. Phys.* **2018**, *20* (1), 605−614.

(42) Barbé, J.; Newman, M.; Lilliu, S.; Kumar, V.; Lee, H. K. H.; Charbonneau, C.; Rodenburg, C.; Lidzey, D.; Tsoi, W. C. Localized Effect of PbI2 Excess in Perovskite Solar Cells Probed by High-Resolution Chemical-Optoelectronic Mapping. *J. Mater. Chem. A* **2018**, *6* (45), 23010−23018.

(43) Pydzińska, K.; Karolczak, J.; Kosta, I.; Tena-Zaera, R.; Todinova, A.; Idígoras, J.; Anta, J. A.; Ziółek, M. Determination of

Interfacial Charge-Transfer Rate Constants in Perovskite Solar Cells. *ChemSusChem* **2016**, *9* (13), 1647−1659.

(44) Pydzińska-Białek, K.; Szeremeta, J.; Wojciechowski, K.; Ziółek, M. Insights into the Femtosecond to Nanosecond Charge Carrier Kinetics in Perovskite Materials for Solar Cells. *J. Phys. Chem. C* **2019**, *123* (1), 110−119.

(45) Manser, J. S.; Kamat, P. V. Band Filling with Free Charge Carriers in Organometal Halide Perovskites. *Nat. Photonics* **2014**, *8* (9), 737−743.

(46) Sum, T. C.; Mathews, N.; Xing, G.; Lim, S. S.; Chong, W. K.; Giovanni, D.; Dewi, H. A. Spectral Features and Charge Dynamics of Lead Halide Perovskites: Origins and Interpretations. *Acc. Chem. Res.* **2016**, *49* (2), 294−302.

(47) Brennan, M. C.; Ruth, A.; Kamat, P. V.; Kuno, M. Photoinduced Anion Segregation in Mixed Halide Perovskites. *Trends Chem.* **2020**, *2* (4), 282−301.

(48) Pydzińska, K.; Karolczak, J.; Szafrański, M.; Ziółek, M. Differences in Photoinduced Optical Transients in Perovskite Absorbers for Solar Cells. *RSC Adv.* **2018**, *8* (12), 6479−6487.

(49) Kovalenko, S. A.; Schanz, R.; Farztdinov, V. M.; Hennig, H.; Ernsting, N. P. Femtosecond Relaxation of Photoexcited Para-Nitroaniline: Solvation, Charge Transfer, Internal Conversion and Cooling. *Chem. Phys. Lett.* **2000**, *323* (3−4), 312−322.

(50) Contreras-Bernal, L.; Ramos-Terrón, S.; Riquelme, A.; Boix, P. P.; Idígoras, J.; Mora-Seró, I.; Anta, J. A. Impedance Analysis of Perovskite Solar Cells: A Case Study. *J. Mater. Chem. A* **2019**, *7* (19), 12191−12200.

(51) Guerrero, A.; Garcia-Belmonte, G.; Mora-Sero, I.; Bisquert, J.; Kang, Y. S.; Jacobsson, T. J.; Correa-Baena, J. P.; Hagfeldt, A. Properties of Contact and Bulk Impedances in Hybrid Lead Halide Perovskite Solar Cells Including Inductive Loop Elements. *J. Phys. Chem. C* **2016**, *120* (15), 8023−8032.

(52) Bag, M.; Renna, L. A.; Adhikari, R. Y.; Karak, S.; Liu, F.; Lahti, P. M.; Russell, T. P.; Tuominen, M. T.; Venkataraman, D. Kinetics of Ion Transport in Perovskite Active Layers and Its Implications for Active Layer Stability. *J. Am. Chem. Soc.* **2015**, *137* (40), 13130−13137.

(53) Todinova, A.; Idígoras, J.; Salado, M.; Kazim, S.; Anta, J. A. Universal Features of Electron Dynamics in Solar Cells with TiO_2 Contact: From Dye Solar Cells to Perovskite Solar Cells. *J. Phys. Chem. Lett.* **2015**, *6* (19), 3923−3930.

(54) Guillén, E.; Ramos, F. J.; Anta, J. A.; Ahmad, S. Elucidating Transport-Recombination Mechanisms in Perovskite Solar Cells by Small-Perturbation Techniques. *J. Phys. Chem. C* **2014**, *118* (40), 22913−22922.

(55) Correa-Baena, J.-P.; Turren-Cruz, S.-H.; Tress, W.; Hagfeldt, A.; Aranda, C.; Shooshtari, L.; Bisquert, J.; Guerrero, A. Changes from Bulk to Surface Recombination Mechanisms between Pristine and Cycled Perovskite Solar Cells. *ACS Energy Lett.* **2017**, *2* (3), 681−688.

Supporting Information

for

Understanding the interfaces between triple cation perovskite and electron or hole transporting material

Katarzyna Pydzińska-Białek[a], Viktoriia Drushliak[a],

Emerson Coy[b], Karol Załęski[b], Jessica Flach[c,d],

Jesus Idígoras[e], Lidia Contreras-Bernal[e],

Anders Hagfeldt[c], Juan Antonio Anta[e], Marcin Ziółek[a] *

[a] *Faculty of Physics, Adam Mickiewicz University Poznań,*
Uniwersytetu Poznańskiego 2, 61-614 Poznań, Poland

[b] *NanoBioMedical Centre, Adam Mickiewicz University,*
Wszechnicy Piastowskiej 3, 61-614 Poznań, Poland

[c] *Laboratory of Photomolecular Science, Institute of Chemical Sciences and Engineering,*
Ecole Polytechnique Federale de Lausanne, Lausanne CH-1015, Switzerland

[d] *Department of Chemistry, University of Wisconsin-Madison, 1101 University Avenue,*
Madison, Wisconsin 53706, United States

[e] *Area de Quimica Fisica, Universidad Pablo de Olavide, E-41013 Sevilla, Spain*

* corresponding author, email: marziol@amu.edu.pl
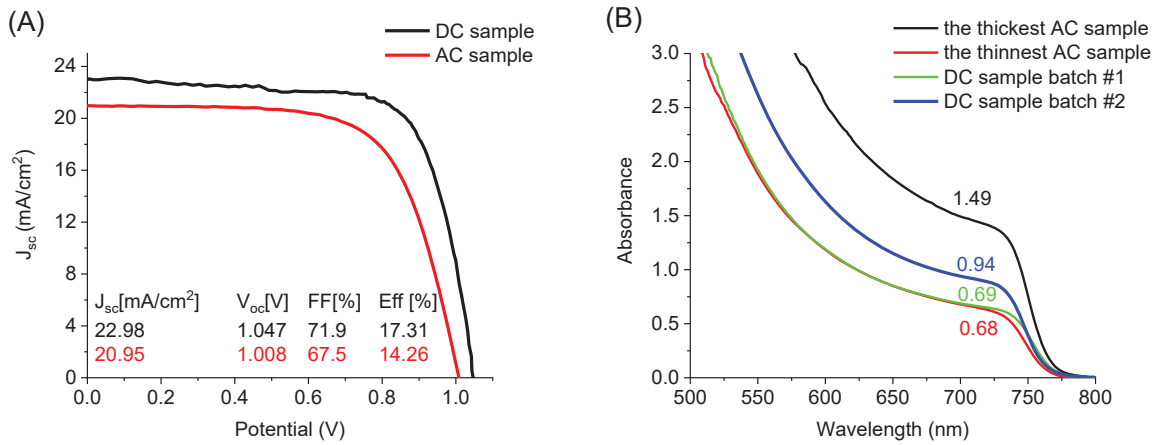
Figure S1. Current-voltage curves for the best samples prepared in drybox (black) and ambient air conditions (red) with listed photovoltaic parameters (A). Absorption spectra of samples from prepared in drybox (green, blue) and two, with extreme thickness prepared at ambient air conditions (black – the thickest, red – the thinnest) (B).
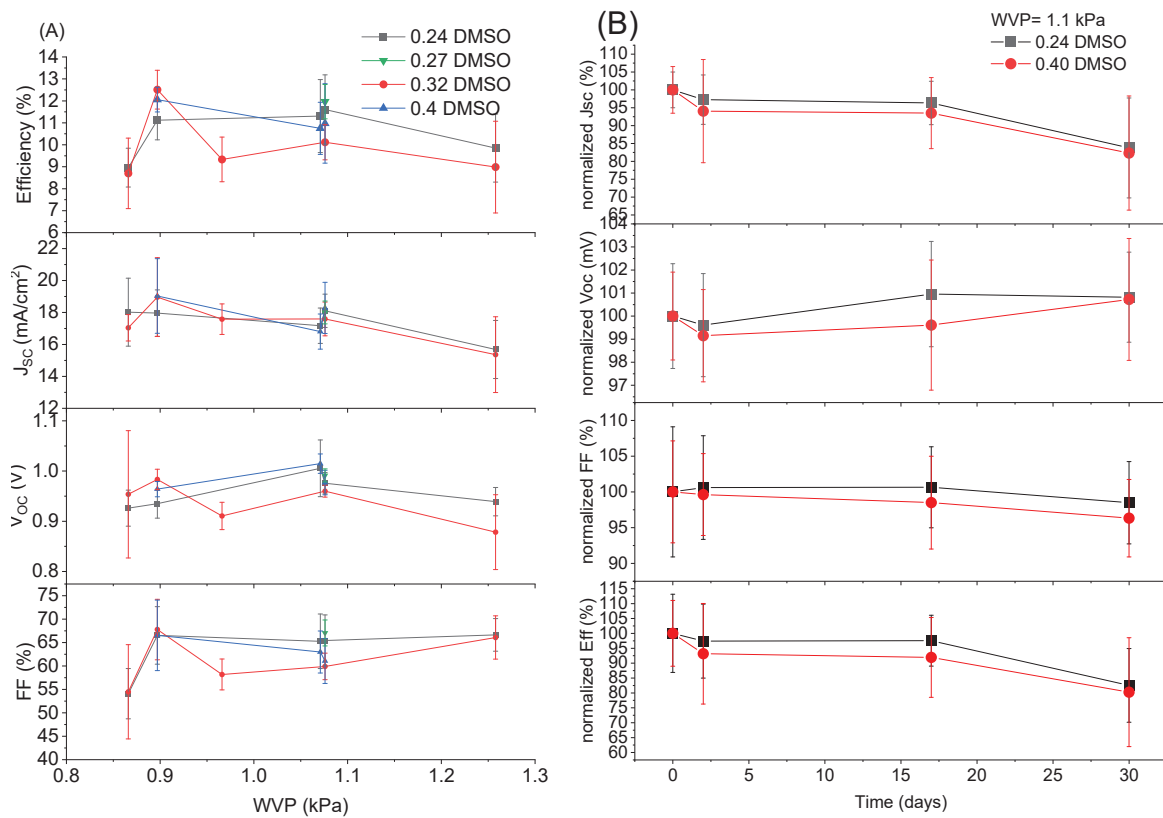
Figure S2. Current-voltage parameters for different water vapor pressure (WVP) during sample preparation (A), normalized current-voltage parameters for two different DMSO concentrations over time (B).
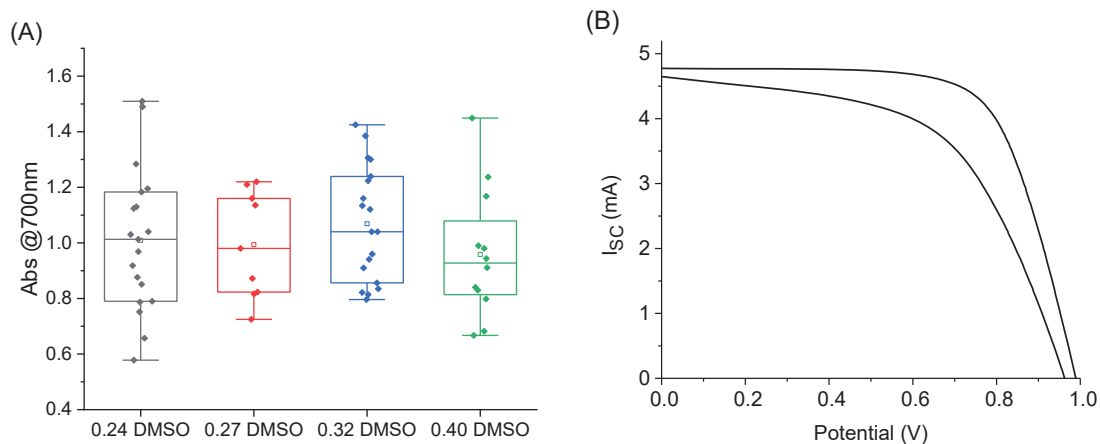
Figure S3. Statistics of the sample thickness (absorbance) for different DMSO:DMF ratios (A). Current vs. voltage curves for exemplary AC sample collected for reverse and forward scanning directions under white LED illumination (at the intensity slightly lower than 1Sun) (B). The average hysteresis index (defined as HI= $\frac{J_{rev}\left(\frac{V_{OC}}{2}\right) - J_{for}\left(\frac{V_{OC}}{2}\right)}{J_{rev}\left(\frac{V_{OC}}{2}\right)}$) is equal to 0.10 ± 0.03 for these samples.
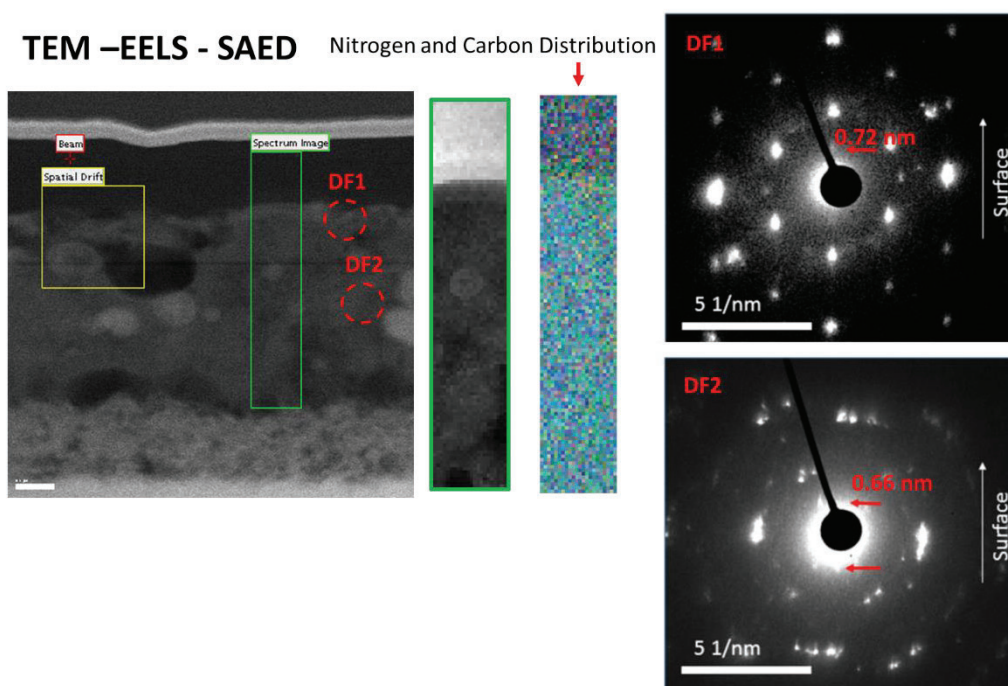
Figure S4. TEM-EELS-SAED analysis for the thinner AC sample. Nitrogen K- edge is plotted in green vs Carbon K-Edge in blue, with homogeneous distribution over the region examined. Diffraction patterns were collected without substrate zone axis optimization, the DF1 point was tuned to display the higher intensity spot, while DF2 was collected with the same DF1 conditions.

TEM-EDX
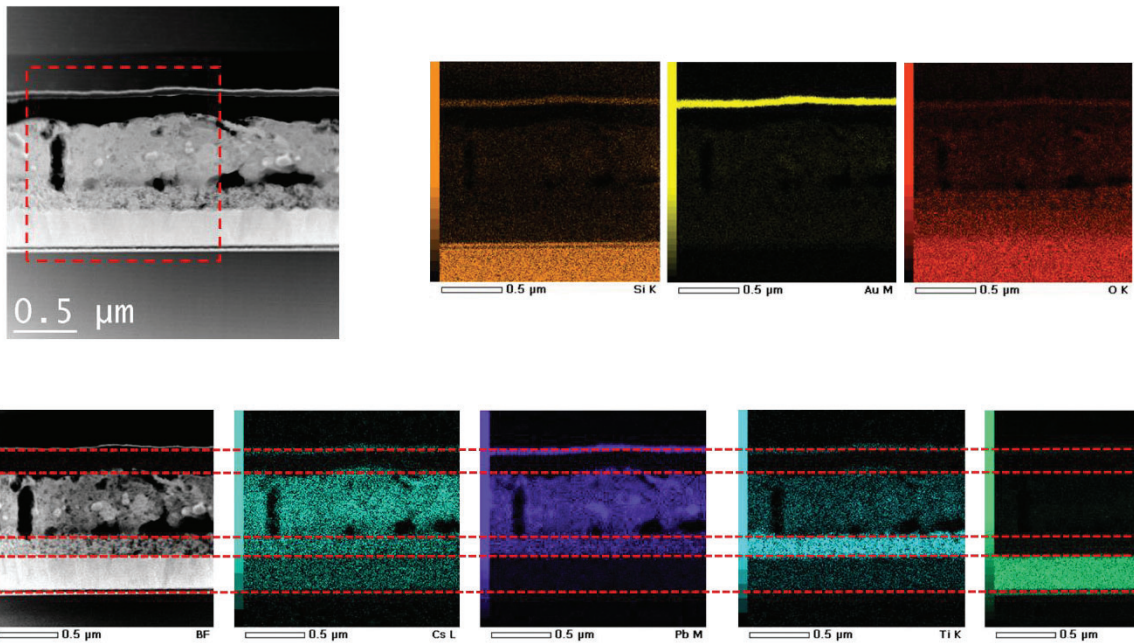
Figure S5. TEM-EDX analysis showing the general distribution of different elements within the thinner AC cell cross section.

Avg CV parameters:

DMSO	Eff. [%]	Jsc [mA/cm2]	Voc [mV]	FF [%]
0.24	11.40	17.6	940	68.9
0.32	12.59	18.5	991	70.0
0.40	12.18	18.2	964	68.8
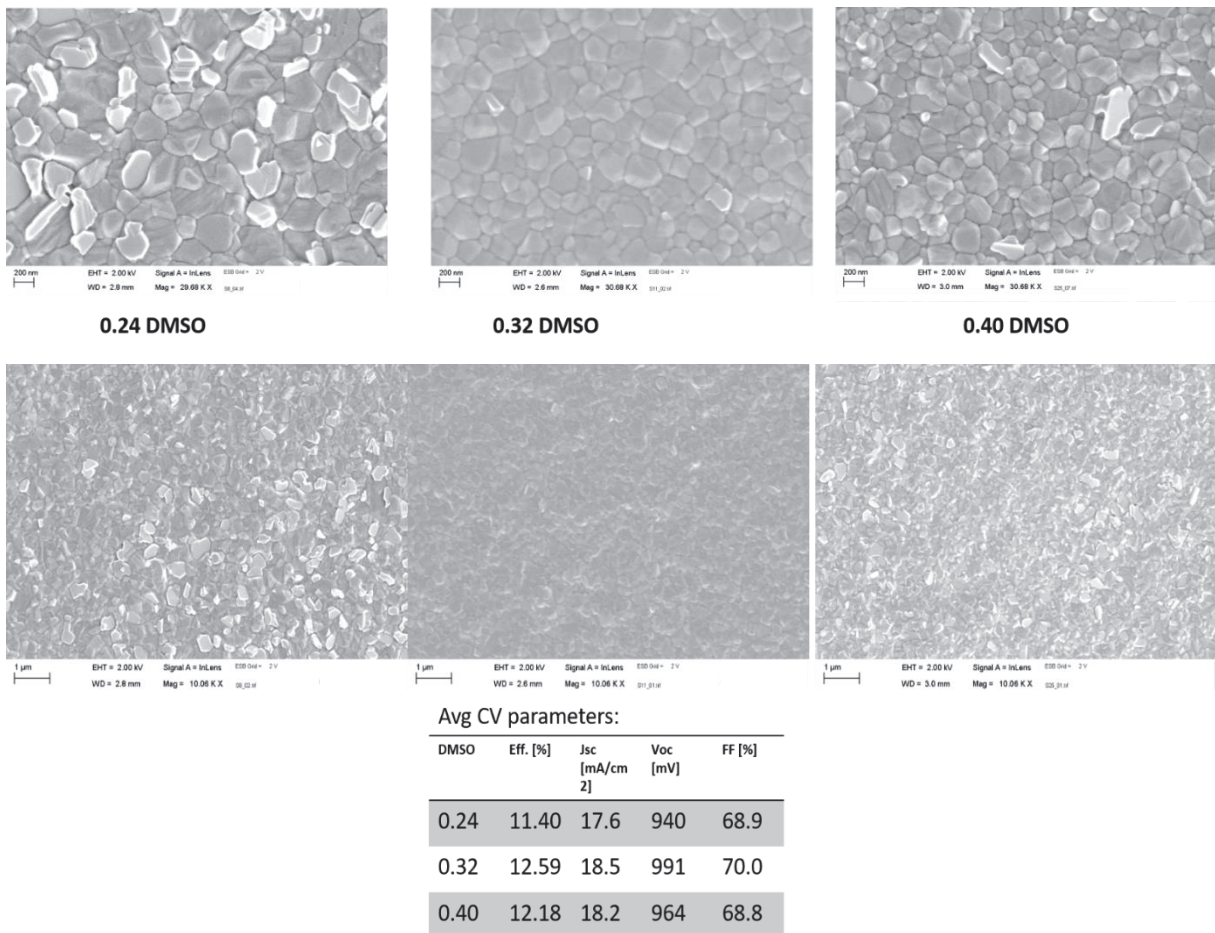
Figure S6. SEM images of one batch of AC samples prepared under WVP= 0.9 kPa with different DMSO:DMF ratio. The averaged CV parameters for this batch are also given.
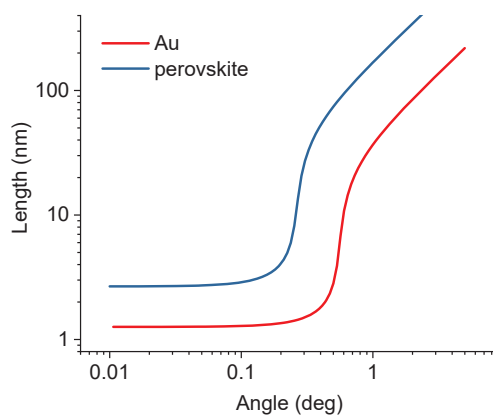
Figure S7. Estimated X-ray attenuation length for Au and perovskite, used to calibrate depth analysis in Figure 2 (calculated from [32]).
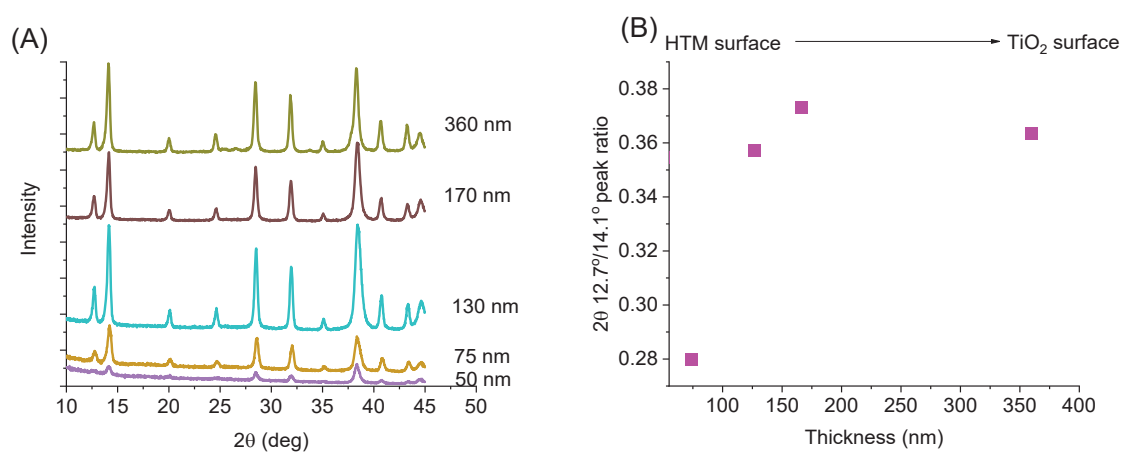
Figure S8. X-ray diffraction pattern for prepared cell, for different X-ray penetration depth (A) 12.7° vs 14.1° peak ratio as a function of penetration depth of the beam (B).
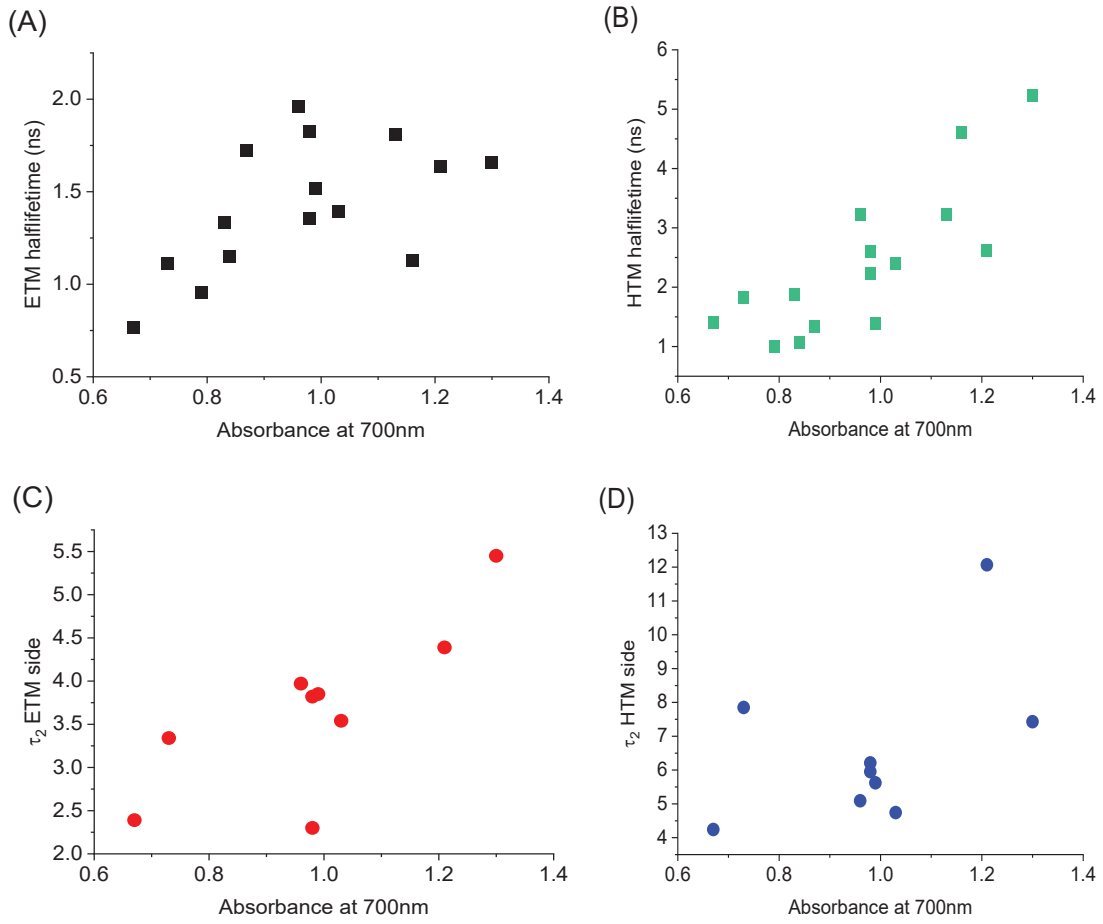
Figure S9. Visualization of the significant correlations between solar cell parameters reported in Tables 1 and 2.

Table S1.

Pearson correlations between the parameters of emission, corrected photocurrent (*total APCE*), and DMSO content in precursor solution; (*) indicates that the correlation is statistically significant at the 0.05 level. On the contrary to Table 1, only the samples of similar absorbance (*A* (700 nm)=1.0 +/- 15%) were taken into account.

	ETM half-lifetime	HTM half-lifetime	*total APCE*	DMSO cont.
ETM half-lifetime	1	-0.03	0.01	-0.49
HTM half-lifetime	-0.03	1	-0.40	-0.29
total APCE	0.01	-0.40	1	0.29
DMSO cont.	-0.49	-0.29	0.29	1

Table S2.

Variation of the emission half-lifetimes from HTM side at different probing wavelength for the selected exemplary AC samples.

Sample	Wavelength, nm	half-lifetime, ns
1	785	2.0
1	775	2.0
1	765	1.7
2	785	1.1
2	775	1.4
2	765	1.5
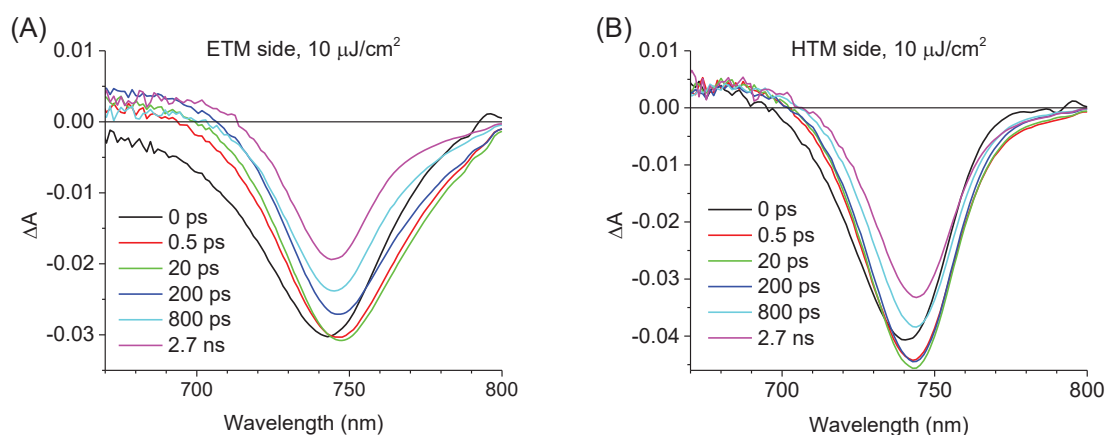
Figure S10. Exemplary transient absorption spectra for selected delay times between pump and probe pulses for AC sample measured from ETM (A) and HTM (B) side.
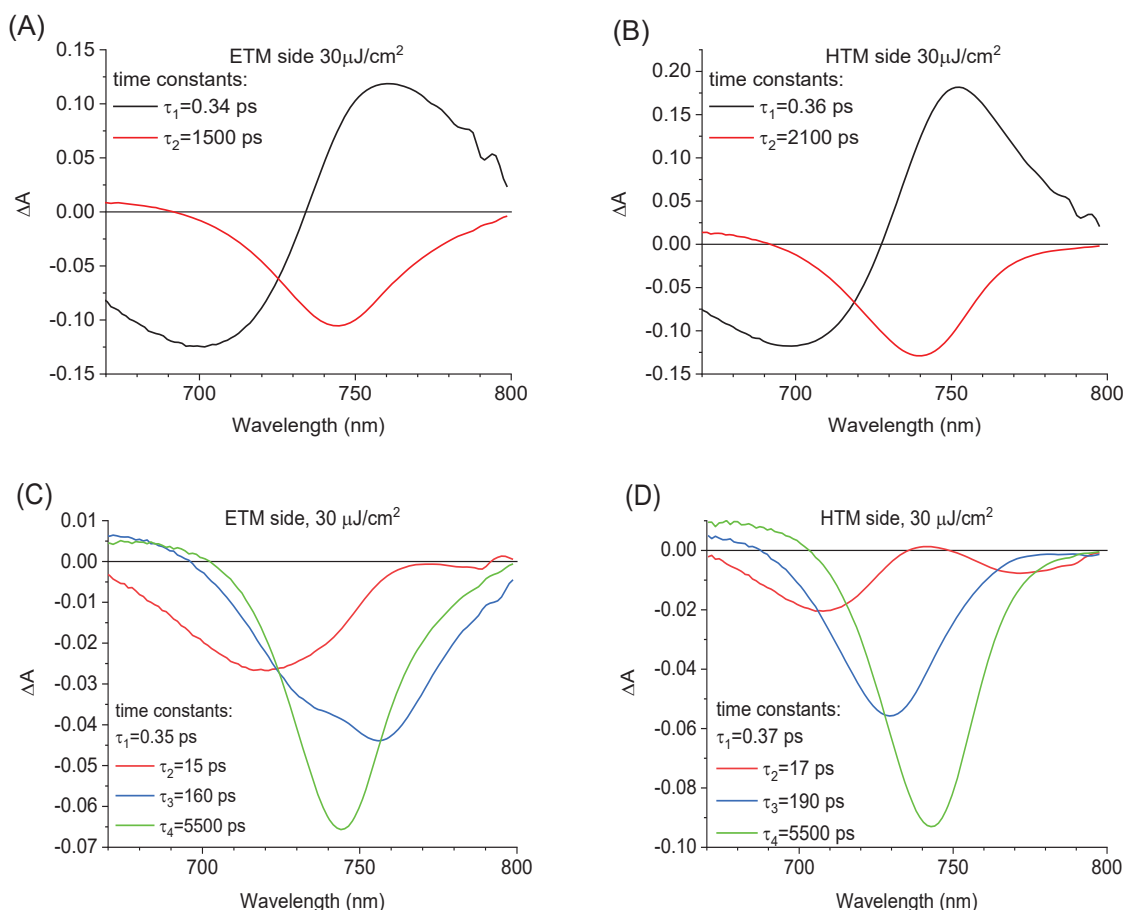
Figure S11. Examples of the global analysis of transient absorption data for the same sample using two-exponential (upper part) and four-exponential (lower part) fit for ETM (left) and HTM (right) side. The graphs present pre-exponential factor spectra associated to the indicated time constants. The pump fluence was 30 $\mu J/cm^2$. For simplicity, the spectra of τ_1 are not shown in (C) and (D) as they are very similar as in(A) and (B).

Table S3.

Pearson correlations between the parameters of transient absorption, corrected photocurrent (*total APCE*), and DMSO content in precursor solution; (*) indicates that the correlation is statistically significant at the 0.05 level. On the contrary to Table 2, only the samples of similar absorbance (*A* (700 nm)=1.0 +/- 15%) were taken into account.

	τ_2 (ETM)	τ_2 (HTM)	*total APCE*	DMSO cont.
τ_2 (ETM)	1	-0.30	-0.98*	-0.43
τ_2 (HTM)	-0.30	1	0.42	0.40
total APCE	-0.98*	0.42	1	0.29
DMSO cont.	-0.43	0.40	0.29	1
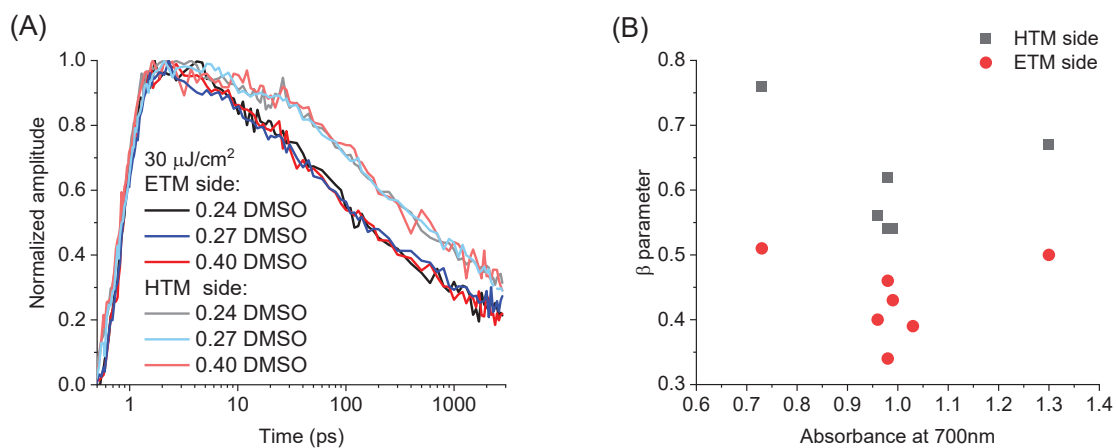
Figure S12. Examples of BI from transient absoprtion data of AC samples (A). The β parameter (compare with Table S4) from stretched exponential function fit to BI (B).
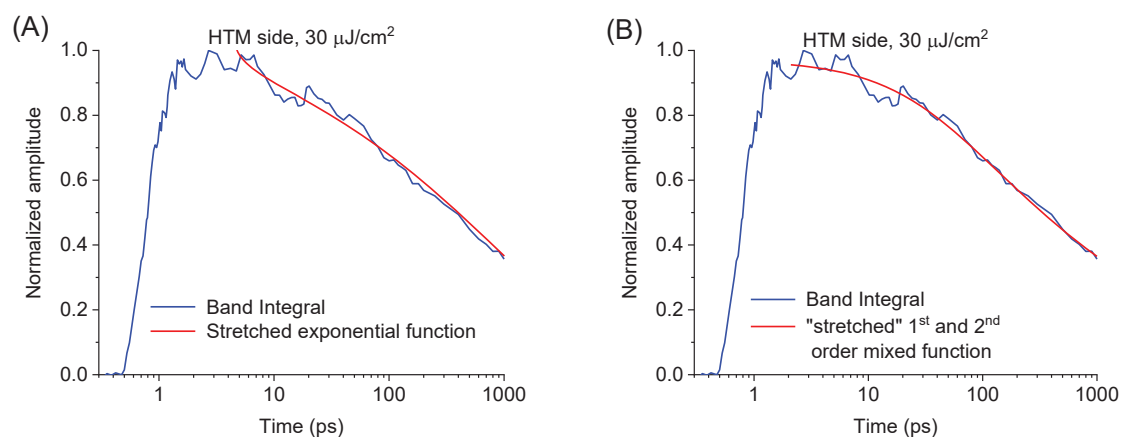
Figure S13. Examples of the fits to BI from transient absoprtion data of AC samples using stretched exponential function (A) and "stretched" mixed first and second order function (B). See Tables S4 and S5 for the formulas of the functions.

Table S4.

Stretched exponential fit to BI of transient absorption for AC samples with absorbance ~1 at 700 nm. The stretched exponential function is defined as $BI(t) = B_0 e^{-(t/\tau)^\beta}$ where β is the stretching parameter and τ is the lifetime.

Pump pulse intensity	Side	τ, ns	β
10 μJ/cm^2	ETM	3.93 ± 0.63	0.40 ± 0.02
	HTM	8.56 ± 0.41	0.57 ± 0.02
30 μJ/cm^2	ETM	0.60 ± 0.04	0.36 ± 0.01
	HTM	1.43 ± 0.10	0.42 ± 0.01

(For all measured AC samples: significant Pearson correlations for 10 μJ/cm^2 are found between τ(ETM) and absorbance at 700nm (0.75) and τ(ETM) and total_APCE (0.71))

Table S5.

"Stretched" mixed first and second order decay fit to BI of transient absorption for AC samples with absorbance ~1 at 700 nm. The function is the modification of the function given by eq (4) by raising it to the power of 0.3: $BI(t) = B_0 \left(\frac{n_0 k_1}{k_1 \exp(k_1 t) + n_0 k_2 (\exp(k_1 t) - 1)} \right)^{0.3}$

Pump pulse intensity	Side	k_2, arb. u.	k_1, ps^{-1}
10 μJ/cm^2	ETM	7.1 ± 2.1	4.0 ± 1.8 x 10^{-10}
	HTM	1.5 ± 0.3	4.5 ± 2.6 x 10^{-4}
30 μJ/cm^2	ETM	51.1 ± 3.8	1.1 ± 1.1 x 10^{-5}
	HTM	18.9 ± 1.3	9.3 ± 7.5 x 10^{-6}
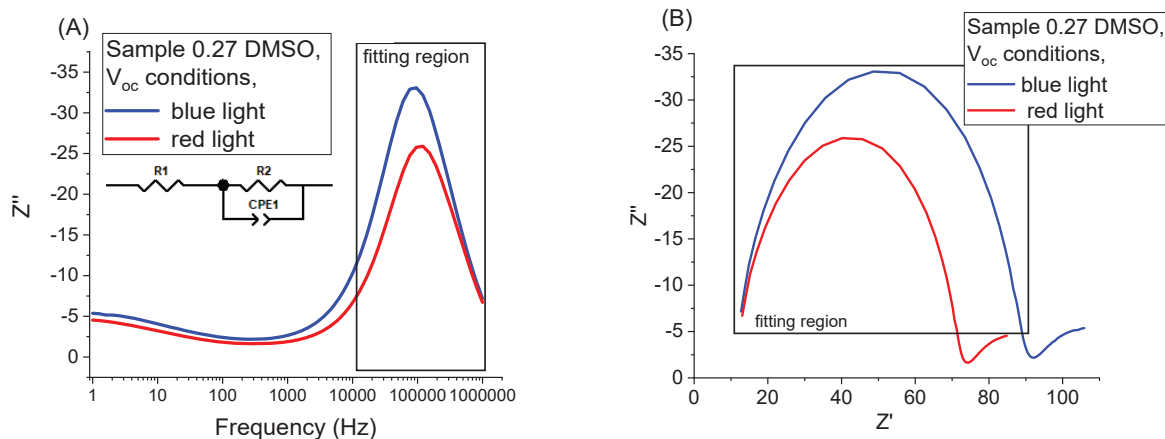
Figure S14. The example of electrochemical impedance data: the Bode peaks (A) and the Nyquist arcs (B). The high frequency region analyzed is indicated. Equivalent circuit is shown in the inset in (A).
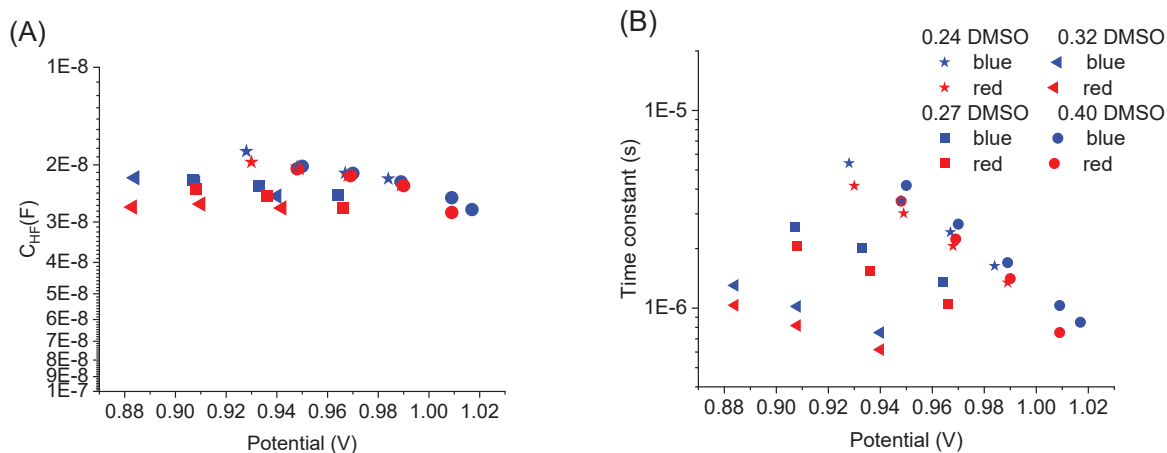
Figure S15. Capacitance (A) and time constant (B) of impedance spectroscopy at high-frequency region for AC samples prepared with different DMSO:DMF ratio. Capacitance values in (A) are obtained from

$C_{HF} = \frac{(R_{HF} \, B)^{\frac{1}{P}}}{R_{HF}}$, where R_{HF} − resistance of high frequency region, B, P − frequency-independent parameters of the constant phase element, P varying from 0 to 1, where 1 correspond to traditional capacitor. Time constant in (B) are obtained by multiplication of R_{HF} resistance and the capacitance from (A).
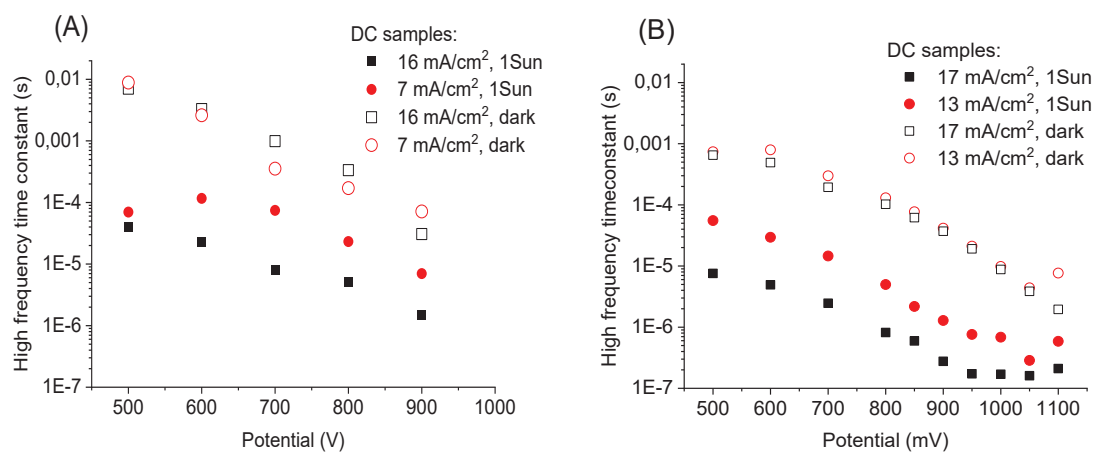
Figure S16. High-frequency time constants for DC samples measured without open circuit conditions, in the dark and illuminated by 1 Sun, for the cells of the indicated photocurrent. Part (A) corresponds to the batch with the absorbance of A=0.69 at 700 nm, and part (B) to the cells with A=0.94 at 700 nm (compare with Figures 2 and S1).

KPB-6

Impact of improvements in mesoporous titania layers on ultrafast electron transfer dynamics in perovskite and dye-sensitized solar cells

K.Pydzińska-Białek, A.Glinka, V.Drushliak, G.Nowaczyk, P.Florczak, M.Ziółek

PCCP

Check for updates

Impact of improvements in mesoporous titania layers on ultrafast electron transfer dynamics in perovskite and dye-sensitized solar cells†

Katarzyna Pydzińska-Białek, [iD] ‡[a] Adam Glinka, [iD] ‡[a] Viktoriia Drushliak, [iD][a] Grzegorz Nowaczyk, [iD][b] Patryk Florczak [iD][b] and Marcin Ziółek [iD] *[a]

Improvement in the performance of perovskite solar cells (PSC) and dye-sensitized solar cells (DSSC) upon modifications of mesoporous titania layers has been studied. For PSC with triple cation perovskite ($FA_{0.76}$ $MA_{0.19}$ $Cs_{0.05}$ Pb ($I_{0.81}$ $Br_{0.19})_3$) about 40% higher photocurrent (up to ~24 mA cm^{-2}) was found for more homogenous, made of larger particles (30 nm) and thinner (150–200 nm) titania layer. For DSSC (both with liquid cobalt-based electrolyte as well as with solid state hole transporter – spiro-OMeTAD), a greater dye loading, rise in photovoltage, and the enhancement in relative photocurrent were observed for the cells prepared from the diluted titania paste (2 : 1 w/w ratio) with respect to those prepared from undiluted one. The impact of these improvements in titania layers on charge transfer dynamics in the complete solar cells as well as in pristine TiO_2 layers was investigated by femtosecond transient absorption. Shorter photocarriers lifetime in perovskite material observed in better PSC, indicated that faster electron transfer at the titania interface was responsible for the higher photocurrent. Moreover, the photoinduced changes close to TiO2 interface were revealed in better PSC, which may indicate that in the efficient devices halide segregation takes place in perovskite material. In liquid DSSC, the fast component of unwanted recombination was slower in the samples with the diluted titania paste than in those made with undiluted ones. In solid state DSSC, hole injection from MK2 dye to spiro-OMeTAD takes place on the very fast ps time scale (comparable to that of electron injection) and the evidence of better penetration of spiro-OMeTAD into thinner and more porous titania layers was provided.

1. Introduction

Perovskite solar cells (PSCs) and dye-sensitized solar cells (DSSCs) belong to the very promising and potentially cheap emerging photovoltaic technologies. PSCs have been developed really rapidly in the latest few years, reaching the highest sunlight power conversion efficiency of 25%,[1] very close to the theoretical limit for single bandgap active material. The best efficiency of DSSC is about 14% achieved when using

cobalt-based electrolyte,[2,3] but this environmentally friendly technology has been recently re-discovered as the best suited for indoor applications.[4] It is because the efficiency of DSSC under low light intensity is greater than any of other common photovoltaic devices.[5] Despite a large number of papers devoted to PSC (> 15 000 papers so far) and DSSC (> 24 000 publications up to now), the fundamental studies of charge transfer processes using time-resolved laser spectroscopies have been relatively rare, especially for the complete solar cell as samples.[6]

A very important element present in the most efficient PSCs and DSSCs is the mesoporous titania layer that accepts electrons from active materials and transfers them to the transparent conductive glass electrode.[7,8] In DSSC, titania nanoparticles form a layer of a few microns in thickness (typically up to 10 μm). Sensitizing dyes are attached to such a scaffold and, after photo-excitation, inject electrons to TiO_2 conduction band in the very fast process (typically on fs and ps time scale), which is the primary charge separation step in DSSC operation. The regeneration of the dye (transfer of the electron to the oxidized form of the dye

obtained after electron injection) in the cells with liquid electrolyte takes place on the time scale much longer than that of electron injection, typically from several hundreds of nanoseconds to single microseconds.[6,8] However, if the electrolyte is substituted by solid state hole transporting material (*e.g.* the most popular spiro-OMeTAD) to enhance the stability of the cell, then the regeneration can occur much faster, even on the time scale comparable to that of electron injection (due to the hole hopping and higher density of charge conductive centers in the polymeric structure instead of redox pair diffusion in the electrolyte).[9–11] Solid state DSSC still suffers from low efficiencies with respect to the cell with liquid electrolyte, mainly due to the problem of sufficient contact between all dyes and hole transporting materials.[8,12,13] It should be noted that one of the most promising recent findings is the solidification of copper-based electrolytes (instead of the use of spiro-OMeTAD),[5] which lead to record efficiency close to 12% for solid state DSSC.[14]

In PSC, the architecture is more similar to that of thin film solar cells where the active perovskite materials is placed between the charge selective layers of electron- and hole-transporting materials.[15] However, in the most efficient devices, the titania mesoporous layer is still present (providing a base on which the perovskite crystalizes),[16] although its thickness is much smaller (a few hundreds of nm) than that in DSSC. The optimization of the thickness and porosity of titania layers in PSC and DSSC is necessary for achieving high total power conversion efficiency. However, often it is unclear whether upon such optimization the fastest charge dynamics is changed and the efficiency of the primary charge separation step (the electron transfer at the interface between active material and titania) is improved.

Therefore, in the present work, we have constructed PSC and DSSC devices using the most efficient compounds and with different mesoporous titania layers to study the fully operating solar cell samples using the femtosecond transient absorption spectroscopy. For PSC, triple cation perovskite (containing methylammonium, formamidinium and cesium) was the active material[17] and spiro-OMeTAD was the hole transporting layer, while titania layers of different thickness and porosity were tested. For DSSC, the efficient commercial carbazole dye MK2[18] and cobalt-based liquid electrolytes[19–21] were used to check the effect of dilution of popular commercial titania paste. Furthermore, also a solid state DSSC with spiro-OMeTAD and three types of titania layers were investigated. Our studies were aimed to establish whether the use of better titania layers (improving the sunlight conversion efficiency) correlates or not with the ultrafast dynamics of electrons and holes. Such information should be important for better understanding and further optimization of PSC and DSSC.

2. Experimental

Substrates for transparent electrodes for the cells were cut out from FTO glass sheet (Sigma-Aldrich, 2.2 mm thickness, 13 Ω sq^{-1}).

At first the glass plates were cleaned by sonication in a solution of commercially available dishwashing detergent (TRILLUX) mixed with distilled water, pure distilled water and ethanol, with each cleaning procedure lasting for 15 min. After drying by air flow, a UV ozone cleaner was used.

For PSC, spin-coating deposition was used in all steps of preparation. Electron transporting material (ETM) consisting of compact and mesoporous TiO_2 layers was deposited at first. A solution of titanium isopropoxide and ethanol was prepared in proportion of 1:9, respectively. Compact layer of TiO_2 was obtained by spin coating at 2000 rpm for 1 minute and then dried at 100 °C on a hot plate for 5 minutes. Next, the samples were gradually heated in the oven and kept at 450 °C for 30 min to form a compact TiO_2 layer. Two different mesoporous layers were used. The first one was prepared from TiO_2 paste for screen-printing of 18–20 nm-sized particle (DN-GPS-18TS, Dyenamo), dissolved in ethanol at the ratio of 1:6 (w:w). The second mesoporous layer was prepared from another TiO_2 paste of larger average particle size of 30 nm (GreatCell Solar, 30NR-D), similarly dissolved in ethanol at the ratio of 1:6 (w/w). The mixtures were preliminarily stirred continuously for 1 day. Mesoporous layers were spin coated at 2000 rpm for 10 s and then dried at 120 °C on the hot plate. Again, the substrates with titania layers were gradually heated in the oven and kept at 450 °C for 30 minutes. The abbreviations of the titania layers studied in this work refer to the deposition method, particles size and the possible use of dilution (see Table S1 in the ESI†). Thus, the two above paste are abbreviated as **SC18dil** and **SC30dil**.

Then, triple cation perovskite layer ($FA_{0.76}$ $MA_{0.19}$ $Cs_{0.05}$ Pb ($I_{0.81}$ $Br_{0.19}$)$_3$, where MA is methylammonium and FA is formamidinium) was deposited by spin coating from 1.5 M precursor solution in DMF:DMSO (4:1 by volume, 10 s, 2000 rpm, then 20 s, 4000 rpm). Chlorobenzene (as anti-solvent) was applied 10 s before the end of the spinning. Subsequently, the substrates were annealed at 100 °C for 40 minutes. The hole transporting material (HTM) layer was obtained by spin-coating (4000 rpm, 30 s) from a solution consisting of 72.3 mg mL^{-1} 2,2′,7,7′-tetrakis[*N,N*-di(4-methoxyphenyl)amino]-9,9′-spirobifluoren (spiro-OMeTAD, Sigma-Aldrich), 28.8 μL mL^{-1} 4-*tert*-butylpyridine (TBP, Aldrich), and 17.5 μL mL^{-1} lithium bis(trifluoromethanesulfonyl) imide (LiTFSI, 520 mg mL^{-1} in acetonitrile, Sigma-Aldrich), all dissolved in chlorobenzene (Sigma-Aldrich). The precursor solutions were prepared in oxygen free glovebox at a humidity RH = 6–7%, while the deposition of perovskite, annealing and deposition of HTM took place in another glovebox with oxygen presence at a humidity RH = 6–7%. Finally, gold electrodes were deposited on the top of HTM by sputtering technique for 60 s or 120 s, giving 25–50 or 50–100 nm layer thicknesses, respectively. The electrode sizes were of 0.05 or 0.20 cm^2 (0.125 cm^2 with the mask).

For DSSC studies, liquid cells (L-DSSC) with cobalt-based electrolyte and solid-state cells (S-DSSC) were constructed. At first, the blocking TiO_2 layer was formed on FTO electrodes by submerging them in 40 mM aqueous solution of $TiCl_4$

21948 | *Phys. Chem. Chem. Phys.*, 2020, **22**, 21947–21960

This journal is © the Owner Societies 2020

for 30 min at 70 °C, followed by rinsing with water, and heating at 150 °C for 5 min, 300 °C for 5 min, then at 450 °C for 30 min. At the next step, the two types of mesoporous titania layer were formed using the screen printing technique and nanoparticle paste of TiO$_2$ (DN-GPS-30TS, Dyenamo with 28–31 nm particles). The first one was made from the undiluted paste (abbreviated as **SP30**), The second, diluted-paste based mesoporous (**SP30dil**) layer, was prepared by mixing the above commercial paste with solution (6 g cellulose, 4 mL ethanol, 15 mL alpha-terpineol) at the ratio 2 : 1. After screen-printing of either diluted or undiluted pastes, the glass plates with mesoporous titania were gradually heated at 150 °C for 5 min, 300 °C for 5 min, and 450 °C for 60 min. After that, the glass plates were submerged in 40 mM aqueous solution of TiCl$_4$ (and treated in the same way as the blocking layer). For photoanode sensitization, the hot plates with TiO$_2$ layers were immersed in MK2 dye solutions in toluene for about 16 h to enable efficient adsorption of the dye. For MK2 sensitization we used either the solution of 0.2 mM dye and 0.1 mM of chenodeoxycholic acid (CDCA) as co-adsorbent or the solution of 0.2 mM dye without co-adsorbent.

Counter electrodes for L-DSSC were prepared from the same FTO glass plates and using the same cleaning procedure as that of photoanodes. Afterwards, they were dried in air and one layer of activated platinum (Platisol T, Solaronix) was deposited by paintbrush. Finally, the plates were heated at 450 °C for 30 min in order to remove any organic contamination. The photoanodes and counter electrode were bonded together by a polymer seal (25 μm Surlyn, Meltronix, Solaronix SA) with the conducting surfaces facing inwards. At the next step, the devices were filled with electrolyte through the 1 mm holes in the counter electrode and sealed with the cover glass on the top. We used the cobalt-bipyridine (bpy) or cobalt-phenanthroline (phen) complexes in acetonitrile solutions as the electrolytes for L-DSSC. The electrodes with MK2 and CDCA were used with the electrolyte consisting of 0.25 M [Co(bpy)$_3$](B(CN)$_4$)$_2$, 0.035 M [Co(bpy)$_3$](B(CN)$_4$)$_3$, 0.1 M LiClO$_4$ and 0.5 M TBP, and this configuration is abbreviated as **CBpy**. The electrodes without CDCA were used with the electrolyte consisting of 0.13 M [Co(phen)$_3$](TFSI)$_2$, 0.035 M [Co(phen)$_3$](TFSI)$_3$, 0.1 M of LiTFSI, and 0.5 M TBP, and this configuration is abbreviated as **Phen**. For S-DSSC, we used MK2 without CDCA for sensitization, and **SC30dil**, **SP30dil** or **SP30** titania layers. Spiro-OMeTAD as HTM and gold electrodes were deposited as described above for PSC.

A UV-VIS-NIR JASCO V-770 spectrophotometer equipped with a 150 mm integrating sphere (LN-925) was used to measure the stationary absorption spectra in the UV-VIS range. The samples were mounted in front of the integrating sphere in order to detect both transmitted and scattered light. The cross section images were recorded by Jeol 7001 TTLS field-emission scanning electron microscope (SEM) working at the acceleration voltage varying from 5 to 15 kV. Current–voltage measurements and IPCE (incident photon to current efficiency) spectra for the studied solar cells were recorded using a potentiostat (model M101, Autolab) coupled to a photoelectric spectrometer, equipped with a solar simulator (Instytut Fotonowy, Poland). A Xe lamp with AM 1.5G spectral filter and irradiance adjusted

to 100 mW cm^{-2} using a calibrated cell (15151, ABET) mimicked the sunlight conditions. The same complete solar cells as those for current–voltage measurements were used for the transient absorption studies. Transient absorption system has been described recently in more details (Helios spectrometer, Ultrafast Systems, and Spectra Physics laser system).[22] The laser pulses were set to 310, 355 or 500 nm and the IRF (pump–probe cross correlation function) duration was from 150 to 300 fs (FWHM). The transient absorption measurements were analyzed using the Surface Explorer software (Ultrafast Systems), including the global analysis. The program allowed fitting a multi-exponential function (convoluted with IRF) to the kinetic vectors of a selected number of singular values. Finally, the characteristic time constants and the wavelength-dependent amplitudes associated with them were obtained (they are also called the decay associated spectra or pre-exponential factor spectra). The fit quality was examined by the comparison of the multi-exponential fitted functions to the kinetic vectors.

3. Results and discussion

3.1. Morphology and stationary absorption

In order to determine the thickness of individual layers in solar cells SEM cross section images were carefully analyzed. The examples are shown in Fig. 1 and Fig. S1 (ESI†). Fig. 1A shows the cross section of **SP30dil** titania layer, while that of **SP30** layer is presented in Fig. S1A (ESI†). The estimated thickness of **SP30dil** layer is 1.3–1.5 μm, while that of **SP30** is 2.5–3 μm. Therefore, the use of diluted paste results in about twice smaller thickness of the mesoporous TiO$_2$ film. Moreover, the **SP30dil** structure has a higher porosity than that of **SP30** one, as indicated by the previous studies with different ethyl cellulose content in the titania paste.[23] The cross section of PVSK solar cell made with a **SC30dil** thin titania layer is shown in Fig. 1B. The total thickness of the cell is about 850 nm, and the following layers deposited on the FTO glass substrate can be recognized: 150–200 nm of **SC30dil** (including very thin compact TiO$_2$ layer which is hard to be distinguished), 450–500 nm of pure triple cation PVSK, 100–150 nm of spiro-OMeTAD and 50–100 nm of Au electrode. The average thickness of the solar cells made with a **SC18dil** layer is 1000 nm (Fig. S1B, ESI†), which indicates that the thickness of **SC18dil** layer is about twice higher than that of **SC30dil** one. Moreover, the homogeneity of the **SC18dil** is also worse with much higher variance in its thickness at different spots.
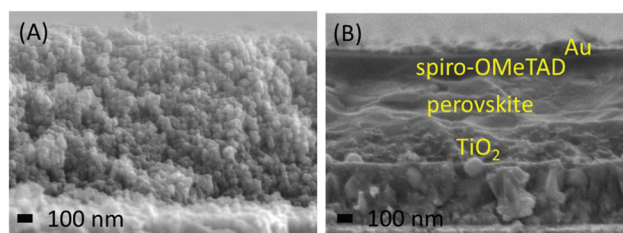
Fig. 1 SEM cross sections of **SP30dil** titania layer (A) and PSC made using **SC30dil** layer (B).

Phys. Chem. Chem. Phys., 2020, **22**, 21947–21960 | **21949**

179

It also agrees with the eye observation of the electrodes (before perovskite deposition): those made with **SC18dil** are much more opaque, suggesting the presence of more scattering grains in **SC18dil** than in **SC30dil** layer. The differences in the thicknesses of the studied mesoporous layers are summarized in Table S1 (ESI†).

The differences in the thickness of **SP30dil** *vs.* **SP30** and **SC30dil** *vs.* **SC18dil** layers were also confirmed by stationary absorption measurements of the electrodes (Fig. S2, ESI†). The absorbance values below 400 nm (where TiO$_2$ absorbs) are higher for **SP30** than **SP30dil** and higher for **SC18dil** than **SC30dil**. However, the exact thickness ratio of different titania layers is hard to estimate in this way, because the absorbance is also affected by the scattering contribution, which results in the baseline signal increasing for shorter wavelength (and observed already at wavelength longer than 400 nm). Moreover, the absorption baseline is also affected by the oscillations appearing due to the light interference at the layers of sub μm sizes[24] present on the electrodes.

The stationary absorption measurements were also used to determine the absorption spectrum of active layers (dyes or perovskite) after the subtraction of titania layers contribution. The examples are shown in Fig. 2. These data are important to estimate the numbers of absorbed photons from 1 Sun irradiation (N_{ph}), which are necessary to calculate and compare the relative photocurrent of different cells (in the next section).

3.2. Photovoltaic parameters

Table 1 shows the photovoltaic parameters of the best cells prepared using different titania layers. The absorbance of the active material at selected wavelength and the number of absorbed photons (N_{ph}) from 1 Sun irradiation are given along with the standard photovoltaic parameters: open circuit voltage (V_{OC}), short circuit current density (J_{SC}), fill factor (FF) and sunlight power conversion efficiency (PCE). Moreover, Table 1 presents also the calculated parameter total APCE (APCE – absorbed photon to current efficiency), describing the relative photocurrent of the cells per the number of absorbed photons. It is defined as the total APCE = $J_{SC}/e\, N_{ph}$, where e is elementary charge. This parameter allows us to compare the efficiency of charge separation between the cells with different amounts of adsorbed dyes, as we did in many of our previous studies.[25–28] The average values of the photovoltaic parameters with errors based on the measurement of several cells of the same type are collected in Table S2 (ESI†).

At first, the DSSC samples with the liquid electrolyte (L-DSSC) will be described. The cells sensitized with popular carbazole dye called MK2 were studied in two configurations: without co-adsorbent in Co-phenanthroline electrolyte (**Phen**), and with CDCA in Co-bipyridine electrolyte (**CBpy**), using both **SP30dil** and **SP30** layers (Table 1A). The absorbance of MK2 (and thus the total amount of MK2 dyes on titania layer) is, as expected, smaller in the samples with the co-adsorption of CDCA. However, for both the cells with and without CDCA, the amount of dyes in **SP30dil** layers is as high as about 75% of that in the corresponding **SP30** layers. Having in mind that the thickness of **SP30** is about twice that of **SP30dil**, it means that the dye loading per layer thickness is significantly higher for the cells prepared with the diluted paste. It can be probably explained by higher porosity of the **SP30dil** titania layer. Furthermore, Table 1A shows that the photocurrent (J_{SC}) of the fresh cells is only slightly smaller for **SP30dil** cells, while IPCE spectra (Fig. S3, ESI†) indicate that it originates mainly from higher absorption on the rising, long-wavelength part of MK2 absorption band. Small difference in J_{SC} results in the higher relative photocurrent (total APCE) for **SP30dil** cells than **SP30** ones. Finally, L-DSSC from diluted titania paste exhibits higher V_{OC} (by about 0.04 V) indicating slightly smaller recombination losses in **SP30dil** cells. Our observations of the above improvements upon dilution of titania paste are consistent with previous reports.[23,29] The layers with higher porosity permit a more effective transport of large redox shuttles like cobalt complexes. However, the studies of the impact of titania modifications on ultrafast charge transfer process, which we present in the next sections, has not been addressed so far.
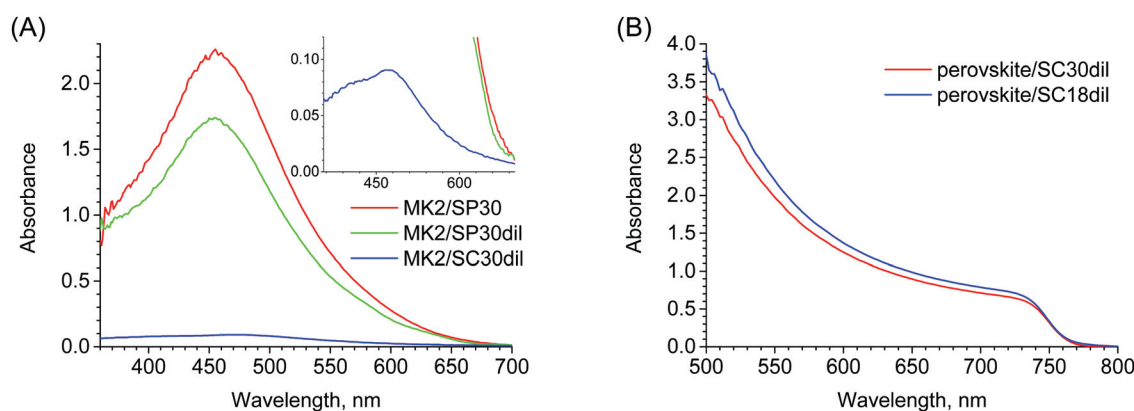
Fig. 2 Stationary absorption of the **SP30**, **SP30dil** and **SC30dil** electrodes sensitized with MK2 dye (without CDCA) (A) and triple cation perovskite on **SC30dil** and **SC18dil** layers (B). The contribution of titania has been subtracted in both figures. The inset in (A) presents the spectra with enlarged absorbance scale.

21950 | *Phys. Chem. Chem. Phys.*, 2020, **22**, 21947–21960

This journal is © the Owner Societies 2020

Table 1 Photovoltaic parameters of the best cells: V_{OC} – open circuit voltage, J_{SC} – short circuit photocurrent density, FF – fill factor, PCE – power conversion efficiency, N_{ph} – number of absorbed photons from 1 Sun, A – absorbance at 500 nm, total APCE – relative photocurrent

Sample	V_{OC} [V]	J_{SC} [mA cm^{-2}]	FF	PCE [%]	N_{Ph} [10^{20} s^{-1} m^{-2}]	A (500 nm)	Total APCE
(A) fresh L-DSSC:							
Phen/SP30	0.84	8.03	0.63	4.30	7.24	1.58	0.69
Phen/SP30dil	0.88	7.44	0.68	4.44	6.60	1.18	0.70
CBpy/SP30	0.79	7.04	0.70	3.93	6.44	1.12	0.68
CBpy/SP30dil	0.83	6.79	0.70	3.98	5.66	0.87	0.75
Sample	V_{OC} [V]	J_{SC} [mA cm^{-2}]	FF	PCE [%]	N_{Ph} [10^{20} s^{-1} m^{-2}]	A (500 nm)	Total APCE
(B) 20 days old L-DSSC:							
Phen/SP30	0.86	6.97	0.71	4.26	7.24	1.58	0.60
Phen/SP30dil	0.86	7.56	0.70	4.53	6.60	1.18	0.71
CBpy/SP30	0.79	7.82	0.70	4.34	6.44	1.12	0.76
CBpy/SP30dil	0.84	7.29	0.73	4.46	5.66	0.87	0.81
Sample	V_{OC} [V]	J_{SC} [mA cm^{-2}]		FF	PCE [%]		Total APCE
(C) fresh PSC and S-DSSC:							
PSC/SC18dil	0.99	17.2		0.62	10.6		0.80
PSC/SC30dil	1.07	24.4		0.68	17.8		1.17
S-DSSC/SC30dil	0.71	0.98		0.57	0.40		0.52
S-DSSC/SP30dil	0.58	3.20		0.42	0.79		0.49
S-DSSC/SP30	0.46	3.74		0.34	0.58		0.38

It should be noted that the same trends in the differences between **SP30dil** and **SP30** cells (higher V_{OC} and total APCE, better dye loading) were confirmed in our preliminary studies of L-DSSC with other dyes (indoline dye D205[30,31] and the 2 : 1 mixture of MK2:D205 in Co-phenanthroline electrolyte). After 20 days, the parameters of L-DSSC were quite stable and most of them even improved, increasing the total efficiency of the cell (Table 1B). The best efficiency of about 4.5% was reached for the cells made with diluted paste. It is not very high comparing this value to that of the best L-DSSC (efficiencies 12–14%);[2,3] however, it should be noted that our result was achieved on the very thin (1.3–1.5 μm) and transparent titania layer only.

PSC with triple cation perovskite, spiro-OMeTAD as hole transporting layer, and **SC18dil** or **SC30dil** titania layers as electron transporting material, were studied. Their photovoltaic parameters are collected in Table 1C. As can be seen, all parameters (V_{OC}, J_{SC}, FF and PCE) are better for the cells prepared on **SC30dil** than **SC18dil**, which confirms that more the homogenous thinner, and made of larger particles meso-porous titania layer is advantageous for the performance of this kind of cells. Better photovoltaic parameters obtained for larger nanoparticles and thinner TiO$_2$ layers are consistent with the previous reports.[7] For example, the efficiency of PCS made of MAPbI$_3$ was 14.34% for 400 nm layer thickness of 25 nm particles, while it improved to 18.72% for 150 nm layer thickness with 41 nm particles.[7] The improvement observed for larger particles was assigned to higher porosity and mean pore diameter of the resultant layer. However, according to our knowledge, the charge transfer dynamics (presented in the next sections) has not been compared so far.

The photovoltage (V_{OC} close to 1.1 V) and photocurrent (J_{SC} above 24 mA cm^{-2}) of our best PSC with **SC30dil** layer are close to the top efficiencies reported for PSC. The very high value of the relative photocurrent (close to 100%) indicates almost no charge recombination at low voltages. The constructed perovskite solar cells exhibit relatively small hysteresis with the hysteresis index of 0.03–0.05 (Fig. S4, ESI†). Our best PSC efficiency is about 18%, and the parameter which mainly limits our efficiency and which is significantly lower with respect to the best PSC devices, is the fill factor. The obtained values of FF below 0.7 in PSC are probably due to the sputtering method of gold electrode depositions used for our cells, instead of typically employed thermal evaporation technique. It is confirmed and explained in ESI† (Table S3 and the short discussion below, ESI†). However, it should be emphasized that low FF values of our PSC (and also our solid state DSSC described below) do not change the main conclusions following from our studies since we are mainly focused on the photocurrents and all samples compared are affected by gold sputtering in the similar way.

The solid state DSSC (S-DSSC) were prepared using **SC30dil** (the same as for PSC), **SP30dil** or **SP30** (the same as for L-DSSC) titania layers sensitized with MK2 dyes (without co-adsorbent). The electrodes were then covered with spiro-OMeTAD and gold electrodes. The photovoltaic parameters are collected in Table 1C. Although J_{SC} increases for thicker titania layers due to more adsorbed dyes, the other parameters (V_{OC}, FF and total APCE) significantly decrease when going from samples with **SC30dil** (thickness 150–200 nm) to **SP30dil** (1.3–1.5 μm) and further to **SP30** (2.5–3 μm). The common problem with S-DSSC is the penetration of spiro-OMeTAD to deeper titania layers sensitized with the dye,[8] which is confirmed in our results. The best efficiency of about 0.8% is obtained for the cell with **SP30dil** layer. Fill factor values improve in both PSC and S-DSSC samples for more porous and thinner titania layer due to better pore filling by the precursor solution and spiro-OMeTAD, respectively.

The composition and deposition method of spiro-OMeTAD were optimized for PSC and it is probably one of the reasons

This journal is © the Owner Societies 2020

Phys. Chem. Chem. Phys., 2020, **22**, 21947–21960 | **21951**

181

Paper

PCCP

why the parameters and efficiencies of our S-DSSC are rather poor, comparing to other reports of S-DSSC with MK2 dye (~3%).[32,33] Despite preferable match of HOMO levels of the dye (0.92 eV *vs.* NHE)[34] and the HTM (0.75 eV *vs.* NHE),[35] TiO$_2$ layer is not fully covered by the dyes as it is covered by the perovskite layer in PSC, allowing unwanted direct charge recombination at HTM/ETM interface. However, the total APCE values in our S-DSSC (from 0.52 to 0.38, compared to 0.60–0.80 for L-DSSC) indicate that still about half of the photoinduced charges are successfully separated at low voltages, therefore the findings from transient absorption studies presented in the next sections are still informative for the operation of S-DSSC.

3.3. Transient absorption of titania layers

We will begin with presentation of the transient absorption results obtained for isolated electrodes with titania layers excited at 310 or 355 nm. Such excitation leads to the direct absorption of light by TiO$_2$ and creation of electron–hole pairs. Fig. S5 (ESI†) shows the exemplary transient spectra for **SC30dil** in UV-VIS and NIR ranges at selected time delays between pump and probe pulses. The results of global three-exponential analysis of the same sample are presented in Fig. 3A and B. Initially, the negative bleach signal in the spectral range of TiO$_2$ stationary

absorption can be observed below 380 nm. At longer wavelength in the VIS range the positive signal from holes and trapped electrons can be observed, while the positive signals in NIR range are dominated by free and shallowly trapped electrons.[36] After 1 ns the majority of signals decay due to charge recombination, but below 400 nm a positive, a long-lasting band appears, which we assign to the thermal artifact – broadening of the titania absorption band upon local sample heating. Indeed, our stationary absorption measurements showed that TiO$_2$ electrodes increase their absorption in the range from 340 to 400 nm upon heating, with approximately 0.0008 change in absorption per 1 Celsius degree at 340 nm (Fig. S6, ESI†). This artifact, being responsible for the existence of transient absorption signal, even when no excited state population is present, has been reported recently for some metal oxide semiconductors: BiVO$_4$,[37] hematite, LaFeO$_3$ or LaMnO$_3$.[38] However, according to our knowledge, this effect has not been reported for TiO$_2$ as yet.

The multi-exponential global analysis reveals that the majority of free electrons decays occur with the time constant of about 1 ps (amplitudes of τ_1 component in Fig. 3B, increasing for longer wavelength in the infrared range)[36,39] and that the signals of trapped electrons and holes do not decay in the single exponential way (components τ_1 and τ_2 in Fig. 3A). Fig. 3C and D
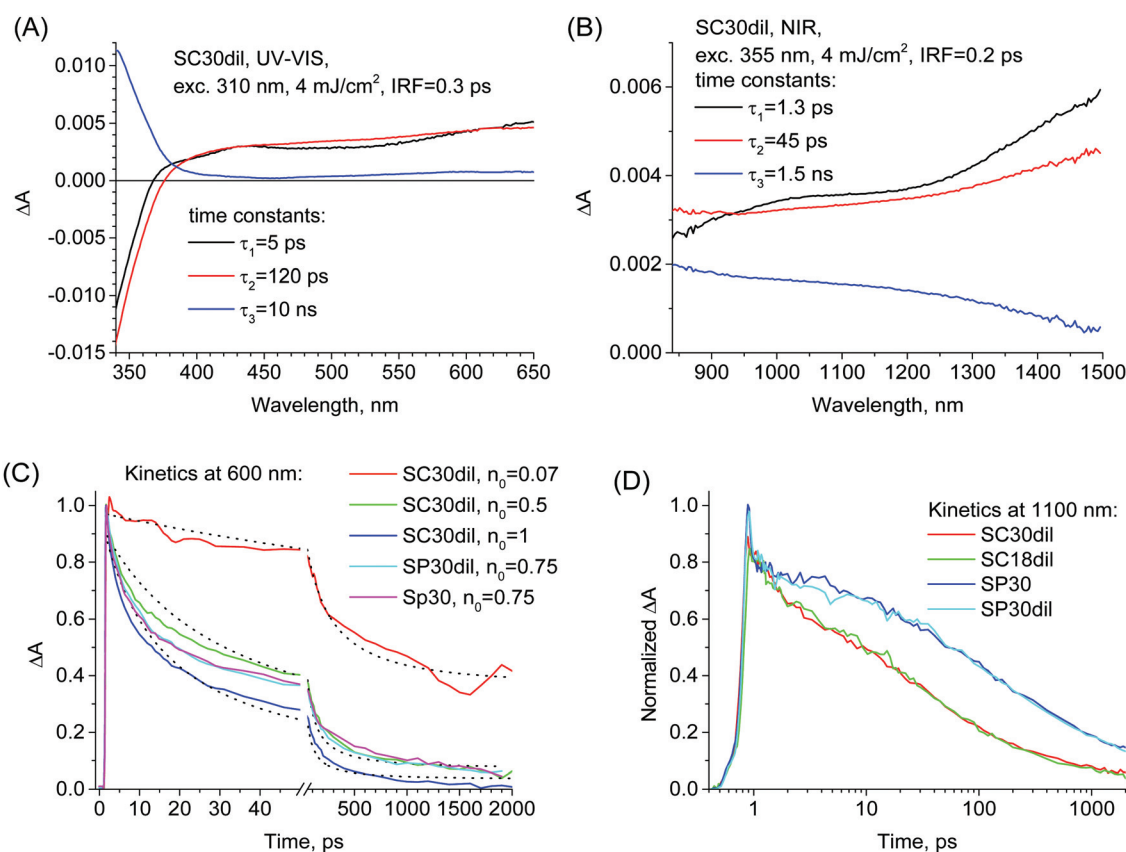
Fig. 3 Examples of the global analysis of transient absorption data using a three-exponential function with a constant offset for **SC30dil** electrode: in UV-VIS (A) and NIR ranges (B). The normalized kinetics at 600 nm for the indicated samples at fluences from 0.5 to 4 mJ cm^{-2}, together with mixed first and second order functions fitted (dotted lines) for **SC30dil** samples (C). The scaling factors for the initial photoexcited charge concentration (n_0) are also given. The normalized kinetics at 1100 nm for different titania samples measured at the same fluence (D). The amplitudes of **SC30dil** and **SC18dil** were multiplied by 1.85 in (D) to have the same value as those of **SP30** and **SP30dil** samples.

21952 | *Phys. Chem. Chem. Phys.*, 2020, **22**, 21947–21960

This journal is © the Owner Societies 2020

present the kinetics at 600 nm (dominated by holes) and 1100 nm (dominated by electrons). As can be seen, the dynamics of hole decay is similar for **SC30dil**, **SP30dil** and **SP30** layers (Fig. 3C). Interestingly, the decay of electrons is significantly slower for **SP30dil** and **SP30** layers than for **SC30dil** and **SC18dil** ones (Fig. 3D), indicating the difference in the distribution of trapped states below the titania conduction band. The decay of holes at 600 nm was analyzed at different excitation fluence (Fig. 3C). The higher the initial amplitude (and thus the population of the charges), the faster the decay. It can be justified by the contribution of second order process (hole-electron radiative recombination). Indeed, the mixed first and second order fit (see SI for the function definition) reveals trap-assisted first order rate constants $k_1 = 1$ ns^{-1} and second order rate constant $k_2 = 3.4$ ns^{-1} $(m\Delta A)^{-1}$ (absorbance signal is used instead of charge concentration, because of difficult estimation of the latter). The fit is not perfect (Fig. 3C), which is probably due to the effect of the diffusion of charges in the sample of a certain thickness (therefore, the initial density of charges changes in time). The contribution of the second order process in the measured range of excitation fluence at 310 nm (0.5–4 mJ cm^{-2}) varies from 81% to 98%.

3.4. Transient absorption of L-DSSC

Next, the transient absorption results for solar cell samples with different titania layers are presented and compared. L-DSSC, PSC and S-DSSC were excited at 500 nm, at which the light is absorbed by the active materials (MK2 dye or triple cation perovskite) and not by TiO$_2$. The measurements for L-DSSC refer to a 20 days old cell, whose parameters were slightly improved with respect to the as-obtained one (Table 1B). The pump pulse was directed from the titania side and excitation fluence for L-DSSC was 100 μJ cm^{-2}. Fig. S7 (ESI†) shows the exemplary spectra of **CBpy/SP30dil** sample at selected time delays between the pump and probe pulses, while representative pseudo-color 2D spectra of transient absorption data are presented in Fig. 4A and B.

The transient absorption spectra and their evolution are analogous to those reported by us earlier for L-DSSC with MK2 dye.[25,26,40,41] Similarly, global analysis assuming a two-exponential function and constant offset was employed to extract the characteristic time constants. The representative results are presented in Fig. 4C–F. The constant offset component with a bleach band below 650 nm (corresponding to stationary absorption of MK2 dye – compare with Fig. 2A) and a positive band with a maximum at 750 nm is assigned to the oxidized dye. Thus, its amplitude with respect to the initial one is proportional to the number of successfully separated charge carriers. The relative amplitude of the positive band is higher for the cells with CDCA (**CBpy**, Fig. 4C and D) than for those without co-adsorbent (**Phen**, Fig. 4E and F). It agrees with the higher total APCE values for the former than for the latter samples (Table 1B), and is in line with our previous findings.[25]

The pre-exponential factor spectra of the second, longer component (τ_2 in the range from 130 to 180 ps, slightly faster for **Phen** than **CBpy** cells) have the shape similar to that of the constant offset spectra. Therefore, the second component is

assigned to the recombination of injected electron from titania to MK2 dye, decreasing the population of the oxidized dye. Finally, the fastest extracted component (τ_1 of several ps) is the only one for which the small but systematic differences between **SP30dil** and **SP30** samples can be observed. This component should be ascribed to the fast part of electron recombination (that occurs over many time scales), but it is also influenced by the electron injection; therefore, its pre-exponential factor spectra are different than those of τ_2 and constant offset components. In particular, the electron injection is accompanied with the decay of the S_1 state of the dye, and *e.g.* the indentation in the spectra in 600–750 nm range is due to the stimulated emission (Fig. 4C–F).[26] It is more visible in **CBpy** than **Phen** samples because, as we analyzed in more details earlier, the electron injection is slower for MK2 with CDCA than without CDCA.[25] Nevertheless, the electron injection times are below 1 ps in both cases, so the differences in values of τ_1 are mainly due to electron recombination. Thus, the fast component of recombination is slightly slower in the samples with the diluted titania phase (τ_1 of about 6 ps with respect to 4 ps for undiluted samples, Fig. 4C–F), which is beneficial for charge separation. It might be explained by a closer distance between the dyes on titania nanoparticle surface in **SP30** than **SP30dil** layer, which enhance fast recombination.[25,41] Although dye loading is higher in **SP30dil** cells than **SP30** ones, it is the loading per the layer thickness that we consider, and due to higher porosity of **SP30dil** than **SP30** layer, the average distance between adjacent dyes might be even larger in **SP30dil** than **SP30**. It should be also noted that the charge transfer processes observed on the time scales up to few nanoseconds are only related to the interaction between dye molecules and single TiO$_2$ nanoparticle. Different titania thickness in DSSC samples can affect the kinetics on much longer time scales (*e.g.* electron transport through the titania nanoparticles net or titania-redox couple recombination).

3.5. Transient absorption of PSC

We will discuss now the transient absorption results obtained for as-obtained PSC. Fig. S8 (ESI†) presents the exemplary spectra at different time delays between the pump and probe pulses while representative pseudo-color 2D spectra of transient absorption data are shown in Fig. 5A and B. They are similar to many previous reports on standard MAPbI$_3$ perovskites,[42–50] including our studies,[28,51,52] as well as to our recent studies of the same triple cation perovskite compositions prepared under drybox or ambient air conditions.[53] The initial changes at times below 1 ps are due to the charge carrier relaxation.[43,45,46,54] After that, the signals are dominated by the strong and sharp negative bleach close to the absorption edge, appearing due to the band filling mechanism and being proportional to the population of the excited carriers.[42,46,47] The decay of this signal is due to the charge recombination, charge diffusion and charge transfer to contact layers (electron injection into TiO$_2$ and hole injection into spiro-OMeTAD).[44,49,52,55]

To compare the charge dynamics in PSC with **SC30dil** and **SC18dil** layers, the global multi-exponential analysis was employed,

Paper
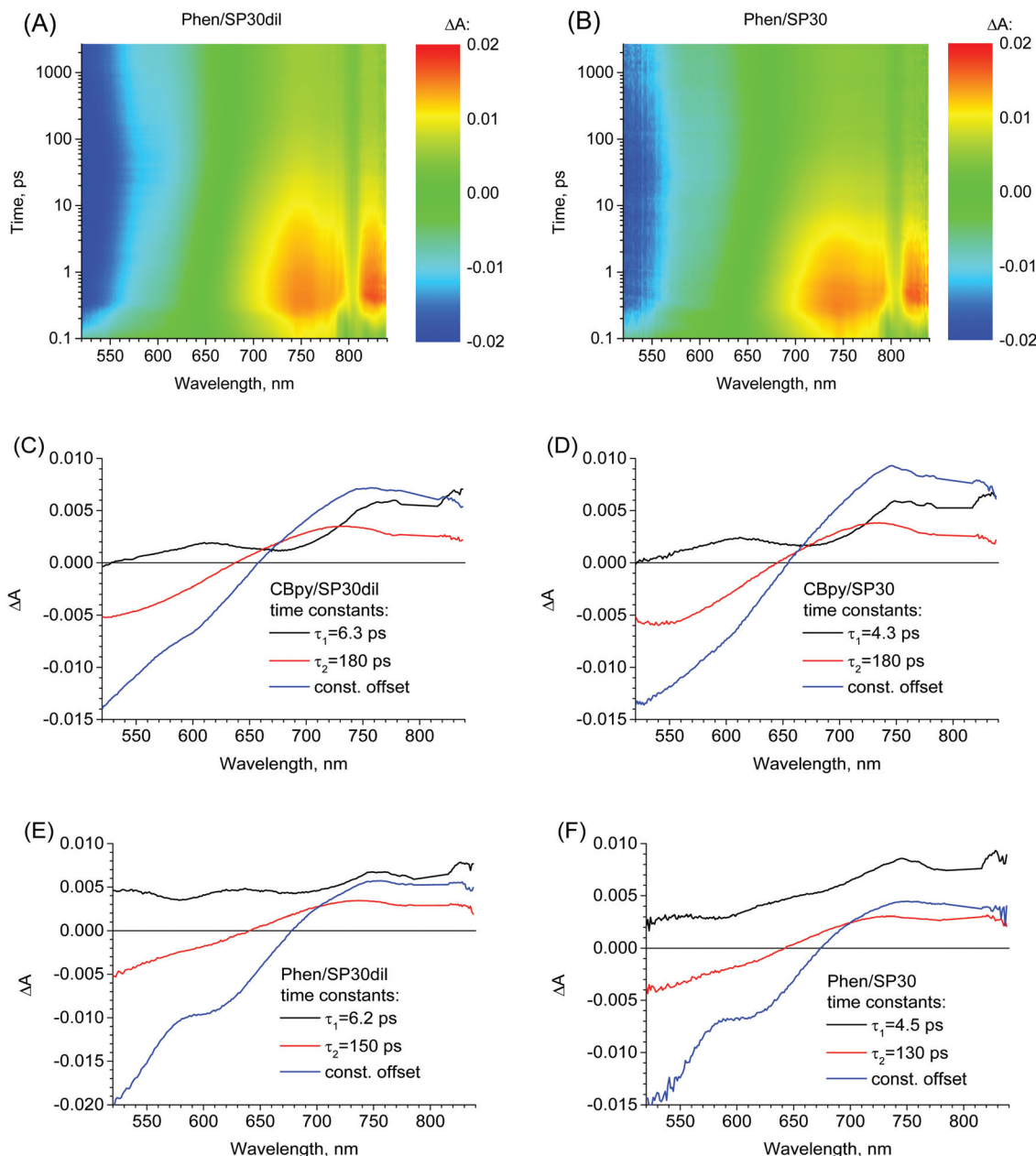
Fig. 4 Pseudo-color 2D spectra of original transient absorption data for L-DSSC with **SP30dil** and **SP30** titania layers (A and B). Examples of the global analysis of transient absorption data using a two-exponential function with a constant offset for L-DSSC samples (C–F). The graphs present pre-exponential factor spectra associated to the indicated time constants. The pump fluence was 100 µJ cm^{-2} and IRF was 0.3 ps.

similarly as in our previous studies.[28,51,52] As we have discussed,[52] the exponential functions (being the solution of the first order kinetic equations) do not strictly follow the kinetics of charge population, which include *e.g.* second order radiative recombination and charge diffusion.[47,48,56] However, the fitted time constants of exponential components and the associated pre-exponential factor spectra can be used to identify the occurring processes and compare their characteristic, average times. Fig. 5C–F shows the results of 3-exponential global analysis of the data obtained with the excitation fluence 30 µJ cm^{-2} from both ETM (TiO$_2$) and HTM (spiro-OMeTAD) sides.

Due to the high absorbance of the samples at the excitation wavelength ($A > 3$ at 500 nm, see Fig. 2B), the initial excitation of perovskite is localized close to the contact layers, therefore the excitations from different sides of PSC probe more selectively the charge transfer to one, particular layer (ETM or HTM). The first, sub picosecond component has a shape characteristic of the band-edge shift, which is due to charge cooling and/or exciton dissociation.[43,45,46] Its value of $\tau_1 = 0.3$ ps is the same for the samples with **SC30dil** and **SC18dil** titania layers. In contrast, the next two time components (having the amplitude spectra dominated by the bleach signal and showing the charge population decay) are
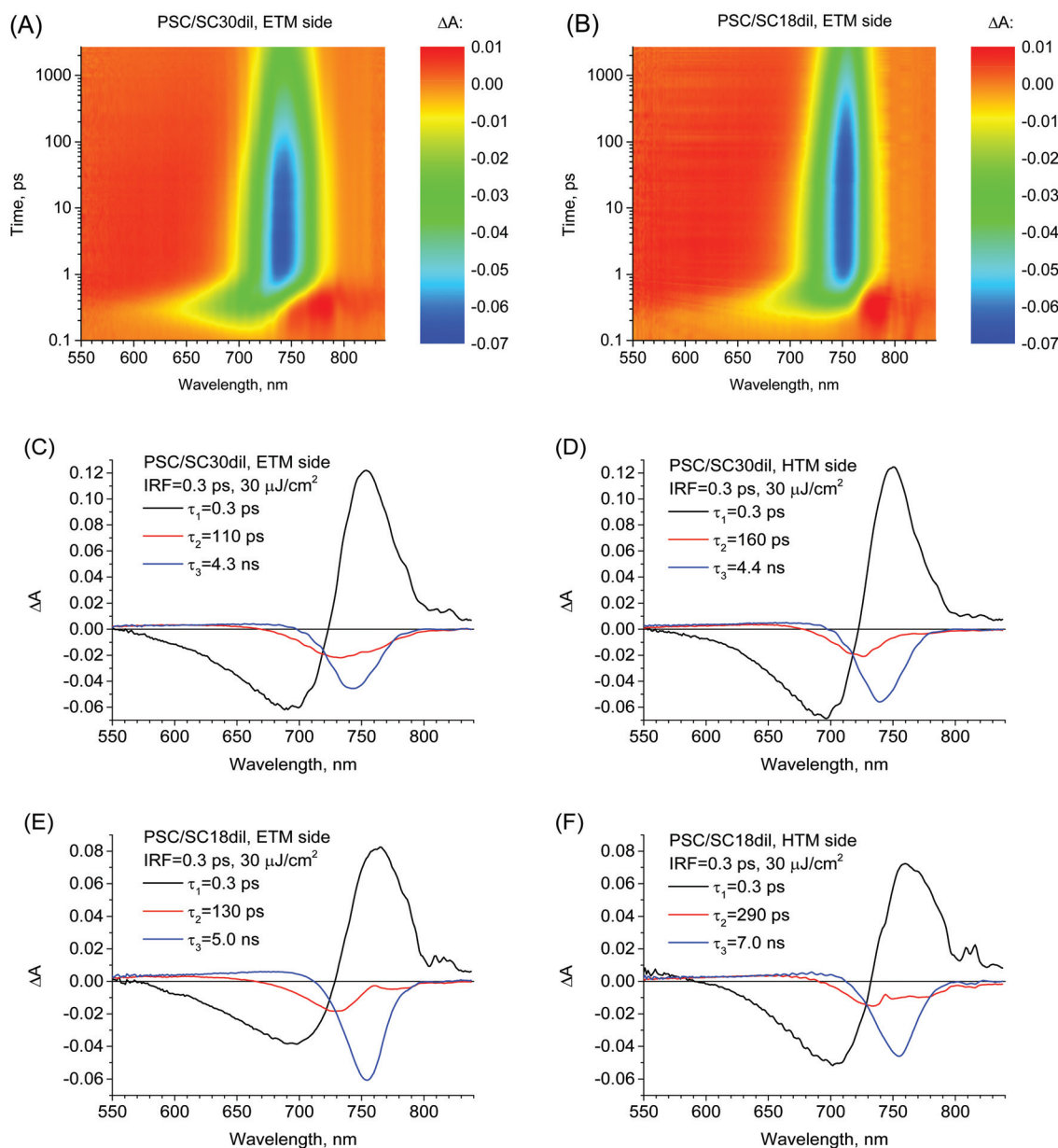
Fig. 5 Pseudo-color 2D spectra of original transient absorption data (A and B). Examples of the global analysis of transient absorption data using three-exponential function for PSC samples. The graphs present pre-exponential factor spectra associated to the indicated time constants. The pump fluence was 30 μJ cm^{-2} and IRF was 0.3 ps.

always shorter for **SC30dil** than **SC18dil** layers, which indicates that the electron transfer to titania is faster for **SC30dil** cells with a higher photocurrent. The spectrum of the second component (τ_2, from 100 to 300 ps in Fig. 5C–F) is usually blue-shifted with respect to that of the third one (τ_3, in the nanosecond range) because the charges filling the bands of higher energy depopulate faster.[52] It should be noted that the fitted time constant are only partly related to the charge injection times, because they are strongly affected by the second order charge recombination within the perovskite, as evidenced *e.g.* by the higher values of τ_2 and τ_3 at lower excitation fluence (10 μJ cm^{-2}, see Fig. S9, ESI†).

To simplify the comparison between **SC30dil** and **SC18dil** layers, we have also performed 2-exponential global analysis,[51]

in which the second component reflects the average charge population decay (despite poor fit quality, at least for the excitation fluence 30 μJ cm^{-2}). The obtained mean values are the following: τ_{AVG} (**SC30dil**, ETM side) = 1.9 ns, τ_{AVG} (**SC30dil**, HTM side) = 2.5 ns, τ_{AVG} (**SC18dil**, ETM side) = 3.3 ns and τ_{AVG} (**SC18dil**, HTM side) = 3.3 ns, all with the error ± 0.1 ns based on standard deviation from 4-7 measurements.

As can be seen, the charge decay is faster for **SC30dil** than **SC18dil** samples, which is also visualized by the comparison of kinetics at bleach maximum presented in Fig. 6A or the pseudo-color 2D spectra in Fig. 5A and B. Moreover, the difference is higher for the excitation at ETM side where the contribution of electron injection to titania is higher than that at HTM side.

This journal is © the Owner Societies 2020

Phys. Chem. Chem. Phys., 2020, **22**, 21947–21960 | **21955**

185
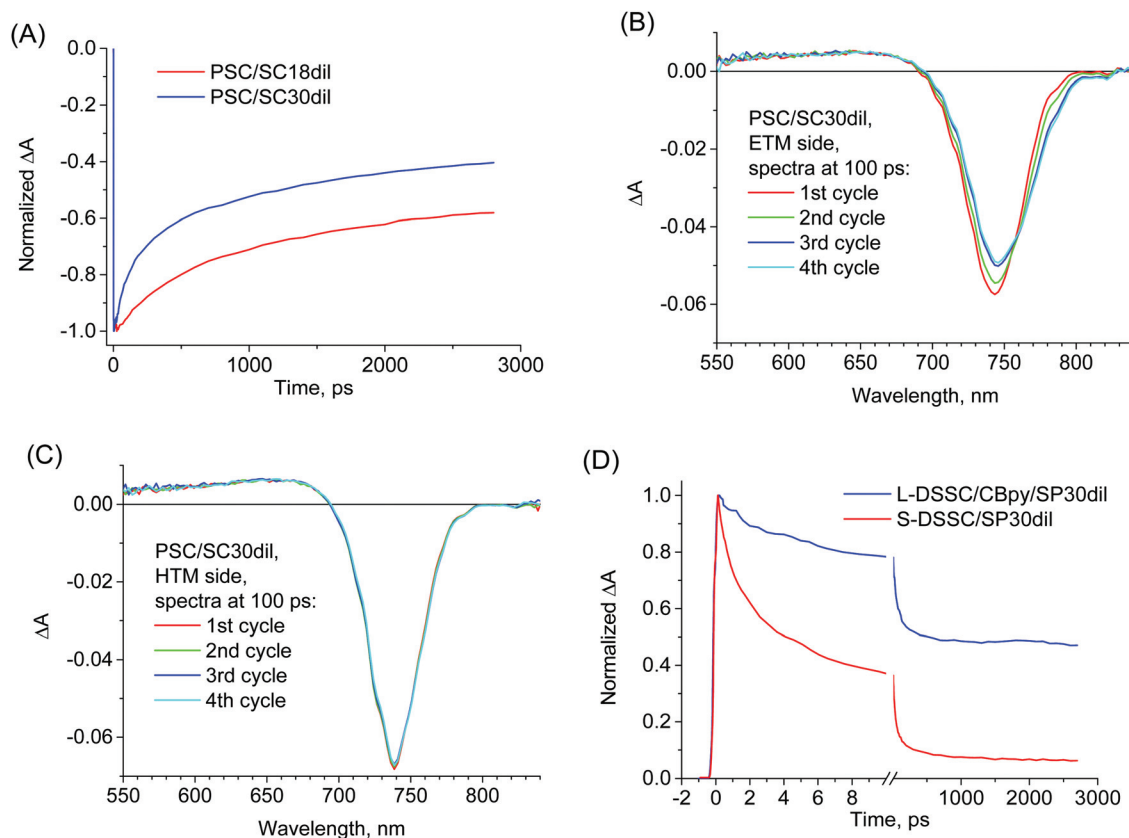
Fig. 6 Normalized kinetics for PSC measured from ETM side at the maximum of the bleach signal for **SC18dil** and **SC30dil** layers (A). Transient absorption spectra for PSC with **SC30dil** layer measured at 100 ps for different consecutive cycles at ETM (B) and HTM (C) sides. The pump fluence was 30 μJ cm^{-2} in A–C. Normalized kinetics for L-DSSC and S-DSSC measured at 750 nm (D).

Therefore, it confirms that the faster electron injection from the perovskite to TiO$_2$ is responsible for the observed faster bleach recovery dynamics in the **SC30dil** samples, because all other parameters that might influence the population decay (excitation fluence, perovskite layer thickness, HTM material) are the same in both samples. However, it should be noted that the magnitude of lifetime shortening do not directly represent the values of intrinsic electron injection times, which might be much shorter than nanoseconds due to the occurrence of charge diffusion process. For example, it was shown that the half-decay of the bleach signal of the perovskite layer studied (of 80 nm in thickness) can decrease from 4 ns to 2 ns when the intrinsic electron transfer time is shortened from 50 ps to 10 ps.[47]

Finally, we would also like to address another important issue related to the interface between triple-cation perovskite and the titania layer. In our recent contribution we have reported the differences in morphology (PbI$_2$ content) and spectra between the perovskite close to ETM and that near HTM interface.[53] In particular, the transient bleach band showed additional red-shifted spectral features of perovskite close to ETM side. One of the proposed explanations was the ion segregation leading to different ratios of bromide/iodide close to the TiO$_2$ that could modify the bandgap.[57] This effect can be enhanced by irradiation.[58] In the study presented here we

provide more evidence for this mechanism by comparing the changes in transient absorption spectra during the following cycles in the femtosecond experiment (each cycle lasted about 3 minutes). As can be seen in Fig. 6, upon increasing irradiation time, some clear changes (with isosbestic point) of bleach spectrum at 100 ps are observed at ETM side (Fig. 6B), while no such changes are visible at HTM side (Fig. 6C). This result was obtained for the PSC/**SC30dil** sample showing high photocurrent. On the contrary, for worse performing PSC/**SC18dil** cell the changes on ETM side were much smaller (Fig. S10A, ESI†). We have also passivated **SC30dil** layer by sensitization with MK2 dye (before perovskite deposition). For such test PSC the photocurrent was very small (total APCE = 0.61) and the changes on ETM side were also hardly observed (Fig. S10B, ESI†). Therefore, the photoinduced bleach changes near TiO$_2$ (due to probable ion segregation in mixed halide perovskite) occur efficiently only for the cells with high photocurrent. It is consistent with the recent supposition that ion segregation is enhanced by hole accumulation at the interface where electrons were efficiently injected.[58]

3.6. Transient absorption of S-DSSC

In the last section we will present the transient absorption data measured for the as-obtained S-DSSC. Similarly as in the previous sections, the representative spectra at selected time

21956 | *Phys. Chem. Chem. Phys.*, 2020, **22**, 21947–21960

This journal is © the Owner Societies 2020

186

delays are shown in ESI† (Fig. S11), while representative pseudo-color 2D spectra of transient absorption data are shown in Fig. 7A. Fig. 7B–D presents the results of the global fit using the same model as for L-DSSC (two-exponential function with constant offset). The results for solid state cells should be compared with those of liquid solar cell made with the same dye (Fig. 4C–F).

The most important differences are the smaller contribution of the constant offset component and the shorter times τ_1 and τ_2 for S-DSSC (Fig. 7B–D) with respect to those of L-DSSC (Fig. 4C–F). The time constants obtained from the global fit are about three times shorter for S-DSSC than those for L-DSSC. The difference can be also clearly visualized by comparing the kinetics at the maximum of the oxidized dye band (750 nm), which are presented in Fig. 6D. Therefore, the additional quenching of the oxidized dye is observed for S-DSSC, which should be explained by fast regeneration of the dye by spiro-OMeTAD. In our systems, such a hole transfer occurs on the time scale of single and tens of ps. In the cells with liquid electrolyte the dye regeneration by redox couple (*e.g.* cobalt complex or iodide/iodine pair) occurs on the time scale of µs, but the hole injection from solid HTM can occur much faster, even competing with electron injection. Such a fast dye

regeneration has been reported for several systems,[6] however, according to our knowledge, we show it for the first time for the popular carbazole dyes and spiro-OMeTAD.

In principle, the observed quenching of the oxidized MK2 dye in S-DSSC could be also explained by greatly enhanced electron recombination.[33] However, the decrease in the total APCE of S-DSSC is not more than half with respect to that of L-DSSC (Table 1), so we could expect not more than twice decrease in the residual signal in transient absorption.[25] The drop in the residual amplitude for S-DSSC is much larger than that, therefore, the quenching must be dominated by the fast hole transfer. Moreover, we can observe a clear correlation of the relative amplitude of constant offset component and life-times with the thickness of the mesoporous layer (Fig. 7B–D). The residual signal is the smallest and the time constants τ_1 and τ_2 are the shortest for **SC30dil** sample (thickness 150–200 nm). For **SP30dil** sample (1.3–1.5 µm) the values are intermediate, while for the thickest **SP30** layer (2.5–3 µm) the residual signal is the strongest and the time constants are the longest. As mentioned before, the problem in S-DSSC is the penetration of spiro-OMeTAD to deep parts of the mesoporous layer for the thickness above 1 µm. The limited penetration of HTM into titania can thus explain the trends we observe for
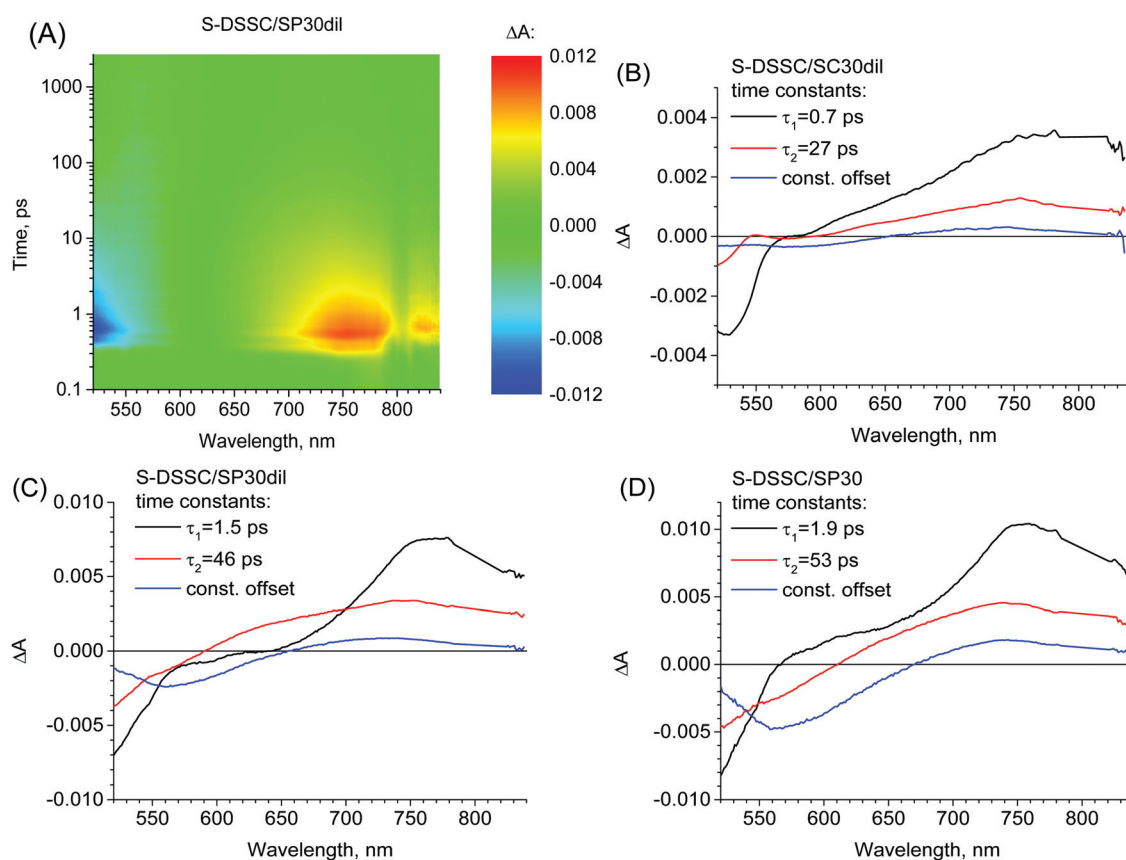
Fig. 7 Pseudo-color 2D spectra of original transient absorption data for S-DSSC with **SP30dil** titania layer (A). Examples of the global analysis of transient absorption data using two-exponential function with constant offset for S-DSSC samples with the indicated titania layers: **SC30dil** (B), **SP30dil** (C) and **SP30** (D). The graphs present pre-exponential factor spectra associated to the indicated time constants. The pump fluence was 100 µJ cm^{-2}, IRF was 0.3 ps and the excitation was from HTM side.

187

SC30dil, **SP30dil** and **SP30**: spiro-OMeTAD is probably not in contact with all dyes for **SP30dil** and especially for **SP30**, so their regeneration is slowed down. The observed differences in the quenching yield of oxidized MK2 by HTM correlates with the relative photocurrent (total APCE) of the cells: the highest for **SC30dil** and the lowest for **SP30** layers (Table 1C). It is in agreement with the previous reports about higher photocurrent in S-DSSC for better spiro-OMeTAD penetration and higher hole transfer yield.[59–61]

Finally, another confirmation of poor pore filling in **SP30** samples comes from the analysis of the decomposition of the samples during transient absorption measurements (Table S4, ESI†). When the cell with **SP30** layer is excited from ETM side (which is hard to be reached by spiro-OMeTAD) a significant decrease (more than 12%) in the transient absorption signal for the consecutive cycles of the experiment is found. For the same **SP30** sample excited from HTM side, and for **SC30dil** and **SC30dil** samples excited at both sides, the changes in the signals are much smaller and probably random. The fast photodegradation under femtosecond pulse excitation occurs when the dyes are not in contact with regenerating medium (*e.g.* in the isolated sensitized electrodes) because the lifetime of the reactive oxidized state is very long.[6]

To summarize the transient absorption parts, the results prove that efficient charge transfer from perovskite to TiO_2 is responsible for improved performance in PSCs utilizing larger particle size. For DSSC utilizing liquid electrolyte a weaker electron recombination in TiO_2 films prepared with diluted TiO_2 is observed. For solid HTM based DSSC higher regeneration rates are observed for spin coated TiO_2 films whereas slower regeneration rates in screen printed films is found.

4. Conclusions

Improvement in the performance of perovskite solar cells (PSC) and dye-sensitized solar cells (DSSC) upon modifications of mesoporous titania layers has been studied. Its impact on the charge transfer dynamics in the complete solar cells as well as in pristine TiO_2 layers have been investigated by femtosecond transient absorption.

For PSC with triple cation perovskite ($FA_{0.76} MA_{0.19} Cs_{0.05} Pb(I_{0.81} Br_{0.19})_3$) the best efficiency of $\sim 18\%$ and photocurrent of ~ 24 mA cm^{-2} were obtained for homogenous TiO_2 mesoporous layer made of 30 nm nanoparticles and with the thickness 150–200 nm. For about twice thicker, less homogenous and made of smaller particles (diameter 18 nm) titania layer, the best efficiency of only $\sim 11\%$ and photocurrent of ~ 17 mA cm^{-2} were found. Shorter photocarriers lifetime in perovskite material was observed for the more efficient cells with respect to those with a worse TiO_2 layer (*e.g.* the average lifetime 1.9 ns *vs.* 3.3 ns when excited from TiO_2 side by 30 μJ cm^{-2} pulse at 500 nm). It indicates that faster electron transfer from perovskite to the optimized TiO_2 is responsible for the higher photocurrent in these triple-cation PSC. Moreover, for better TiO_2 layer the photoinduced changes (appearance of red-shifted feature) in transient bleach signal were

revealed, which may indicate the occurrence of halide segregation in perovskite close to TiO_2 interface.

For DSSC, the effect of dilution of the commercial titania paste has been explored for popular MK2 dye and liquid cobalt-based electrolyte or solid state hole transporter (spiro-OMeTAD). The rise in the photovoltage (up to ~ 0.9 V), higher dye loading per layer thickness and the improvement in relative photocurrent were observed for the liquid cells prepared from the diluted paste (2:1 w/w ratio) with respect to those obtained for the cells prepared from undiluted one. The best efficiency of $\sim 4.5\%$ was obtained for DSSC having the titania mesoporous layer of thickness as small as 1.3–1.5 μm and in the absence of scattering layer. The dynamics of electron injection and recombination was similar in the cells with both diluted and undiluted titania pastes. However, the fast component of unwanted recombination was slightly slower (by about 30%) in the samples with the diluted titania phase than in those made with undiluted ones.

For solid state DSSC, the use of diluted paste results in higher voltage and better relative photocurrent, similar to those of liquid DSSC. The transient absorption studies reveal that the hole injection from MK2 dye to spiro-OMeTAD takes place on the very fast ps time scale (comparable to that of electron injection) and the evidence of the deeper penetration of spiro-OMeTAD into the mesoporous titania is presented.

Moreover, all titania layers (for PSC and DSSC) have been also studied separately in other transient absorption experiments by direct excitation in UV range and observation of electron and hole dynamics. The transient signals of different species have been identified in distinct spectral regions and compared between the samples of different layers: free and trapped electrons from 800 to 1500 nm, trapped holes around 600 nm and thermal artifacts below 400 nm. The decay of free electrons was observed to occur mainly with the time constants <1 ps, and the recombination of holes and electrons took place in the combined first and second order processes. The decay of trapped electrons was slower in the thicker titania layers used for DSSC than in the thinner layers in PSC.

Conflicts of interest

There are no conflicts to declare.

References

1 NREL, Best Res. Effic. Chart | Photovolt. Res. | NREL, 2019.
2 A. Yella, H.-W. Lee, H. N. Tsao, Ch. Yi, A. K. Chandiran, Md. K. Nazeeruddin, E. W.-G. Diau, Ch.-Y. Yeh, S. M. Zakeeruddin and M. Grätzel, *Science*, 2011, **334**, 629–634.

21958 | *Phys. Chem. Chem. Phys.*, 2020, **22**, 21947–21960

This journal is © the Owner Societies 2020

188

3 K. Kakiage, Y. Aoyama, T. Yano, K. Oya, J. I. Fujisawa and M. Hanaya, *Chem. Commun.*, 2015, **51**, 15894–15897.

4 H. Michaels, M. Rinderle, R. Freitag, I. Benesperi, T. Edvinsson, R. Socher, A. Gagliardi and M. Freitag, *Chem. Sci.*, 2020, **11**, 2895–2906.

5 M. Freitag, Q. Daniel, M. Pazoki, K. Sveinbjörnsson, J. Zhang, L. Sun, A. Hagfeldt and G. Boschloo, *Energy Environ. Sci.*, 2015, **8**, 2634–2637.

6 C. Martín, M. Ziółek and A. Douhal, *J. Photochem. Photobiol., C*, 2016, **26**, 1–30.

7 D. G. Lee, M. Ch. Kim, B. J. Kim, D. H. Kim, S. M. Lee, M. Choi, S. Lee and H. S. Jung, *Appl. Surf. Sci.*, 2019, **477**, 131–136.

8 A. Hagfeldt, G. Boschloo, L. Sun, L. Kloo and H. Pettersson, *Chem. Rev.*, 2010, **110**, 6595–6663.

9 U. Bach, D. Lupo, P. Comte, J. E. Moser, F. Weissörtel, J. Salbeck, H. Spreitzer and M. Grätzel, *Nature*, 1998, **395**, 583–585.

10 H. J. Snaith, A. Petrozza, S. Ito, H. Miura and M. Graätzel, *Adv. Funct. Mater.*, 2009, **19**, 1810–1818.

11 U. B. Cappel, A. L. Smeigh, S. Plogmaker, E. M. J. Johansson, H. Rensmo, L. Hammarstroöm, A. Hagfeldt and G. Boschloo, *J. Phys. Chem. C*, 2011, **115**, 4345–4358.

12 I. K. Ding, N. Tétreault, J. Brillet, B. E. Hardin, E. H. Smith, S. J. Rosenthal, F. Sauvage, M. Grätzel and M. D. McGehee, *Adv. Funct. Mater.*, 2009, **19**, 2431–2436.

13 C. T. Weisspfennig, D. J. Hollman, C. Menelaou, S. D. Stranks, H. J. Joyce, M. B. Johnston, H. J. Snaith and L. M. Herz, *Adv. Funct. Mater.*, 2014, **24**, 668–677.

14 W. Zhang, Y. Wu, H. W. Bahng, Y. Cao, C. Yi, Y. Saygili, J. Luo, Y. Liu, L. Kavan, J. E. Moser, A. Hagfeldt, H. Tian, S. M. Zakeeruddin, W. H. Zhu and M. Grätzel, *Energy Environ. Sci.*, 2018, **11**, 1779–1787.

15 H. J. Snaith, *J. Phys. Chem. Lett.*, 2013, **4**, 3623–3630.

16 W. S. Yang, B. W. Park, E. H. Jung, N. J. Jeon, Y. C. Kim, D. U. Lee, S. S. Shin, J. Seo, E. K. Kim, J. H. Noh and S. I. Seok, *Science*, 2017, **356**, 1376–1379.

17 M. Saliba, T. Matsui, J.-Y. Seo, K. Domanski, J.-P. Correa-Baena, M. K. Nazeeruddin, S. M. Zakeeruddin, W. Tress, A. Abate, A. Hagfeldt and M. Grätzel, *Energy Environ. Sci.*, 2016, **9**, 1989–1997.

18 N. Koumura, Z. S. Wang, S. Mori, M. Miyashita, E. Suzuki and K. Hara, *J. Am. Chem. Soc.*, 2006, **128**, 14256–14257.

19 T. W. Hamann, *Dalton Trans.*, 2012, **41**, 3111–3115.

20 S. M. Feldt, E. A. Gibson, E. Gabrielsson, L. Sun, G. Boschloo and A. Hagfeldt, *J. Am. Chem. Soc.*, 2010, **132**, 16714–16724.

21 A. Pradhan, M. Sai Kiran, G. Kapil, S. Hayase and S. S. Pandey, *Sol. Energy Mater. Sol. Cells*, 2019, **195**, 122–133.

22 J. Idígoras, G. Burdziński, J. Karolczak, J. Kubicki, G. Oskam, J. A. Anta and M. Ziółek, *J. Phys. Chem. C*, 2015, **119**, 3931–3944.

23 H. S. Kim, S. B. Ko, I. H. Jang and N. G. Park, *Chem. Commun.*, 2011, **47**, 12637–12639.

24 P. D. T. Huibers and D. O. Shah, *Langmuir*, 1997, **13**, 5995–5998.

25 M. Gierszewski, A. Glinka, I. Gradzka, M. Jancelewicz and M. Ziółek, *ACS Appl. Mater. Interfaces*, 2017, **9**, 17102–17114.

26 A. Glinka, M. Gierszewski and M. Ziółek, *J. Phys. Chem. C*, 2018, **122**, 8147–8158.

27 M. Gierszewski, A. Glinka, I. Grądzka, B. Gierczyk and M. Ziółek, *J. Phys. Chem. C*, 2018, **122**, 25764–25775.

28 K. Pydzińska, P. Florczak, G. Nowaczyk and M. Ziółek, *Synth. Met.*, 2017, **232**, 181–187.

29 Y. Chen, F. Huang, W. Xiang, D. Chen, L. Cao, L. Spiccia, R. A. Caruso and Y. B. Cheng, *Nanoscale*, 2014, **6**, 13787–13794.

30 S. Ito, H. Miura, S. Uchida, M. Takata, K. Sumioka, P. Liska, P. Comte, P. Péchy and M. Grätzel, *Chem. Commun.*, 2008, 5194–5196.

31 A. Glinka, M. Gierszewski, B. Gierczyk, G. Burdziński, H. Michaels, M. Freitag and M. Ziółek, *J. Phys. Chem. C*, 2020, **124**, 2895–2906.

32 U. B. Cappel, T. Daeneke and U. Bach, *Nano Lett.*, 2012, **12**, 4925–4931.

33 A. Abate, M. Planells, D. J. Hollman, S. D. Stranks, A. Petrozza, A. R. S. Kandada, Y. Vaynzof, S. K. Pathak, N. Robertson and H. J. Snaith, *Adv. Energy Mater.*, 2014, **4**, 1400166.

34 I. R. Perera, A. Gupta, W. Xiang, T. Daeneke, U. Bach, R. A. Evans, C. A. Ohlin and L. Spiccia, *Phys. Chem. Chem. Phys.*, 2014, **16**, 12021–12028.

35 B. Xu, H. Tian, L. Lin, D. Qian, H. Chen, J. Zhang, N. Vlachopoulos, G. Boschloo, Y. Luo, F. Zhang, A. Hagfeldt and L. Sun, *Adv. Energy Mater.*, 2015, **5**, 1401185.

36 R. Katoh, M. Murai and A. Furube, *Chem. Phys. Lett.*, 2010, **500**, 309–312.

37 J. K. Cooper, S. E. Reyes-Lillo, L. H. Hess, C. M. Jiang, J. B. Neaton and I. D. Sharp, *J. Phys. Chem. C*, 2018, **122**, 20642–20652.

38 K. E. Knowles, M. D. Koch and J. L. Shelton, *J. Mater. Chem. C*, 2018, **6**, 11853–11867.

39 T. Berger, J. A. Anta and V. Morales-Flórez, *J. Phys. Chem. C*, 2012, **116**, 11444–11455.

40 J. Sobuś, J. Kubicki, G. Burdziński and M. Ziółek, *ChemSusChem*, 2015, **8**, 3118–3128.

41 J. Sobuś, B. Gierczyk, G. Burdziński, M. Jancelewicz, E. Polanski, A. Hagfeldt and M. Ziółek, *Chem. – Eur. J.*, 2016, **22**, 15807–15818.

42 J. S. Manser and P. V. Kamat, *Nat. Photonics*, 2014, **8**, 737–743.

43 F. Deschler, M. Price, S. Pathak, L. E. Klintberg, D. D. Jarausch, R. Higler, S. Hüttner, T. Leijtens, S. D. Stranks, H. J. Snaith, M. Atatüre, R. T. Phillips and R. H. Friend, *J. Phys. Chem. Lett.*, 2014, **5**, 1421–1426.

44 L. Wang, C. McCleese, A. Kovalsky, Y. Zhao and C. Burda, *J. Am. Chem. Soc.*, 2014, **110**, 12205–12208.

45 M. T. Trinh, X. Wu, D. Niesner and X.-Y. Zhu, *J. Mater. Chem. A*, 2015, **3**, 9285–9290.

46 T. C. Sum, N. Mathews, G. Xing, S. S. Lim, W. K. Chong, D. Giovanni and H. A. Dewi, *Acc. Chem. Res.*, 2016, **49**, 294–302.

47 J. Leng, J. Liu, J. Zhang and S. Jin, *J. Phys. Chem. Lett.*, 2016, **7**, 5056–5061.

48 T. W. Crothers, R. L. Milot, J. B. Patel, E. S. Parrott, J. Schlipf, P. Müller-Buschbaum, M. B. Johnston and L. M. Herz, *Nano Lett.*, 2017, **17**, 5782–5789.

This journal is © the Owner Societies 2020

Phys. Chem. Chem. Phys., 2020, **22**, 21947–21960 | **21959**

189

49 E. Serpetzoglou, I. Konidakis, G. Kakavelakis, T. Maksudov, E. Kymakis and E. Stratakis, *ACS Appl. Mater. Interfaces*, 2017, **9**, 43910–43919.

50 P. Piatkowski, B. Cohen, F. Javier Ramos, M. Di Nunzio, M. K. Nazeeruddin, M. Grätzel, S. Ahmad and A. Douhal, *Phys. Chem. Chem. Phys.*, 2015, **17**, 14674–14684.

51 K. Pydzińska, J. Karolczak, I. Kosta, R. Tena-Zaera, A. Todinova, J. Idígoras, J. A. Anta and M. Ziółek, *ChemSusChem*, 2016, **9**, 1647–1659.

52 K. Pydzińska-Białek, J. Szeremeta, K. Wojciechowski and M. Ziółek, *J. Phys. Chem. C*, 2019, **123**, 110–119.

53 K. Pydzińska-Białek, V. Drushliak, E. Coy, K. Załęski, J. Flach, J. Idígoras, L. Contreras-Bernal, A. Hagfeldt, J. A. Anta and M. Ziółek, *ACS Appl. Mater. Interfaces*, 2020, **12**, 30399–30410.

54 T. R. Hopper, A. Gorodetsky, J. M. Frost, C. Müller, R. Lovrincic and A. A. Bakulin, *ACS Energy Lett.*, 2018, **3**, 2199–2205.

55 Q. Lin, Z. Wang, H. J. Snaith, M. B. Johnston and L. M. Herz, *Adv. Sci.*, 2018, **5**, 1–8.

56 L. M. Herz, *Annu. Rev. Phys. Chem.*, 2016, **67**, 65–89.

57 M. C. Brennan, A. Ruth, P. V. Kamat and M. Kuno, *Trends Chem.*, 2020, **2**, 282–301.

58 J. T. Dubose and P. V. Kamat, *J. Am. Chem. Soc.*, 2020, **142**, 5362–5370.

59 J. E. Kroeze, N. Hirata, L. Schmidt-Mende, C. Orizu, S. D. Ogier, K. Carr, M. Grätzel and J. R. Durrant, *Adv. Funct. Mater.*, 2006, **16**, 1832–1838.

60 J. Melas-Kyriazi, I. K. Ding, A. Marchioro, A. Punzi, B. E. Hardin, G. F. Burkhard, N. Tétreault, M. Grätzel, J. E. Moser and M. D. McGehee, *Adv. Energy Mater.*, 2011, **1**, 407–414.

61 Y. S. Kwon, J. Lim, I. Song, I. Y. Song, W. S. Shin, S. J. Moon and T. Park, *J. Mater. Chem.*, 2012, **22**, 8641–8648.

21960 | *Phys. Chem. Chem. Phys.*, 2020, **22**, 21947–21960

This journal is © the Owner Societies 2020

190

Supplementary Information

for

Impact of improvements in mesoporous titania layers
on ultrafast electron transfer dynamics
in perovskite and dye-sensitized solar cells

Katarzyna Pydzińska-Białek,[a] Adam Glinka,[a] Viktoriia Drushliak,[a]

Grzegorz Nowaczyk,[b] Patryk Florczak [b] and Marcin Ziółek [a] *

[a] Faculty of Physics, Adam Mickiewicz University,

Uniwersytetu Poznańskiego 2, 61-614 Poznań, Poland

[b] NanoBioMedical Centre, Adam Mickiewicz University,

Wszechnicy Piastowskiej 3, 61-614 Poznań, Poland
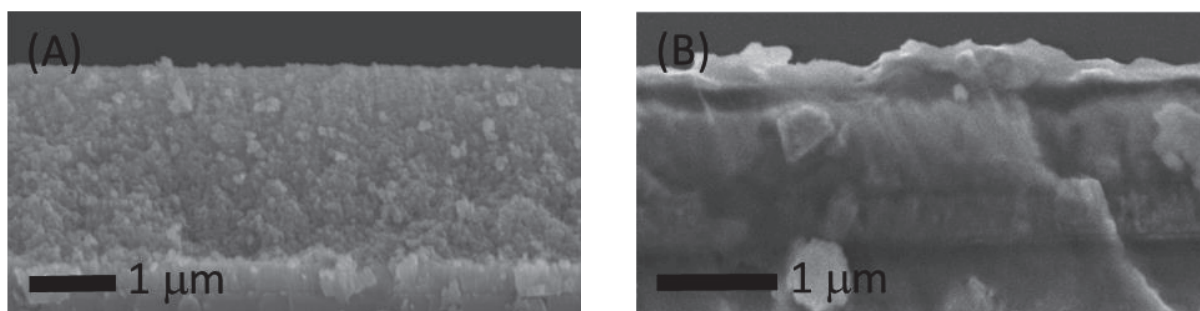
Figure S1. SEM cross sections of **SP30** titania layer (A) and PSC made using **SC18dil** layer (B).
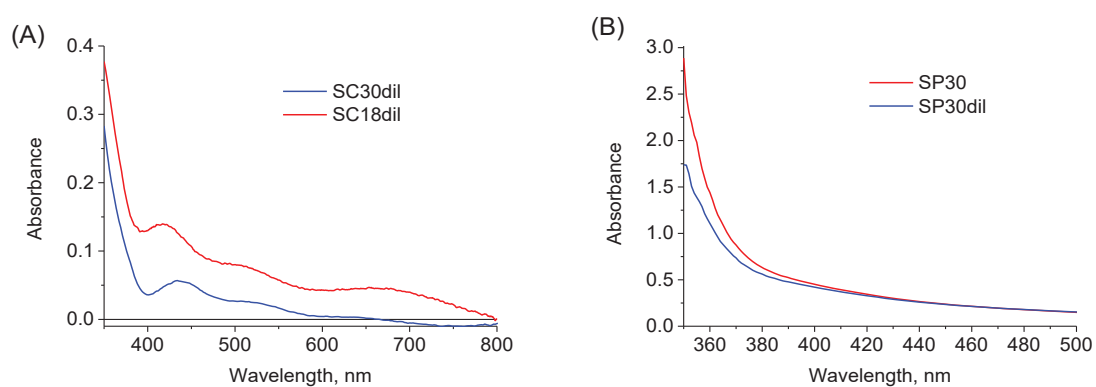
Figure S2. Stationary absorption of the electrodes with titania layers: **SC30dil** and **SC18dil** (A), **SP30dil** and **SP30** (B).
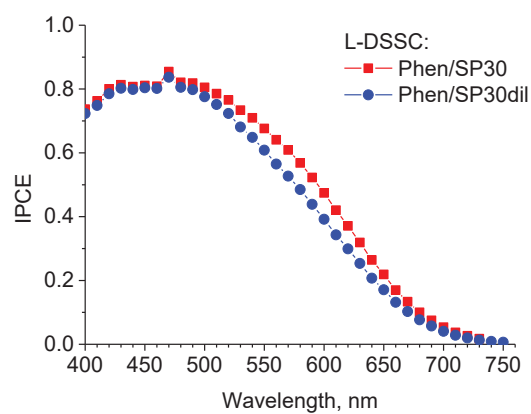
Figure S3. IPCE spectra of L-DSSC with **SP30dil** and **SP30** layers.
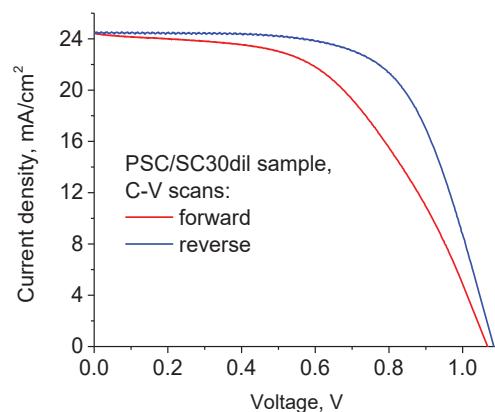
Figure S4. Example of current-voltage curves of PSC made using **SC30dil** layer measured at forward and backward directions (scanning rate 50mV/s). Hysteresis index *HI* obtained from the graph ($HI = \frac{J_{rev}\left(\frac{V_{oc}}{2}\right) - J_{for}\left(\frac{V_{oc}}{2}\right)}{J_{rev}\left(\frac{V_{oc}}{2}\right)}$) is equal to 0.05.
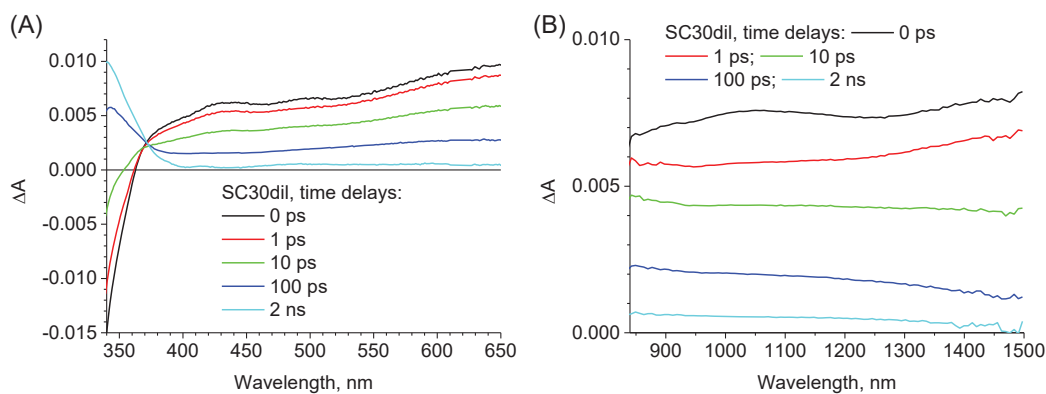
Figure S5. Transient absorption spectra at selected time delays between pump and probe pulses for electrode with SC30dil layer: in UV- VIS range excited at 310 nm with 4 mJ/cm² (A) and in NIR range excited at 355 nm with 4 mJ/cm² (B).

Mixed first and second order function:

The change of the population of the excited carriers (n) over time (t) in the semiconductor can be described by:

$$-\frac{dn}{dt} = k_1 n + k_2 n^2$$

The first order decay with the rate constant k_1 is related to the trap-assisted recombination (Shockley-Read-Hall recombination). The second order process described by the rate constant k_2 is due to free carrier recombination (band-to-band radiative recombination). Solution of the above equation can be given by the following analytical function, which is the mixed first and second order decay function:

$$n(t) = \frac{n_0 k_1}{k_1 \exp(k_1 t) + n_0 k_2 (\exp(k_1 t) - 1)},$$

where n_0 is initial number of excited carriers.
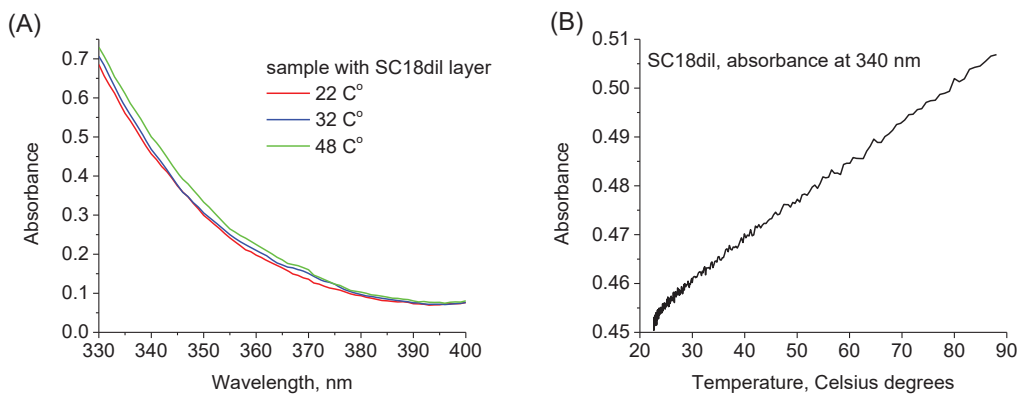
Figure S6. Temperature dependence of the stationary absorption of the electrodes with titania.
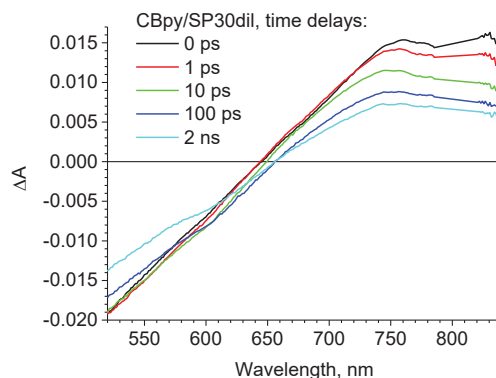
Figure S7. Transient absorption spectra at selected time delays between pump and probe pulses for **CBpy/SP30dil** liquid DSSC sample. The excitation wavelength was 500 nm with 100 μJ/cm^2 fluence.
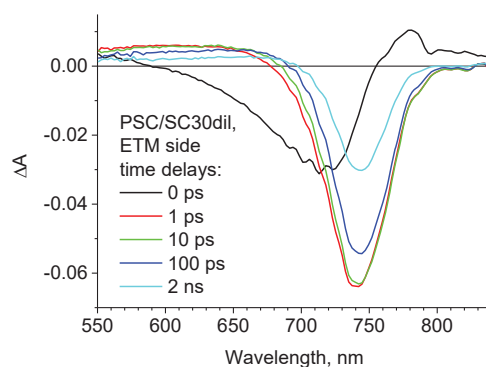
Figure S8. Transient absorption spectra at selected time delays between pump and probe pulses for **PSC/SC30dil** sample pumped from ETM side. The excitation wavelength was 500 nm with 30 μJ/cm^2 fluence.
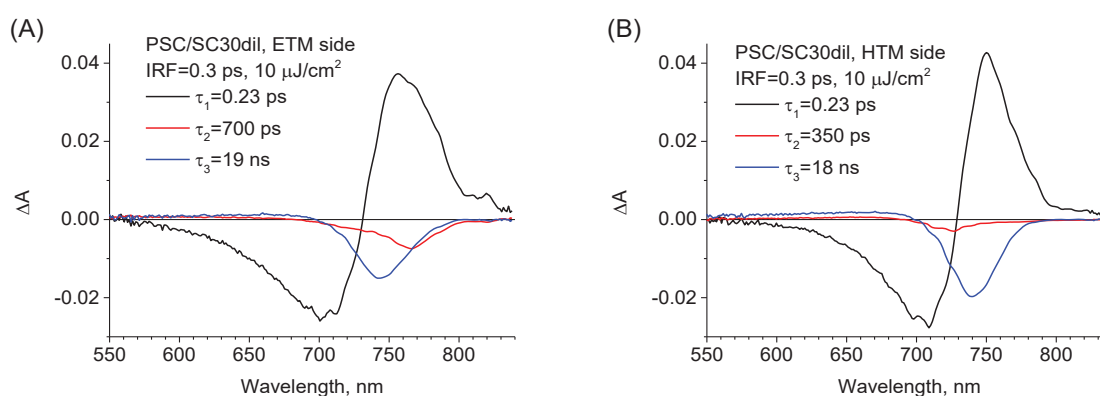
Figure S9. The results of global analysis of transient absorption data using three-exponential function for PSC samples. The graphs present pre-exponential factor spectra associated to the indicated time constants. The pump fluence was 10 μJ/cm^2 and IRF was 0.3 ps.
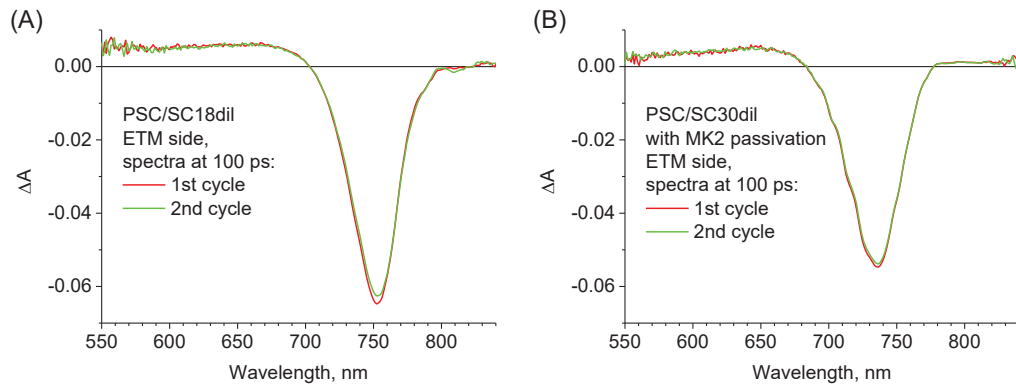
Figure S10. Transient absorption spectra for PSC with **SC18dil** layer (A) and with **SC30dil** layer passivated with MK2 dyes (B), both measured at 100 ps for different consecutive cycles at ETM side. The pump fluence was 30 μJ/cm².
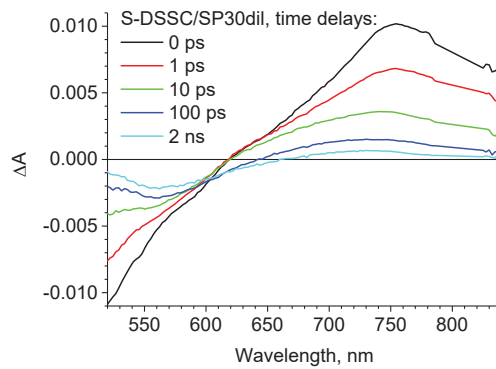
Figure S11. Transient absorption spectra at selected time delays between pump and probe pulses for S- DSSC cell with **SP30dil** layer pumped from HTM side.
The excitation wavelength was 500 nm at 100 μJ/cm² fluence.

Table S1. Parameters of the different mesoporous titania layers:

Abbre-viation	Deposition method	Particle size [nm]	Preparation	Resulted layer thickness [nm]
SC18dil	**S**pin-**C**oating	**18**	Dyenamo DN-GPS-18TS paste **dil**uted 1:6 in ethanol	300-350
SC30dil	**S**pin-**C**oating	**30**	GreatCell Solar 30NR-D paste **dil**uted 1:6 in ethanol	150-200
SP30	**S**creen-**P**rinting	**30**	Dyenamo DN-GPS-30TS paste without any dilution	2500-3000
SP30dil	**S**creen-**P**rinting	**30**	Dyenamo DN-GPS-30TS paste **dil**uted 2:1 in (cellulose + ethanol + alpha-terpineol)	1300-1500

Table S2. Averaged photovoltaic parameters and their errors (standard deviation) of the different cells:

Sample	V_{OC} [V]	J_{SC} [mA/cm^2]	FF	PCE [%]
L-DSSC/Phen/SP30	0.85 ± 0.01	7.79 ± 0.25	0.66 ± 0.03	4.32 ± 0.02
L-DSSC/Phen/SP30dil	0.88 ± 0.01	7.43 ± 0.10	0.69 ± 0.01	4.43 ± 0.02
PSC/SC30dil	1.08 ± 0.01	22.5 ± 2.1	0.63 ± 0.04	15.2 ± 2.3
S-DSSC/SC30dil	0.72 ± 0.01	0.95 ± 0.04	0.57 ± 0.01	0.39 ± 0.02
S-DSSC/SP30dil	0.45 ± 0.13	3.52 ± 0.32	0.35 ± 0.07	0.57 ± 0.23
S-DSSC/SP30	0.44 ± 0.03	2.67 ± 0.88	0.35 ± 0.03	0.41 ± 0.12

Table S3. Effects of spattered gold thickness and smaller or bigger active surface on the photovoltaic parameters of the cells:

Sample	Thickness [nm]	Surface [cm²]	V_{OC} [V]	J_{SC} [mA/cm²]	FF	PCE [%]	Total APCE
PSC/SC30dil	50-100	0.05	1.09	24.5	0.64	17.1	1.17
PSC/SC30dil	25-50	0.05	1.07	24.4	0.68	17.8	1.17
PSC/SC30dil	50-100	0.125	0.98	15.5	0.56	8.5	0.74
PSC/SC30dil	25-50	0.125	1.02	16.8	0.66	11.3	0.81
S-DSSC/SP30dil	50-100	0.05	0.32	3.83	0.28	0.34	0.59
S-DSSC/SP30dil	25-50	0.05	0.58	3.20	0.42	0.79	0.49

Effect of gold sputtering method

As reported, sputtering method may introduce additional series resistance between spiro-OMeTAD and Au or cause partial damage to the organic HTM, which results in lowering *FF* and, for very high resistance, even the photocurrent. To confirm this possibility we prepared the test PSCs with gold electrodes of larger surface (resulting in the active surface increase from 0.05 cm² to 0.125 cm²) and also we checked the effect of thinner gold layer (25-50 nm instead of 50-100 nm). As can be seen in Table S2, indeed the larger active surface decreases *FF*, while the shorter deposition increases *FF*.

Table S4. Average decrease of the amplitude for consecutive scans during transient absorption measurements of S-DSSC:

Sample and excitation side	Difference in the amplitude
SC30dil HTM side	-1%
SP30dil ETM side	+1.5%
SP30dil HTM side	-5%
SP30 ETM side	**-12.5%**
SP30 HTM side	-2.5%

KPB-7

Complete perovskite solar cells with gold electrodes studied in the visible and near-infrared range

K.Pydzińska-Białek, G.Nowaczyk, M.Ziółek

Complete Perovskite Solar Cells

with Gold Electrodes

Studied in the Visible and Near-infrared Range

Katarzyna Pydzińska-Białek [a] [*], Grzegorz Nowaczyk [b] and Marcin Ziółek [a][*]

[a] Faculty of Physics, Adam Mickiewicz University Poznań,

Uniwersytetu Poznańskiego 2, 61-614 Poznań, Poland

[b] NanoBioMedical Centre, Adam Mickiewicz University Poznań,

Wszechnicy Piastowskiej 3, 61-614 Poznań, Poland

[*] corresponding authors: katarzyna.pydzinska@amu.edu.pl (KP), marziol@amu.edy.pl (MZ)

Abstract

The complete solar cells with the triple cation perovskite ($FA_{0.76}MA_{0.19}Cs_{0.05}Pb(I_{0.81}Br_{0.19})_3$) sandwiched between spiro-OMeTAD (2,2',7,7'-tetrakis-(N,N-di-4methoxyphenylamino)-9,9'-spirobifluorene) and mesoporous titania layers were examined using femtosecond transient absorption (TA) and steady-state absorption in the visible (VIS) and near-infrared (NIR) regions. We demonstrate in this paper that the transmission spectroscopic measurements through a gold layer are possible and open the way to investigate the solar cells in working conditions (with applied voltage and/or additional illumination). We show that a gold electrode does not exhibit a significant TA signal itself but causes a difference in the perovskite response at around 800 nm and in the NIR range. The irradiation with a femtosecond laser, 1Sun stationary illumination or applied voltage, cause significant changes in the TA spectra and kinetics at the TiO_2 interface, most probably due to ion segregation or ion rearrangement process. Transmission signal in NIR is shown to be dominated by spectral modulation due to light interference, however, the process of hole injection at spiro-OMeTAD interfaces can be extracted. Finally, application of a proper forward bias enables the suppression of electron and hole injection to contact materials and results in increased lifetime of charge population in the perovskite.

Introduction

Understanding and further improvement of perovskite solar cells (PSC) operation have brought about the outstanding 25.5% efficiency record in 2021.[1] Triple cation perovskite ($FA_{0.76}MA_{0.19}Cs_{0.05}Pb(I_{0.81}Br_{0.19})_3$) is one of the most promising perovskite formulas showing better water resistance and less susceptibility to structural impurities than the originally used $MAPbI_3$.[2] One of the most important aspects in PSC development is optimization of charge transport within a cell. Several time-domain techniques are used to characterize charge carrier behavior, such as impedance spectroscopy,[3–5] terahertz spectroscopy,[6–9] time-resolved emission spectroscopy[6,10,11] as well as transient absorption[6,8,12–16] and reflectance.[17,18]

However, examination of a complete (with electron and hole transporting material) solar cell has been a subject of not many reports, excluding those concerning impedance spectroscopy, in which measurements for a complete cell are essential. Moreover, we cannot rely only on impedance spectroscopy in that matter because it describes processes taking place on the time scale from millisecond to a second, i.e. back charge transport from electron or hole transporting material.[3] To cover a shorter time scale, the employment of ultrafast and fast laser techniques is crucial. Popular examination of an incomplete solar cell gives some information about charge transport in a cell but it is still unclear how to correlate it with the operating conditions of the device. Without doubt, the time-resolved laser spectroscopy studies of a complete solar cell with gold electrodes are highly important, but experiments of this type have not been reported yet.

Transient absorption spectroscopy of PSCs is usually focused on the VIS region in which the main perovskite material signal appears. However, the near infrared range can deliver useful information about the cell operation due to the presence of the oxidized forms of the hole transporting material molecules (e.g. spiro-OMeTAD)[19–22] and charge carrier interband transitions.[23] Unfortunately, it has been also reported that the NIR spectra suffer from

interference signal caused by photo-induced refractive index changes in a perovskite material,[24,25] which can make it extremely hard to untangle the information required.

It is also important to keep in mind that the use of laser pulses in time resolved techniques implies a few problems with proper interpretation of their results. One of them is the fact that a laser pulse perturbation creates photoexcited charge distribution different from that in the operating solar cell conditions (under continuous 1Sun illumination and applied voltage). It is also hard to simply correlate the conditions of monochromatic, pulse laser illumination with a constant 1Sun bias. Another problem is ion segregation in the perovskite structure caused by laser illumination.[26] Fortunately, the investigated $FA_{0.76}MA_{0.19}Cs_{0.05}Pb(I_{0.81}Br_{0.19})_3$ triple cation perovskite is known as one of the compositions most resistant to ion segregation.[27]

In this study, we focused on the investigation of the complete cells covered with gold electrodes in order to describe charge transport in their working conditions, using the method of transmission spectroscopy. The idea of our study is presented in Scheme S1 (in the supporting information). This opens a possibility to design more advanced experiments providing new information on the PCS operation which would allow deeper understanding and further development of photovoltaic devices of this type. To the best of our knowledge, spectroscopic findings obtained from measurements through different thickness gold electrodes in the full PSC, especially using femtosecond transient absorption, are shown for the first time in this work. We compare the results obtained in the conditions when only femtosecond laser illumination is present to those collected with additional applied potential and 1Sun illumination during experiments. Among others, the experiments through gold electrodes allow the creation of conditions in which no charges are transported to the electrodes during the experiment thanks to the applied additional potential close to V_{oc}. We also made an attempt at untangling the information on the dynamics of oxidized spiro-OMeTAD from the signal recorded in the near IR region contaminated by interference pattern.

Materials & Methods

Perovskite solar cells preparation

Our target sample was a complete triple cation perovskite cell of the structure: FTO glass/compact TiO_2/mesoporous TiO_2/Perovskite/Spiro-OMeTAD/Gold. Different control samples were also made by exclusion of a particular layer or layers. Preparation protocol followed that published by Saliba et al..[28] Plates of the size 2.4 x 2.4 cm of FTO substrates (FTO glass, ≈13 Ω/sq, Sigma-Aldrich) were cut and a part of the FTO conductive layer was etched by Zn powder and HCl to prevent charge recombination between gold electrodes and FTO. The etched substrates were brushed with detergent (Hellmanex) and then bathed in detergent, distilled water and isopropanol in ultrasounds, each step lasting for 15 min. Finally, an UV ozone cleaner was used for 15 min. A compact TiO_2 layer was deposited by spray pyrolysis at 450 ˚C using titanium diisopropoxide in ethanol (1 mL + 14 mL EtOH) as a precursor solution. Mesoporous titania layer was obtained by deposition of titania paste (30NR-D, GreatCell Solar, diluted 1:6 w/w in EtOH) by spin coating (10 s, 2000 rpm) and annealing the substrate at 500 ˚C for 30 min. $FA_{0.76}MA_{0.19}Cs_{0.05}Pb(I_{0.81}Br_{0.19})_3$ precursor solutions were prepared in a glovebox conditions (in nitrogen flux) as described before.[29] 1.5 M precursor solution was spin-coated on a mesoporous layer in a drybox with additional argon flow for 10 s at 2000 rpm and then for 20 s at 4000 rpm; 10 s before the end of this process chlorobenzene as antisolvent was used. A solution of 2,2',7,7'-tetrakis-(N,N-di-4methoxyphenylamino)-9,9'-spirobifluorene (Spiro-OMeTAD, Sigma-Aldrich) (72.3 mg/mL in ChB) with additives (17.5 µL/mL of 520 mg/mL LiTFSI solution in acetonitrile and 28.8 µL/mL *4-tert*-buthylpyridine) was also spin coated (4000 rpm, 30 s). Gold electrodes were sputtered on the spiro-OMeTAD layer for 60 or 120 s, depending on the desired thickness.

Solar cells characterization

Steady-state absorption experiments were performed with an UV-VIS-NIR JASCO V-770 spectrophotometer. The UV-VIS region was investigated using an additional 150 mm integrating sphere (ILN-925). Transmission mode without the integrating sphere was used in the NIR region to obtain better noise-to-signal ratio (spectra presented in Figure 1A, S2). Current-Voltage characteristics were recorded by a potentiostat (model M101, Autolab) coupled to a photoelectric spectrometer, equipped with a solar simulator (Instytut Fotonowy, Poland). The simulator provides standard 1Sun illumination conditions using a Xe lamp and AM1.5G filter (calibrated by silicon solar cell 15151, ABET). Scanning electron microscopy (SEM) images were provided by Jeol 7001 TTLS field-emission scanning electron microscope with acceleration voltage varying from 5 to 15 kV. Femtosecond transient absorption spectroscopy studies were performed using 1 kHz repetition rate and 0.4 ps response function setup delivered by Ultrafast Systems (Spectra-Physics laser system and Helios spectrometer). Measurements were carried out in the UV-VIS (500-850 nm) or NIR (800-1600 nm) regions, with 475 nm or 495 nm excitation wavelengths chosen. Transient absorption data were analyzed by Surface Explorer (Ultrafast Systems) software. Additional bias during transient absorption measurement was applied to the electrodes by a compact potentiostat (model PGSTAT204, Autolab). 1Sun illumination was simulated by white LED by adjusting the short circuit current (J_{SC}) of the cell to a value similar to that measured using the solar simulator.

Results & Discussion

Basic characterization

As described in the experimental section, a complete solar cell consists of a compact TiO_2 ($cTiO_2$) layer deposited on the FTO glass, mesoporous TiO_2 ($mTiO_2$), triple cation perovskite (PVSK), spiro-OMeTAD and gold electrodes. Therefore, the complete cell is abbreviated as: $FTO/cTiO_2/mTiO_2/PVSK/spiro/Au$. Different reference samples were also prepared by exclusion of a particular layer or layers from the PCS structure during the fabrication process. We fabricated cells with three thicknesses of the gold electrode, varied from 30 to 100 nm, to obtain different semitransparent electrode layers. In transient absorption measurements, the complete cell samples called "without" gold were actually the samples with deposited gold electrodes but for which measurements were made at a site between the electrodes.

The open circuit voltage (V_{OC}) of our cells was 970 ± 20 mV and the short-circuit current density (J_{SC}) was 20 ± 3 mA/cm^2. The efficiency of complete solar cells reached $11 - 14$ %, limited mainly by poor fill factor (FF) caused by high resistance of the sputtered gold and a thinner than usual perovskite layer. The photovoltaic parameters of the best cell (PCE = 14 %) were $V_{OC} = 990$ mV, $J_{SC} = 23$ mA/cm^2 and FF = 0.61. For the cells prepared recently in our group in an analogous way but with a smaller area of sputtered gold electrodes and a slightly thicker perovskite layer, the best efficiencies reached 18 %.[29] What is important, the total absorbed photon to current efficiency (Total APCE= J_{SC} /e*N_{ph}, where N_{ph} is the number of absorbed photons calculated from the absorption spectra) for the cells is close to 100 % and the cells show relatively low hysteresis index equal to 0.024 ± 0.007 (averaged from 4 samples, see an exemplary curve in Figure S1). Therefore, the results obtained for them should be representative for a large class of triple cation perovskite solar cells with titania as the electron transporting layer.

Steady-state absorption spectra in the VIS and NIR ranges of selected cells and reference samples are shown in Figure 1A. ETM stands for the electron transporting material (TiO_2), while HTM – for the hole transporting material (spiro-OMeTAD). In the VIS range the quick rise in the triple cation perovskite absorption occurs in the range from 780 to 730 nm, corresponding to the direct bandgap in this material. In the NIR region the apparent spectral oscillations in the absorption signal occur due to the interference of light partially reflected from different layers of the samples.[24,25] Perovskite layer is clearly involved in the formation of these oscillations in the NIR range since they are absent in the reference samples with only FTO and titania layers (Fig. S2A). We will analyze them in more detail in the next section.

Perovskite film thickness can be estimated from the absorbance value at 700 nm as previously,[30,31] whose value was 0.62 ± 0.07 (the error is standard mean deviation from 13 samples). Cross-section images were taken by scanning electron microscopy (SEM), showing 340 ± 30 nm of the active layer thickness. So, both absorption and SEM data show that our cells exhibit around 10 % variation in thickness (from sample to sample). Figure 1B shows an exemplary SEM cross-section image. The thicknesses of all layers of the cell could be clearly distinguished and measured to be ~350 nm for FTO, ~60 nm for compact TiO_2, ~230 nm for mesoporous TiO_2, ~340 nm for pure triple cation perovskite, and ~170 nm for spiro-OMeTAD. Gold thickness depends on the sputtering parameters and was estimated as 30, 50 or 100 nm.

Most of the transient absorption experiments were conducted upon excitation at 475 or 495 nm with the energy density of 30 $\mu J/cm^2$. At such a density, the decay of excited carriers population depends on the excitation fluence because, apart from the first order recombination (due to trap states), at least the second order recombination (due to band-to-band recombination) plays an important role.[32] Therefore, it is important to compare the dynamics measured for the samples having similar signal amplitude after excitation, thus characterized by similar contributions of higher order recombination processes.

(A)

(B)

(C)
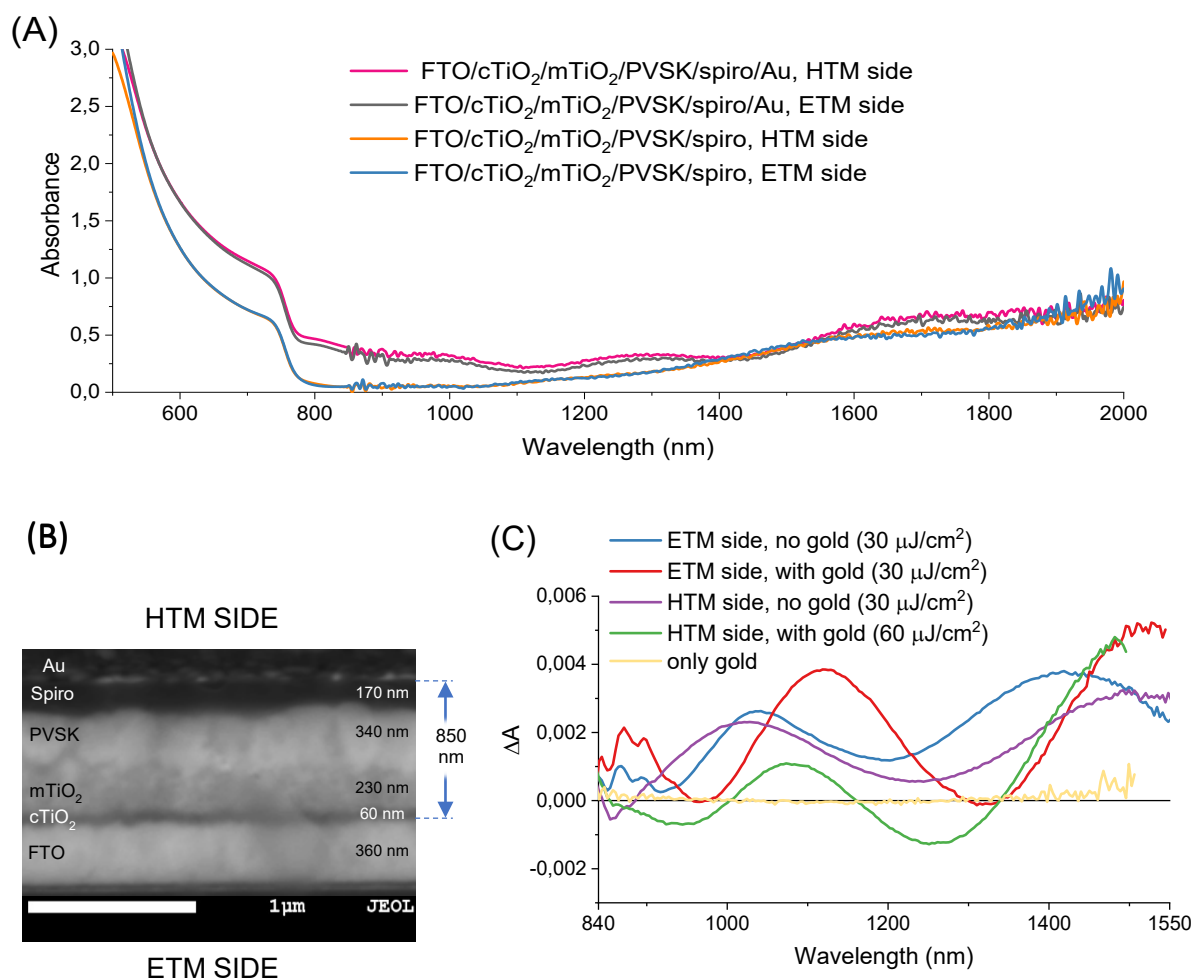
Figure 1 A – Steady-state absorption spectra of a complete solar cell, with and without gold, measured from the ETM or the HTM side. B – SEM cross-section image of an exemplary cell ~~with 100 nm gold layer~~ with averaged layer thickness labels. C – Transient absorption spectra at 1 ps pump-probe delay for different excitation sides (ETM or HTM), with and without gold, and for 50 nm gold layer deposited on FTO glass. Excitation wavelength was equal to 495 nm, energy density: 30 μJ/cm² for the ETM side and the HTM no gold, 60 μJ/cm² for HTM with gold.

The evolution of transient absorption spectra of the perovskite material from femtoseconds to nanoseconds exhibits two distinct stages (Figure S3). First, immediately after absorption, the cooling process dominates, when electrons and holes minimize their energy in the conduction and valence bands down to their edges, respectively. This process is characterized by a band-edge shift due to the charge screening or band-gap renormalization effect and is finished after single picoseconds.[33,34] When electrons and holes thermalize, a strong bleach signal at the edge of absorption spectrum appears due to the band filling mechanism. At that point, the second stage becomes dominant, because of the repopulation of the valence band due to the

recombination processes, as well as the injections of electrons or holes to the selective transporting materials (ETM or HTM), if present.[35] Both of them contribute to the signal vanishing in up to several nanoseconds.

Transient absorption signal in the NIR range is dominated by the interference pattern, similarly as in the steady-state absorption. The spectral oscillations decay on a time scale similar to that of the bleach in the visible range. The differences in NIR transient response after 1 ps pump-probe delay for complete solar cells are shown in Figure 1C. Spectral oscillations of the perovskite on a glass substrate observed in the TA experiment in the NIR region have been described by Pasanen et al.,[24] indicating the refractive index changes due to photogenerated free carriers as a source of the optoelectric change in the system causing the interference. The exact simulation of the effect is quite complex, however, in the SI we show a simplified approximation based on the interference of light reflected from two main interfaces (Figure S4 and accompanying text). Under such approximation, the qualitative agreement of the experiment finding with the calculated signal amplitude and spectral oscillation periods is maintained. The apparent layer thickness at different configurations, extracted from the oscillation periods, will be discussed in more details in the next sections.

Finally, it should be noted that due to a high absorption of the perovskite material at the pump excitation wavelength (475 or 495 nm), the pump pulse is absorbed close to the titania layer when illuminated from the ETM side and nearby the spiro-OMeTAD/perovskite interface when excited from the HTM side. This allows almost exclusive investigation of the excited carriers behavior (e.g. injection and recombination) at both perovskite interfaces in the cell (unless the photoexcited charges diffuse deeper inside the bulk perovskite on hundreds of ps time scale), as we have noted previously.[30] We will take advantage of this property in the next sections when studying the spectroscopic effect of gold electrode presence, irradiation and electric bias. In view of the above, some differences in transient absorption recorded from the ETM and HTM

sides can be expected. For example, the higher transient absorption from the ETM side than from the HTM side at early times (1 ps) in the NIR range, shown in Figure 1C, is probably due to a higher contribution of absorption of electrons in TiO_2 than that of oxidized spiro-OMeTAD (especially in the range below 1300 nm). It should be also mentioned that we observed some differences in the charge cooling process at the ETM and HTM sides, but their deeper analysis is beyond the scope of this work.

Effect of gold electrodes in spectroscopic studies

In spectroscopic studies when using transmitted light it is crucial to provide high enough intensity of the probing light signal passing through the cell to analyze the signal changes with a sufficient signal to noise ratio. Gold electrodes highly reduce the light intensity and probably that is why no time-resolved absorption experiments have been reported as yet for complete cells with gold electrodes. Before conducting the transient absorption experiment, we tested how much of ~~visible~~ light passes through gold electrodes of a certain thickness. We measured the steady-state absorption spectra of gold electrodes on the FTO glass as shown in Figure 2A-B. At 750 nm, at which the main transient absorption feature (bleach) appears, light intensity is in 43 % suppressed by a 30 nm gold layer. The gold layers of the thicknesses 50 and 100 nm block 55 % and 67 % of the light intensity, respectively. At the excitation wavelength of 475 nm the suppression is equal to 49, 58 and 76 % for gold layers of 30, 50 and 100 nm in thickness, respectively. The white light continuum (probe in femtosecond transient absorption) suffers from similar changes (shown in Figure S5). Figure 2B shows the light suppression by gold electrodes for two different light sources (continuous light in a steady-state spectrophotometer and the pulsed light in femtosecond transient absorption spectrometer) as well as two different substrate materials, as a function of gold thickness. Independently from light source and substrate material, similar light intensity suppression was observed. Therefore, the decrease in

the light intensity is significant (up to 80 %), but it still enables performing transient absorption experiments, at least near the bleach region with a strong signal which gives the most important information on the charge transfer dynamics. We also noticed that the gold layer structure changes from that of a smooth layer after deposition to that of separated gold islands over time. Table S1 shows the SEM images of fresh gold layers with different thickness (50 and 100 nm) deposited on the FTO glass substrate only and on a cell with spiro-OMeTAD as well as the images of the same samples after 80 days. The aggregation has been observed regardless of the presence or absence of spiro-OMeTAD. Separation distance of the gold islands after such time is about 100-140 nm, and the gold filling of the surface is less than 50%, so the conductivity of the layer is highly reduced and can be one of the factors reducing perovskite solar cells efficiency over time.

Gold layers exhibit non-zero steady-state absorption, almost constant and structureless from 750 to 900 nm (Figure 2A) that extends further into NIR. That's why the spectra of the samples with gold in Figures 1A and S2B are vertically shifted towards higher absorbance. We have not observed any effect of different gold layer thickness on the photovoltaic parameters of the cells. The differences in PCE between the samples of 30, 50 and 100 nm of gold layer are smaller than its relative error equal to 3-5 % (statistics based on almost 60 samples in total). The only effect on the performance of the device with a thinner gold layer is that it may be scratched more easily during the photovoltaic measurements and more separate islands are formed in the gold layer upon aging (Table S1), therefore, it is less durable.
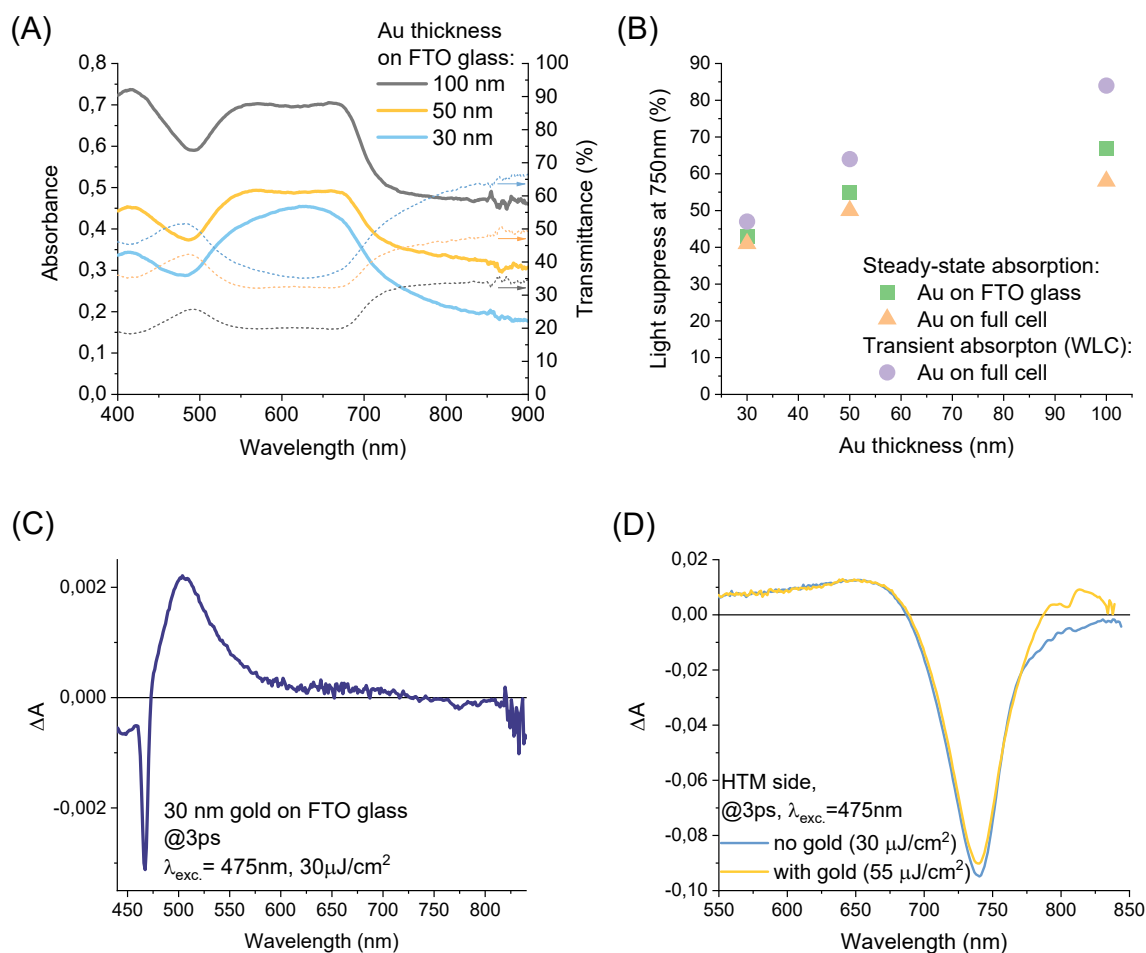
Figure 2 A – Steady-state absorbance (solid lines) and transmittance (dashed lines) spectra of 30, 50 and 100 nm gold layer on FTO glass with FTO glass as baseline. B – The light suppression at 750 nm by gold electrodes of different thicknesses depending on the used techniques and substrate materials. C,D – Transient absorption spectra after 3 ps pump-probe delay of 30 nm gold layer deposited on FTO glass, pump energy density: 30 μJ/cm², λ$_{exc.}$=475 nm (C) and full cell excited from HTM side with 30 nm (orange) and without (blue) gold layer for energy densities equal to 55 and 30 μJ/cm² respectively, λ$_{exc.}$=475 nm (D).

As for the excitation pulse (pump), its fluence has to be of course increased when the sample is examined from the HTM side through the gold, to obtain the same charge recombination dynamics as without gold. In our experiments, for the excitation wavelength of 475 nm, we had to apply about twice higher pump pulse energy density (30 vs 60 μJ/cm²) for the samples with 50 nm gold layer to obtain the same initial transient absorption signal as when the gold is absent. There is no need to increase the pump energy for the samples excited from the ETM side because the excitation pulse reaches the absorbing material (PVSK) without going through the gold (passing only FTO glass and TiO$_2$). We did not observe a significant transient absorption

signal from gold layer itself (i.e. for the reference samples FTO/Au and FTO/spiro/Au) in the spectral window in which the main perovskite features appear (600-810 nm, Figure 2C). Only a small positive signal (50 times smaller than the perovskite bleach amplitude) around 500 nm appeared and disappeared within several picoseconds. Its presence is due to an increase in the optical reflection near the threshold of the interband transition of gold, which corresponds to the minimum in its steady-state absorption (Figure 2A). Under a strong pump pulse this minimum is "bleached" and the optical reflection increases.[36,37]

Interestingly, although a gold film itself does not show significant transient absorption features, when deposited, it causes some differences in the perovskite sample signal. An additional positive absorption signal appeared around 770-840 nm only when the HTM side was excited. Figure 2D presents the bleach signal around 740 nm after 3 ps pump-probe delay for the sample examined through a gold film or without it. Differences in the transient absorption signal measured for these two systems are distinctive. Figure 3A-B presents the time evolution of the signal of complete PCSs in the presence (red) and absence (blue) of gold as well as only for gold on the FTO glass as a control measurement (green) at the minimum bleach (740 nm, Figure 3A) and at 810 nm (Figure 3B). The gold layer gives an insignificant absorption signal (500 times smaller at 740 nm and 30 times smaller at 810 nm than a complete cell) in both investigated regions. The kinetics of full PCS at the minimum bleach with and without gold do not exhibit significant differences. The small difference in the amplitude (Figures 2D and 3B) is due to not exactly accurate match of the pump pulse fluence with and without gold. In contrast to this kinetics, the absorption signal dynamics at 810 nm shows different characters. The cell without gold reveals firstly a positive absorption which drops within 1.5 ps (charge cooling process) to negative values (due to stimulated emission of perovskite), and then it decays on the time scale of tens and hundreds of picoseconds up to several nanoseconds. In contrast, the kinetics of the complete cell with gold exhibits a positive signal in the whole time range. The

fundamental differences in the range 770-840 nm (Figures 2D and 3B) can be due to a decreased contribution of negative stimulated emission signal when gold is present. A possible explanation is that the presence of gold suppress the stimulated emission from the perovskite due to the plasmonic effects or the gold layer may enhance the absorption coefficient of spiro-OMeTAD[38] or spiro-OMeTAD bound to additives $(TFSI)_2$[39]. However, a direct mechanism is not clear for us yet.
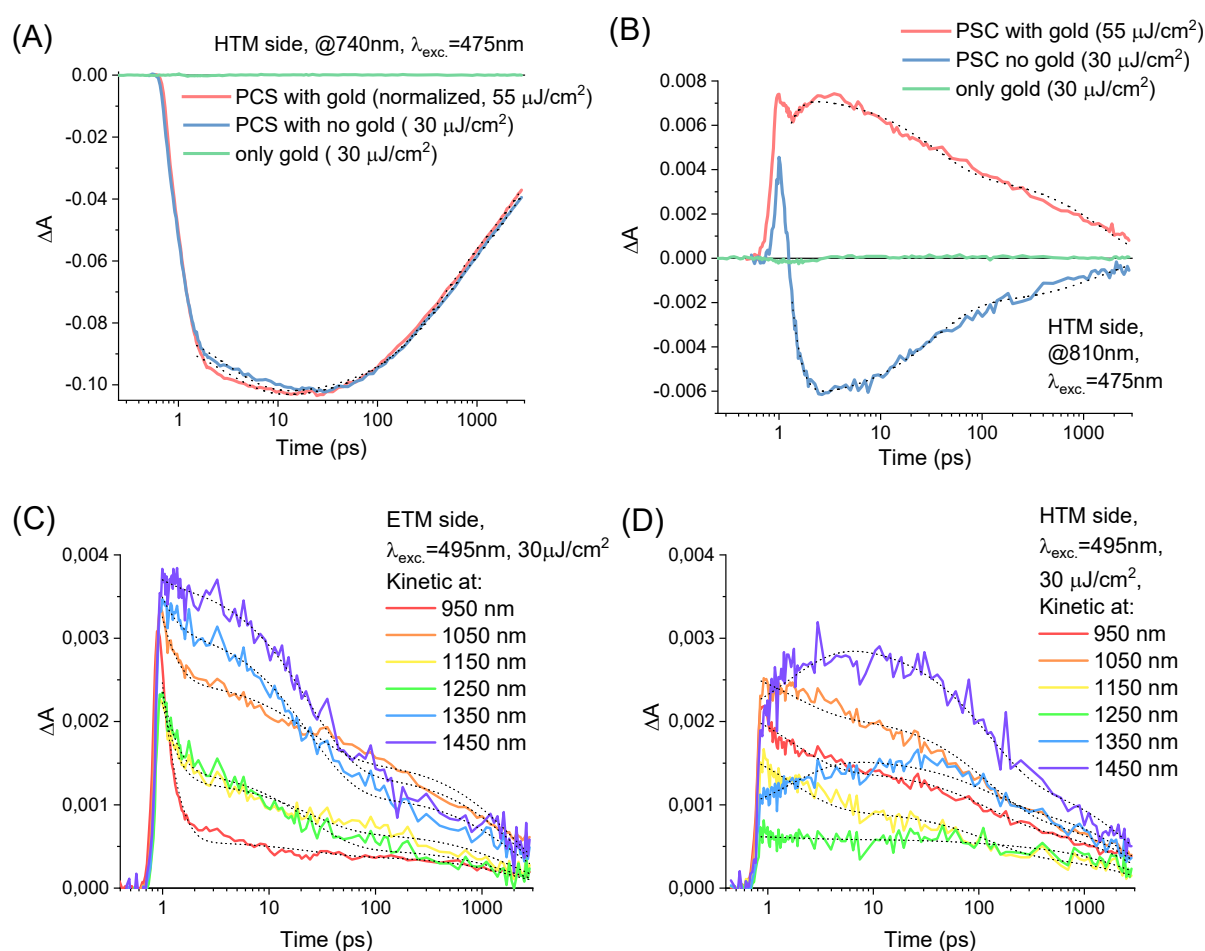
Figure 3 A,B – Transient absorption kinetics at 740 nm (A) and 810 nm (B) of a complete PSC examined through (red) and without (blue) 30 nm gold electrodes, excited from the HTM side as well as through a gold layer on the FTO glass (green). Excitation wavelength was chosen as 475 nm, energy density was equal to 30 for the PSC without electrode and the gold on FTO substrate and 55 μJ/cm² for the sample with gold. Time zero was shifted 1 ps to better show the kinetics in logarithmic scale. C,D – Kinetics at different wavelengths in NIR region of a full cell without gold, excited from the ETM (C) or the HTM (D) side. Excitation wavelength: 495 nm, energy density: 30 μJ/cm². Black dotted lines in all figures shows multi-exponential fit with the parameters given at the end of the supporting information.

The spectra in the NIR range are dominated by the light interference both in steady-state and in transient absorption experiments (as mentioned in the previous section, Figure 1A,C and S2). Under the approximation of a single "resonator", the following simple formula can be used to deduce the apparent thickness of such a resonator partially reflecting light at both ends:[40]

$$D = \frac{\lambda_1 \lambda_2}{4(\lambda_1 n_1 - \lambda_2 n_2)},$$ eq. (1)

Where λ_1 and λ_2 are wavelengths at the subsequent signal minimum and maximum, while n_1 and n_2 are refractive indexes of the resonator material corresponding to λ_1 and λ_2.

Table 1 Apparent thickness (D) of a resonating layer from the steady-state and the transient absorption spectra in the NIR region of different sample compositions. Apparent D was computed from eq (1) when λ_1 lie in 950-1100 nm range. Refractive index values were taken from Raoult et al. and extrapolated for whole analyzed range if needed.[41]

Technique	Sample composition	Apparent D [nm]	Error of D (mean std dev) [nm]
Steady-state	FTO/cTiO$_2$/mTiO$_2$/PVSK	760	10
	FTO/cTiO$_2$/mTiO$_2$/PVSK/Au	910	20
	FTO/cTiO$_2$/mTiO$_2$/PVSK/spiro/Au	1040	20
Transient	FTO/PVSK	500	70
	FTO/ cTiO$_2$/mTiO$_2$/PVSK	770	20
	FTO/ cTiO$_2$/mTiO$_2$/PVSK/spiro	960	60
	FTO/ cTiO$_2$/mTiO$_2$/PVSK/spiro/Au	1090	70

The calculated apparent thicknesses of different samples are collected in Table 1. Analysis of the refractive index changes at different interfaces of our cells (Table S2) indicates that the main change in the refractive index (and thus the highest reflections) for the samples without gold is at the cTiO$_2$/mTiO$_2$ interface on the one side, and at the interface with air on the other side (either PVSK/air or spiro/air). Comparison between the calculated apparent thicknesses and the real distances between the two most reflecting interfaces (from SEM studies) reveals that the former are about 40-50 % greater than the latter. A probable explanation might be that the refractive index values of the triple cation perovskite are actually slightly different than those

used in our calculations (there are not many literature data on this cell's composition) or that the additional resonators formed (due to smaller reflections at the other interfaces) complicate the spectral oscillations pattern. Despite this discrepancy, the same trends are observed from both experimental and calculation results. Most importantly, significant changes upon gold deposition can be observed in the oscillations (Figure 1C). A gold electrode addition causes an increase in the intensity of the interference pattern (reaching negative amplitudes in transient absorption), shift of the interference maxima/minima and also a decrease in the distance between them. The latter leads to an increase in the apparent thickness calculated from eq. (1), as confirmed in Table 1. The above changes can be, at least partly, explained by a great enhancement in the reflection when gold is added (spiro/Au interface in Table S2). It should be noted that gold itself does not introduce any additional transient absorption in NIR region (Figure 1C), but the changes are rather due to higher light reflection from the interfaces with gold, resulting in the higher amplitude of the spectral oscillations (interference pattern) and a modification of the period of these oscillations.

Transient absorption of the cells in the NIR range reveals interesting differences between the ETM and the HTM sides (Figure 3C-D). Although the signal is dominated by the interference pattern, additional rising feature can be observed in the spectrum of the sample excited from the HTM side. While for the excitation from the ETM side the transient absorption amplitude decays for all wavelengths (Figure 3C, the same behavior is observed for the cell with gold Figure S6A), for that from the HTM side, the amplitude rises (or at least remains unchanged) up to ~30 ps for wavelengths longer than 1200 nm (Figure 3D). We assign this effect to the appearance of an oxidized spiro-OMeTAD due to the hole injections from the perovskite. Indeed, the spectrum of the oxidized form of spiro-OMeTAD is reported to show a strong absorption band in the NIR range, with a maximum at ~1500 nm.[22] For the solar cell samples with gold, similar features can be noted when excited from the HTM side (Figure S6B),

however, their observation is more difficult because gold enhances the contribution of interference oscillations, including the negative transient absorption signals. Our findings shed more light on the proper interpretation of the transient signals in the NIR range, which so far have been attributed either exclusively to the HTM oxidation/ETM reduction[19,20] or exclusively to the interference artifact.[24,25,40]

Effect of irradiation in spectroscopic studies

To investigate changes in the perovskite layer properties upon light illumination, at first we performed steady-state absorption experiment: prior to 1 Sun irradiation, in 30 min and 60 min after it (Figure 4A). We also let the sample rest in the dark for the next 60 min and then tested it again. The illumination caused a redshift of the absorption edge, which could be assigned to ion segregation in the mixed ion perovskite material, as will be further supported by the transient absorption results. The observed redshift of 1-2 nm is not so pronounced as e.g. for $MAPbI_xBr_{3-x}$[26,42,43] but clearly visible. The longer the sample was kept under illumination, the greater the shift, which partially recovered when keeping the sample in the dark. The steady-state absorption changes upon irradiation and recovery in the dark are accompanied with a strong variation observed in the current-voltage measurements (Figure S7). Current drops to 30 % of the initial value after an hour of 1 Sun illumination and recovers up to 60 % of the initial when kept in the dark for another 60 min. Such a reversible spectroscopic and electric changes upon 1Sun illumination are characteristic of the ionic movement in PSCs.[27]
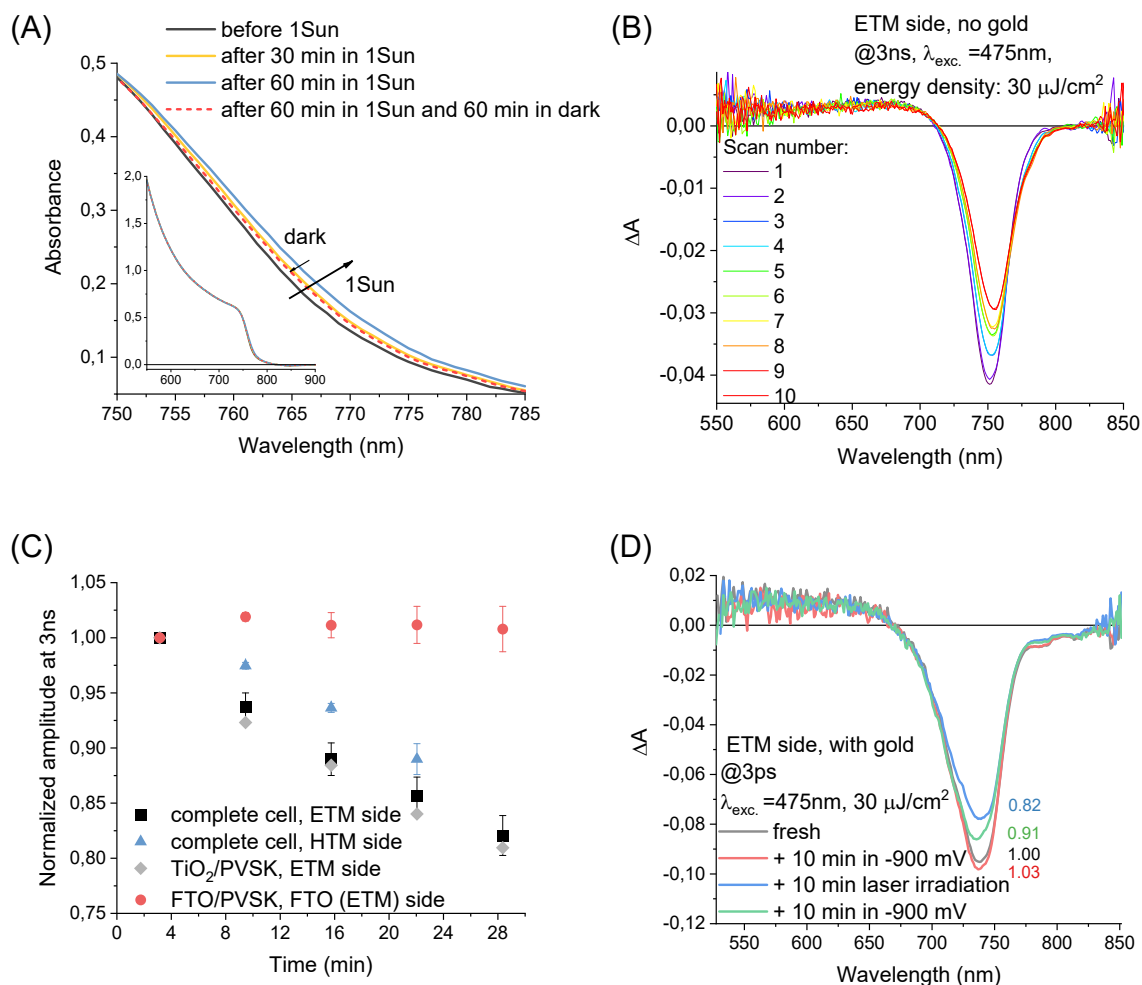
Figure 4 A – Steady-state absorbance spectra recorded before illumination (black), after 30 min (yellow), 60 min (blue) under 1Sun and 60 min in the dark after 60 min 1Sun bias (dashed, red). B – Transient absorption signal after 3 ns pump-probe delay for subsequent scans for a full cell without gold electrode, excited from ETM side by 475 nm, 30 µJ/cm² pump. C – Averaged normalized bleach amplitude at 3 ns (each subsequent scan pair) as a function of time (one scan pair duration was equal to 189 s., giving about 6 min. difference between points) for samples with and without gold (black squares), with FTO glass and perovskite layer only (red dots), with (blue triangles) and without HTM (green diamonds) measured from HTM side and sample composed of TiO₂ and perovskite on glass without FTO layer (grey triangles) D – Single shot transient absorption spectra after 3 ps pump-probe delay of a complete cell with 100 nm gold, excited from ETM side for different pretreatment. Measurements were made for an as-obtained cell (gray) then the sample was kept at -900 mV for 10 min (red), after that it was subjected to laser irradiation for 10 min (blue) and the cell was kept at -900 mV for 10 min again (green).

As we have noted previously, the results of TA experiment (lasting from a few to tens of minutes) could be also affected by slow changes (taking place in minutes) in the sample induced by illumination.[29] In order to describe in details in which way the laser illumination time modifies the signal of PCS, we performed femtosecond transient absorption experiments consisting of over a dozen scans upon excitation with the pump fluence of 30 µJ/cm². The

bidirectional scan mode was chosen, which means that in the odd scans the pump-probe delay was varied from fs to ns (increasing) and in the even scans – in the opposite direction (decreasing). In this way the photoinduced changes in the two consecutive scans (assuming the linear change in time) are compensated for. Because of that, we compared pairs of scans of ~3 min duration each.

Figure 4B shows the spectra at 3 ns pump-probe delay (the maximum of experiment time window) of a complete cell sample, measured form the ETM side with a characteristic bleach at around 750 nm for subsequent scans. It is clearly seen that the bleach is vanishing with the experiment time. The changes were much smaller when the sample was excited from the HTM side (Figure S8A). The decrease in the bleach amplitude was accompanied by its small red-shift and widening. We did not observe clear additional bands of "fully segregated" phases, like MAPbBr$_3$ band at ~530 nm (as observed by DuBose et al. for MAPbI$_{1.5}$Br$_{1.5}$[26]) or FAPbBr$_3$ at 545 nm.[44] It is due to the presence of FA$^+$ and Cs$^+$ ions which make the lattice more resistant to ion segregation.[27] Although the triple cation perovskites are known to show the strongest resistance against ion segregation from among other perovskite mixes,[27] the red-shift and widening could be caused by different rearrangement of the ions in the perovskite structure which results in a variety of band gaps. However, the conservation of the total bleach signal integral is not fulfilled. We can point to a few possible reasons, e.g. different (smaller) absorption coefficients of the rearranged perovskites than that of the original arrangement or the appearance of many perovskite mixes whose contributions are small and disappear in the noise. The widening of the bleach can be also caused by a red-shift of the stimulated emission band at the long-wavelength slope of the bleach.

Averaged normalized ΔA amplitudes at 3 ns as a function of the experiment time for a complete solar cell measured from ETM and HTM sides as well as for reference samples are shown in Figure 4C. The TA amplitude of a complete cell excited from the titania layer (black squares)

exhibits significant linear decrease in time. The initial signal at 2 ps delay behaves in the same way (Figure S8B): the amplitudes of both signals decrease by about 20 % after 35 min of irradiation during the experiment. The excitation from the HTM side (Figure 4C blue triangles) results in a smaller decrease in the signal. To further investigate this phenomenon, we tested the reference samples with some of the layers missing. One such sample was made on the unconducive glass without spiro-OMeTAD (TiO_2/PVSK, gray diamonds) and another one without a titania layer and spiro-OMeTAD (FTO/PVSK, red dots), both samples were excited from the ETM side (glass side). When TiO_2 is present, the signal's waning during the experiment looks similar as for the complete cell. In the absence of the titania layer, the bleach signal does not decrease at all. This is in line with the Dubose et al. findings for $MAPbI_{1.5}Br_{1.5}$ who claimed that only charge extraction by TiO_2 causes ion segregation.[26]

In the next step, the TA data were globally fitted by the multi-exponential decay function in the whole spectral window (550-850 nm). Exemplary fitting results – pre-exponential factor spectra of the fitted time constants – are presented in Figure S9 for subsequent scan pairs of reference samples. A clear decrease in the amplitude of all fitting components in subsequent scans can be observed for the perovskite deposited on the TiO_2 layer, while no decrease is observed for the sample without TiO_2. The obtained time constants (τ_i) are listed in Tables S3 and S4. The shortest time constant (τ_1, an order of hundreds of femtoseconds) describes the initial charge cooling and its values are unchanged for both samples. Longer time constants characterize charge recombination and charge injection dynamics and take values from single to teens of picosecond (τ_2), via tens of ps (τ_3) till single nanoseconds (τ_4). All time constants are unchanged when perovskite is deposited on the FTO glass only. However, the samples with TiO_2 layer show a shortening of these time constants. For more quantitative data, several complete solar cell samples excited from the ETM side (475 nm, 30 $\mu J/cm^2$) were investigated. The time constant shortenings (averaged from 5 experiments) for the

FTO/cTiO$_2$/mTiO$_2$/PVSK/spiro samples after 13 min of the experiment are equal to 0 ± 2 %, 17 ± 4 %, 9 ± 2 % and 4 ± 2 % for τ_1, τ_2, τ_3 and τ_4 respectively. It indicates that processes such as electron injection and/or charge recombination accelerate with irradiation time (ion rearrangement).

Next, we compared the effect of irradiation with femtosecond pulses to that of irradiation with continuous 1Sun illumination on TA results. We illuminated the complete cell with 1Sun source (LED) and collected spectra at 2 ps after excitation in a single shot experiment (to minimalize the sample exposure to laser pulses). The collected spectra are shown in Figure S10A and exhibit the same features as observed upon laser irradiation: amplitude decrease and redshift of the bleach, probably caused by ion movement and further the formation of some lower energy perovskite composition. Normalized minimal amplitudes at 2 ps for the illumination with 1Sun or laser are plotted in Figure S10B. The results show that femtosecond laser illumination at 475 nm, 30 $\mu J/cm^2$ during TA experiments leads to approximately the same decrease rate in the bleach signal as the continuous 1Sun illumination (it reduces the signal by about 15 % after 25 min).

Effect of additional bias

Successful realization of TA experiments of complete cells through gold layer makes it possible to observe charge transport and ion movement in the PCSs under the applied bias. We chose three different bias points: the forward -900 mV (close to V_{oc}), 0 V and the reverse +900 mV. Under the bias of -900 mV, the current is close to zero (when the system is illuminated) or flows in the opposite direction (from anode of TiO$_2$ to cathode with a spiro-OMeTAD layer) under no illumination. For the bias of 0 V, the current is maximized when the sample is illuminated

or equal to 0 A without illumination, while for the bias of +900 mV, the current is similar to that for 0 V and has the same direction.

We first examined the "stationary" (or long-term) effects of the applied voltage. Figure 4D depicts the TA spectra at 3 ps pump-pulse delay (excitation from ETM side) without any bias, after 10 min in the dark with -900 mV, after another 10 min of laser illumination without applied voltage and again for 10 min in the dark under -900 mV bias. The spectra were taken at single time delay point (single-shot) to avoid long-term changes described above. When -900 mV bias was applied in the dark (which means forward current direction – electron transport from ETM to HTM) an increase in the bleach by a few percent was noted (but with no changes to the bleach shape) in comparison to that of the fresh sample. As expected, the TA signal decreases (by about 20 %) as well as bleach widens, upon laser illumination (without additional bias). Then, the TA amplitude regenerates partially when the sample is kept again in the dark at the bias of -900 mV (to about 90 % of the initial amplitude). Therefore, a voltage bias in the forward direction can counteract the photoinduced ion rearrangement in the perovskite.
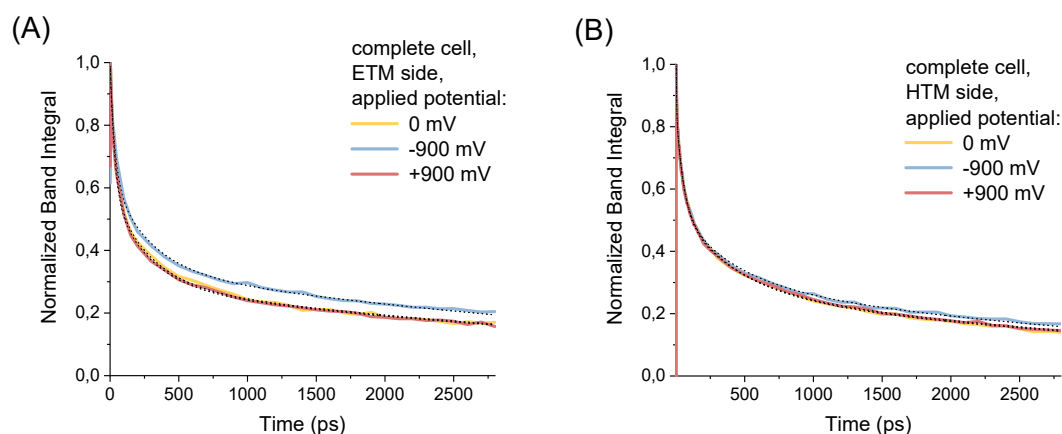
Figure 5 Normalized minimum band integral decay of a complete cell with gold, excited from ETM (A) or HTM (B) side for different applied potential. λexc.=475 nm, pump fluence: 30 μJ/cm², integration range: 660-800 nm. Black dotted line in all figures shows multi-exponential fit with the parameters given at the end of the supporting information.

The applied potential not only changes the TA spectra in a long time scale of ion migration, but it also affects the charge population dynamics after excitation in the ps-ns time scale. To properly investigate such dynamics we calculated the band integral (*BI*) over a broad spectral range, defined as:

$$BI(t, \Delta\lambda) = \int \Delta A(t, \lambda) \frac{d\lambda}{\lambda}. \tag{2}$$

As we have shown previously,[45] *BI* better describes charge population than kinetics at a single wavelength (e.g. at bleach minimum), especially for moderate and high pump fluence. Figure 5 presents decays of the *BI* signal (integration range: 660-800 nm) for different applied potentials during the TA experiment. For the excitation from the HTM side we applied experiment of normal duration, while for the excitation from ETM we used faster experiment to minimize photoinduced changes (total duration reduced to 140 seconds by decreasing the number of scans and time point, especially below 1 ps). At -900 mV bias with laser irradiation the injection of the charges to ETM and HTM is significantly reduced because the photocurrent is close to zero near V_{OC} (as shown in previous section, fluence 30 μJ/cm^2 provides similar conditions to 1Sun). Therefore, we are able to observe the charge dynamics in full cells when only recombination processes occur with minimized influence of charge injections. Indeed, reduction of charge carriers injection (applied bias of -900 mV, blue) causes an increase in the electron and hole lifetimes in both cases (Figure 5). *BI* signals for the other two potentials (+900 mV and 0 mV) show very similar characters of decay.

Table 2 Three-exponential global analysis results for a cell with different applied bias for excitations from ETM and HTM side. The shortest time constant for excitation from ETM side is fixed due to a small number of pump-probe delays up to 1 ps ("fast experiment"). The relative error of all time constants is 3-6%. Pre-exponential factor spectra corresponding to the time constants determined for excitation from ETM side are shown in Figure S11.

Excitation side	Applied bias [mV]	τ_1 [ps]	τ_2 [ps]	τ_3 [ns]
ETM	-900	0.5 (fixed)	87	3.6
ETM	0	0.5 (fixed)	77	3.0
ETM	+900	0.5 (fixed)	79	3.0
HTM	-900	0.54	42	2.3
HTM	0	0.54	39	1.9
HTM	+900	0.55	40	2.0

Further confirmation of longer lifetimes upon a bias close to V_{OC} is presented in Table 2 which lists 3-exponential global analysis results of the TA data for the same samples. Pre-exponential factor spectra of the fitting for each potential point are shown in Figure S11, and they exhibit no significant differences in the spectral shape for different potentials. In the experiment with excitation from the ETM side, the fastest time constant was kept fixed at value 0.5 ps due to reduced number of time points in the fast experiment. The longest time constants for excitation from the ETM and HTM sides were obtained for -900 mV (except for τ_1, which corresponded to charge cooling). Although we mostly see differences in nanosecond time scale, it is still hard to determine the injection rate because even a picosecond injection process can affect charge population decay in nanosecond time scale due to the charge diffusion in the perovskite.[18] Determination of exact intrinsic charge injection dynamics requires the fits to numerical solutions of the differential charge population equations, which is beyond the scope of this work. However, a significant methodological importance of our findings should be emphasized: in principle the transient absorption measurements under different applied voltage for complete cells with metal (gold) electrodes enable separation of the electron and hole injection dynamics from the electron and hole recombination processes.

Coming back to the long–term changes, the band integral analysis reveals also that we are able to minimize the photoinduced ion rearrangement changes by applying a potential at which the

charge carrier injection is significantly decreased. We performed the "normal" (long) TA experiment with -900 mV bias and excitation from the ETM side and, unlike the other experiments with excitation from the ETM side, we did not see a significant signal decrease (either in bleach minimum or in *BI* amplitude, Figure S12). It confirms that the ion migration/rearrangement requires not only the presence of TiO_2 layers but it needs non-open circuit conditions in which current flows and electron injection process takes place.

Summary

In this paper we examined the complete solar cells with deposited gold electrodes and mixed halide triple cation perovskite ($FA_{0.76}MA_{0.19}Cs_{0.05}Pb(I_{0.81}Br_{0.19})_3$) sandwiched between spiro-OMeTAD and titania layers. First of all, we revealed that the characterization of such samples using transmission absorption spectroscopy in the visible and near infrared ranges is possible. With the gold layer of 100 nm (the thickest of those used in our studies) the light suppression is up to 80 %, which lowers the signal to noise ratio but is still high enough to get all the information regarding the spectral features and charge dynamics in a reasonable measurement time. The gold electrode does not modify significantly the spectral and temporal features in transient absorption, in particular the main bleach dynamics is exactly the same as for the reference samples without gold, provided that the pump pulse fluence is increased accordingly to ensure the same amplitude of the transient absorption signal. The only effects of gold presence are the appearance of an additional positive signal in the range 770-840 nm and modification of the interference pattern in the range 900-1600 nm due to light resonance at thin cell layers (increased amplitude and decreased period of the spectral oscillations). Despite the dominant role of the interference signal in the near-infrared range, we were able to observe the signal of oxidized spiro-OMeTAD formed upon hole injection from the perovskite and extract its dynamics.

The main advantage of using the full cells with gold electrodes as the samples is the possibility of absorption measurements with the additional bias applied. To the best of our knowledge, the processes on nanosecond and picosecond time scale in fully operating and biased perovskite solar cells have not been investigated as yet. As an example, we have compared the charge population dynamics in the short circuit conditions (bias 0 mV) and when the current flow in the cell is minimized under forward bias close to V_{OC} (-900 mV in our case) and irradiation close to 1Sun (excitation at 475 nm with 30 $\mu J/cm^2$ in our case). In the latter case the perovskite charge population lifetimes (on picosecond and nanosecond time scale) were increased by 10-20 % due to the lack of electron and hole injection to the contact materials.

Moreover, application of forward bias enabled us to suppress the unwanted photoinduced degradation of the cells. Without the bias we observed significant changes in the bleach signal during the transient absorption experiment: a decrease in its amplitude to 20 % in 30 minutes (using pump pulses of 30 $\mu J/cm^2$) and a small bathochromic shift. The charge population lifetimes were also changed (about 10 % decrease after 15 minutes of experiment). We assigned such photoinduced changes to ion rearrangement that can still occur despite relative stability of triple cation perovskite, and we confirmed that they are strictly related to the presence of mesoporous TiO_2 layer. The photoinduced changes are partially reversible and can be minimized by applying a forward bias and/or excitation from the spiro-OMeTAD side.

We believe that our studies will increase the understanding of perovskite solar cells operation and will pave the way to a new class of spectroscopic measurements of full cells at different operating conditions, especially, to investigation of short and ultrashort processes (from femtoseconds to nanoseconds) under applied bias voltage.

Acknowledgments

Supporting Information

Scheme S1 (the main idea of the study); Figures S1−S12 (additional steady-state and transient absorption data); Tables S1-S4 (SEM images of upper gold layer, reflectivity of different interfaces and the time constants from 4-exponential global analysis); simplified calculations of spectral oscillations in NIR range and parameters fitted to the kinetics. The Supporting Information is available free of charge at ….

References

(1) National Renewable Energy Laboratory. Best Research Cell Efficiencies Chart. https://www.nrel.gov/pv/cell-efficiency.html (accessed 2022-05-15)

(2) Dong, C.; Wang, Z. K.; Liao, L. S. Progress of Triple Cation Organometal Halide Perovskite Solar Cells. *Energy Technol.* **2020**, *8* (4), 1–14.

(3) Bou, A.; Pockett, A.; Raptis, D.; Watson, T.; Carnie, M. J.; Bisquert, J. Beyond Impedance Spectroscopy of Perovskite Solar Cells: Insights from the Spectral Correlation of the Electrooptical Frequency Techniques. *J. Phys. Chem. Lett.* **2020**, *11* (20), 8654–8659.

(4) Riquelme, A.; Gálvez, F. E.; Contreras-Bernal, L.; Míguez, H.; Anta, J. A. Internal Quantum Efficiency and Time Signals from Intensity-Modulated Photocurrent Spectra of Perovskite Solar Cells. *J. Appl. Phys.* **2020**, *128* (13), 133103.

(5) Liu, D.; Wang, Q.; Traverse, C. J.; Yang, C.; Young, M.; Kuttipillai, P. S.; Lunt, S. Y.; Hamann, T. W.; Lunt, R. R. Impact of Ultrathin C60 on Perovskite Photovoltaic Devices. *ACS Nano* **2018**, *12* (1), 876–883.

(6)   Hutter, E. M.; Kirchartz, T.; Ehrler, B.; Cahen, D.; Von Hauff, E. Pitfalls and Prospects of Optical Spectroscopy to Characterize Perovskite-Transport Layer Interfaces. *Appl. Phys. Lett.* **2020**, *116* (10), 100501.

(7)   Ulatowski, A. M.; Farrar, M. D.; Snaith, H. J.; Johnston, M. B.; Herz, L. M. Revealing Ultrafast Charge-Carrier Thermalization in Tin-Iodide Perovskites through Novel Pump-Push-Probe Terahertz Spectroscopy. *ACS Photonics* **2021**, *8* (8), 2509–2518.

(8)   Li, C.; Wang, A.; Deng, X.; Wang, S.; Yuan, Y.; Ding, L.; Hao, F. Insights into Ultrafast Carrier Dynamics in Perovskite Thin Films and Solar Cells. *ACS Photonics* **2020**, *7* (8), 1893–1907.

(9)   Ponseca, C. S.; Hutter, E. M.; Piatkowski, P.; Cohen, B.; Pascher, T.; Douhal, A.; Yartsev, A.; Sundstrom, V.; Savenije, T. J. Mechanism of Charge Transfer and Recombination Dynamics in Organo Metal Halide Perovskites and Organic Electrodes, PCBM, and Spiro-OMeTAD: Role of Dark Carriers. *J. Am. Chem. Soc.* **2015**, *137* (51), 16043–16048.

(10)   Kirchartz, T.; Márquez, J. A.; Stolterfoht, M.; Unold, T. Photoluminescence-Based Characterization of Halide Perovskites for Photovoltaics. *Adv. Energy Mater.* **2020**, *10* (26), 1904134–190455.

(11)   Kumar Ravi, V.; Scheidt, R. A.; Nag, A.; Kuno, M.; Kamat, P. V. To Exchange or Not to Exchange. Suppressing Anion Exchange in Cesium Lead Halide Perovskites with PbSO4 − Oleate Capping. *ACS Energy Lett.* **2018**, *3*, 1049–1055.

(12)   Hopper, T. R.; Gorodetsky, A.; Frost, J. M.; Müller, C.; Lovrincic, R.; Bakulin, A. A. Ultrafast Intraband Spectroscopy of Hot-Carrier Cooling in Lead-Halide Perovskites. *ACS Energy Lett.* **2018**, *3* (9), 2199–2205.

(13)   Chen, X.; Lu, H.; Yang, Y.; Beard, M. C. Excitonic Effects in Methylammonium Lead Halide Perovskites. *J. Phys. Chem. Lett.* **2018**, *9* (10), 2595–2603.

(14)   Piatkowski, P.; Cohen, B.; Javier Ramos, F.; Di Nunzio, M.; Nazeeruddin, M. K.; Grätzel, M.; Ahmad, S.; Douhal, A. Direct Monitoring of Ultrafast Electron and Hole Dynamics in Perovskite Solar Cells. *Phys. Chem. Chem. Phys.* **2015**, *17* (22), 14674–14684.

(15)   Shen, Q.; Ripolles, T. S.; Even, J.; Ogomi, Y.; Nishinaka, K.; Izuishi, T.; Nakazawa, N.; Shen, Q.; Ripolles, T. S.; Even, J.; et al. Slow Hot Carrier Cooling in Cesium Lead Iodide Perovskites Slow Hot Carrier Cooling in Cesium Lead Iodide Perovskites. *Appl. Phys. Lett.* **2017**, No. 111, 153903.

(16)   Wu, J.; Li, X.; Lian, X.; Su, B.; Pang, J.; Li, M. De; Xia, Z.; Zhang, J. Z.; Luo, B.; Huang, X. C. Ultrafast Study of Exciton Transfer in Sb(III)-Doped Two-Dimensional

[NH3(CH2)4NH3]CdBr4Perovskite. *ACS Nano* **2021**, *15* (9), 15354–15361.

(17)   Yang, Y.; Yang, M.; Moore, D. T.; Yan, Y.; Miller, E. M.; Zhu, K.; Beard, M. C. Top and Bottom Surfaces Limit Carrier Lifetime in Lead Iodide Perovskite Films. *Nat. Energy* **2017**, *2* (2), 1–7.

(18)   Zhou, M.; Sarmiento, J. S.; Fei, C.; Wang, H. Charge Transfer and Diffusion at the Perovskite/PCBM Interface Probed by Transient Absorption and Reflection. *J. Phys. Chem. C* **2019**, *123* (36), 22095–22103.

(19)   Kulshreshtha, C.; Clement, A.; Pascher, T.; Sundström, V.; Matyba, P. Investigating Ultrafast Carrier Dynamics in Perovskite Solar Cells with an Extended π-Conjugated Polymeric Diketopyrrolopyrrole Layer for Hole Transportation. *RSC Adv.* **2020**, *10* (11), 6618–6624.

(20)   Grancini, G.; Viola, D.; Lee, Y.; Saliba, M.; Paek, S.; Cho, K. T.; Orlandi, S.; Cavazzini, M.; Fungo, F.; Hossain, M. I.; et al. Femtosecond Charge-Injection Dynamics at Hybrid Perovskite Interfaces. *ChemPhysChem* **2017**, *18* (17), 2381–2389.

(21)   Klein, J. R.; Scholz, M.; Oum, K.; Lenzer, T. Quantifying Ultrafast Charge Carrier Injection from Methylammonium Lead Iodide into the Hole-Transport Material H101 and Mesoporous TiO2 Using Vis-NIR Transient Absorption. *Phys. Chem. Chem. Phys.* **2017**, *19* (27), 17952–17959.

(22)   Bouduban, M. E. F.; Burgos-Caminal, A.; Ossola, R.; Teuscher, J.; Moser, J. E. Energy and Charge Transfer Cascade in Methylammonium Lead Bromide Perovskite Nanoparticle Aggregates. *Chem. Sci.* **2017**, *8* (6), 4371–4380.

(23)   Pollock, T. P.; Schlenker, C. W. Electromodulation and Transient Absorption Spectroscopy Suggest Conduction Band Electron Lifetime, Electron Trapping Parameters, and CH3NH3PbI3 Solar Cell Fill Factor Are Correlated. *J. Phys. Chem. C* **2019**, *123* (30), 18160–18170.

(24)   Pasanen, H. P.; Vivo, P.; Canil, L.; Hempel, H.; Unold, T.; Abate, A.; Tkachenko, N. V. Monitoring Charge Carrier Diffusion across a Perovskite Film with Transient Absorption Spectroscopy. *J. Phys. Chem. Lett.* **2020**, *11* (2), 445–450.

(25)   Pasanen, H. P.; Vivo, P.; Canil, L.; Abate, A.; Tkachenko, N. Refractive Index Change Dominates the Transient Absorption Response of Metal Halide Perovskite Thin Films in the near Infrared. *Phys. Chem. Chem. Phys.* **2019**, *21* (27), 14663–14670.

(26)   Dubose, J. T.; Kamat, P. V. TiO2-Assisted Halide Ion Segregation in Mixed Halide Perovskite Films. *J. Am. Chem. Soc.* **2020**, *142* (11), 5362–5370.

(27)   Knight, A. J.; Herz, L. M. Preventing Phase Segregation in Mixed-Halide Perovskites: A

Perspective. *Energy Environ. Sci.* **2020**, *13* (7), 2024–2046.

(28)   Saliba, M.; Wol, C. M.; Stolterfoht, M.; Phung, N.; Albrecht, S.; Neher, D.; Abate, A. How to Make over 20% E Ffi Cient Perovskite Solar Cells in Regular (n − i − p) and Inverted (p − i − n) Architectures. *Chem. Mater.* **2018**, *30*, 4193–4201.

(29)   Pydzińska-Białek, K.; Glinka, A.; Drushliak, V.; Nowaczyk, G.; Florczak, P.; Ziółek, M. Impact of Improvements in Mesoporous Titania Layers on Ultrafast Electron Transfer Dynamics in Perovskite and Dye-Sensitized Solar Cells. *Phys. Chem. Chem. Phys.* **2020**, *22* (38), 21947–21960.

(30)   Pydzińska-Białek, K.; Drushliak, V.; Coy, E.; Załęski, K.; Flach, J.; Idígoras, J.; Contreras-Bernal, L.; Hagfeldt, A.; Anta, J. A.; Ziółek, M. Understanding the Interfaces between Triple-Cation Perovskite and Electron or Hole Transporting Material. *ACS Appl. Mater. Interfaces* **2020**, *12* (27), 30399–30410.

(31)   Quere, B.; Pydzińska-Białek, K.; Karolczak, J.; Nowaczyk, G.; Coy, E.; Ziółek, M. Understanding the Effect of Different Synthesis Conditions on the Physicochemical Properties of Mixed-Ion Perovskite Solar Cells. *Chem. - A Eur. J.* **2019**, *25* (23), 5978–5986.

(32)   Li, X.; Bi, D.; Yi, C.; Décoppet, J.-D.; Luo, J.; Zakeeruddin, S. M.; Hagfeldt, A.; Grätzel, M. A Vacuum Flash-Assisted Solution Process for High-Efficiency Large-Area Perovskite Solar Cells. *Science.* **2016**, *353* (6294), 58–62.

(33)   Deschler, F.; Price, M.; Pathak, S.; Klintberg, L. E.; Jarausch, D. D.; Higler, R.; Hüttner, S.; Leijtens, T.; Stranks, S. D.; Snaith, H. J.; et al. High Photoluminescence Efficiency and Optically Pumped Lasing in Solution-Processed Mixed Halide Perovskite Semiconductors. *J. Phys. Chem. Lett.* **2014**, *5* (8), 1421–1426.

(34)   Trinh, M. T.; Wu, X.; Niesner, D.; Zhu, X. Y. Many-Body Interactions in Photo-Excited Lead Iodide Perovskite. *J. Mater. Chem. A* **2015**, *3* (17), 9285–9290.

(35)   Herz, L. M. Charge-Carrier Mobilities in Metal Halide Perovskites: Fundamental Mechanisms and Limits. *ACS Energy Lett.* **2017**, *2* (7), 1539–1548.

(36)   Cun, P.; Wang, M.; Huang, C.; Huang, P.; He, X.; Wei, Z.; Zhang, X. Conductive Connection Induced Speed-up of Localized-Surface-Plasmon Dynamics. *J. Opt.* **2018**, *20*, 014011.

(37)   Zhang, X.; Huang, C.; Wang, M.; Huang, P.; He, X.; Wei, Z. Transient Localized Surface Plasmon Induced by Femtosecond Interband Excitation in Gold Nanoparticles. *Sci. Rep.* **2018**, *8* (1), 1–7.

(38)   Grisorio, R.; Iacobellis, R.; Listorti, A.; De Marco, L.; Cipolla, M. P.; Manca, M.; Rizzo, A.;

Abate, A.; Gigli, G.; Suranna, G. P. Rational Design of Molecular Hole-Transporting Materials for Perovskite Solar Cells: Direct versus Inverted Device Configurations. *ACS Appl. Mater. Interfaces* **2017**, *9* (29), 24778–24787.

(39) Nguyen, W. H.; Bailie, C. D.; Unger, E. L.; McGehee, M. D. Enhancing the Hole-Conductivity of Spiro-OMeTAD without Oxygen or Lithium Salts by Using Spiro(TFSI)2 in Perovskite and Dye-Sensitized Solar Cells. *J. Am. Chem. Soc.* **2014**, *136* (31), 10996–11001.

(40) Zhyrair, G.; Lenrik, M.; Karapet, A.; Valeri, H. Determination of the Complete Set of Optical Parameters of Micron-Sized Polycrystalline CH 3 NH 3 PbI 3 − x Cl x Films from the Oscillating Transmittance and Reflectance Spectra Determination of the Complete Set of Optical Parameters of Micron- Sized Poly. *Mater. Res. Express* **2020**, *7*, 01408.

(41) Raoult, E.; Bodeux, R.; Jutteau, S.; Rives, S.; Yaiche, A.; Coutancier, D.; Rousset, J.; Collin, S. Optical Characterizations and Moddeling of Semitransparent Perovskite Solar Cells for Tandem Applications. In *36th European Photovoltaic Solar Energy Conference and Exhibition, Marseille, France*; 2019; Vol. 36, pp 757–763.

(42) Knight, A. J.; Borchert, J.; Oliver, R. D. J.; Patel, J. B.; Radaelli, P. G.; Snaith, H. J.; Johnston, M. B.; Herz, L. M. Halide Segregation in Mixed-Halide Perovskites: Influence of A-Site Cations. *ACS Energy Lett.* **2021**, *6* (2), 799–808.

(43) Brennan, M. C.; Draguta, S.; Kamat, P. V.; Kuno, M. Light-Induced Anion Phase Segregation in Mixed Halide Perovskites. *ACS Energy Lett.* **2018**, *3* (1), 204–213.

(44) Jana, A.; Mittal, M.; Singla, A.; Sapra, S. Solvent-Free, Mechanochemical Syntheses of Bulk Trihalide Perovskites and Their Nanoparticles. *Chem. Commun.* **2017**, *53* (21), 3046–3049.

(45) Pydzińska-Białek, K.; Szeremeta, J.; Wojciechowski, K.; Ziółek, M. Insights into the Femtosecond to Nanosecond Charge Carrier Kinetics in Perovskite Materials for Solar Cells. *J. Phys. Chem. C* **2019**, *123* (1), 110–119.

TOC:
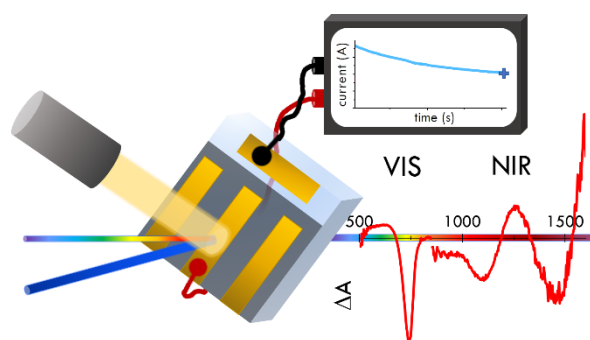
Supporting information

for

Complete Perovskite Solar Cells

with Gold Electrodes

Studied in the Visible and Near-infrared Range

Katarzyna Pydzińska-Białek [a] *, Grzegorz Nowaczyk [b] and Marcin Ziółek [a]*

[a] Faculty of Physics, Adam Mickiewicz University Poznań,

Uniwersytetu Poznańskiego 2, 61-614 Poznań, Poland

[b] NanoBioMedical Centre, Adam Mickiewicz University Poznań,

Wszechnicy Piastowskiej 3, 61-614 Poznań, Poland

(A)

(B)
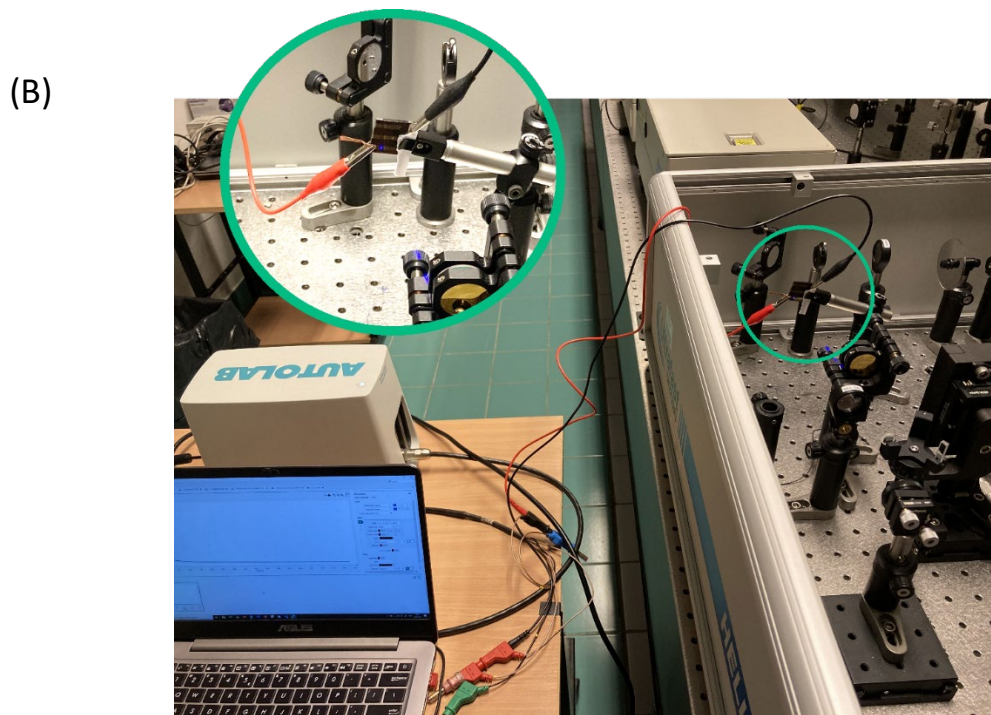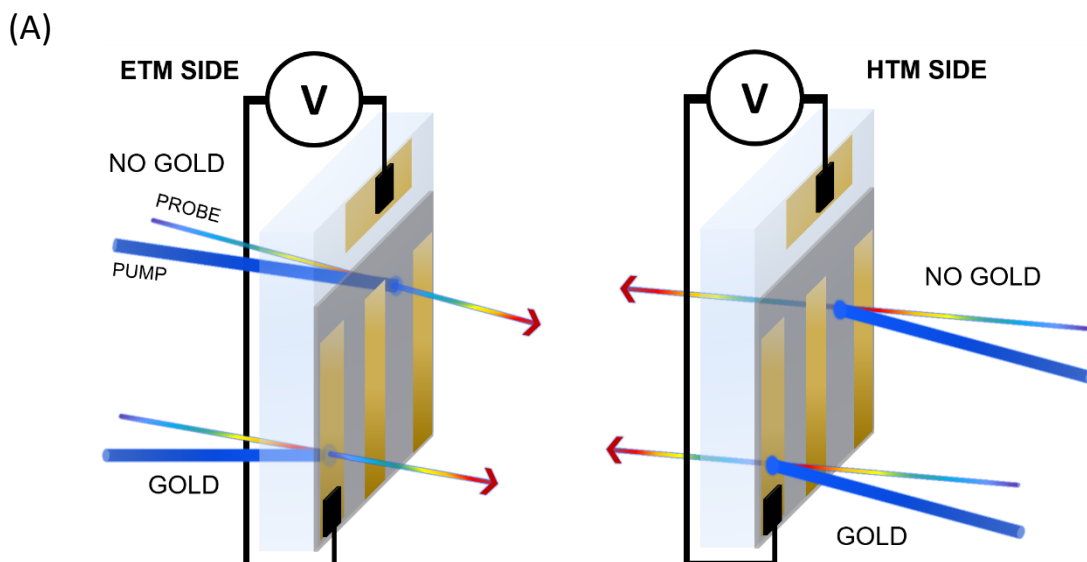
Scheme S1 A – Schematic presentation of the TA experiment configuration with and without gold from ETM or HTM side. B – Image of the TA experiment setup with bias voltage control. LED was added to the setup, when 1Sun illumination conditions were desired.
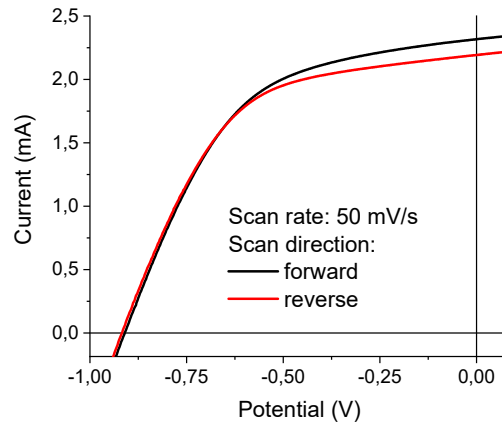
Figure S1 Current-voltage curve scanned in forward (from J_{sc} to V_{oc}) and reverse (from V_{oc} to J_{sc}) direction. Hysteresis index of the measured sample is equal to 0.04 ($HI = \frac{J_{rev}\left(\frac{V_{oc}}{2}\right) - J_{for}\left(\frac{V_{oc}}{2}\right)}{J_{rev}\left(\frac{V_{oc}}{2}\right)}$).
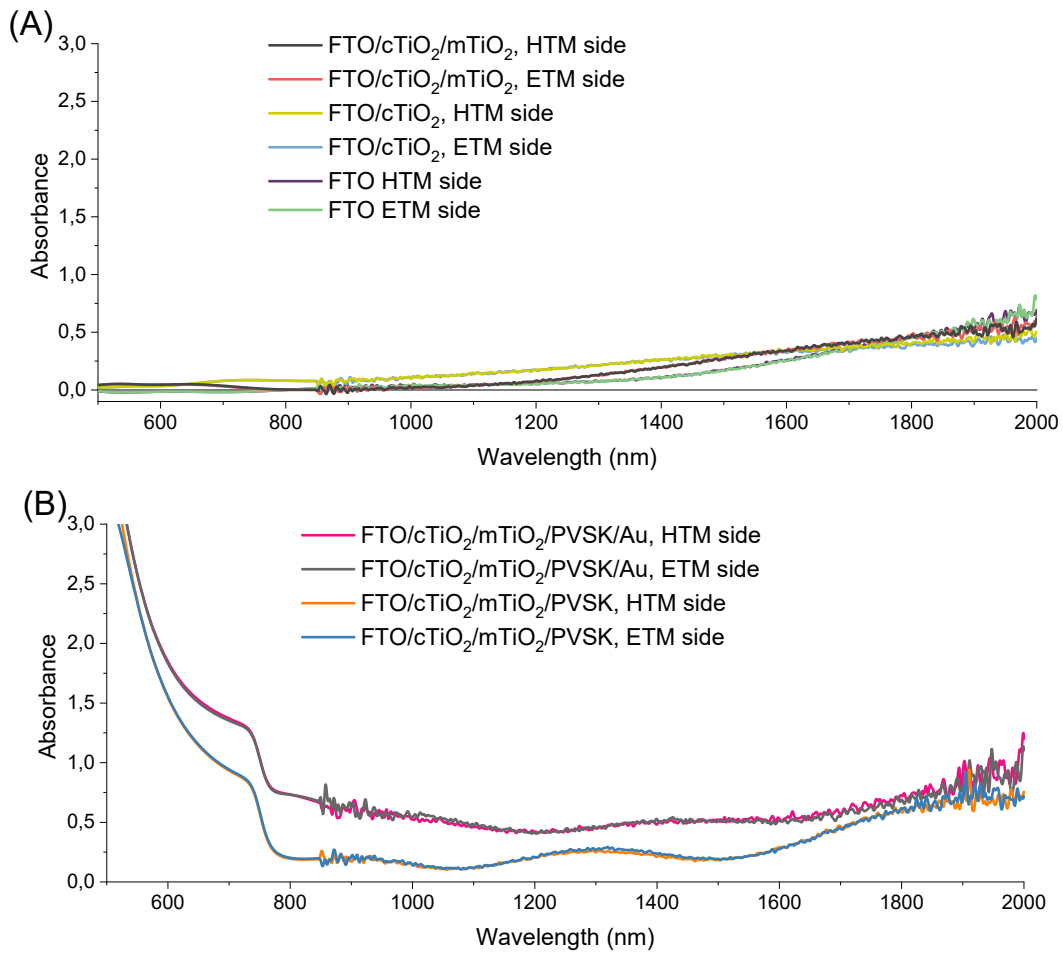
Figure S2 Steady state absorption spectra of the listed samples, excited from ETM or HTM side.
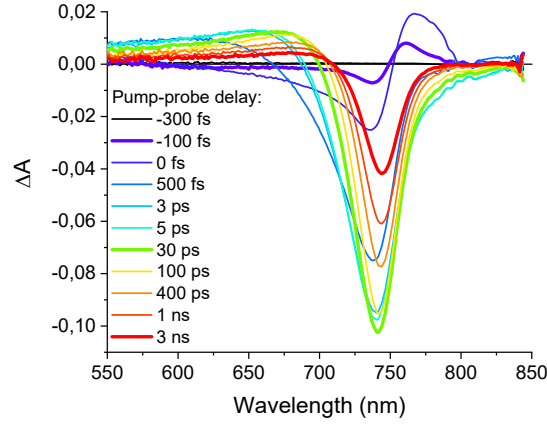
Figure S3 Femtosecond transient absorption spectra after certain pump-probe delay of a complete solar cell excited from the HTM side by 475 nm (30 µJ/cm²) laser pulse. Time "zero" corresponds to the maximum temporal pump-probe overlap.

Simplified calculations of spectral oscillations in the amplitude of stationary and transient absorption in the NIR range, based on the interference of light reflected from two main interfaces.

Below we present a simple simulation of the spectral oscillations observed in the absorption measurements in the NIR range. It is assumed that only a single perovskite layer of the thickness D contributes to the oscillations which appear due to the interference of the light reflected from the interfaces at both sides (one with FTO, the other with the air). The intensity of incident light as a function of the wavelength of light transmitted through a transparent film at normal incidence can be calculated from the formula:[1,2]

$$I(\lambda) = \frac{I_0(1-r)^2}{1+r^2-2r\cos(\frac{4\pi n_2 D}{\lambda})},$$
(S1)

where I_0 is the incident light intensity, n_2 is the index of refraction of the perovskite film, and r is the reflection coefficient, which can be calculated as:

$$r(\lambda) = \left(\frac{n_1-n_2}{n_1+n_2}\right)^2.$$
(S2)

The average refractive indexes in the NIR range are: n_1=1.35 for FTO, n_1=1.00 for air, and n_2=2.1 for perovskite.[3] Therefore, from eq. (S2) the mean reflection coefficients at PVSK/FTO

and PVSK/air interfaces are r=0.047 and r=0.126, respectively. The average reflection coefficient r=0.086 was used to calculate the light intensity $I(\lambda)$ from formula (S1), and then the absorbance was calculated from the relation $A(\lambda)$=log $(I_0/I(\lambda))$. The results for a perovskite of the thickness D=700 nm are shown in Figure S4A. Although the approximation is rough, the amplitudes of the oscillations and their periods are in qualitative good agreement with the experimental results of stationary absorption shown in Figures 1A and S2B.

The absorbance with the pump presence was calculated in the analogous way but the refractive index of perovskite (n_2) was decreased by the mean value of -0.003, reported by Pasanen et al. for a similar pump pulse energy density as used in our experiments.[4] As can be seen in Figure S4A, such a change in the refractive index of the film results in the red-shift of the absorption by 1-2 nm. The shift causes the appearance of the transient absorption signal with periodically changing negative and positive amplitudes (the period is the same as in stationary absorption). Figure S4B presents the transient absorption signal calculated from the formula $\Delta A = A_{with\ pump} - A_{no\ pump}$. Again, the agreement with the experimental spectra (Figure 1C) is quite good. Moreover, we calculated the transient absorption for 50 nm thinner and thicker perovskite film (Figure S4B). As seen, the maxima and minima undergo remarkable shifts, which can explain the variations of their positions in our experiments since the thickness of our perovskite film can vary by ±10 %.

(A)

(B)
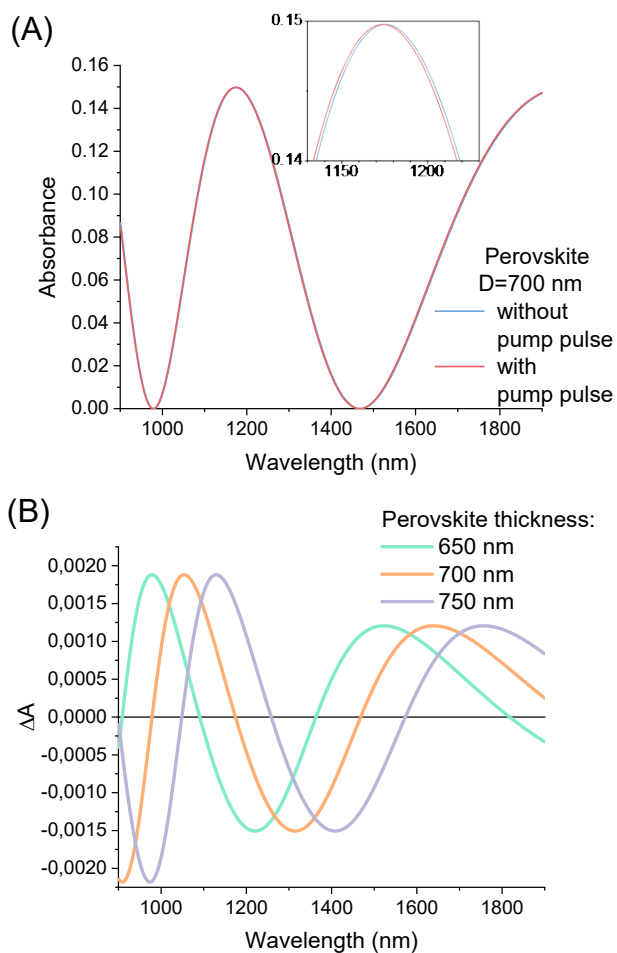
Figure S4 Simulated absorption signal according to Pasanen et al. with (red) and without (blue) pump (A) and transient absorption signal using eq.S1 for three different perovskite layer thicknesses (B).
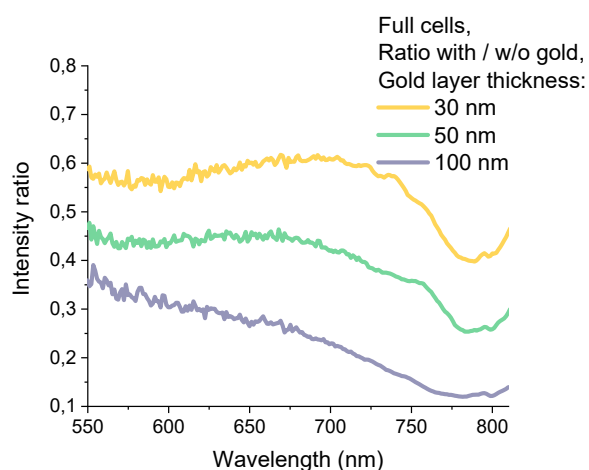
Figure S5 Intensity ratio of a complete cell with and without gold for three different gold thicknesses. Light source was provided by white light continuum of femtosecond transient absorption setup (probe).

Table 1 SEM images of different gold layer thicknesses right after deposition and after 80 days, deposited on FTO glass only and complete cell. Scale: ▭=100 nm

Substrate	Gold layer thickness	Fresh layer	80 days old layer
FTO glass	50 nm		
	100 nm		
Complete cell	50 nm		
	100 nm		
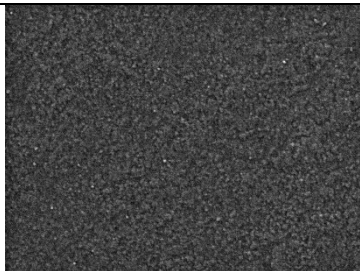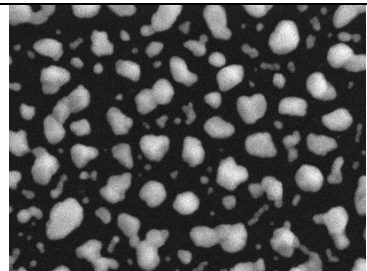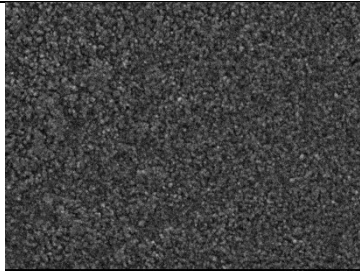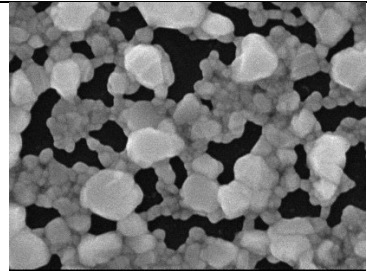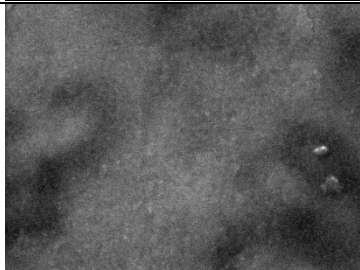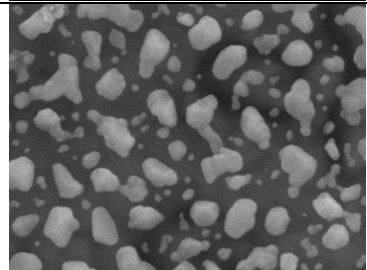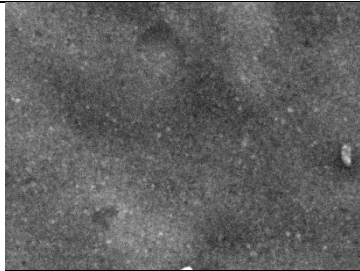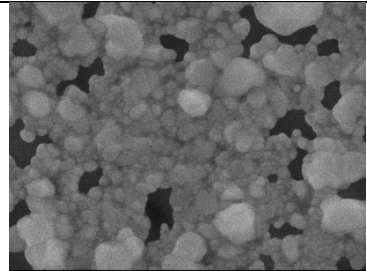
Table S2 Averaged (800-1200 nm) refractive index (n) of different PCS layer and reflectivity (R) of each PCS interface.
R=[(n₁-n₂)/(n₁+n₂)]². ³

layer	n		interface	R [%]
Air	1.00		air/glass	3.37
Glass	1.45		glass/FTO	0.06
FTO	1.52		FTO/cTiO$_2$	0.54
cTiO$_2$	1.76		cTiO$_2$/mTiO$_2$	1.14
mTiO$_2$	2.18		mTiO$_2$/PVSK	0.00
PVSK	2.18		PVSK/spiro	3.07
spiro-OMeTAD	1.53		spiro/Au	14.32
Au	0.69		Au/Air	3.36
Air	1.00		spiro/air (no Au)	4.39
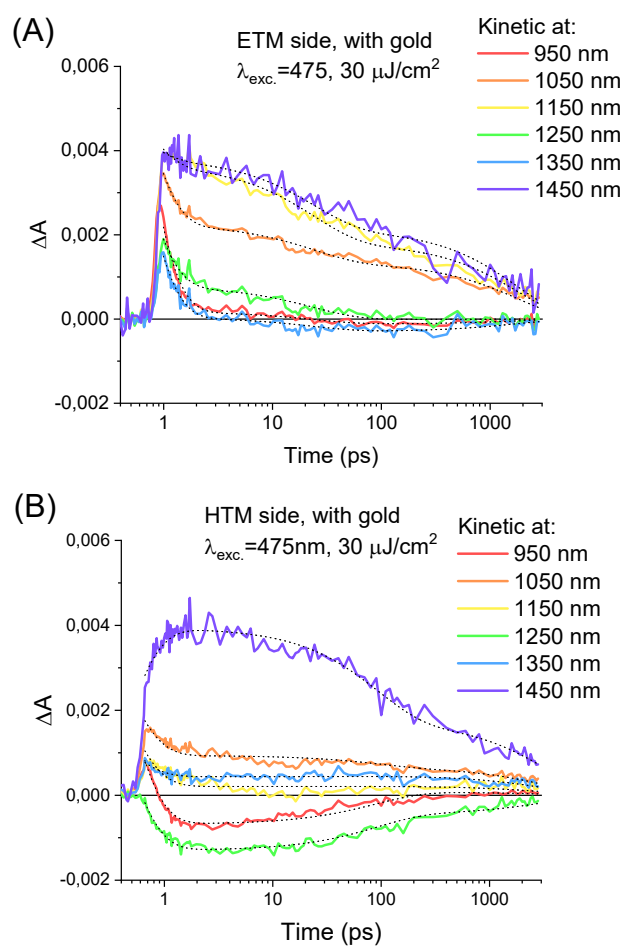
Figure S6 Kinetics of TA signal for complete cell with gold at different wavelengths, excited from the ETM (A) and HTM (B) side. Excitation wavelength: 495 nm, energy density: 30 μJ/cm². Black dotted lines in all figures shows multi-exponential fit with the parameters given at the end of the supporting information.
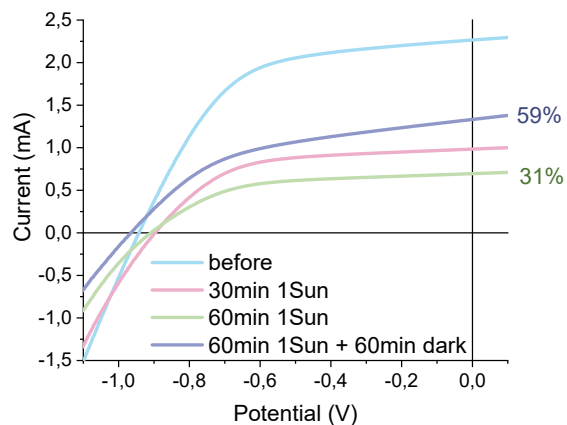
Figure S7 Current-voltage curve of exemplary sample before, after 30 and 60 min under 1Sun illumination (scan rate: 50 mV/s).
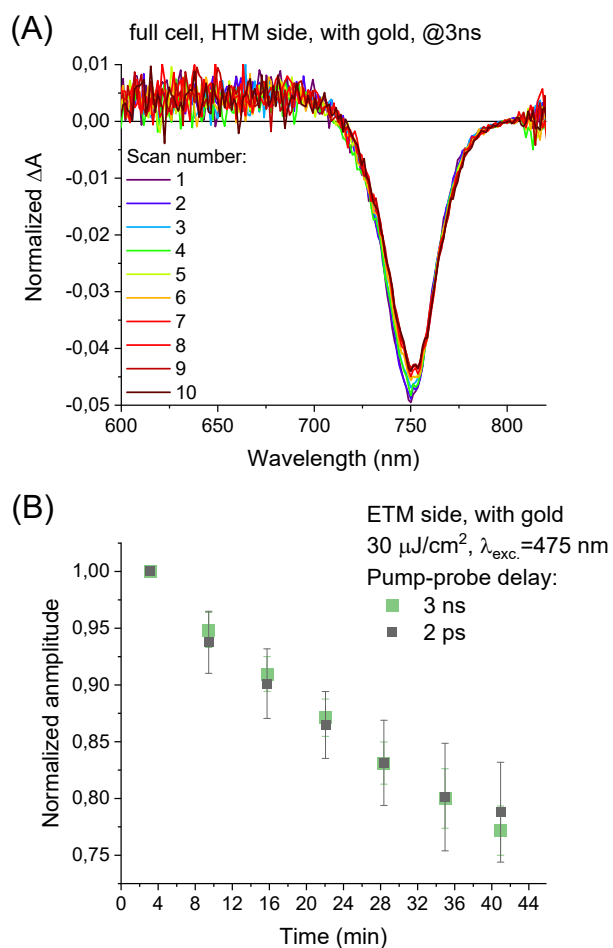
Figure S8 A – Transient absorption signal after 3 ns pump-probe delay for subsequent scans for a complete cell with gold electrode, excited from HTM side. B – its normalized amplitude at 2 ps and 3 ns.
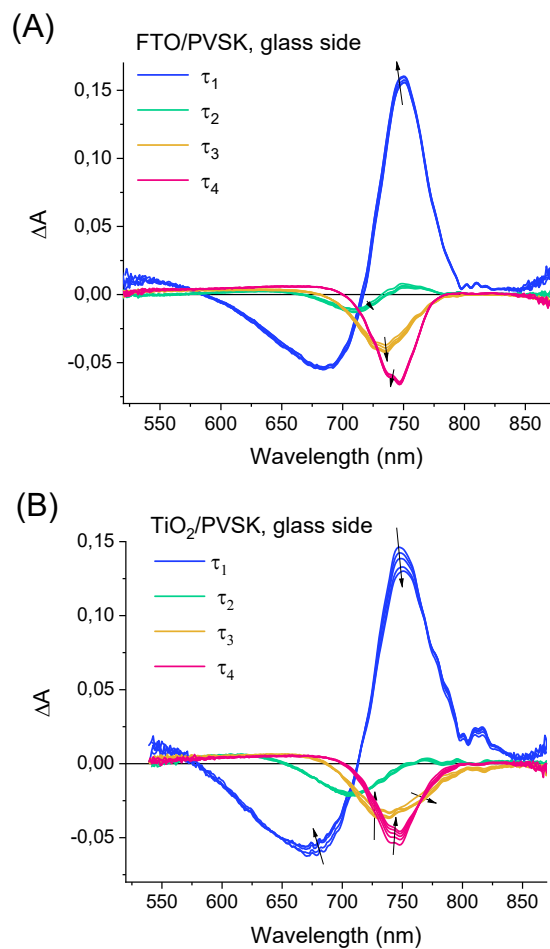
Figure S9 Pre-exponential factor spectra obtained from global analysis of subsequent scans pairs of glass/FTO/PVSK (A) and glass/TiO₂/PVSK samples, excited from glass side. Arrow indicates the direction of spectral changes in time (from scan to scan).

Table S3 4-exponential global analysis results for each averaged scan pair for glass/FTO/PVSK sample at glass side. The relative error of all time constants is 3-6%.

Averaged scan pair	Averaged experiment duration time [s]	τ_1 [fs]	τ_2 [ps]	τ_3 [ps]	τ_4 [ns]
1-2	189	370	11	219	4.3
3-4	567	370	12	224	4.4
5-6	945	370	12	208	4.3
7-8	1323	380	12	215	4.3
9-10	1701	380	12	225	4.3

Table S4 4-exponential global analysis results for each averaged scan pair for glass/TiO2/PVSK sample at glass side. The relative error of all time constants is 3-6%.

Averaged scan pair	Averaged experiment duration time [s]	τ_1 [fs]	τ_2 [ps]	τ_3 [ps]	τ_4 [ns]
1-2	189	380	13	140	4.0
3-4	567	380	11	128	3.9
5-6	945	390	9	125	3.9
7-8	1323	390	9	119	3.7
9-10	1701	380	8	121	3.7

(A) full cell, glass side, @2ps

(B)
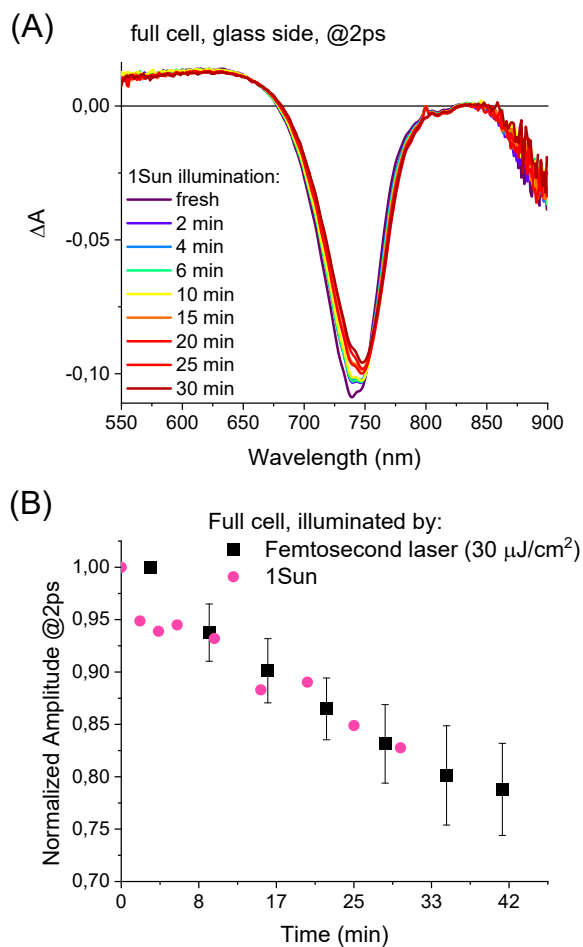
Figure S10 A – Transient absorption spectra after 2 ps pump-probe delay (single shot) without and after certain 1Sun illumination (provided by LED). B – Normalized minimum bleach amplitude of these spectra with a calibration plot (constructed in the same way as that from figure 4C)
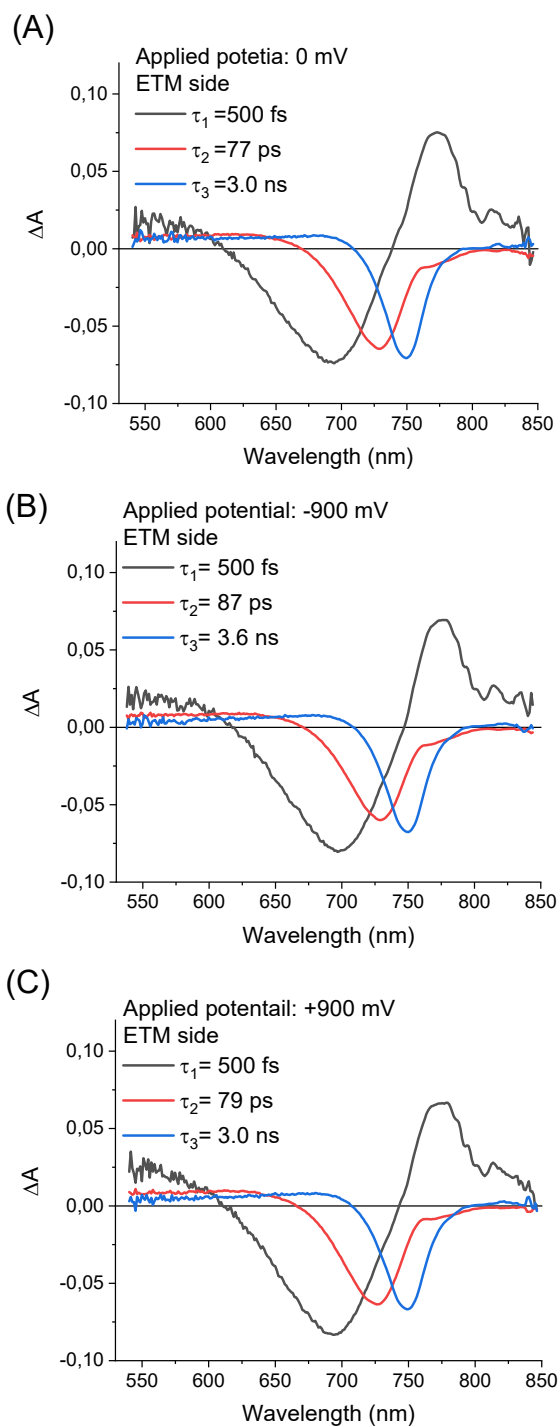
Figure S11 Results of a three-exponential global analysis (decay associated spectra) with the fixed shortest time constant (0.5 ps) for a complete cell with applied 0 mV (A), - 900 mV (B) and +900 mV (C) bias during experiment. The relative error of all time constants is 3-6%.
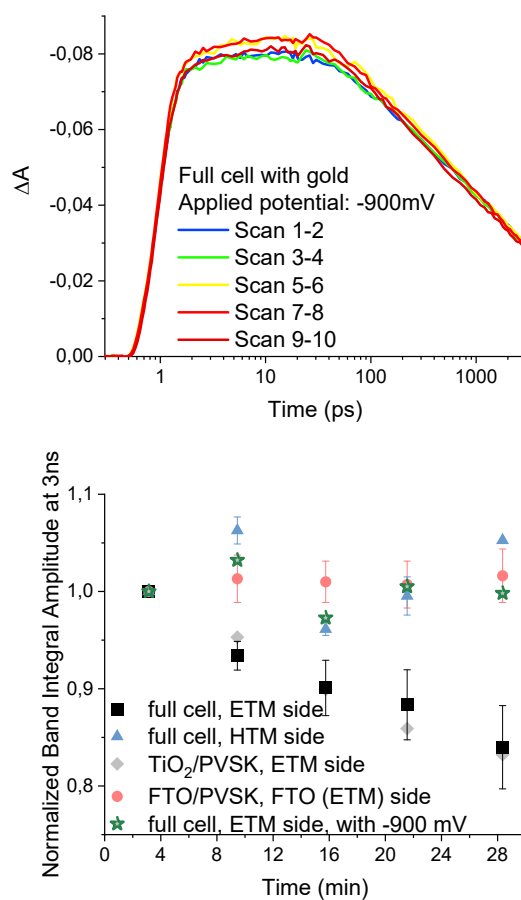
Figure S12 A – Minimum bleach kinetics for subsequent averaged scan pairs of complete cell with applied -900 mV during experiment. Excited from ETM side by 30 μJ/cm² pump (λ$_{exc.}$=475 nm). B – Normalized Band Integral Amplitude at 3 ns for the listed samples.

Parameters fitted to the kinetics:

3-exponential fit, equation: $y = y_0 + A_1 \exp\left(\frac{-(x-x_0)}{t_1}\right) + A_2 \exp\left(\frac{-(x-x_0)}{t_2}\right) + A_3 \exp\left(\frac{-(x-x_0)}{t_3}\right)$

Figure 3A: HTM side @740 nm, global fit:

	no gold	**with gold**
y_0	0 ± 0	0 ± 0
x_0	1.5 ± 0	1.5 ± 0
A_1	0.0163 ± 0.0005	0.0142 ± 0.0005
t_1	3.1 ± 0.2 ps	3.1 ± 0.2 ps
A_2	-0.0344 ± 0.001	-0.0390 ± 0.001
t_2	370 ± 20 ps	370 ± 20 ps
A_3	-0.069 ± 0.001	-0.066 ± 0.001
t_3	4800 ± 200 ps	4800 ± 200 ps

R-Square (COD)=0.997

Figure 3B: HTM side @810 nm, global fit:

	no gold	**with gold**
y_0	0 ± 0	0 ± 0
x_0	1.34 ± 0	1.34 ± 0
A_1	-0.0011 ± 0.0001	0.0043 ± 0.0001
t_1	0.30 ± 0.02 ps	0.30 ± 0.02 ps
A_2	0.00348 ± 0.0001	-0.00415 ± 0.0001
t_2	33.3 ± 1.7 ps	33.3 ± 1.7 ps
A_3	0.0037 ± 0.0001	-0.0021 ± 0.0001
t_3	1520 ± 70 ps	1520 ± 70 ps

R-Square (COD)=0.997

Figure 3C: 950-1450 nm, ETM side no gold, global fit:

	950 nm	**1050 nm**	**1150 nm**	**1250 nm**	**1350 nm**	**1450 nm**
y_0	0 ± 0	0 ± 0	0 ± 0	0 ± 0	0 ± 0	0 ± 0
x_0	1 ± 0	1 ± 0	1 ± 0	1 ± 0	1 ± 0	1 ± 0
A_1	7E-5 ± 6E-5	0.0018 ± 0.0001	7.7E-4 ± 0.6E-4	9.3E-4 ± 0.6E-4	9.3E-4 ± 0.6E-4	4.1E-4 ± 0.6E-4
t_1	0.37 ± 0.02 ps	0.37 ± 0.02 ps	0.37 ± 0.02 ps	0.37 ± 0.02 ps	0.37 ± 0.02 ps	0.37 ± 0.02 ps
A_2	0.0022 ± 0.0001	1.7E-4 ± 0.4E-4	9.4E-4 ± 0.4E-4	6.1E-4 ± 0.4E-4	9.4E-4 ± 0.4E-4	0.0020 ± 0.0001
t_2	23.9 ± 0.9 ps	23.9 ± 0.9 ps	23.9 ± 0.9 ps	23.9 ± 0.9 ps	23.9 ± 0.9 ps	23.9 ± 0.9 ps
A_3	0.0014 ± 0.0001	3.8E-4 ± 0.3E-4	0.0015 ± 0.0001	6.7E-4 ± 0.2E-4	4.7E-4 ± 0.2E-4	0.0011 ± 0.0001
t_3	2100 ± 70 ps	2100 ± 70 ps	2100 ± 70 ps	2100 ± 70 ps	2100 ± 70 ps	2100 ± 70 ps

R-Square (COD)=0.989

Figure 3D: 950-1450 nm, HTM side no gold, global fit:

	950 nm	**1050 nm**	**1150 nm**	**1250 nm**	**1350 nm**	**1450 nm**
y_0	0 ± 0	0 ± 0	0 ± 0	0 ± 0	0 ± 0	0 ± 0
x_0	0.86 ± 0	0.86 ± 0	0.86 ± 0	0.86 ± 0	0.86 ± 0	0.86 ± 0
A_1	5.7E-4 ± 0.4E-4	4.2E-4 ± 0.4E-4	5.6E-4 ± 0.4E-4	3E-5 ± 4E-5	-4.8E-4 ± 0.4E-4	-6.7E-4 ± 0.4E-4
t_1	1.7 ± 0.2 ps	1.7 ± 0.2 ps	1.7 ± 0.2 ps	1.7 ± 0.2 ps	1.7 ± 0.2 ps	1.7 ± 0.2 ps
A_2	6.5E-4 ± 0.5E-4	0.0012 ± 0.0001	5.3E-4 ± 0.4E-4	5E-5 ± 4E-5	5.6E-4 ± 0.5E-4	0.0016 ± 0.0001
t_2	120 ± 8 ps	120 ± 8 ps	120 ± 8 ps	120 ± 8 ps	120 ± 8 ps	120 ± 8 ps
A_3	7.6E-4 ± 0.4E-4	8.8E-4 ± 0.4E-4	4.0E-4 ± 0.3E-4	5.3E-4 ± 0.3E-4	9.9E-4 ± 0.4E-4	0.0013 ± 0.0001
t_3	3000 ± 200 ps	3000 ± 200 ps	3000 ± 200 ps	3000 ± 200 ps	3000 ± 200 ps	3000 ± 200 ps

R-Square (COD)=0.979

Figure S6A: 950-1450 nm, ETM side with gold, global fit:

	950 nm	**1050 nm**	**1150 nm**	**1250 nm**	**1350 nm**	**1450 nm**
y_0	0 ± 0	0 ± 0	0 ± 0	0 ± 0	0 ± 0	0 ± 0
x_0	1 ± 0	1 ± 0	1 ± 0	1 ± 0	1 ± 0	1 ± 0
A_1	0.0020 ± 0.0001	0.0012 ± 0.0001	4.5E-4 ± 0.8E-4	0.0011 ± 0.0001	0.0014 ± 0.0001	2.1E-4 ± 0.8E-4
t_1	0.41 ± 0.03 ps	0.41 ± 0.03 ps	0.41 ± 0.03 ps	0.41 ± 0.03 ps	0.41 ± 0.03 ps	0.41 ± 0.03 ps
A_2	2.8E-4 ± 0.6E-4	8.8E-4 ± 0.6E-4	0.0017 ± 0.0001	7.5-4 ± 0.6E-4	3.2-4 ± 0.6E-4	0.0016 ± 0.0001
t_2	23.6 ± 1.4 ps	23.6 ± 1.4 ps	23.6 ± 1.4 ps	23.6 ± 1.4 ps	23.6 ± 1.4 ps	23.6 ± 1.4 ps
A_3	-1.2E-4 ± 0.3E-4	0.0013 ± 0.0001	0.0018 ± 0.0001	-0.8E-5 ± 3E-5	-3.0E-4 ± 0.3E-4	0.0021 ± 0.0001
t_3	1770 ± 70 ps	1770 ± 70 ps	1770 ± 70 ps	1770 ± 70 ps	1770 ± 70 ps	1770 ± 70 ps

R-Square (COD)=0.987

Figure S6B: 950-1450 nm, HTM side with gold, global fit:

	950 nm	**1050 nm**	**1150 nm**	**1250 nm**	**1350 nm**	**1450 nm**
y_0	0 ± 0	0 ± 0	0 ± 0	0 ± 0	0 ± 0	0 ± 0
x_0	0.66 ± 0	0.66 ± 0	0.66 ± 0	0.66 ± 0	0.66 ± 0	0.66 ± 0
A_1	0.0015 ± 0.0001	8.2E-4 ± 0.7E-4	8.4E-4 ± 0.7E-4	0.0011 ± 0.0001	3.3E-4 ± 0.7E-4	-0.0011 ± 0.0001
t_1	0.29 ± 0.02 ps	0.29 ± 0.02 ps	0.29 ± 0.02 ps	0.29 ± 0.02 ps	0.29 ± 0.02 ps	0.29 ± 0.02 ps
A_2	-7.5E-4 ± 0.4E-4	2.7E-4 ± 0.5E-4	-1E-5 ± 4E-5	-8.4E-4 ± 0.5E-4	-3E-5 ± 4E-5	0.0022 ± 0.0001
t_2	89 ± 6 ps	89 ± 6 ps	89 ± 6 ps	89 ± 6 ps	89 ± 6 ps	89 ± 6 ps
A_3	8E-5 ± 3E-5	6.6E-4 ± 0.4E-4	2.2E-4 ± 0.3E-4	-4.6E-4 ± 0.3E-4	4.6-4 ± 0.3E-4	0.0017 ± 0.0001
t_3	3300 ± 300 ps	3300 ± 300 ps	3300 ± 300 ps	3300 ± 300 ps	3300 ± 300 ps	3300 ± 300 ps

R-Square (COD)=0.989

Parameters fitted to the kinetics:

4-exponential fit, equation:

$$y = y_0 + A_1 \exp\left(\frac{-(x-x_0)}{t_1}\right) + A_2 \exp\left(\frac{-(x-x_0)}{t_2}\right) + A_3 \exp\left(\frac{-(x-x_0)}{t_3}\right) + A_4 \exp\left(\frac{-(x-x_0)}{t_4}\right)$$

Figure 5A: band integral, ETM side no gold, global fit:

	-900 mV	**0 V**	**+900 mV**
y_0	0 ± 0	0 ± 0	0 ± 0
x_0	3 ± 0	3 ± 0	3 ± 0
A_1	0.0106 ± 0.0090	0.0099 ± 0.0091	0.0269 ± 0.0091
t_1	0.5 ± 0	0.5 ± 0	0.5 ± 0
A_2	0.3371 ± 0.0134	0.3862 ± 0.0144	0.3734 ± 0.0140
t_2	34 ± 2 ps	34 ± 2 ps	34 ± 2 ps
A_3	0.2911 ± 0.0114	0.3024 ± 0.0121	0.2934 ± 0.0118
t_3	278 ± 20 ps	278 ± 20 ps	278 ± 20 ps
A_4	0.3428 ± 0.0076	0.2901 ± 0.0068	0.2853 ± 0.0067
t_4	4920 ± 270 ps	4920 ± 270 ps	4920 ± 270 ps

R-Square (COD)=0.9993

Figure 5B: band integral, HTM side no gold, global fit:

	-900 mV	**0 mV**	**+900 mV**
y_0	0 ± 0	0 ± 0	0 ± 0
x_0	2.1 ± 0	2.1 ± 0	2.1 ± 0
A_1	0.1500 ± 0.0037	0.1364 ± 0.0036	0.1582 ± 0.0037
t_1	2.81 ± 0.10 ps	2.81 ± 0.10 ps	2.81 ± 0.10 ps
A_2	0.3074 ± 0.0062	0.3010 ± 0.0073	0.3010 ± 0.0068
t_2	51 ± 2 ps	51 ± 2 ps	51 ± 2 ps
A_3	0.2353 ± 0.0069	0.2750 ± 0.0064	0.2565 ± 0.0065
t_3	392 ± 25 ps	392 ± 25 ps	392 ± 25 ps
A_4	0.3052 ± 0.0083	0.2766 ± 0.0081	0.2828 ± 0.0080
t_4	4270 ± 220 ps	4270 ± 220 ps	4270 ± 220 ps

R-Square (COD)=0.9996

(Longer lifetimes for the samples at -900 mV are manifested as higher amplitudes of the longer and lower amplitudes of the shorter components with respect to the samples at 0mV and +900 mV bias)

(1)   Born, M.; Wolf, E. *Principles of Optics, 7th (Expanded) Edition*; 1999.

(2)   Huibers, P. D. T.; Shah, D. O. Multispectral Determination of Soap Film Thickness. *Langmuir* **1997**, *13* (22), 5995–5998.

(3)   Raoult, E.; Bodeux, R.; Jutteau, S.; Rives, S.; Yaiche, A.; Coutancier, D.; Rousset, J.; Collin, S. Optical Characterizations and Moddeling of Semitransparent Perovskite Solar Cells for Tandem Applications. In *36th European Photovoltaic Solar Energy Conference and Exhibition, Marseille, France*; 2019; Vol. 36, pp 757–763.

(4)   Pasanen, H. P.; Vivo, P.; Canil, L.; Abate, A.; Tkachenko, N. Refractive Index Change Dominates the Transient Absorption Response of Metal Halide Perovskite Thin Films in the near Infrared. *Phys. Chem. Chem. Phys.* **2019**, *21* (27), 14663–14670.

STATEMENTS OF THE CO-AUTHORS
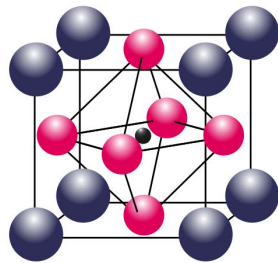
Poznań, dnia 29.06.2022r.

Katarzyna Pydzińska-Białek
Wydział Fizyki UAM,
ul. Uniwersytetu Poznańskiego 2,
61-614 Poznań
e-mail:
katarzyna.pydzinska@amu.edu.pl

Oświadczenie

Oświadczam, że jako autorka niniejszej rozprawy doktorskiej opartej o cykl opublikowanych artykułów naukowych, jestem współautorką wszystkich publikacji wchodzących w jej skład wraz z następującym udziałem:

1. K.Pydzińska, P.Florczak, G.Nowaczyk, M.Ziółek, *Effect of different small molecule hole transporters on the performance and charge transfer dynamics of perovskite solar cells*, Synthetic Metals, **232** (2017), 181-187

W powyższej pracy przygotowałam wszystkie badane ogniwa, wykonywałam samodzielnie lub brałam w udział we wszystkich przeprowadzonych eksperymentach, analizowałam dane, brałam udział w przygotowaniu manuskryptu.

2. K.Pydzińska, J.Karolczak, M.Szafrański, M.Ziółek, *Differences in photoinduced optical transients in perovskite absorbers for solar cells*, RSC Advances, **8** (2018), 6479-6487

Mój udział w publikacji polegał na przygotowaniu wszystkich badanych ogniw i większości próbek, wykonywałam samodzielnie lub brałam w udział we wszystkich przeprowadzonych eksperymentach, analizowałam dane, brałam udział w przygotowaniu manuskryptu.

3. K.Pydzińska-Białek, J.Szeremeta, K.Wojciechowski, M.Ziółek, *Insights into the Femtosecond to Nanosecond Charge Carrier Kinetics in Perovskite Materials for Solar Cells*, The Journal of Physical Chemistry C, **123** (2019), 110-119

W powyższej pracy wykonywałam samodzielnie lub brałam w udział we wszystkich przeprowadzonych eksperymentach na Wydziale Fizyki UAM, analizowałam dane, brałam udział w przygotowaniu manuskryptu.

4. B.Quere, K.Pydzińska-Białek, J.Karolczak, G.Nowaczyk, E.Coy, M.Ziółek, *Understanding the Effect of Different Synthesis Conditions on the Physicochemical Properties of Mixed-Ion Perovskite Solar Cells*, Chemistry-A European Journal, **25** (2019), 5978-5986

Mój udział w publikacji polegał na nadzorowaniu wytwarzania badanych ogniw, dodatkowej analizie danych i przygotowaniu manuskryptu.

5. K.Pydzinska-Białek, V.Drushliak, E.Coy, K.Załęski, J.Flach, J.Idigoras, L.Contreras-Bernal, A.Hagfeldt, J.A.Anta, M.Ziółek, *Understanding the interfaces between triple cation perovskite and electron or hole transporting material*, ACS Applied Material Interfaces, **12** (2020), 30399-30410.

Mój udział w publikacji polegał na przygotowaniu wszystkich badanych ogniw (na Politechnice w Lozannie jak i na Uniwersytecie Pablo Olavide w Sewilli). Wykonywałam samodzielnie lub brałam w udział w większości przeprowadzonych eksperymentach (poza technikami TEM i XRD), analizowałam dane oraz przygotowywałam manuskrypt.

6. K.Pydzińska-Białek, A.Glinka, V.Drushliak, G.Nowaczyk, P.Florczak, M.Ziółek, *Impact of improvements in mesoporous titania layers on ultrafast electron transfer dynamics in perovskite and dye-sensitized solar cells*, Physical Chemistry Chemical Physics, **22** (2020), 21947-21960

Mój udział w powyższej publikacji związany był z częścią dotyczącą fotoogniw perowskitowych. Nadzorowałam ich przygotowanie, uczestniczyłam w pomiarach i analizie uzyskanych wyników, a także brałam udział w korekcie manuskryptu.

7. K.Pydzińska-Białek, G.Nowaczyk, M.Ziółek, *Complete Perovskite Solar Cells with Gold Electrodes Studied in the Visible and Near-infrared Range*, ACS Chemistry of Materials, (2022), DOI: 10.1021/acs.chemmater.2c00845

Mój udział w publikacji polegał na przygotowaniu wszystkich badanych ogniw. Wykonywałam samodzielnie lub brałam w udział we wszystkich przeprowadzonych eksperymentach, analizowałam dane oraz przygotowywałam manuskrypt.

Poznań, dnia 26.04.2022

Prof. UAM dr hab. Emerson Coy

Centrum NanoBioMedyczne UAM,

ul. Wszechnicy Piastowskiej 3,

61-614 Poznań

e-mail: coyeme@amu.edu.pl

Oświadczenie o współautorstwie w publikacjach

Oświadczam, że jestem współautorem następujących publikacji, które weszły w skład rozprawy doktorskiej lic. Katarzyny Pydzińskiej-Białek:

1. B. Quere, K. Pydzińska-Białek, J. Karolczak, G. Nowaczyk, E. Coy, M. Ziółek, *Understanding the Effect of Different Synthesis Conditions on the Physicochemical Properties of Mixed-Ion Perovskite Solar Cells*, Chem. Eur. J., **25** (2019) 5978-5986.

2. K.Pydzinska-Białek, V.Drushliak, E.Coy, K.Załęski, J.Flach, J.Idigoras, L.Contreras-Bernal, A.Hagfeldt, J.A.Anta, M.Ziółek, *Understanding the interfaces between triple cation perovskite and electron or hole transporting material*, ACS Appl. Mater. Interfaces, **12** (2020) 30399-30410.

Mój udział w pierwszej publikacji związany był z przeprowadzeniem i analizą eksperymentów spektroskopii rentgenowskiej oraz edycją manuskryptu.

Mój udział w drugiej publikacji związany był z częścią badań dotyczącą mikroskopii elektronowej oraz spektroskopii rentgenowskiej. Przeprowadziłem eksperymenty, analizę ich wyników, a także brałem udział w korekcie manuskryptu.

Poznań, dnia 26.04.2022

Mgr Viktoriia Drushliak
Wydział Fizyki UAM,
ul. Uniwersytetu Poznańskiego 2,
61-614 Poznań
e-mail: vikdru@amu.edu.pl

Oświadczenie o współautorstwie w publikacjach

Oświadczam, że jestem współautorką następujących publikacji, które weszły w skład rozprawy doktorskiej lic. Katarzyny Pydzińskiej-Białek:

1. K.Pydzinska-Białek, V.Drushliak, E.Coy, K.Załęski, J.Flach, J.Idigoras, L.Contreras-Bernal, A.Hagfeldt, J.A.Anta, M.Ziółek, *Understanding the interfaces between triple cation perovskite and electron or hole transporting material*, ACS Applied Material Interfaces, **12** (2020), 30399-30410.

2. K.Pydzińska-Białek, A.Glinka, V.Drushliak, G.Nowaczyk, P.Florczak, M.Ziółek, *Impact of improvements in mesoporous titania layers on ultrafast electron transfer dynamics in perovskite and dye-sensitized solar cells*, Physical Chemistry Chemical Physics, **22** (2020), 21947-21960.

Mój udział w pierwszej publikacji polegał na uczestnictwie w wybranych pomiarach i analizie części uzyskanych wyników, a także brałam udział w korekcie manuskryptu.

Mój udział w drugiej publikacji związany był z częścią dotyczącą fotoogniw perowskitowych. Uczestniczyłam w ich przygotowaniu, pomiarach i analizie uzyskanych wyników, a także brałam udział w edycji manuskryptu.

Viktoriia Drushliak

Dr Patryk Florczak

Centrum NanoBioMedyczne UAM,

ul. Wszechnicy Piastowskiej 3,

61-614 Poznań

e-mail: patryk84@amu.edu.pl

Oświadczenie o współautorstwie w publikacjach

Oświadczam, że jestem współautorem następujących publikacji, które weszły w skład rozprawy doktorskiej lic. Katarzyny Pydzińskiej-Białek:

1. K.Pydzińska, P. Florczak, G.Nowaczyk, M.Ziółek, *Effect of different small molecule hole transporters on the performance and charge transfer dynamics of perovskite solar cells*, Synthetic Metals, **232** (2017), 181-187

2. K.Pydzińska-Białek, A.Glinka, V.Drushliak, G.Nowaczyk, P.Florczak, M.Ziółek, *Impact of improvements in mesoporous titania layers on ultrafast electron transfer dynamics in perovskite and dye-sensitized solar cells*, Physical Chemistry Chemical Physics, **22** (2020), 21947-21960

Mój udział w powyższych publikacjach polegał na pomocy przy przygotowaniu fotoogniw perowskitowych w atmosferze beztlenowej w komorze rękawicowej.

Patryk Florczak

Dr inż. Adam Glinka
Wydział Fizyki UAM,
ul. Uniwersytety Poznańskiego 2,
61-614 Poznań
e-mail: adam.glinka@amu.edu.pl

Poznań, dnia 26.04.2022r.

Oświadczenie o współautorstwie w publikacji

Oświadczam, że jestem współautorem następującej publikacji, która weszła w skład rozprawy doktorskiej lic. Katarzyny Pydzińskiej-Białek:

K. Pydzińska-Białek, A. Glinka, V. Drushliak, G. Nowaczyk, P. Florczak, M. Ziółek, *Impact of improvements in mesoporous titania layers on ultrafast electron transfer dynamics in perovskite and dye-sensitized solar cells*, Phys. Chem. Chem. Phys., **22** (2020) 21947-21960.

Mój udział w powyższej publikacji związany był z częścią dotyczącą fotoogniw barwnikowych. Uczestniczyłem w ich przygotowaniu, pomiarach i analizie uzyskanych wyników, a także brałem udział w edycji manuskryptu.

259

Dr Grzegorz Nowaczyk
Centrum NanoBioMedyczne UAM,
ul. Wszechnicy Piastowskiej 3,
61-614 Poznań
e-mail: nowag@amu.edu.pl

Poznań, dnia 26.04.2022r.

Oświadczenie o współautorstwie w publikacjach

Oświadczam, że jestem współautorem następujących publikacji, które weszły w skład rozprawy doktorskiej lic. Katarzyny Pydzińskiej-Białek:

1. K.Pydzińska, P. Florczak, G.Nowaczyk, M.Ziółek, *Effect of different small molecule hole transporters on the performance and charge transfer dynamics of perovskite solar cells*, Synthetic Metals, **232** (2017), 181-187

2. B.Quere, K.Pydzińska-Białek, J.Karolczak, G.Nowaczyk, E.Coy, M.Ziółek, *Understanding the Effect of Different Synthesis Conditions on the Physicochemical Properties of Mixed-Ion Perovskite Solar Cells*, Chemistry-A European Journal, **25** (2019), 5978-5986

3. K.Pydzińska-Białek, A.Glinka, V.Drushliak, G.Nowaczyk, P.Florczak, M.Ziółek, *Impact of improvements in mesoporous titania layers on ultrafast electron transfer dynamics in perovskite and dye-sensitized solar cells*, Physical Chemistry Chemical Physics, **22** (2020), 21947-21960

4. K.Pydzińska-Białek, G.Nowaczyk, M.Ziółek, *Complete Perovskite Solar Cells with Gold Electrodes Studied in the Visible and Near-infrared Range*, ACS Chemistry of Materials, (2022), under review

Mój udział w powyższych publikacjach polegał na wykonaniu zdjęć fotoogniw za pomocą techniki SEM (Scanning Electron Microscopy) oraz pomocy przy nakładaniu złotych elektrod na fotoogniwa.

260

27.04.2022

Brian Quere

e-mail: quere.b@laposte.net

Co-author statement

I declare that I'm a co-author of the following publication:

B.Quere, K.Pydzińska-Białek, J.Karolczak, G.Nowaczyk, E.Coy, M.Ziółek, *Understanding the Effect of Different Synthesis Conditions on the Physicochemical Properties of Mixed-Ion Perovskite Solar Cells*, Chemistry-A European Journal, **25** (2019), 5978-5986.

My contribution in the above paper consisted of fabrication of the perovskite solar cell samples, participation in the spectroscopic and structural studies of the samples, and analysis of their results. This work has been done as a part of my Master Degree thesis.

Signature:

Poznań, dnia 26.04.2022

Prof. dr hab. Marek Szafrański

Wydział Fizyki UAM,

ul. Uniwersytetu Poznańskiego 2,

61-614 Poznań

e-mail: masza@amu.edu.pl

Oświadczenie o współautorstwie w publikacji

Oświadczam, że jestem współautorem następującej publikacji, która weszła w skład rozprawy doktorskiej lic. Katarzyny Pydzińskiej-Białek:

K.Pydzińska, J.Karolczak, M.Szafrański, M.Ziółek, *Differences in photoinduced optical transients in perovskite absorbers for solar cells*, RSC Advances, **8** (2018), 6479-6487

Mój udział w powyższej publikacji związany był z dostarczeniem kryształów $MAPbI_3$ oraz edycją manuskryptu.

M. Szafrański

Dr Konrad Wojciechowski

Technology Center Saule Technologies,

ul. Duńska 11,

54-427 Wrocław

e-mail:

konrad.wojciechowski@sauletech.com

Oświadczenie o współautorstwie w publikacji

Oświadczam, że jestem współautorem następującej publikacji, która weszła w skład rozprawy doktorskiej lic. Katarzyny Pydzińskiej-Białek:

K.Pydzińska-Białek, J.Szeremeta, K.Wojciechowski, M.Ziółek, *Insights into the Femtosecond to Nanosecond Charge Carrier Kinetics in Perovskite Materials for Solar Cells*, The Journal of Physical Chemistry C, **123** (2019), 110-119

Mój udział w powyższej publikacji związany był z dostarczeniem próbek do badań, nadzorem merytorycznym oraz korektą manuskryptu.

Poznań, dnia 26.04.2022

Dr Karol Załęski

Centrum NanoBioMedyczne UAM,

ul. Wszechnicy Piastowskiej 3,

61-614 Poznań

e-mail: zaleski@amu.edu.pl

Oświadczenie o współautorstwie w publikacji

Oświadczam, że jestem współautorem następującej publikacji, która weszła w skład rozprawy doktorskiej lic. Katarzyny Pydzińskiej-Białek:

K.Pydzinska-Białek, V.Drushliak, E.Coy, K.Załęski, J.Flach, J.Idigoras, L.Contreras-Bernal, A.Hagfeldt, J.A.Anta, M.Ziółek, *Understanding the interfaces between triple cation perovskite and electron or hole transporting material*, ACS Applied Material Interfaces, **12** (2020), 30399-30410.

Mój udział w powyższej publikacji związany był z częścią badań dotyczącą mikroskopii elektronowej oraz spektroskopii rentgenowskiej. Uczestniczyłam w ich wykonaniu oraz analizie, a także brałam udział w korekcie manuskryptu.

Poznań, dnia 26.04.2022

Prof. dr hab. Marcin Ziółek
Wydział Fizyki UAM,
ul. Uniwersytetu Poznańskiego 2,
61-614 Poznań
e-mail: marziol@amu.edu.pl

Oświadczenie o współautorstwie w publikacjach

W związku z rozprawą doktorską lic. Katarzyny Pydzińskiej-Białek, której jestem promotorem, oświadczam, że jestem współautorem następujących publikacji, które weszły w skład jej rozprawy doktorskiej:

1. K.Pydzińska, P.Florczak, G.Nowaczyk, M.Ziółek, *Effect of different small molecule hole transporters on the performance and charge transfer dynamics of perovskite solar cells*, Synthetic Metals, **232** (2017), 181-187.

2. K.Pydzińska, J.Karolczak, M.Szafrański, M.Ziółek, *Differences in photoinduced optical transients in perovskite absorbers for solar cells*, RSC Advances, **8** (2018), 6479-6487.

3. K.Pydzińska-Białek, J.Szeremeta, K.Wojciechowski, M.Ziółek, *Insights into the Femtosecond to Nanosecond Charge Carrier Kinetics in Perovskite Materials for Solar Cells*, The Journal of Physical Chemistry C, **123** (2019), 110-119.

4. B.Quere, K.Pydzińska-Białek, J.Karolczak, G.Nowaczyk, E.Coy, M.Ziółek, *Understanding the Effect of Different Synthesis Conditions on the Physicochemical Properties of Mixed-Ion Perovskite Solar Cells*, Chemistry-A European Journal, **25** (2019), 5978-5986.

5. K.Pydzinska-Białek, V.Drushliak, E.Coy, K.Załęski, J.Flach, J.Idigoras, L.Contreras-Bernal, A.Hagfeldt, J.A.Anta, M.Ziółek, *Understanding the interfaces between triple cation perovskite and electron or hole transporting material*, ACS Applied Material Interfaces, **12** (2020), 30399-30410.

6. K.Pydzińska-Białek, A.Glinka, V.Drushliak, G.Nowaczyk, P.Florczak, M.Ziółek, *Impact of improvements in mesoporous titania layers on ultrafast electron transfer dynamics in perovskite and dye-sensitized solar cells*, Physical Chemistry Chemical Physics, **22** (2020), 21947-21960.

7. K.Pydzińska-Białek, G.Nowaczyk, M.Ziółek, *Complete Perovskite Solar Cells with Gold Electrodes Studied in the Visible and Near-infrared Range*, ACS Chemistry of Materials, (2022), w trakcie recenzji.

Mój udział w powyższych publikacjach polegał na sprawowaniu merytorycznej opieki nad pomiarami, dyskusji wyników, uczestniczeniu w pomiarach z użyciem femtosekundowej absorpcji przejściowej i analizie uzyskanych wyników, a także na pisaniu fragmentów manuskryptów i ich korekcie.

M. Ziółek

Prof. dr hab. Marcin Ziółek
Wydział Fizyki UAM,
ul. Uniwersytetu Poznańskiego 2,
61-614 Poznań
e-mail: marziol@amu.edu.pl

Oświadczenie o współautorstwie ś. p. dr. Jerzego Karolczaka

W związku z rozprawą doktorską lic. Katarzyny Pydzińskiej-Białek, której jestem promotorem, oświadczam, że ś.p. dr Jerzy Karolczak był współautorem następujących publikacji, które weszły w skład jej rozprawy doktorskiej:

1. K. Pydzińska, J. Karolczak, M. Szafrański, M. Ziółek, *Differences in photoinduced optical transients in perovskite absorbers for solar cells*, RSC Advances, **8** (2018), 6479-6487.
2. B. Quere, K. Pydzińska-Białek, J. Karolczak, G. Nowaczyk, E. Coy, M. Ziółek, *Understanding the Effect of Different Synthesis Conditions on the Physicochemical Properties of Mixed-Ion Perovskite Solar Cells*, Chemistry-A European Journal, **25** (2019), 5978-5986.

Jako autor korespondencyjny powyższych publikacji oświadczam, że udział ś. p. dr. Jerzego Karolczaka w ich powstaniu polegał na wykonywaniu lub nadzorowaniu pomiarów zaników fluorescencyjnych oraz na pomocy przy dopasowywaniu funkcji wielowykładniczych do zmierzonych zaników.

M. Ziółek

Poznań, dnia 31.05.2022

Prof. dr hab. Marcin Ziółek
Wydział Fizyki UAM,
ul. Uniwersytetu Poznańskiego 2,
61-614 Poznań
e-mail: marziol@amu.edu.pl

Oświadczenie o współautorstwie dr. Janusza Szeremety

W związku z rozprawą doktorską lic. Katarzyny Pydzińskiej-Białek, której jestem promotorem, oświadczam, że dr Janusz Szeremeta jest współautorem następującej publikacji, która weszła w skład rozprawy doktorskiej:

K. Pydzińska-Białek, J. Szeremeta, K. Wojciechowski, M. Ziółek, *Insights into the Femtosecond to Nanosecond Charge Carrier Kinetics in Perovskite Materials for Solar Cells*, The Journal of Physical Chemistry C, **123** (2019), 110-119.

Jako autor korespondencyjny powyższej publikacji oświadczam, że udział dr Janusza Szeremety w ich powstaniu polegał na przygotowaniu próbek do badań, wykonaniu ich charakterystyki morfologiczno-strukturalnej (SEM oraz XRD), a także charakterystyki prądowo-napięciowej i wyznaczeniu parametrów fotowoltaicznych dla tych próbek, które były pełnymi ogniwami słonecznymi. Nie udało nam się skontaktować z dr. Szeremetą i uzyskać oświadczenie bezpośrednio od niego. Nie pracuje on już w Saule Technologies, gdzie był zatrudniony w czasie naszej współpracy, jego poprzedni przełożony nie ma aktualnych danych kontaktowych, a pisząc na poprzednie adresy mailowe nie uzyskaliśmy żadnej odpowiedzi.

M. Ziółek

Declaration

Oświadczenie

Ja, niżej podpisana, Katarzyna Pydzińska-Białek, doktorantka Wydziału Fizyki Uniwersytetu im. Adama Mickiewicza w Poznaniu oświadczam, że przedkładaną rozprawę doktorską pt.:

Determination of Charge Transfer and Recombination Dynamics in Perovskite Solar Cells

Napisałam samodzielnie. Oznacza to, że przy pisaniu pracy, poza niezbędnymi konsultacjami, nie korzystałam z pomocy innych osób, a w szczególności nie zleciłam opracowania rozprawy lub jej istotnych części innym osobom, ani nie odpisywałam tej rozprawy lub jej istotnych części od innych osób.

Równocześnie wyrażam zgodę na to, że w sytuacji gdyby powyższe oświadczenie okazało się nieprawdziwe, decyzja o nadaniu mi stopnia naukowego doktora zostanie cofnięta.

Katarzyna Pydzińska-Białek